Developments for the observation and characterization of gravitational wave multi-messenger sources during LIGO-Virgo-KAGRA observation campaigns

Ramodgwendé Weizmann Kiendrébéogo

UNIVERSITÉ CÔTE D'AZUR | ÉCOLE DOCTORALE SCIENCES FONDAMENTALE ET APPLIQUÉES

UNIVERSITÉ JOSEPH KI-ZERBO

THÈSE DE DOCTORAT

Développements pour l'observation et la caractérisation des sources multi-messagers d'ondes gravitationnelles lors des campagnes d'observation LIGO-Virgo-KAGRA

Ramodgwendé Weizmann KIENDRÉBÉOGO

Artemis UMR 7250, Observatoire de la Côte d'Azur

Présentée en vue de l'obtention du grade de docteur en Sciences de la Planète et de l'Univers d'Université Côte d'Azur et de l'Université Joseph KI-ZERBO

Dirigée par : Nelson Christensen / Jean KOULIDIATI, Pr.
Soutenue le : 25 Septembre 2024 à Nice

Devant le jury, composé de :
S. Zacharie KAM, Pr., Université Joseph KI-ZERBO (Examinateur)
Antoine BERE, Pr., Université Joseph KI-ZERBO (Examinateur)
Marie-Anne Bizouard, DR., Université Côte d'Azur (Examinatrice)
Jean KOULIDIATI, Pr., Université Joseph KI-ZERBO (Directeur de thèse)
Nelson Christensen, DR., Université Côte d'Azur (Directeur de thèse)
Nicolas Leroy, DR., Université Paris-Saclay (Rapporteur)
Alain Klotz , Pr., Université Paul Sabatier-Toulouse III (Rapporteur)
Michael, coughlin, Prof., University of Minnesota (Invité)
Irina Dvorkin, Mc., Institut d'Astrophysique de Paris (Invitée)

UNIVERSITÉ CÔTE D'AZUR | ÉCOLE DOCTORALE SCIENCES FONDAMENTALE ET APPLIQUÉES

UNIVERSITÉ JOSEPH KI-ZERBO

THÈSE DE DOCTORAT

Developments for the observation and characterization of gravitational wave multi-messenger sources during LIGO-Virgo-KAGRA observation campaigns

Ramodgwendé Weizmann KIENDRÉBÉOGO

Laboratoire de Physique et de Chimie de l'Environnement, Université Joseph KI-ZERBO, Ouagadougou, Burkina Faso

Presented for the purpose of obtaining the degree of Doctor in Sciences et Technologies: Astrophysique from Université Joseph KI-ZERBO

Supervised by: Nelson Christensen / Jean KOULIDIATI, Prof.
Defended on: September 25, 2024, in Nice

In front of the jury, composed of:
S. Zacharie KAM, Prof., Université Joseph KI-ZERBO (Examiner)
Antoine BERE, Prof., Université Joseph KI-ZERBO (Examiner)
Marie-Anne Bizouard, DR., Université Côte d'Azur (Examiner)
Jean KOULIDIATI, Prof., Université Joseph KI-ZERBO (Thesis Advisor)
Nelson Christensen, DR., Université Côte d'Azur (Thesis Advisor)
Nicolas Leroy, DR., Université Paris-Saclay (Reviewer)
Alain Klotz, Prof., Université Paul Sabatier-Toulouse III (Reviewer)
Michael Coughlin, Prof., University of Minnesota (Invited)
Irina Dvorkin, Mc., Institut d'Astrophysique de Paris (Invited)

Développements pour l'observation et la caractérisation des sources multi-messagers d'ondes gravitationnelles lors des campagnes d'observation LIGO-Virgo-KAGRA

Developments for the observation and characterization of gravitational wave multi-messenger sources during LIGO-Virgo-KAGRA observation campaigns.

Jury :

Présidente du jury :
Marie-Anne Bizouard, Directrice de Recherche, Laboratoire Artemis, Observatoire de la Côte d'Azur, Université Côte d'Azur, Nice

Rapporteurs :
Nicolas Leroy, Directeur de Recherche, Université Paris-Saclay
Alain Klotz, Professeur, Université Paul Sabatier-Toulouse III

Examinateurs :
S. Zacharie KAM, Professeur, Laboratoire de Physique et de Chimie de l'Environnement, Université Joseph KI-ZERBO, Ouagadougou, Burkina Faso
Antoine BERE, Pofesseur Titulaire, Laboratoire de Physique et de Chimie de l'Environnement, Université Joseph KI-ZERBO, Ouagadougou, Burkina Faso

Directeurs de thèse :
Jean KOULIDIATI, Pofesseur Titulaire, Laboratoire de Physique et de Chimie de l'Environnement, Université Joseph KI-ZERBO, Ouagadougou, Burkina Faso
Nelson Christensen, Directeur de Recherche, Laboratoire Artemis, Observatoire de la Côte d'Azur, Université Côte d'Azur, Nice

Invités :
Michael Coughlin, Professeur assistant, School of Physics and Astronomy, University of Minnesota
Irina Dvorkin, Maître de conférences, Institut d'Astrophysique de Paris

Résumé

***

Développements pour l'observation et la caractérisation des sources multi-messagers d'ondes gravitationnelles lors des campagnes d'observation LIGO-Virgo-KAGRA.

Les campagnes d'observation Advanced LIGO/Virgo ont révélé la physique riche et diverse des fusions d'étoiles à neutrons binaires et de trous noirs binaires. En 2017, la découverte simultanée des ondes gravitationnelles et des contreparties électromagnétiques d'une fusion d'étoiles à neutrons binaires a offert une vision détaillée de ce phénomène extrême, avec de nombreux résultats en astrophysique et en physique, notamment sur le comportement de la matière ultra-dense. Cependant, malgré d'énormes efforts déployés, aucune nouvelle détection multi-messagers n'a été réalisée depuis lors. Cela s'explique par le formidable défi observationnel que représentent les alertes rapides et précises des ondes gravitationnelles, la réactivité immédiate d'un réseau de télescopes et le traitement en ligne des données pour l'identification des contreparties électromagnétiques.

L'identification des contreparties électromagnétiques permet de nombreuses études scientifiques de premier plan, comme les contraintes sur l'équation d'état des étoiles à neutrons, la mesure du taux d'expansion de l'univers ainsi que le processus de désintégration radioactive des éléments lourds produits lors de la kilonova. Pour un suivi rapide des contreparties possibles de ces événements, nous devons réduire la zone de localisation du ciel où l'événement a lieu. Mais les sensibilités très différentes des détecteurs montrent à quel point le suivi des ondes gravitationnelles peut être difficile. C'est le cas pour la quatrième (en cours) et la cinquième campagnes d'observation LIGO/Virgo/KAGRA. De nombreux signaux d'ondes gravitationnelles issus de la fusion de binaires compactes se trouvent cachés par le bruit des détecteurs et peuvent être détectés si le bruit est suffisamment réduit. Pour maximiser les résultats scientifiques des détecteurs d'ondes gravitationnelles LIGO/Virgo/KAGRA, comme la détectabilité des signaux avant la fusion, il faut réduire le bruit de façon considérable. Plusieurs facteurs sont à la base de ce bruit qui mine la sensibilité des détecteurs, parmi lesquels le bruit environnemental, les artefacts instrumentaux ainsi que certains bruits plus fondamentaux et irréductibles. L'identification d'événements supplémentaires en dessous du seuil est donc liée à notre capacité à réduire le bruit dans les instruments. Le bruit et la sensibilité influencent directement notre capacité à extraire des informations des signaux d'ondes gravitationnelles.

Afin de réduire ces effets, j'ai d'abord entrepris le développement de nouveaux outils et techniques, tout en apportant plusieurs améliorations aux anciens. Ces outils d'analyse incluent, entre autres, i) l'amélioration des capacités du Nuclear Multi-messenger Astronomy (NMMA), une bibliothèque Python pour sonder la physique nu-

cléaire et la cosmologie avec une analyse multi-messagers ; ii) la mise à jour et la configuration de télescopes tels que le *Zwicky Transient Facility* (*ZTF*), le *Vera C. Rubin Observatory's Legacy Survey of Space and Time* (*LSST*), et l'*Ultraviolet Transient Astronomy Satellite* (*ULTRASAT*) au sein de Gravitational-wave Electromagnetic Optimization (gwemopt), un outil permettant de simuler une détection à l'aide d'un télescope et des informations considérant la carte du ciel de l'événement ; iii) l'injection d'une nouvelle distribution, *PBD/GWTC-3*, dans *Ligo.Skymap* pour les scénarios d'observations. Cette nouvelle distribution a le mérite de pouvoir définir, avec une seule et même loi, toutes les populations de coalescence de binaires compacts ; iv) le développement du *NMMA-Skyportal*, une pipeline qui intègre les alertes du ZTF, l'outil *Skyportal*, une plate-forme collaborative pour l'astronomie dans le domaine temporel, et *NMMA* dans le but de discriminer la nature des courbes de lumière en temps réel.

En outre, ce travail fournit des projections aux astronomes qui s'intéressent aux données produites par les détecteurs d'ondes gravitationnelles, ainsi qu'aux contraintes attendues sur le taux d'expansion de l'Univers sur la base des données à venir (campagnes O4 et O5). Ces résultats sont utiles à ceux qui analysent les données d'ondes gravitationnelles et à ceux qui recherchent des contreparties électromagnétiques aux fusions d'étoiles à neutrons. Enfin, pour répondre à la problématique des "signaux astrophysiques baignés" sous le seuil du bruit, j'ai appliqué l'algorithme `DeepClean`, un réseau de neurones convolutif unidimensionnel, pour estimer, analyser et soustraire les bruits *stationnaires* et *non-stationnaires* dans le détecteur Virgo. Une première pour le détecteur Virgo. En plus de préserver l'intégrité du signal astrophysique, l'algorithme améliore le rapport signal sur bruit du détecteur.

Mots-clés : Étoile à neutron, Trou noir, Coalescence de binaire compacte, Ondes gravitationnelle, Multi-messager, Courbes de lumière, Inférence bayésienne, Apprentissage automatique, Ajustement de modèle, Apprentissage profond.

Abstract

***

Developments for the Observation and Characterization of Multi-Messenger Sources of Gravitational Waves during the LIGO-Virgo-KAGRA Observation Campaigns.

The Advanced LIGO/Virgo observation campaigns have revealed the rich and diverse physics of binary neutron star and binary black hole mergers. In 2017, the simultaneous discovery of gravitational waves and electromagnetic counterparts from a binary neutron star merger provided an detailed view of this extreme phenomenon, yielding numerous results in both astrophysics and physics, particularly on the behavior of ultra-dense matter. However, despite enormous efforts, no new multi-messenger detections have been made since. This is due to the formidable observational challenge posed by the rapid and precise alerts of gravitational waves, the immediate reactivity of a network of telescopes, and the online data processing required for the identification of electromagnetic counterparts.

The identification of electromagnetic counterparts enables numerous high-priority scientific studies, such as constraints on the equation of state of neutron stars, the measurement of the universe's expansion rate, and the *r*-process nucleosynthesis of heavy elements produced during a kilonova. For a rapid follow-up of possible counterparts to these events, we must reduce the sky localization area where the event occurs. However, the significantly different sensitivities of the detectors demonstrate how challenging gravitational-wave follow-up can be. This is the case for the fourth (ongoing) and fifth LIGO/Virgo/KAGRA observation campaigns. Many gravitational-wave signals from compact binary mergers are hidden by detector noise and can be detected if the noise is sufficiently reduced. To maximize the scientific outcome of the LIGO/Virgo/KAGRA gravitational-wave detectors, such as the detectability of pre-merger signals, noise must be significantly reduced. Several factors contribute to this noise, undermining the detector's sensitivity, including environmental noise, instrumental artifacts, and some more fundamental and irreducible noises. The identification of additional subthreshold events is therefore linked to our ability to reduce noise in the instruments. Noise and sensitivity directly influence our capacity to extract information from gravitational-wave signals.

To mitigate these effects, I initially developed new tools and techniques while also making several improvements to existing ones. These analysis tools include, among others, i) enhancing the capabilities of the Nuclear Multi-messenger Astronomy (NMMA), a Python library for probing nuclear physics and cosmology with multi-messenger analysis; ii) updating and configuring telescopes such as the *Zwicky Transient Facility* (*ZTF*), the *Vera C. Rubin Observatory's Legacy Survey of Space and Time* (*LSST*), and the *Ultraviolet Transient Astronomy Satellite* (*ULTRASAT*) within

Gravitational-wave Electromagnetic Optimization (gwemopt), a tool for simulating detections using a telescope and event sky map information; iii) injecting a new distribution, *PBD/GWTC-3*, into *Ligo.Skymap* for “observing scenarios". This new distribution can define all populations of compact binary coalescences with a single law; iv) developing *NMMA-Skyportal*, a pipeline that integrates ZTF alerts, the *Skyportal* tool, a collaborative platform for time-domain astronomy, and *NMMA* to discriminate the nature of light curves in real-time.

Moreover, this work provides projections for astronomers interested in data produced by gravitational-wave detectors, as well as expected constraints on the universe’s expansion rate based on forthcoming data (campaigns O4 and O5). These results are useful to those analyzing gravitational-wave data and those seeking electromagnetic counterparts to neutron star mergers.

Finally, to address the problem of "astrophysical signals bathing" below the noise threshold, I applied the `DeepClean` algorithm, a one-dimensional convolutional neural network (CNN), to estimate, analyze and subtract *stationary* and *non-stationary* noises in the Virgo detector. A first for the Virgo detector. In addition to preserving the integrity of the astrophysical signal, the algorithm improves the detector’s signal-to-noise ratio.

Keywords: Neutron star, Black hole, Compact binary Coalescence, Gravitational-wave, Multi-messenger, Light curves, Bayesian inference, Machine learning, Model fitting, Deep learning.

Développements pour l'observation et la caractérisation des sources multi-messagers d'ondes gravitationnelles lors des campagnes d'observation LIGO-Virgo-KAGRA.

Developments for the observation and characterization of gravitational wave multi-messenger sources during LIGO-Virgo-KAGRA observation campaigns.

Ramodgwendé Weizmann Kiendrébéogo
Email Address: kiend.weizman7@gmail.com

September 25, 2024

Remerciement

***

Cette thèse a été pour moi l'une des plus grandes étapes de mon parcours scolaire. Dès ma tendre enfance, il n'a jamais été question pour moi d'être un chercheur en astrophysique, mais plutôt d'être aux commandes d'un gros porteur, en tant que pilote d'avion. C'était une autre époque, une toute autre histoire, un rêve, et oui, un rêve suffisamment grand comme l'horizon, grand comme les cœurs de toutes ces personnes qui, de près ou de loin, ont contribué à cette transition. Du Pilotage à l'Astrophysique, cela n'a pas été facile pour moi, de voir ce rêve d'enfance, ce qui donnait un sens à mes orientations scolaires dans le domaine des mathématiques et de la physique. Ce rêve restera à jamais ancré en moi, d'autant plus que je n'avais qu'un seul plan : être pilote ou être pilote. Une chose est sûre, j'ai trouvé une nouvelle passion, l'astrophysique, qui me procure des sensations aussi fortes et passionnantes, comblant ce vide laissé par l'assombrissement du rêve d'enfance d'un gamin innocent.

Aux premières heures de ce parcours passionnant, je tiens à remercier Morgan Freeman, cet inconnu, qui m'a donné envie de percer les mystères du cosmos. J'ai effectué mes premiers pas dans la recherche à l'Observatoire de Paris/LESIA aux côtés de Frédéric Vincent et Thibaut Paumard, qui m'ont initié au domaine de la recherche théorique comme pratique, à travers l'étude de M87* en tant que trou noir vs trou de ver, une expérience très enrichissante. C'est l'occasion pour moi de remercier, du fond de mon cœur, toutes ces personnes que j'ai côtoyées durant ce voyage tel une sonde dans l'espace interstellaire.

Je tiens tout d'abord à remercier mes superviseurs, le Pr. Jean KOULIDIATI et le Dr. S. Zacharie KAM, de m'avoir guidé sur ce chemin depuis le LPCE. J'ai beaucoup appris à leurs côtés grâce à leur sens élevé de la responsabilité. Merci, chers professeurs, pour votre présence, vos sacrifices et votre disponibilité, j'y ai été très sensible. Je remercie également tous les enseignants que j'ai rencontrés tout au long de mon parcours et qui m'ont appris, au-delà de l'instruction, des valeurs morales et le dévouement au travail.

Ma rencontre avec Nelson a été rendue possible par le concours d'une circonstance hasardeuse qui s'est transformée en une grande collaboration scientifique. À la question de savoir si le hasard existe réellement... Lauréat de la bourse Poincaré junior de l'Observatoire de la Côte d'Azur, je devais travailler avec Olivier Minazzoli sur le fond stochastique. Mais suite à un souci administratif, il s'est fait remplacer par Nelson. Nos premières discussions scientifiques ont été très riches, moi lui parlant de trous de ver, des objets hypothétiques dans l'univers, et lui de trous noirs primordiaux. À la fin de ce stage, il me proposa deux sujets de thèses de doctorat, et j'en ai retenu celui-ci. Nous avons travaillé tant dans le domaine scientifique qu'administratif, pour la recherche de financements afin de supporter mes travaux. Merci pour cette collaboration riche.

Ensuite, je souhaite remercier Michael Coughlin, qui a toujours été là pour me guider. Nous avons collaboré ensemble sur de nombreux projets du projet NMMA, gwemopt, ULTRASAT et le Vera C. Rubin Observatory, pour ne citer que ceux-là. Merci aussi de m'avoir invité à l'University of Minnesota. J'en ai appris tant scientifiquement que culturellement. Je remercie également tous mes collaborateurs.

Cela m'amène à remercier Marie-Anne et toute l'équipe de Virgo DetChar et LIGO DetChar, qui m'ont facilité l'accès et le transfert des données de Virgo. Marie-Anne, merci de m'avoir assisté dans les débogages de certains de mes scripts. Un grand merci à Sarah de m'avoir permis d'analyser et de traiter les données de la campagne "ReadyforO4" de la collaboration GRANDMA.

En outre, je remercie mes collègues de bureau du côté du LPCE, à savoir André, Aymard, Fabrice, et du côté d'Artémis, je pense à Kamiel, Guillaume, Hugo, Debanjan et Li. Je remercie toute l'équipe de la cantine de l'observatoire pour leur accueil formidable ainsi que tout le personnel chargé de l'entretien de notre espace de travail, qui s'assure que nous effectuons nos travaux dans de meilleures conditions.

Un merci spécial à Angélique Guitard pour sa réactivité, sa disponibilité tant dans le domaine administratif que social. Merci pour toutes ces fois où vous m'avez ramené, ce qui me permettait de rester travailler au-delà des horaires du bus.

Enfin,

Une pensée très spéciale pleine de reconnaissance inspirée par l'amour, l'affection, l'éducation, le soutien, la gentillesse et les conseils... que ma mère a su manifester à mon attention. Cette grande dame au cœur tendre s'est battue et se bat toujours contre vents et marées en se réveillant entre 2h00 et 3h00 du matin afin de s'assurer que nous, ses enfants, ne manquions de rien. Je dois tous mes succès et réussites à sa grande détermination et à son assistance, de jour comme de nuit, elle est toujours présente pour nous.
Une pensée à mon père qui a su nous inculquer la notion de la responsabilité et les grandes valeurs de la vie telles que l'humilité, le courage et la sagesse à travers une éducation exigeante et très rigoureuse, ce qui m'a toujours permis de me démarquer des autres.
Une pensée à ma petite sœur Natacha, à mon grand frère Wilfried ainsi qu'à ma grande sœur Séraphine qui sont toujours disponibles pour moi. Une pensée à mes oncles, mes tantes, mes amis, mes cousins et à yaaba (grand-mère) qui ont su me soutenir tout au long de mon cursus.

À toutes ces personnes qui de près ou de loin ont contribué à la réalisation du contenu de ce présent document, je vous dis merci.

LIST OF PUBLICATIONS

***

Important Papers

1. **Updated Observing Scenarios and Multimessenger Implications for the International Gravitational-wave Networks O4 and O5**,
Kiendrebeogo et al. 2023,
The Astrophysical Journal **958** (2023), 2-158,
DOI: 10.3847/1538-4357/acfcb1,
Contribution : Entire Project Execution.

2. **DeepClean: Non-Linear Regression for Noise Reduction in the Virgo Detector**,
Kiendrebeogo et al. 2024,
In preparation,
Contribution : Entire Project Execution.

3. **NMMA-SkyPortal: Real-time Analysis of the light curves of Fast-Evolving Transients**,
Kiendrebeogo et al. 2025,
In preparation,
Contribution : Entire Project Execution.

4. **An updated nuclear-physics and multi-messenger astrophysics framework for binary neutron star mergers**,
Pang et al. 2023,
Nature Communications **14** (2023), 8352,
DOI: 10.1038/s41467-023-43932-6,
Contribution : Software Development.

5. **ULTRASAT WG2 - Work package**,
Ofek et al. 2024,
In preparation,
Contribution : Simulation, Conducted statistical analysis of predictions and Writting.

6. **GRANDMA observations of ZTF/Fink transients during summer 2021**,
Aivazyan et al. 2022,
Monthly Notices of the Royal Astronomical Society **515** (2022), 6007,
DOI: 10.1093/mnras/stac2054,
Contribution : Data Analysis, Model Fitting, Scientific Interpretation.

7. **Searching for gravitational wave optical counterparts with the Zwicky Transient Facility: summary of O4a**,
Ahumada et al. 2024,
Submitted,
DOI: 10.48550/arXiv.2405.12403,
Contribution : Data set simulations and analysis.

8. **A data science platform to enable time-domain astronomy**,
Coughlin et al. 2023,
The Astrophysical Journal Supplements **267** (2023), 31,
DOI: 10.3847/1538-4365/acdee1,
Contribution : Software Development, NMMA analysis service.

9. **Enabling Kilonova Science with Nancy Grace Roman Space Telescope**,
Andreoni et al. 2023,
Astroparticle Physics **155** (2023), 102904,
DOI: 10.1016/j.astropartphys.2023.102904,
Contribution : Simulation and Data Provider.

10. **Bayesian model selection for GRB 211211A through multiwavelength analyses**,
Kunert et al. 2023,
Monthly Notices of the Royal Astronomical Society **527** (2023), 3900–3911,
DOI: 10.1093/mnras/stad3463,
Contribution : Data Simulation.

11. **Ready for O4 II: GRANDMA observations of Swift GRBs over eight weeks in spring 2022**,
Tosta et al. 2024,
Astronomy & Astrophysics **682** (2024), 14,
DOI: 10.1051/0004-6361/202347938,
Contribution : Observations Role.

12. **GRANDMA and HXMT Observations of GRB 221009A: The Standard Luminosity Afterglow of a Hyperluminous Gamma-Ray Burst—In Gedenken an David Alexander Kann**,
Kann et al. 2023,
The Astrophysical Journal Letters **948** (2020), L12,
DOI: 10.3847/2041-8213/acc8d0,
Contribution : Observations Role.

Other Papers

13. **Observation of Gravitational Waves from the Coalescence of a 2.5-4.5 $M_\odot$ Compact Object and a Neutron Star**,
The LIGO/Virgo/KAGRA Collaborations et al. 2024,

Submitted to The Astrophysical Journal Letters.
DOI: doi.org/10.48550/arXiv.2404.04248.

14. **The GRANDMA network in preparation for the fourth gravitational-wave observing run**,
Agayev et al. 2022,
SPIE **12186** (2022),
DOI: 10.1117/12.2630240.

15. **Ultralight vector dark matter search using data from the KAGRA O3GK run**,
The LIGO/Virgo/KAGRA Collaboration et al. 2024,
DOI: 10.48550/arXiv.2403.03004.

List of acronyms

***

2D two-dimensional

3D three-dimensional

aLIGO Advanced LIGO

AdVirgo Advanced Virgo

ASD amplitude spectral density

BAYESTAR BAYESian TriAngulation and Rapid localization

BBH binary black hole

BH black hole

BNS binary neutron star

CBC compact binary coalescence

CNN convolutional neural network

EM electromagnetic

EOS equation of state

FAR false alarm rate

FOV field of view

GCN Gamma-ray Coordinates Network

GR general relativity

GRANDMA Global Rapid Advanced Network Devoted to Multi-messenger Addicts

GRB gamma-ray burst

GW gravitational-wave

gwemopt Gravitational-wave Electromagnetic Optimization

GWTC-3 Gravitational Wave Transient Catalogue 3

H_0 Hubble-Lemaître constant

HEALPix Hierarchical Equal Area isoLatitude Pixelization

IGWN international gravitational-wave network

ISCO innermost stable circular orbit

KAGRA KAmioka GRAvitational-wave observatory

KDE kernel density estimator

KN kilonova

LHO Laser Interferometer GW Observatory (LIGO) Hanford Observatory

LIGO Laser Interferometer GW Observatory

LISA The Laser Interferometer Space Antenna

LLO LIGO Livingston Observatory

LRR Living Reviews in Relativity

LSC LIGO Scientific Collaboration

LSST Large Synoptic Survey Telescope

$M_\odot$ sun mass

MLE maximum likelihood (ML) estimator

ML maximum likelihood

NIR near infrared

NMMA Nuclear-physics and Multi-Messenger Astrophysics

NSBH neutron star–black hole

NSBH neutron star–black hole

NS neutron star

O1 LIGO's first observing run

O2 LIGO/Virgo's second observing run

O3 LIGO/Virgo's third observing run

O4 LIGO/Virgo/KAGRA's fourth observing run

O5 LIGO/Virgo/KAGRA's fifth observing run

O6 LIGO/Virgo/KAGRA/LIGO-India's fifth observing run

PSD power spectral density

PDB Power Law + Dip + Break

PDB/GWTC-3 Power Law + Dip + Break/GWTC-3

SED spectral energy distribution

SN supernova

SN II Type II supernova (SN)

SN Ia Type Ia SN

SN IIb Type IIb SN

SN Ib Type Ib SN

SN Ic Type Ic SN

SN Ic/Ib Type Ic/b SN

S/N signal-to-noise ratio

SVD singular value decomposition

TOO target-of-opportunity

ULTRSAT Ultraviolet Transient Astronomy Satellite

UV ultraviolet

UVEX Ultraviolet Explorer

Roman Nancy Grace Roman Space Telescope

Rubin Observatory Vera C. Rubin Observatory

WD white dwarf

ZTF Zwicky Transient Facility

Contents

***

Chapter 1

General relativity in the era of Multi-messenger astronomy

***

Mass tells space-time how to curve, and space-time tells matter how to move.
John Wheeler

The theory of general relativity (GR) predicts the existence of highly compact astrophysical objects, each characterized by a compactness parameter Ξ, defined as $\Xi = \frac{GM}{rc^2}$. It is important to note that a Ξ value of 1 does not denote only objects of immense density, such as black holes (BHs). Instead of neutron stars (NSs), which shows compactness values from 0.1 to 0.4. These dense celestial bodies are known to be some of the densest objects in the universe within the binary systems and are the primary sources of GWs that propagate at the speed of light. When a merger involves at least one NS, it could generate a variety of phenomena, including gamma-ray bursts (GRBs), neutrinos, and kilonovae (KNe), the latter arising from the rapid neutron capture process (r-process). The landmark detection of GW170817 has opened new directions in multi-messenger astrophysics, then subsequent observations further affirming the abundant nature of these events. This chapter 1 sets the groundwork to understanding the fundamental concepts crucial to appreciating the new research findings discussed in later sections of this dissertation. Provides a comprehensive examination of GR, BHs, NSs, and KNe setting the stage for advanced discussions and analyses.

1.1 General Relativity

Space-time—Fundamentally, space-time is characterized by its metric $g_{\mu\nu}$, which is a symmetric two-dimensional (2D) tensor, or matrix. In the context of flat space-time, also referred to as Minkowski space, this metric is commonly represented by $\eta_{\mu\nu}$. The convention $\eta_{\mu\nu} = \text{diag}(-1,+1,+1,+1)$ is adopted, which facilitates the description of space-time intervals in an approach that is particularly advantageous for special relativity and provides a basis for GR in areas where gravitational influences are minimal or nonexistent. On 25 November 1915, Albert Einstein submitted a groundbreaking paper on GR to the Royal Prussian Academy of Sciences, fundamentally altering our understanding of gravitation. This theory suggests that what we perceive as the gravitational force is actually the manifestation of the curvature of space-time by mass and energy. This idea moves away from the Newtonian concept, where gravity is seen as a force between masses. Einstein's field equations describe how matter and energy modify space-time's geometry [201]. We can define this equation as,

$$G_{\mu\nu} = \frac{8\pi G}{c^4} T_{\mu\nu}, \tag{1.1}$$

where $G_{\mu\nu}$ is a 4×4 matrix (tensor), the Einstein tensor that describes the curvature of space-time, $T_{\mu\nu}$, a 4×4 matrix, is the energy-momentum tensor that represents the distribution of mass and energy in space-time, and G, c the universal gravitational constant and the speed of light. This equation (Equation 1.1) is simplified for systems smaller than a galaxy, where the cosmological constant, Λ, is negligible. The implications of Einstein's theory extend beyond our solar system, providing a framework to understand BHs, the structure of the universe, and the propagation of GWs, among other phenomena. GWs result from GR and are generated when accelerating masses perturb space-time, creating ripples that travel through it at the speed of light. These disturbances move through space-time, carrying information from cosmic events and revealing regions of the universe that are not visible in EM radiation, similar to BHs.

In astrophysical terms, a BH is a region in space resulting from the gravitational collapse of a massive star characterized by a central singularity where the gravitational forces and density become infinite. This singularity is enveloped by an event horizon, the boundary beyond which nothing, not even light, can escape to the external universe (No-hair theorem; [82]). The event horizon marks the boundary of the observable universe, beyond which the traditional laws of physics locally cease to apply. We explore the effects of BHs on their surroundings using metrics, exact solutions to Einstein's equations. The Schwarzschild metric describes nonrotating BHs, while the Kerr metric (Eq. 1.2), an extension for rotating BHs, is more relevant because most observed BHs originate from rotating massive stars. Angular momentum conservation during such collapses suggests that nonrotating BHs are unlikely.

$$ds^2 = -(1 - \frac{2Mr}{\Sigma})dt^2 - \frac{4Mar\sin^2\theta}{\Sigma}dtd\varphi + \frac{\Sigma}{\Delta}dr^2 + \Sigma^2 d\theta + \sin^2\theta(r^2 + a^2 + \frac{2Ma^2 r\sin^2\theta}{\Sigma})d\varphi^2 \quad (1.2)$$

$$\text{where, } \begin{cases} \Sigma \equiv r^2 + a^2\cos^2\theta \\ \\ \Delta \equiv r^2 - 2Mr + a^2 \end{cases}$$

M and a, representing mass and angular momentum per unit mass, define the Kerr parameter $\bar{a} = \frac{a}{M} = \frac{J}{M^2}$. The coordinates (t, r, θ, φ), similar to the spherical coordinates for distant observers, are used in this metric.

Cosmological redshift—The Cosmology explores the origins, nature, structure, and evolution of the universe, becoming a formal science with discoveries that revealed its dynamic nature. In the 1920s, Edwin Hubble, conducted spectroscopic measurements on 24 nebulae (now known as galaxies), showed in 1929 that these galaxies are uniformly receding from us [153]. This states that the radial velocity of nearby galaxies is proportional to their distance from Earth. Before Hubble, Lemaître suggested in 1927 the expanding universe theory, supported by increasing galaxy distances [178]. His model introduced the singularity, later called the Big Bang, refined to include universe expansion, high initial temperature, and cooling. The model of Big Bang line up with observations of cosmic microwave background radiation and galaxy distribution. The cosmology now merges theoretical physics and observational astronomy to improve our understanding of the universe's past and present, and investigates dark matter and dark energy, its predominant but mysterious components.

The expansion of universe, denoted by Hubble-Lemaître constant (H_0), is significant within the curved space-time framework. It serves as a quantitative measure of the expansion rate. As radiation from distant objects propagates toward us, its wavelength increases, becoming longer than its original emission by the time it reaches the observer [290]. This phenomenon is the cosmic redshift, represented by z, which provides a means to gauge the dynamism of the universe. Mathematically, it is expressed as

$$z \equiv \frac{\lambda_r}{\lambda_e} - 1,$$

where λ_e and λ_r are the wavelengths of light at emission and reception, respectively [200]. This redshift indicates the expansion of the universe, stretching space-time, and altering the path of light through the cosmos. For nearby galaxies, the relationship between velocity and redshift can be approximated as the following:

$$v \approx cz,$$

where v is the velocity, c is the speed of light. At small redshifts, when $z \ll 1$, the approximation,

$$cz \approx H_0 d,$$

relates the recessional velocity of galaxies to their distance d through H_0. This simplification holds within the Einstein equations (Equation 1.1), but at greater distances, H_0 helps decode the complex expansion of the universe and acceleration, influenced by dark energy and mass energy distribution. Since the discovery of the accelerated expansion of the universe [239, 221], determining H_0 remains a challenge. This measurement has previously been found to show that the cosmic microwave background is consistent with the Big Bang cosmological model Λ-cold-dark matter (ΛCDM) cosmology [227], and this tension with other measurements from Type Ia SN (SN Ia) observations [240]. A SN Ia occurs when a white dwarf (WD) explodes in a binary system. The tension might indicate experimental errors or suggest new physics. However, it is clear that additional cosmological probes are necessary and that enough independent measurements can eventually motivate a consensus on the true source of the tension. The measurement and interpretation of H_0 involve an extensive exploration into the nature of the universe, integrating cosmic and quantum aspects, and deepening our understanding of the structure of the universe, influenced by matter, energy, and space-time geometry.

The analysis of mergers of compact binary systems, which generate GW and potentially their EM counterparts, provides an additional pathway to measure H_0 [253]. The measurement of H_0 using compact binary mergers is particularly interesting because it does not rely on the cosmic distance ladder or assume any cosmological model *a priori* [4]. In fact, GWs provide a direct measure of the energy output from astrophysical events, enabling accurate distance estimations. This capability establishes them as "standard sirens". By combining data from GW observations with measurements of recession velocities, we can compute H_0. Although this measurement is limited by the uncertainty in the distance, which is highly degenerate with the inclination angle measured from GW alone, combining it with EM observations has been shown to significantly improve this measurement [151, 111, 114].This approach is promising and could mitigate tension related to the measurement of H_0.

1.2 Compact Objects

1.2.1 Life Cycle of Stars

The life cycle of stars begins in dense molecular clouds in interstellar space, which is mainly composed of hydrogen and helium, with traces of heavier elements. Gravitational instabilities within these cold clouds cause them to fragment into denser cores, initiating the stage of star formation [203]. As these cores accumulate mass and the internal pressure and temperature increase, hydrogen fusion ignites. This marks the transition of the protostar to the main sequence stage, where a star spends the majority of its life. During the main sequence phase, the mass of the star critically influ-

ences its nuclear burning processes and lifetime. The intense thermodynamic conditions within stars can lead to several nucleosynthetic processes, including the explosive burning stages related to the major hydrostatic fuels within stars. Main sequence stars fuse hydrogen into helium, releasing energy that supports the star against gravitational collapse. This energy release determines both its luminosity and surface temperature.

Low-mass and intermediate-mass—There stars (less than 8 sun mass ($M_\odot$)) spend an extensive period on the main sequence because they slowly consume their fuel while emitting weak light. Once a star has burnt out the hydrogen in its core, it leaves the main sequence and enters the next phase of its life, corresponding to the final stages of their life cycle. As the hydrogen in the core of the star is consumed, the star begins to contract under its own gravity. This increases the temperature and pressure in the core, inducing the fusion of helium into carbon. At the same time, hydrogen in the outer layers starts to fuse, creating a burning hydrogen shell that causes the star to expand into a red giant. During this period, the star shines thousands of times brighter than when it was on the main sequence, despite a much lower surface temperature, giving the star its characteristic red color. At the end of the red giant phase, the star ejects its outer layers into space, creating a planetary nebula. The remaining core becomes a WD, a compact and dense object formed of degenerate electrons [134]. The equilibrium is maintained by degeneracy pressure, based on the Pauli exclusion principle [168]. No longer undergoing fusion reactions or radiation, it gradually cools down, eventually becoming a black dwarf.

Massive stars—For massive stars, those exceeding eight $M_\odot$, the main sequence lifetime is shorter because of their higher core temperatures and increased luminosity. The evolution of such stars is governed by a sequence of nuclear burning stages, during which lighter elements are progressively transformed into heavier ones [71]. For each phase, the main product is converted from the previous phase into its primary fuel, progressing through hydrogen (H), helium (He), carbon (C), oxygen (O), neon (Ne), and silicon (Si), eventually leading to an iron (Fe) core. At this stage, despite the contraction, its internal temperature is insufficient to overcome Coulomb's law to fuse iron into heavier nuclei, ceasing nuclear fusion. The star then transforms into a red supergiant. As the core collapse exceeds 1.4 $M_\odot$, the Chandrasekhar limit [83], the electron degeneracy pressure can no longer counteract the gravitational forces, leading to rapid core collapse and significant increases in density. This results in general neutronization and a massive emission of electron neutrinos through electron capture, $p \rightarrow n + e^+ + \nu_e$, and the inverse of β-decay, $p + e^- \rightarrow n + \nu_e$. The star finally collapses under its own weight into a cataclysmic explosion known as a Type II SNe (SNe II). At nuclear saturation density (n_{sat}), the neutron degeneracy pressure stops the collapse, stabilizing the core and forming a NS with temperatures greater than 10^{11} K. If the progenitor star is greater than 30 $M_\odot$, this leads to the formation of a BH [170].

Figure 1.1 depicts the life cycle of stars. When these stellar remnants are part of a binary system, they often undergo significant evolution. The merger of NS double can lead to the formation of a BH. Similarly, WDs in binary systems frequently accrete matter from their companions, leading to an increase in mass. If this mass exceeds the Chandrasekhar limit, the WD undergoes a thermonuclear explosion, in SN Ia. This

explosive event culminates in the formation of either a NS or a BH [214].

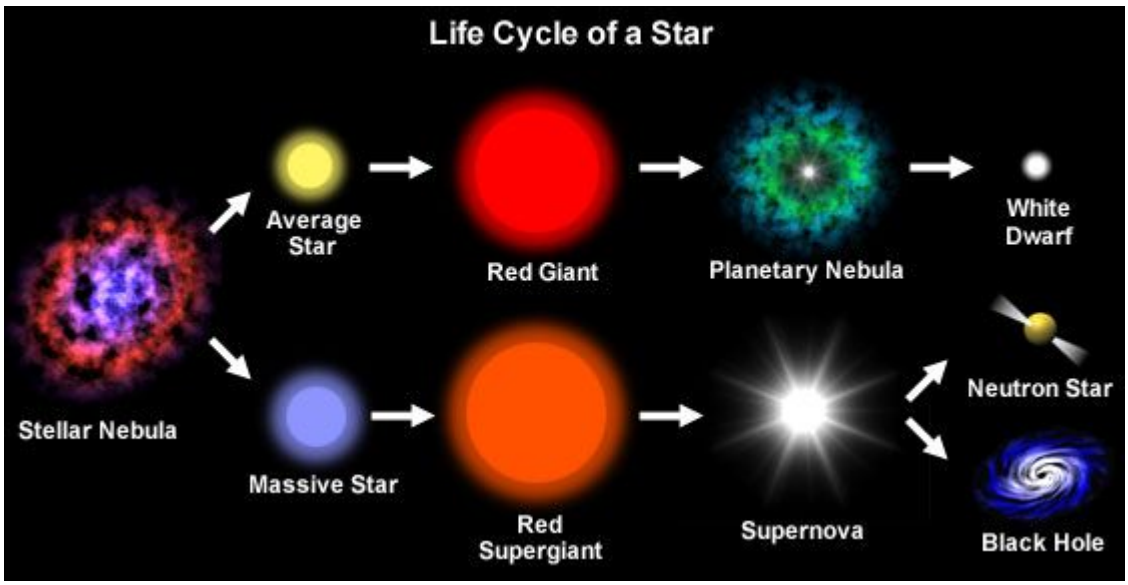

Figure 1.1: Stellar Evolution Illustrated: This diagram depicts the life cycles of stars, showing how intermediate-mass stars become WD and massive stars undergo SN explosions to form NSs or BHs. It outlines the transformation from birth in stellar nebulae to the end, emphasizing crucial cosmic processes. Figure credit: NASA.

1.2.2 Types of supernovae

SNe are classified into two main types: thermonuclear SNe (SNe Ia) and core-collapse SNe (SNe II). Each type has different characteristics and progenitors.

Thermonuclear Supernovae—These result from a WD in a binary system that accretes enough mass to exceed the Chandrasekhar limit, leading to a runaway thermonuclear explosion [134]. SNe Ia are characterized by strong silicon lines in their spectra and form a relatively homogeneous group [204]. Their consistent luminosity makes them useful as standard candles for measuring cosmic distances.

Core-Collapse Supernovae—These occur from the gravitational collapse of massive stars (greater than eight $M_\odot$). Core-collapse SNe are subdivided based on their spectral lines and light curves.

The SNe II display prominent hydrogen lines in their spectra. They are further classified by their light curves. SNe IIP show a plateau-shaped light curve, while SNe IIL show a linear decline in brightness. SNe IIn are characterized by narrow hydrogen emission lines, with multi-component Balmer line profiles, particularly H_α [233].

The Type Ib SNe (SNe IIb) lack hydrogen lines but show helium lines in their spectra. They are the result of massive stars that have lost their hydrogen envelopes. The Type Ic SNe (SNe IIc) are similar to SN Ib but without hydrogen and helium lines, coming from stars that have lost both envelopes. The Type IIb SN (SN IIb) initially

display hydrogen lines that fade over time, eventually resembling the SN Ib spectra as the hydrogen envelope is lost [204]. Classifying SNe reveals the evolutionary paths and fates of stars. Figure 1.2 shows the types of SN and their progenitors.

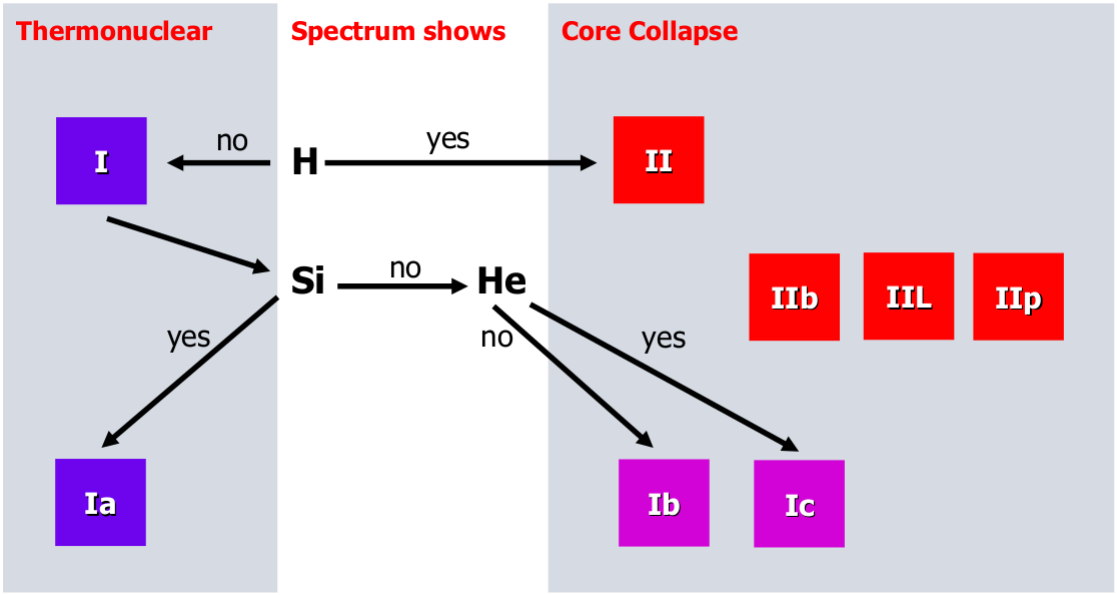

Figure 1.2: Types of SNe classified by spectral lines and progenitors. Credit: From **Röpke F.**, Type Ia supernovae http://theor.jinr.ru/~ntaa/07/files/program.html.

1.2.3 Compact Binaries Coalescence

The evolution of binary star systems is significantly influenced by the presence of the companion star, which primarily alters evolutionary trajectories through mass and angular momentum transfer [146]. The fate of binary stars depends on the individual evolution of each component, where the most massive star typically collapsing first in a SN event, leading to the formation of a NS or a BH [272]. The companion star, with mass m_2, emits a stellar wind that the denser object (m_1) accretes. This material heats up and emits X-rays [206]. A mass ratio $q = m_2/m_1 < 1$ leads to a low-mass X-ray binary, while $q \geq 1$ forms a high-mass X-ray binary [85]. The geometry of the binary system is often described by the presence of *Roche lobe*.

Roche Lobe—In binary star systems, the Roche lobe defines a teardrop-shaped volume around each star, dictated by the gravitational forces of the components, and meeting at the Lagrangian point L1. If a star exceeds its Roche lobe, it begins to transfer mass to its companion through this inner Lagrangian point as shown in Figure 1.3. This mass exchange profoundly impacts the evolution of stars, possibly leading to events such as the SNe explosion or the formation of NSs or BHs. In systems with a red giant and a WD, ejected matter can trigger nova or SN explosions, forming these compact remnants. A key stage is the formation of a common envelope, shared by both stars, which can be ejected, revealing the cores and significantly changing the system [154,

117]. Such observations are fundamental for understanding binary dynamics and the destiny of massive stars.

Following the intense phase of mass transfer and the potential formation of a common envelope, the binary system may experience further evolutionary complexities. In particular scenarios where rapid mass transfer leads to an unstable configuration, a direct collapse into a BH can occur, avoiding the dramatic SN explosion typically expected. This provides a deeper understanding of the mass distribution among compact objects and offers insight into the characteristics of binaries with specially short orbital periods. As these systems evolve, their final stages often emit intense GWs, detectable by LIGO, Virgo, and KAmioka GRAvitational-wave observatory (KAGRA). GW detection provides unique insights into the end stages of stellar evolution in compact binaries.

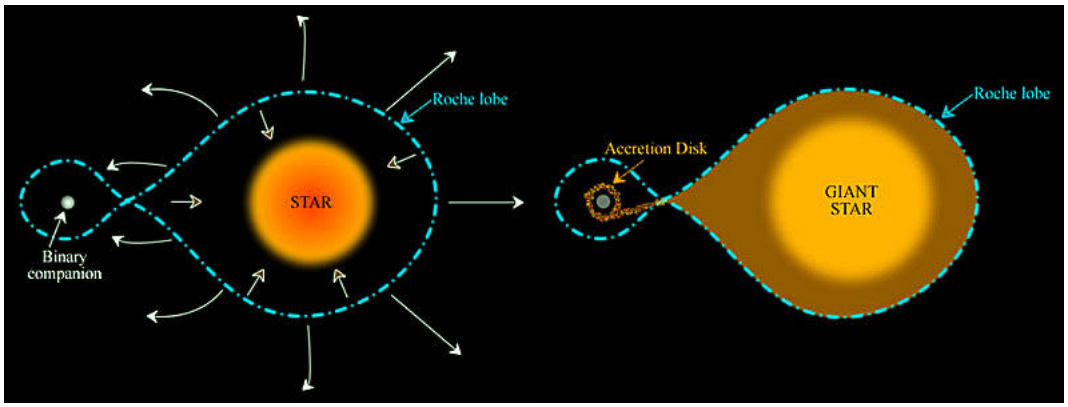

Figure 1.3: This illustration shows the Roche lobes in a binary star system, highlighting how material is gravitationally bound within each lobe. The left image shows a detached system, and the right image shows mass transfer from a star exceeding its Roche lobe to its companion. Figure credit : From [69] and The SAO Encyclopedia of Astronomy.

Compact Binary Coalescence—When binary star systems consist of combinations such binary neutron stars (BNSs), binary black holes (BBHs), or neutron star–black holes (NSBHs), a pair of compact objects orbit around each other, they are collectively referred to as compact binary coalescence (CBC). These compact objects are destined to merge if their initial orbital separation is small enough to coalesce within a Hubble time [255], due to energy loss through GWs release [222]. The detection of these events provides a unique opportunity to investigate many science cases pertaining to the properties of the sources, including their mass, spin, distance, and equation of state (EOS), especially for the NSs [60, 187, 94, 93, 281, 47]. These mergers are significant not only for their GW emissions but also for their potential EM counterparts, when one of the binary components is a NSs. Such events can lead to the production of heavy elements via rapid nucleosynthesis processes, known as the *r*-process [88, 103, 106, 224, 243, 266].

1.3 Gravitational-waves Astronomy

1.3.1 Introduction to gravitational-waves

The GWs are disturbances in the geometry of space-time that propagates through the universe at the speed of light and carry detailed information about their astrophysical sources. These waves interact weakly with matter, allowing them to travel large distances without significant alteration. To detect these signals, ground-based laser interferometer detectors such as LIGO, Virgo, and KAGRA are employed. These instruments detect minuscule modifications in length induced by passing GWs, typically on the order of 10^{-20} meters. The most promising sources of detectable GWs are compact objects like NSs or BHs in binary systems. When these objects orbit each other, they lose energy through GWs emission, leading to a progressive decrease in their orbital distance and eventual merger. This process, characterized by strong gravitational fields and rapid accelerations, culminates in a burst of gravitational radiation just before coalescence. In these last moments before fusion, the amplitude of GWs increases considerably as we approach the fusion time, making them detectable by the GW observatories. The initial observational evidence confirming the existence of GWs was the observation of orbital decay in the binary system PSR B1913+16, which consists of two NSs, including a pulsar [285]. A pulsar is a type of highly magnetized NS that emits beams of EM radiation from its magnetic poles. These poles do not align with the rotation of NS axis. As a result of the rapid rotation of the pulsar, these beams scan the space in a way similar to that of a lighthouse. Figure 1.4 shows the orbital decay.

1.3.2 Mathematical formulation of gravitational-waves emission

GWs, as predicted by the theory of GR, represent perturbations in the curvature of space-time propagating at the speed of light. These perturbations are derived from the second-order time-varying quadrupole moment of a mass-energy distribution, causing the ripples in space-time. Henri Poincaré and Albert Einstein established the foundation for understanding of the GWs physics, which are now detectable phenomena associated with some of the most cataclysmic events in the universe [196, 118, 119]. The theoretical foundation for the emission of GWs lies within the linearized approximation of Einstein's field equations, wherein the metric tensor $g_{\mu\nu}$ can be expressed as a perturbation $h_{\mu\nu}$ of the Minkowski metric $\eta_{\mu\nu}$ [200]:

$$g_{\mu\nu} = \eta_{\mu\nu} + h_{\mu\nu}, \tag{1.3}$$

where the absolute value of $h_{\mu\nu}$ is significantly smaller than 1, with indices μ and ν ranging from 0 to 3, corresponding to the temporal (0) and spatial (1, 2, 3) dimensions respectively [48].

The transverse-traceless (TT) gauge simplifies GWs analysis by imposing con-

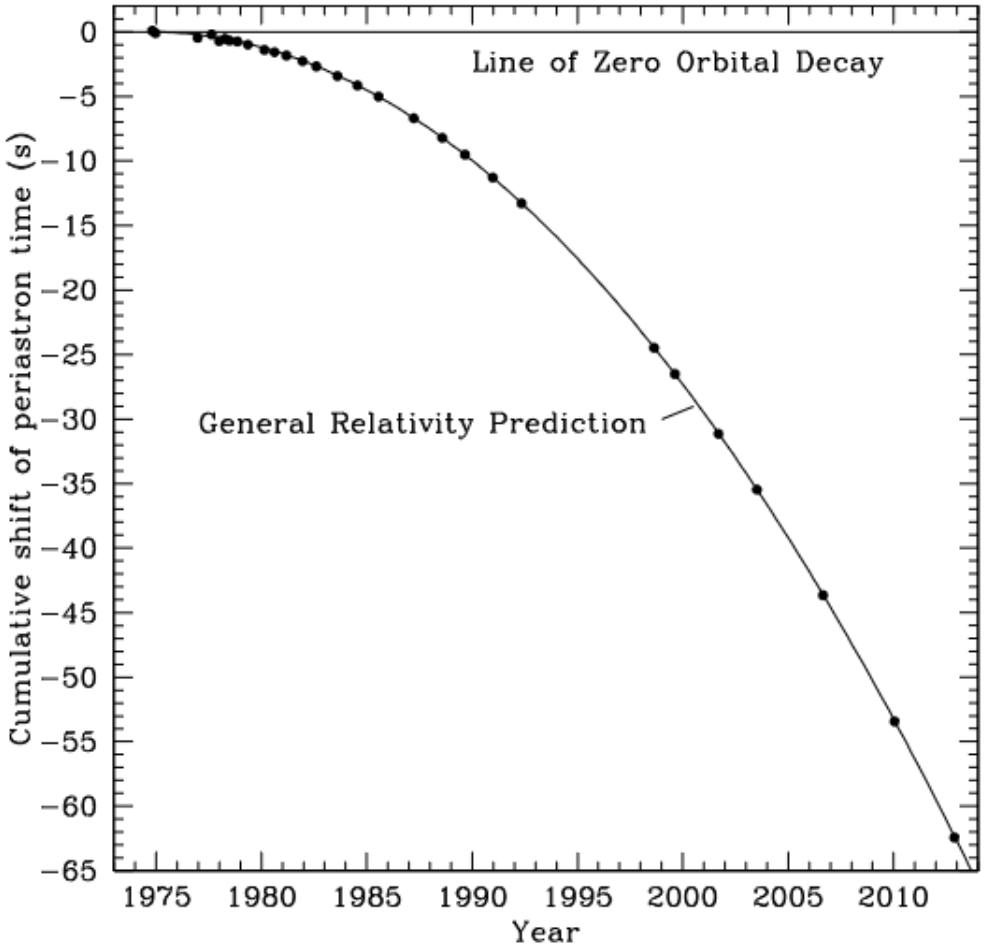

Figure 1.4: The cumulative shift in periastron time for binary pulsar PSR B1913+16, demonstrating energy loss through gravitational radiation. The masses of NSs are $m_1 = 1.4398 \pm 0.0002 M_\odot$ and $m_2 = 1.3886 \pm 0.0002 M_\odot$. The plotted data validate the predictions of GW emission, illustrating the decrease in orbital period and providing early experimental support for the existence of GWs. Credit for the figure: Figure from [285].

ditions that reflect their physical characteristics. This gauge ensures that the perturbation $h^{\mathrm{TT}}_{\mu\nu}$ satisfies two key properties:

- It is *transverse*, meaning that the direction of the wave propagation is perpendicular to the plane defined by the oscillations of the wave. This ensures a distinct observation and measurement of GWs interactions with matter.
- It is *traceless*, indicating that the trace (the sum of diagonal elements) of the perturbation tensor is zero. This condition reflects the conservation of mass-energy in the system and is crucial for isolating the pure GW effects from other potential sources of disturbance.

Under the Lorenz gauge condition [141], $\partial^\mu h^{\mathrm{TT}}_{\mu\nu} = 0$, the wave equation on the

TT gauge is:

$$\Box h_{\mu\nu}^{\mathrm{TT}} = -\frac{16\pi G}{c^4} T_{\mu\nu}, \tag{1.4}$$

with $\Box$ is the d'Alembert operator, characterized by the combination of time and space derivatives, given as $\frac{-1}{c^2}\frac{\partial^2}{\partial t^2} + \nabla^2$, and $T_{\mu\nu}$ is the energy-momentum tensor (defined in the section 1.1). This equation succinctly relates space-time perturbations from GWs to the mass-energy distribution that generates them. The effects of the waves are shown by their interaction with matter. In the TT gauge, GWs influence test particles by inducing relative acceleration, primarily from the quadrupole moment of their source. For a localized source, the distant GW field is:

$$h_{\mu\nu}^{\mathrm{TT}}(\vec{x},t) = \frac{4G}{c^4|\vec{x}|}\ddot{Q}_{\mu\nu}^{\mathrm{TT}}(t-|\vec{x}|/c), \tag{1.5}$$

where $Q_{\mu\nu}(t)$ represents the second mass moment tensor of the source, and the double dots indicate a second-order time derivative. This equation describes the radiative aspect of GWs as space-time metric fluctuations, connecting astrophysical systems to the GWs detectable from distance.

1.3.3 Interaction of gravitational-waves on particle distributions

GWs are ripples in the geometry of space-time that travel at the speed of light, influencing the motion of nearby particles. Predicted by GR, these waves are characterized by two polarization states: the $+$ (plus) and $\times$ (cross) polarizations, which create distinct oscillation configurations in the particle. These configurations are crucial for GW observatories in this case LIGO, Virgo, and KAGRA. There, polarizations in the transverse-traceless gauge is given by the polarization tensor: For a GW traveling in the $\vec{z}$ direction.

$$h_{ij}^{T} = \begin{pmatrix} h_+ & h_\times & 0 \\ h_\times & -h_+ & 0 \\ 0 & 0 & 0 \end{pmatrix}, \text{ for a GW traveling in the } \vec{z} \text{ direction,} \tag{1.6}$$

with h_+ and $h_\times$ denoting the amplitudes of the plus and cross polarizations, respectively. As GW propagate through space, they alter the positions of the particle, described by:

$$\begin{cases} x' = x(1+h_+) + yh_\times, \\ y' = y(1+h_+) - xh_\times, \end{cases} \tag{1.7}$$

In this context, x and y are the initial coordinates of a particle, while x' and y' represent its coordinates after a GW passage. The h_+ polarization modifies distances along the

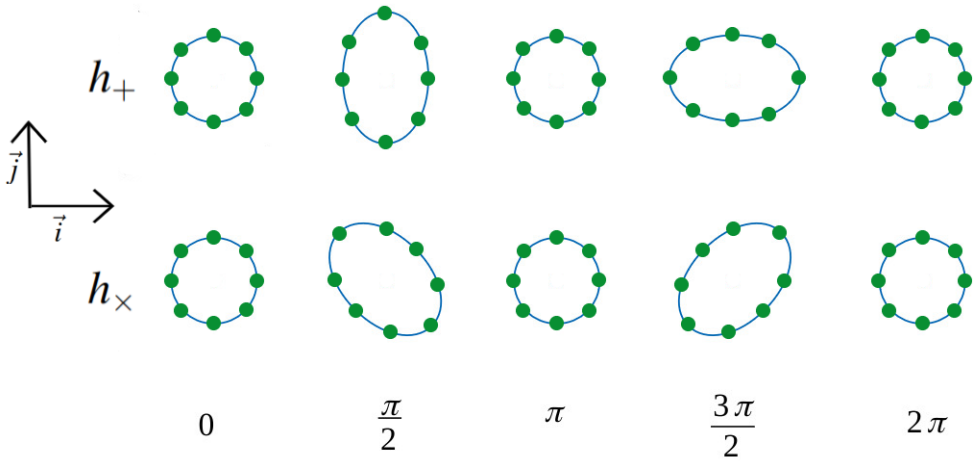

Figure 1.5: Diagram showing the deformation of a ring of particles in the plane perpendicular to GWs propagation, varying with wave phase. The diagram displays both $+$ and $\times$ polarizations in the TT gauge, with the top row representing the $+$ polarization and the bottom row representing the $\times$ polarization.

same axis, whereas $h_\times$ induces diagonal shifts, illustrating the orthogonal effects of these polarizations. To assess GW effects, measuring the induced length difference ΔL and the fractional change $\Delta L/L$ due to GW strain h plays an important role for GWs detection. Equation(1.7) describes the displacement caused by GW polarization in the TT gauge, illustrating how GWs impact on space-time. Figure 1.5 visualizes the deformation of a ring of particles located in the x-y plane, perpendicular to the GW propagation direction (along the z direction).

1.3.4 Gravitational-waves sources

GWs arise from a multitude of astrophysical phenomena. Transient sources, characterized by brief durations of milliseconds to seconds, include cataclysmic events such as the core collapse of massive stars, often resulting in SN, referred to as *bursts* [166], and the mergers of BHs, which are among the most energetic events in the universe. Moreover, there exist extended-duration transients, showed by NS mergers [255]. These phenomena not only generate GWs but are also associated with other astrophysical phenomena, such as GRBs [166]. For continuous and stable emissions, we turn to pulsars, which are rotating NSs with asymmetric mass distributions that facilitate a constant GW signal [285]. The stochastic background also presents a potential source, conjectured as an incoherent superposition of GWs from a multitude of unresolved discrete sources, potentially harking back to the primal moments of the nascent universe [176]. In particular, wormholes, theoretical tunnels connecting disparate space-time locales, are frequently conjectured as GW sources [110], yet remain speculative within the confines of theoretical physics. The violation of energy conditions by quantum phenomena supports the idea that singularities are a limitation of GR and would be resolved in a more comprehensive theory of quantum gravity [174]. The concept of wormholes re-

mains purely theoretical: their existence and physical formation in the universe have not been verified [225]. These hypothetical constructs, solutions to Einstein's field equations without event horizons or central singularities, could theoretically mimic certain astrophysical signatures attributed to BH. The emission of GWs from CBC sources occurs in several sequential stages according to the evolution of the binary star system.

1.3.5 Dynamical progression of gravitational-waves emission

The simultaneous detection of GW150914 by the two LIGO detectors [184] marked the first direct observation of a GW [13]. This event involved the coalescence and merger of a binary system of BHs orbiting around each other, generating a GW signal. The signal delineates several sequential phases in a CBC system: the *inspiral*, *merger* and *ringdown*.

During the *inspiral* stage, the BHs orbit in close proximity, gradually spiraling inward as gravitational radiation dissipates orbital energy. This period is accurately described by post-Newtonian theory, where the GW amplitude increases along with the orbital frequency. A plunge phase begins at the end of the quasi-static phase *inspiral* [78]. During this phase, the two compact objects continue to have distinct apparent horizons, which differ from event horizons and are defined as the boundaries where light rays directed outward move outward and, respectively, inward. The *merger* phase occurs when the two apparent horizons coincide, giving rise to a common apparent horizon [183]. This represents the peak of GW amplitude. This phase is brief but dynamically complex, and numerical relativity provides the most precise simulations of these intense gravitational interactions. Following *merger*, the newly formed, perturbed BH enters the *ringdown* phase, characterized by the emission of damped GWs as the BH settles into a stable state. These distinct quasi-normal oscillations, with their specific frequencies and damping times, provide insight into the inherent properties of BHs as predicted by GR [73, 65].

To address the late *inspiral* phase, the post-Newtonian theory is advanced to higher orders in v/c, with v the relative velocity of the binary system [269]. The method produces analytical approximations closely aligned with the actual solution, affected by parameters such as masses and spins [252]. In the *merger* and *ringdown* phases, numerical relativity becomes essential to solve the complete Einstein field equations, which requires extensive computational effort [79]. Figure 1.6 illustrates the compact binary *merger*, showing the decreasing orbital separation until reaching the innermost stable circular orbit (ISCO), after which the separate entities merge into a single, perturbed BH.

1.3.6 Implications for gravitational-waves Astronomy

Summary of GWs Detection Campaigns—In 2015, the LIGO-Virgo collaboration detected for the first time GWs from the coalescence and merger of two BHs, each with mass of 29 and 36 $M_\odot$, respectively. This landmark detection opened up great possibili-

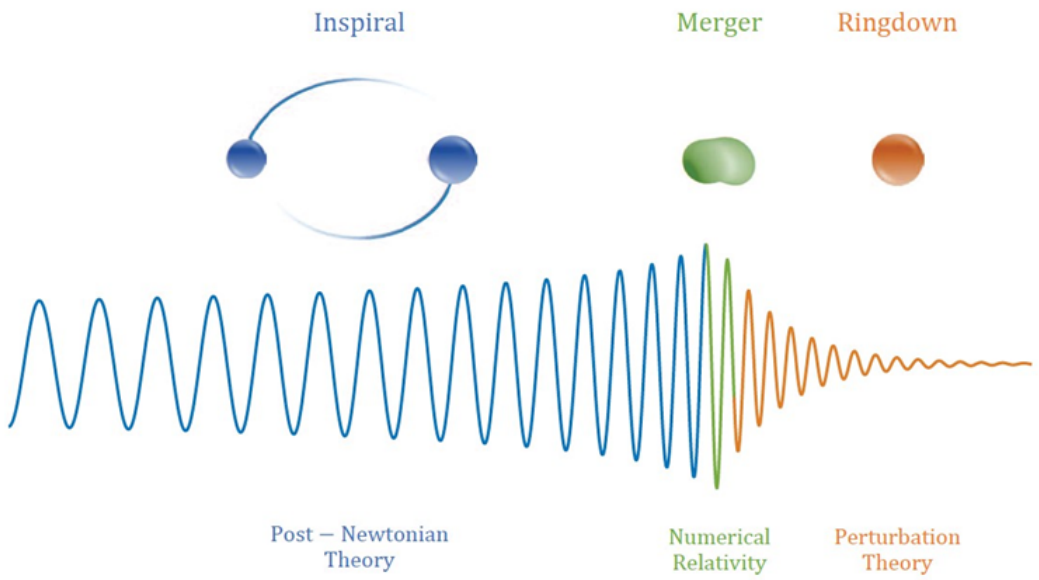

Figure 1.6: Chronological depiction of GW emission in CBC, showing evolution phases. Sequentially, *inspiral* (blue waveform), *merger* (green waveform), and *ring-down* (orange waveform) are displayed. The GW strain profile illustrates increasing amplitude and frequency during the *inspiral*, leading to *merger* and then decaying *ring-down*. This sequence represents orbital tightening peaking at the ISCO before the final coalescence, modeled by numerical relativity. This figure is from [48].

ties [13], marking the beginning of the era of GW astronomy. These observations allow for unprecedented tests of GR in strong gravitational regime and provide insight into the properties and dynamics of compact binary systems [197, 14]. GWs offer highly accurate estimations of binary system parameters due to their negligible interaction with matter, thereby maintaining the consistency of the data transmitted over cosmological expanses. In GR, the transmission of gravitational effects is not instantaneous, but propagates at the speed of light, a principle that underlies the prediction and observation of GWs.

Currently, the international gravitational-wave network (IGWN), which includes the two American Advanced LIGO (aLIGO) detectors, including the LIGO Livingston Observatory (LLO) and the LIGO Hanford Observatory (LHO), the European Advanced Virgo (AdVirgo) detector, and the Japanese KAGRA detector, organizes the detection of GWs in observation campaigns. Since the first GW detection, up until the LIGO/Virgo/KAGRA's fourth observing run (O4) campaign, 188 BBH mergers have been observed, along with numerous BNS and NSBH events. During the LIGO's first observing run (O1) and LIGO/Virgo's second observing run (O2) campaigns, from September 2015 to August 2017, a total of 11 merger events were observed: 3 BBH mergers during O1, and 7 BBH mergers along with one BNS merger during O2 [12]. The LIGO/Virgo's third observing run (O3)a campaign, from April to September 2019, detected 39 merger events: 35 BBH mergers, 3 NSBH mergers, and 1 BNS merger [16]. The O3b campaign, from November 2019 to March 2020, observed 35 merger

events, consisting of 32 BBH mergers and 3 NSBH mergers [25]. Most recently, the O4a campaign, running from May 2023 to January 2024, resulted in the detection of 89 merger events, including 81 BBH mergers, 6 NSBH mergers, and 1 BNS merger. The Gravitational Wave Transient Catalogue 3 (GWTC-3) contains all CBC detections during the O1, O2, and O3 campaigns, as shown in Figure 1.7.

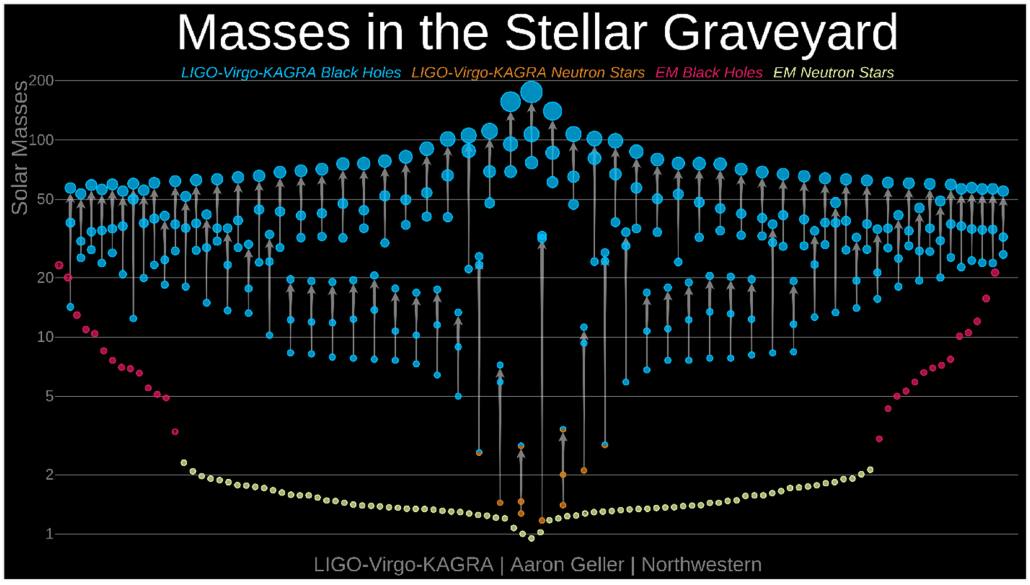

Figure 1.7: The graphic represents the masses of GW detections, alongside BHs in blue, NSs in orange and previously known compact objects from EM observations including BHs in red and NSs in yellow.
Figure Credit: from LIGO/Virgo/KAGRAs | Aaron Geller | Northwestern University.

Gravitational-wave analysis—The analysis of data from the LIGO/Virgo/KAGRA collaboration, spanning from O1 to O3a, has been crucial in defining the upper mass limit for NSs and the lower mass limit for BHs, thus refining the classification of compact binary systems. This extensive analysis has revealed a stiffening in the power law describing the masses of NSs and low-mass BHs with a 99.3% confidence level below $2.4^{+0.5}_{-0.5}\ M_{\odot}$ [122].

Through this study, we developed a new distribution for CBCs that supports current IGWN "observing scenarios," anticipating the statistical outcomes of future observation campaigns. The compact binaries are classified into three astrophysical populations: BNSs, NSBHs, and BBHs. Our distribution is derived from the population model described in [122] and [25], known as the Power Law + Dip + Break (PDB) model. By fitting this model to all CBCs in GWTC-3 from [25] and using the maximum *a posteriori* value of the resulting fit, we refined our understanding of these populations. Previous "observing scenarios" used the Living Reviews in Relativity (LRR) distribution, drawn from the population model outlined in [17] and [223]. This distribution consists of a normal distribution for NS masses and a power law for BH masses. The new one, Power Law + Dip + Break/GWTC-3 (PDB/GWTC-3) will be detailed in Chapter 2. A fundamental result of our analysis is to demonstrate that a single power law cannot accurately describe the mass distribution of BHs and NSs, thus helping to

define the mass boundaries between NSs and BHs [129, 21].

The BNSs and NSBHs populations are of particular interest in this dissertation, as they can be accompanied by EM counterparts to the GWs, opening up opportunities for additional science cases, such as constraints on the EOS [114, 218, 274], the measurement of the expansion rate of universe [101, 100, 150, 211, 114, 125, 210], and evaluate the *r*-process [271, 181].

1.4 Multi-messenger Astronomy

1.4.1 Background

Multi-messenger Signals—Following a series of BBHs observations [23, 19, 18], the field of multi-messenger astronomy exploded with the combined detection of the BNS merger GW170817 [24], the GRB GRB170817A [22], and the EM transient AT2017gfo [5], which manifested as a KN and a GRB afterglow emitting from X-ray to radio [36, 88, 121]. Multi-messenger astronomy aims to integrate data from GWs, EM observations, and potentially other messengers such as neutrinos, to create a comprehensive synthesis of cosmic events. However, this field faces significant challenges, including the limited understanding of KNe, which are radioactive explosions resulting from the merger of NSs or a NS with a BH.

Our knowledge of KNe, which is crucial to understanding the mechanisms of heavy element production and cosmic chemical evolution, is limited due to the absence of comprehensive data sets. The event GW170817 [24] is an excellent example, but additional data, especially those associated with GRB follow-ups. Questions about the merger rates of BNS and NSBH systems [25], the nature of GRB, including distinctions between short and long bursts [32, 52, 236, 235], and the EOS of NSs [60, 187, 94, 93, 281, 47, 202, 231, 173, 114, 155] remain unresolved, underscoring the need for more comprehensive data. The advent of current and forthcoming GW detectors, along with advanced space-based observatories such as the *Neil Gehrels Swift Observatory* (*Swift*; [137]), the *James Webb Space Telescope* (*JWST*; [136]), and the Ultraviolet Transient Astronomy Satellite (ULTRSAT) [259] highlights the necessity for enhanced real-time coordination and the expedited identification of transient candidates within the realm of multi-messenger astronomy as `Skyportal`, a collaborative platform for time-domain astronomy [282, 98].

Gamma-ray burst—GRBs, among the most energetic phenomena in the universe, release vast amounts of energy in γ-rays, equivalent to up to $1M_{\odot}$ assuming isotropic emission [172, 54]. These events are also especially bright in the optical domain [34, 158]. GRBs classified as "short/hard" have durations of a few seconds or less and feature a harder spectrum in terms of their energy release [198]. They have been associated with GWs, with their progenitors predominantly being CBCs, such as BNSs evidenced by GRB170817A [22] or NSBH systems [205]. Conversely, "long/-soft" GRBs typically last longer than a few seconds, possess a softer spectrum, and are

believed to originate from the core collapse of rapid rotating massive stars [288]. The luminosity of γ-ray afterglows, which cover the X-ray to optical/near infrared (NIR) energy range, further underscores the diverse nature and observational implications of these astrophysical phenomena.

Kilonova—KNe, characterized by their ultraviolet, optical, and infrared emission, are transient astrophysical phenomena that provide cosmic observatories in the aftermath of mergers involving binary NS systems or NSBH pairs. These cataclysmic events are essential for understanding the synthesis of the heavy elements of the universe, such as gold and platinum, through the rapid neutron capture process, or *r*-process [271, 181]. All matter in the universe is made up of 118 chemical elements, varying in mass from hydrogen to oganesson. Most of the naturally occurring elements heavier than iron and nickel are produced by the *r*-process. The *r*-process cannot be recreated here on Earth, and so we rely on astrophysical observations to understand how and where heavy elements form. The BNSs create the highest density of matter in the cosmos (aside from BHs), making these systems ideal laboratories for studying matter [244, 59, 284, 254, 243]. By measuring the radius and the mass of NSs, we can infer the microscopic interactions between neutrons and protons in the NS core. These interactions are described by the EOS a relation between the star's pressure and density. The emission from KNe, unlike the collimated emission from GRBs associated with these mergers, is relatively isotropic, making it an ideal EM counterpart to GW signals [84, 195]. The discovery of EM emission associated the GW chirp has the potential to reveal a much richer understanding of these cataclysmic events [70].

In addition, by identifying the host galaxies of the merging systems and their precise locations within or around their hosts, we obtain valuable information on the binary formation channels, the age of the stellar population, and evidence for dynamical formation channels in dense stellar systems, or displacement due to NS events, in an approach similar to techniques applied to GRBs and KNe [135]. Then, the measure of the GW polarization is important to deduce the binary inclination. This inclination, ι, is defined as the angle between the line of sight to the detector and the orbital angular momentum vector of the binary system. For EM phenomena, it is generally not possible to determine whether a system orbits clockwise or counterclockwise (or equivalently, face-on or not), so sources are usually characterized by an observation view angle: $min(\iota, 180^\circ - \iota)$. However, GW measurements can identify the rotation direction.

GW170817—The landmark observation of GW170817, the GW signature from a BNS merger with an optical counterpart in the NGC 4993 galaxy, approximately 130 million light years away, marked the significance of KNe in astrophysical research [41]. This event highlighted the role of KNe in probing the nucleosynthesis of elements beyond iron [159, 289, 241, 7], investigating the properties of ultra-dense matter [58, 3, 232, 61], and understanding the expansion rate of the universe [5, 151, 102, 80]. The theory of GR predicts that BNS and NSBH mergers will generate GWs, ripples in the geometry of space-time. The synergy between GW detections and KN observations illustrates multi-messenger astronomy, offering a comprehensive approach to studying these cosmic events and their implications [195]. The peak luminosity of a KN, which can be modeled by the energy deposition rate from the decay of *r*-process nuclei, is

given by:

$$L_{\text{peak}} \approx \frac{M_{\text{ej}} c^2}{\tau}, \tag{1.8}$$

where M_{ej} represents the mass of the ejected material, c is the speed of light, and τ is the decay timescale of the r-process elements.

GW170817's broad EM spectrum not only confirmed the association of KNe with the production of heavy elements but also with shortGRB, reinforcing the importance of KNe in the landscape of multi-messenger astronomy. This event confirmed several theoretical predictions about KNe [175, 180, 194], providing information on the r-process and the EOS of NSs. Observations of GW170817's KN component have confirmed the role of NS mergers as the dominant site for the synthesis of the heavy element [104]. Furthermore, this showcased the potential diversity in KN signatures, driven by varying ejecta properties such as mass, velocity, and composition, underscoring the need for a diverse observational strategy to catch the full range of possible KN emissions [195].

1.4.2 Emission mechanisms

The variety in KN emissions, especially the difference between "blue" and "red" KNe, is mainly due to the electron fraction (Y_e, Equation 1.9) of the ejected matter, which determines the nucleosynthetic products. The electron fraction is the ratio of the number of electrons to the total number of baryons (protons and neutrons) in the ejecta:

$$Y_e = \frac{n_e}{n_p + n_n}, \tag{1.9}$$

where n_e, n_p, and n_n represent the densities of electrons, protons, and neutrons, respectively.

The ejecta with higher Y_e (typically $Y_e > 0.25$) tend to be free of lanthanides and produce "blue" KN emissions. This is because these ejecta have lower opacity, allowing light to escape more easily at shorter wavelengths and earlier times [182, 195]. In contrast, ejecta with a lower electron fraction ($Y_e < 0.25$) undergo a r-process nucleosynthesis that leads to the production of heavy and complex nuclei, including lanthanides. The presence of lanthanides significantly increases the opacity, particularly at optical wavelengths, as a result of the high density of line transitions. This results in "red" KN emissions, characterized by a peak at longer, NIR wavelengths and a longer duration compared to the "blue" KN. The opacities of the lanthanide-rich ejecta ($\kappa_{\text{lanthanides}}$) and lanthanide-free ejecta (iron peak, $\kappa_{\text{iron-peak}}$) differ significantly, with $\kappa_{\text{lanthanides}} \gg \kappa_{\text{iron-peak}}$. The high opacity of the lanthanide-rich matter delays the diffusion of light out of the ejecta, shifting the emission to later times and longer wavelengths.

BNS merger—The aftermath of a BNS merger can result in one of two distinct outcomes: the formation of a BH or a hypermassive NS, depending on the total mass of

the merger. A BH is inevitable if the cumulative mass exceeds 2.8 $M_\odot$, as the remnant's gravity overcomes the repulsion forces. But, a total mass within the range of 2.4 $M_\odot$ to 2.8$M_\odot$ leads to the formation of a hypermassive NS, which eventually collapses into a BH as it cools down and loses angular momentum, typically within a timeframe of approximately 10 seconds [256].

NSBH merger—NSBH mergers are characterized by significant mass ejection and disk formation, particularly when the BH is relatively low in mass and rapidly spinning. This scenario facilitates the tidal disruption of the NS in the final *inspiral* stages, instead of complete engulfment. For a NS with a 12 km radius and 1.4$M_\odot$ mass, the BH mass must be between 4 to 12 $M_\odot$ with a spin parameter ($a_{\rm BH}$) of 0.7 to 0.95. This process contrasts with BBH mergers, which typically do not produce significant ejecta. The KNe from NSBH mergers are bright events, surpassing novae in luminosity by a factor of a thousand, and serving as primary sites for heavy element production [195, 167].

Numerical relativity simulations of dynamical ejecta from CBCs are crucial to understanding how the geometric distribution of the ejecta influences the radiation emitted, particularly the EM emission. These simulations are essential to explain the complex processes that occur during CBCs, especially within populations such as BNS and NSBH mergers [167]. Figure 1.8 illustrates the different ejection mechanisms and their contributions to the nucleosynthesis pathways of the main and weak *r*-processes. The interplay between the electron fraction of the ejecta, the resulting nucleosynthetic yields, and the opacities of the synthesized elements plays a significant role in shaping the observable properties of KNe. This intricate relationship highlights the importance of multi-wavelength observations to fully capture the complex nature of these astrophysical events. To achieve this, we require ground-based and satellite observatories GW observatories like the IGWN and The Laser Interferometer Space Antenna (LISA), the GRB observatories such as *Swift*, the X-ray observatories as *Space-based Variable Objects Monitor* (*SVOM*; [258]), ultraviolet observatories such as the forthcoming ULTRSAT, and optical observatories, including Zwicky Transient Facility (ZTF) [63], and the upcoming Vera C. Rubin Observatory (Rubin Observatory)'s, Large Synoptic Survey Telescope (LSST) [156].

1.5 Gravitational-wave detectors

1.5.1 Ground-base detectors

LIGO/Virgo/KAGRA collaboration—The aLIGO [184] and AdVirgo [29] observatories represent the cutting edge of the second generation of GW detectors. Each uses advanced Michelson interferometer modifications to enhance detection capabilities. The aLIGO system consists of twin facilities, including the LHO and the LLO, both with 4km arm lengths, Fabry-Pérot cavities to extend the GW interaction time, and power recycling to increase laser power. AdVirgo, situated at the European Gravitational Observatory in Cascina, Italy, incorporates 3km arms and takes advantage of state of the

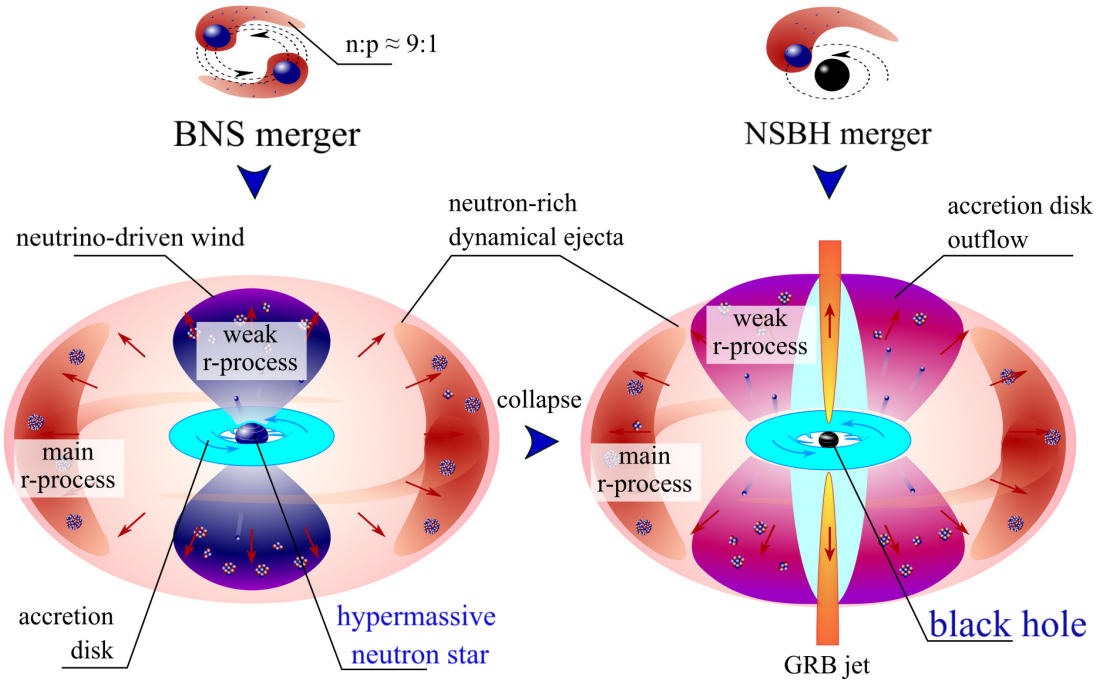

Figure 1.8: Schematic representation of *r*-process nucleosynthesis sites in BNS and NSBH mergers. The left panel shows a BNS merger leading to the formation of a BH and its associated ejecta types, highlighting the role of NS driven outflows. The right panel depicts an NSBH merger, characterizing the accretion disk outflows and the formation of a BH. Detail: A neutron to proton ratio (n:p ≈ 9:1) inside a NS, determine the nature of the *r*-process nucleosynthesis. This figure is adapted from work by Matthew R. Mumpower. The concepts and data presented are based on [167, 256].

art optical technologies to improve its sensitivity to GW signals. The Integration of KAGRA [35] in Japan, with its 3km arms, into the global network alongside aLIGO and AdVirgo for the O4 and forthcoming LIGO/Virgo/KAGRA's fifth observing run (O5) crucial for confident GW detections. This IGWN improves our ability to accurately locate GW sources through coherent detections across multiple detectors. GW sky maps, which are essential for the location of sources, use advanced probability mapping techniques to identify EM counterparts [265, 64]. The continual improvement in detector sensitivity increases our capacity to detect CBCs, a capability further reinforced by the inclusion of KAGRA. The map of detector projects is shown in Figure 1.9.

GWs induce distortions by altering the relative lengths of the interferometer arms. The core detection mechanism involves splitting a laser beam into two perpendicular paths that reflect off mirrors at the ends of the arms and then recombine, creating an interference refers sensitive to GW. The LIGO/Virgo/KAGRA detectors target 100-1000 Hz frequencies, corresponding to BH masses of 1–100 $M_\odot$, and are typically sensitive to BH masses around 150 $M_\odot$, covering *inspiral* and *merger* phases.

Virgo detector configuration in Run O3—During the O3, AdVirgo detector showcased significant advances and specifications within the IGWN. The core of

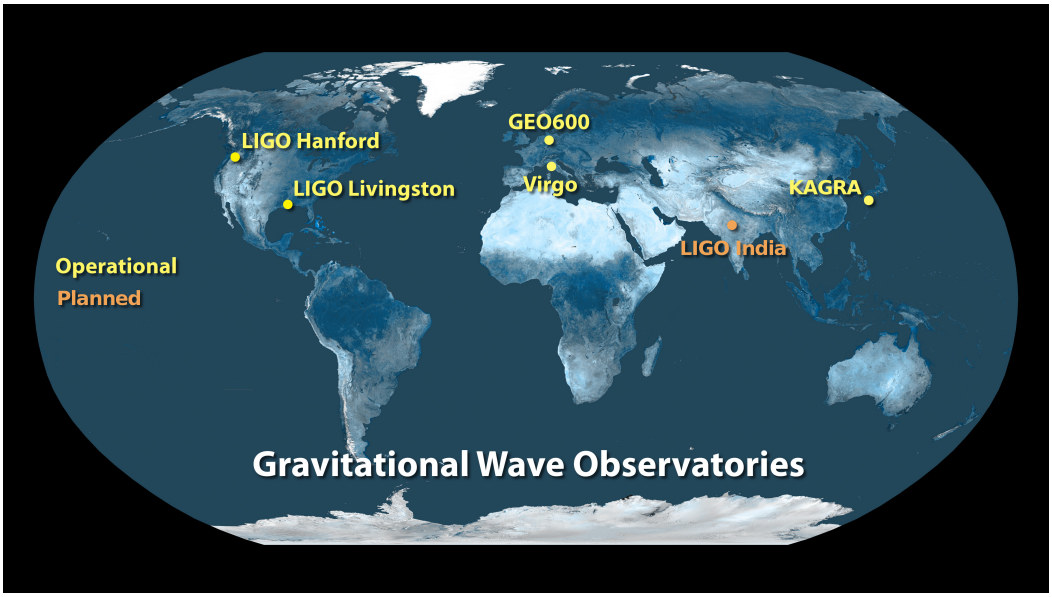

Figure 1.9: Map of detector construction projects. Credit: Caltech/MIT/LIGO Lab

Virgo's operation includes a power-stabilized laser (PSL) providing a consistent light beam. This beam, modulated by an electro-optic modulator (EOM), is purified of spatial shape and frequency noise by an input mode cleaner (IMC), enhancing its suitability for detection. At the beam splitter (BS), the light is divided, traveling through the West and North arms, each several kilometers long, and reflecting off mirrors (B7 and B8) before merging back at the BS. It is at this juncture that GWs manifest, subtly altering arm lengths and inducing a detectable phase shift as the beams recombine [28, 37]. The detection system is supported by sophisticated feedback controls, such as the Power Recycling Cavity Length (PRCL) and the Michelson Interferometer Channel (MICH), which are important for maintaining resonance within the cavities and optimal interference at the BS. Additionally, a Squeezed Vacuum Source and the Subcarrier Servo Feedback System (SSFS) stabilize the laser light frequency and reduce quantum noise, respectively. Photodiodes convert the interference patterns, altered by GWs, from optical to electrical signals, enabling the extraction of GW signals and noise reduction. Advanced signal processing and machine learning techniques analyze photodiode data, isolating GW events from cosmic noise and matching them to theoretical waveforms from astrophysical phenomena, such as binary BH mergers.

The laser power injected into the interferometer was 19W, and a squeezed light source was installed to reduce the noise of the shots at high frequencies. The 3km arm length, 1.2m diameter vacuum tubes maintained at 10^{-9} mbar, and the use of Fabry-Pérot cavities and a high-reflectivity Power Recycling Mirror (PRM) exemplify the technological advances made to enhance sensitivity and precision in GW detection. Operational sensitivity is fundamental for differentiating genuine GW signals from background noise. Achieving this sensitivity involves advanced noise reduction techniques and precise design of the optical and vacuum systems within the detectors. Figure 1.10 provides a detailed schematic of the Virgo detector layout during the O3 run, illus-

trating the integration of critical components such as the laser source, beam splitter, Fabry-Pérot cavities and end mirrors. These elements are key to enhancing the detector's sensitivity to GWs. For a comprehensive discussion on the operational sensitivity and noise reduction strategies in GW detectors, refer to [37], which explores the sophisticated design and technology behind these advancements. The sensitivity of a detector is evaluated by the mean distance at which it can detect the *inspiral* signal of a $1.4M_{\odot}$ BNS with an S/N of 8, known as the BNS *inspiral* range.

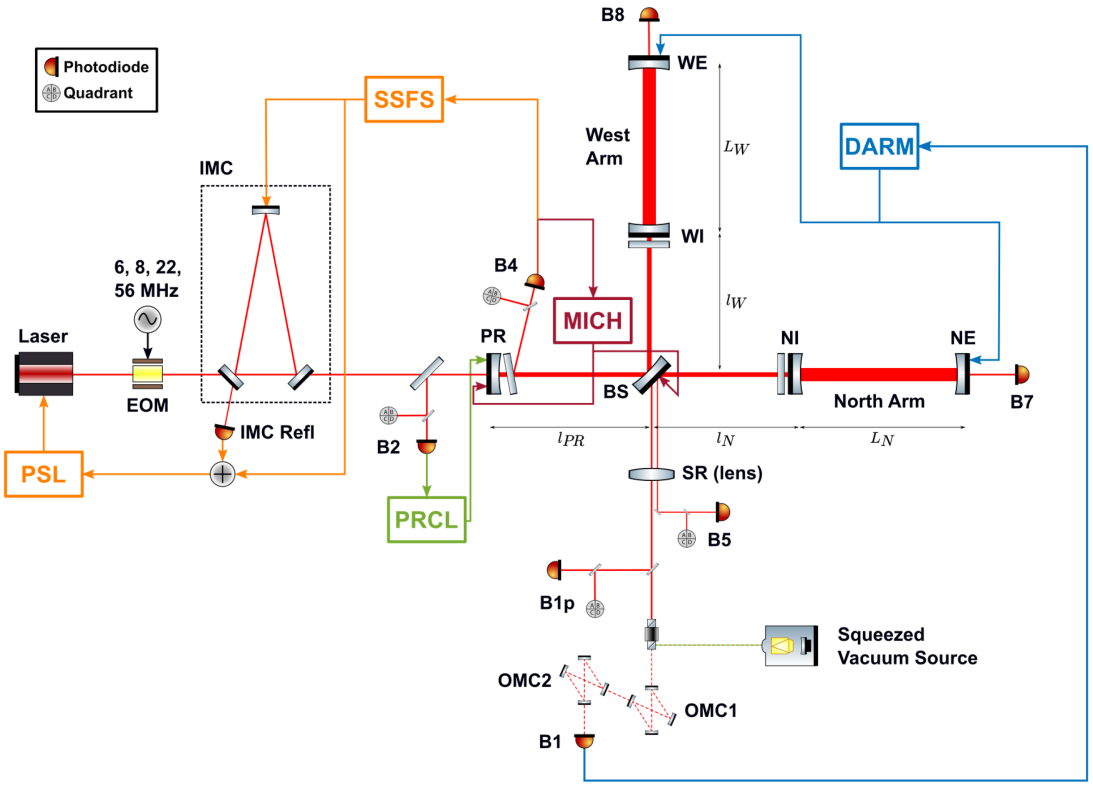

Figure 1.10: Schematic of Virgo detector during O3, illustrating essential elements such as the laser source, beam splitter, Fabry-Pérot cavities, and end mirrors. Figure credit: from [37].

BNS inspiral range—The operational range of GW observatories is determined by the S/N for a given GW signal, $\tilde{h}(f)$, within the ambient noise environment. The power spectral density (PSD) of this noise, $S_n(f)$, is defined as $S_n(f) = \frac{2}{T}|\tilde{n}(f)|^2$, where T represents the total observation time and $\tilde{n}(f)$ is the Fourier transform of the detector's noise time series $n(t)$. The mean S/N, $\langle\rho\rangle$, is determined by the integral:

$$\langle\rho\rangle = \left(\int_{f_{\min}}^{f_{\max}} \frac{|\tilde{h}(f)|^2}{S_n(f)}\, df\right)^{1/2} \tag{1.10}$$

Given the inverse proportionality of $\tilde{h}(f)$ to the luminosity distance d_L and its frequency dependence of $f^{-7/6}$.

At the Newtonian order the signal waveform is:

$$\tilde{h}(f) = \frac{1}{d_L}\left(\frac{5\pi^{3/2}}{24c^3}\right)^{1/2}(G\mathcal{M}_c)^{5/6}(\pi f)^{-7/6}e^{i\Psi(f,M)}, \tag{1.11}$$

where $\mathcal{M}_c$ represents the chirp mass and the phase Ψ is a function of f, which varies with the total mass M.

The horizon distance d_H for the binary, using the waveform above, is calculated with $\langle\rho\rangle = 8$:

$$d_H = \frac{1}{4}\left(\frac{5\pi^{3/2}}{24c^3}\right)^{1/2}(G\mathcal{M}_c)^{5/6}\left(\int_{f_{\min}}^{f_{\max}}\frac{f^{-7/3}}{S_n(f)}df\right)^{1/2}, \tag{1.12}$$

This approach offers a detailed methodology for determining the operational range of GW observatories by considering the S/N and the properties of the GW signal and noise. In this analysis, we have used the TaylorF2 waveform model to calculate $\tilde{h}(f)$ for non-spinning BNS systems with equal masses of $m_1 = m_2 = 1.4M_\odot$, spanning a frequency range from $f_{\min} = 10$Hz to $f_{\max}$, where the latter matches the frequency at theISCO [90]. To assess the efficacy of different interferometers, I use their respective $S_n(f)$ to ascertain the BNS *inspiral* range for a binary system of 1.4 $M_\odot$ detected with an S/N of 8. Figure 1.11 displays the operational timeline and the BNS *inspiral* range values for each interferometer during this interval. The detection of BNS *inspiral* is achievable with an S/N of 8 [128, 87, 127]. In chapter 2, we will perform these calculations for the O4 and O5.

Virgo in O4b run—Virgo has commenced the O4b phase, continuing joint GW detection efforts with LIGO. This starting at 15:00 UTC on 10 April 2024, after the O4a run and commissioning, the aim is to maintain O4b until February 2025 without breaks for upgrades or maintenance. The Virgo detector, now tuned to a sensitivity of 55-60 Mpc, targets a 80% minimum duty cycle, which is useful for ongoing GW data collection and analysis GW. Minor adjustments are expected to further improve Virgo's performance. The LIGO detectors operate at 155-175 Mpc sensitivity, achieving 80 and 98% duty cycles, indicating enhanced network observation capabilities. Figure 1.12 shows the latest Virgo sensitivity curve, including O3b and O4 references, highlighting its detection progress in O4b.

As we will discuss in Chapter 6, several factors contribute to noise in detectors, including environmental noise, instrumental artifacts, quantum sensing noise, thermal fluctuations, and other unknown sources of noise limiting sensitivity. Environmental noise, such as seismic noise, significantly reduces detector performance. To mitigate sensitivity limitations such as seismic noise in third-generation interferometers, significantly larger projects are being considered. These include the Einstein Telescope (ET) project [229] and the American Cosmic Explorer project [237]. Alongside these terrestrial interferometers, the space-based LISA project observes at low mHz frequencies.

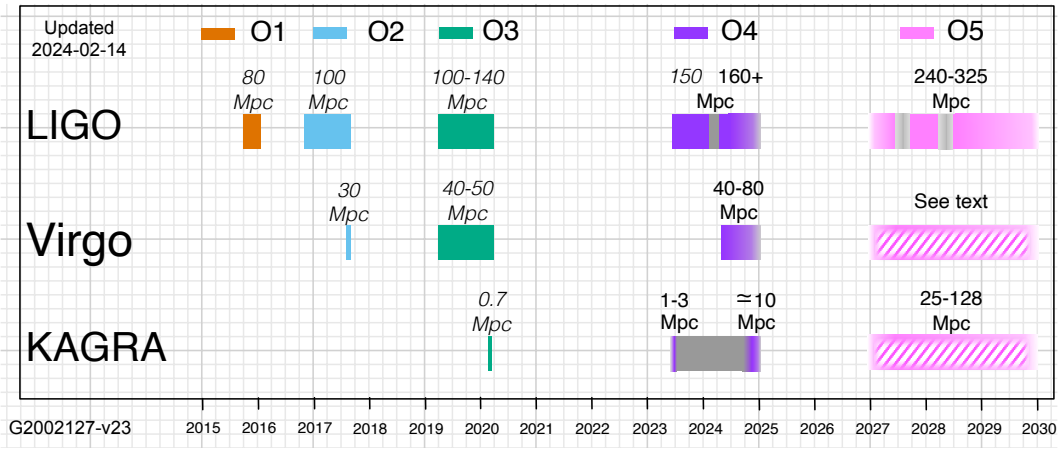

Figure 1.11: Timeline of the O4, which commenced on May 24, 2023, and is slated for a duration of 20 calendar months. It is anticipated that four observatories, LHO, LLO, Virgo, and KAGRA, will be operational and contribute data during this period. The timeline delineates periods of observation and scheduled downtimes, which are allocated for upgrades and commissioning, illustrated by vertical gray bands. In adition, the figure presents the detection range for BNS mergers based on a single-detector S/N threshold of 8 for each run. Accurate monitoring of these ranges is vital for gravitational wave astrophysics, enhancing our understanding of BNS characteristics and distribution.
Credit for data and visualization: LIGO Scientific Collaboration, https://dcc.ligo.org/LIGO-G2002127/public

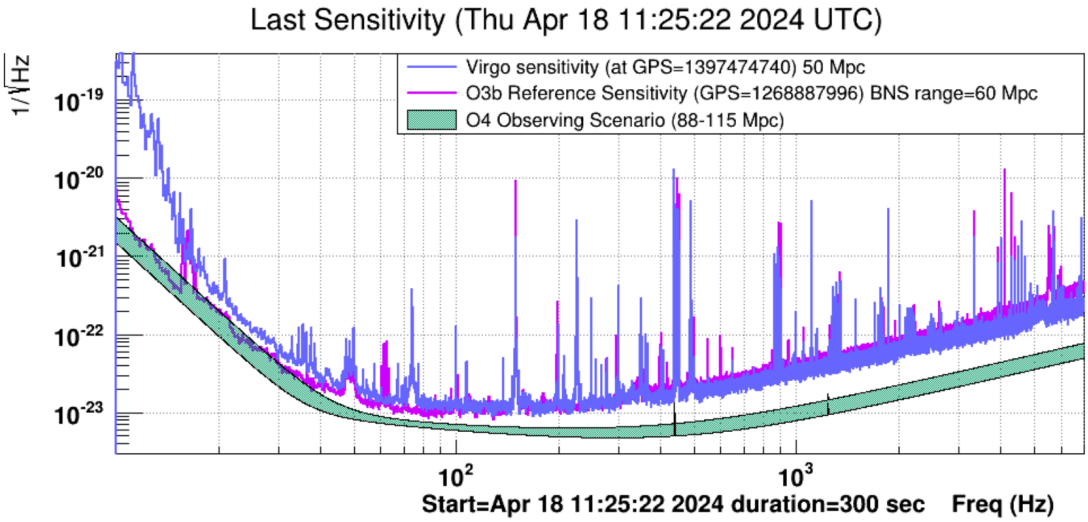

Figure 1.12: This graph, dated April 14, 2024, shows the Virgo detector's sensitivity during the O4b period. It compares the BNS *inspiral* sensitivity of 54 Mpc with the 60 Mpc from the O3b period and the 88 Mpc target for the O4 period, indicating improvements for the upcoming O5 run.
Credit: https://vim.virgo-gw.eu

1.5.2 Space-based detector

The LISA is a major GW astronomy initiative, responding to the call from the European Space Agency (ESA) for the concepts of the L3 mission [39]. Scheduled for a 2035 launch, LISA aims to detect low-frequency GWs (10^{-5} Hz to 10^{-1} Hz), beyond the reach of terrestrial detectors such as LIGO, Virgo, KAGRA and other upcomin GW observatories. The mission will conduct an extensive survey of gravitational transients, offering unique insights into various cosmic events.

LISA mission—The LISA mission involves three spacecraft configured in an equilateral triangle, with each side measuring 2.510^6 km long, as they orbit the Sun alongside Earth. This setup allows for detecting GWs from events like massive BH mergers across the universe and compact binary systems within the Milky Way. The data will test GR, advance knowledge of BH physics, stellar evolution, and provide insights into extreme mass ratio inspirals (EMIs), exploring space-time around massive BHs and compact object properties. Additionally, LISA will monitor the stochastic background [176].

LISA Sensitivity—The sensitivity curve of the LISA is one of the important aspect of its design, showing its capability to detect GWs across a wide low-frequency range. The instrument sensitivity curve, $S_n(f)$, incorporates the effects of both optical metrology noise, $P_{textOMS}$ and acceleration noise, $P_{textacc}$, as described by:

$$S_n(f) = \frac{10}{3L^2}\left(P_{\rm OMS} + 2\left(1+\cos^2\left(\frac{f}{f_*}\right)\right)\frac{P_{\rm acc}}{(2\pi f)^4}\right)\left(1+\frac{6}{10}\left(\frac{f}{f_*}\right)^2\right), \quad (1.13)$$

$$\text{where, } \begin{cases} P_{\rm OMS} = (1.5\times10^{-11}\,\text{m})^2\left(1+\left(\frac{2\,\text{mHz}}{f}\right)^2\right), \\ P_{\rm acc} = (3\times10^{-15}\,\text{m s}^{-2})^2\left(1+\left(\frac{0.4\,\text{mHz}}{f}\right)^2\right)\left(1+\left(\frac{f}{8\,\text{mHz}}\right)^4\right)\text{Hz}^{-1} \end{cases}$$

The characteristic frequency scale $f_* = c/(2\pi L)$ for the detector, where $L = 2.5$ Gm is the arm length of LISA and c is the speed of light [228].

Galactic binaries confusion—The galactic confusion noise, $S_c(f)$, which decreases as the mission progresses, is represented by the equation [92]:

$$S_c(f) = Af^{-7/3}e^{-f^\alpha+\beta f\sin(\kappa f)}\left(1+\tanh\left(\gamma(f_\kappa - f)\right)\right)\text{Hz}^{-1}, \quad (1.14)$$

with parameters depending on the observation time, as shown in Table 1.1.

The overall sensitivity curve for LISA , $S_{\rm Lisa}(f)$, combines instrument noise and unresolved galactic binaries confusion noise, and is illustrated for a four-year mission lifetime in Figure 1.13.

Table 1.1: The parameters of galactic noise confusion adjust based on the observation time.

	6 months	1 year	2 years	4 years
α	0.133	0.171	0.165	0.138
β	243	292	299	-221
κ	482	1020	611	521
γ	917	1680	1340	1680
f_κ	0.00258	0.00215	0.00173	0.00113

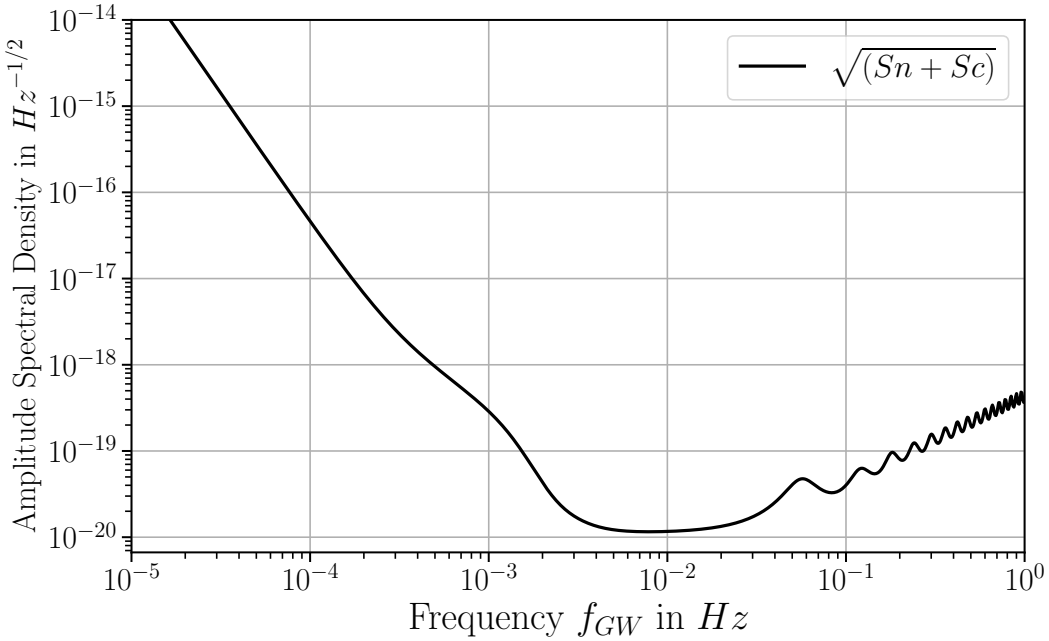

Figure 1.13: LISA overall sensitivity curve, including both the instrument noise and the unresolved galactic binaries confusion noise, over a four-year mission lifetime. The observation frequency range is set between 10^{-5} and 1 Hz.

1.6 Telescopes

The KNe are potential EM counterparts to GWs, emitting across the ultraviolet (UV), optical, and NIR spectra. Prompt, automated UV follow-ups are essential for tracking KN candidates. Effective coordination of upcoming space telescopes like ULTRSAT and Ultraviolet Explorer (UVEX) [171] is critical. The optical emissions from KNe are monitored using ZTF and the Rubin Observatory. In this section, I focus on ULTRSAT, ZTF, and Rubin Observatory, detailed in Chapters 3 and 4.

ULTRASAT mission—The ULTRSAT is designed for a 2026 launch into geostationary orbit, the ULTRSAT mission is set to revolutionize the field of UV astronomy. Although the average limiting magnitude of ULTRSAT, 22.5 absolute in a 900s

exposure for a 5σ detection may appear modest relative to other space telescopes, it is important to appreciate the specific objectives of the mission and observational parameters. Operating within the near-ultraviolet spectrum (230-290 nm), a challenging region for detecting dim sources, ULTRSAT boasts a significant field of view (FOV) of 204 deg^2, enabling it to quickly scan vast areas of the sky for transient phenomena [259]. This extensive field capability is vital for its main objective of identifying and tracking rapid transients such as BNS mergers and KNe. Thus, the limiting magnitude is a deliberate compromise between sensitivity, survey speed and coverage area, establishing ULTRSAT as a distinctive tool for time-domain astronomy and transient sky studies. Additionally, it is an innovative approach to astronomical photometry by integrating a bandpass finely tuned to the radial positions. This unique attribute is crucial for wide-field observations of transient astrophysical events. By sensitively responding to radiation from various radial distances, the ULTRSAT bandpass facilitates detailed detection and analysis of sources, shedding light on their intricate properties. This radial sensitivity is essential for distinguishing between foreground and background events, thereby enhancing the mission's ability to pinpoint and examine rapid transient occurrences and offering a new perspective in the field of time-domain astronomy.

Moreover, the advanced UV capabilities of ULTRSAT are expected to elucidate the dynamics behind tidal disruption events (TDEs) and accretion processes at supermassive black holes. By capturing the early UV signatures of these violent occurrences, ULTRSAT will deliver essential data for understanding the physical conditions and energy dynamics of TDE, and provide insight into the population statistics and evolution of these elusive phenomena. ULTRSAT is set to revolutionize the study of cosmic events with its wide UV time-domain survey capabilities. It is designed for the rapid detection and monitoring of transient events such as BNS mergers and KNe. Equipped with a rapid slew rate of more than 0.5 $deg.s^{-1}$ and a roll-slide readout mode for fast data collection, ULTRSAT is uniquely prepared for ongoing observation and immediate response [259]. Its operational flexibility allows it to provide continuous UV light curves and early alerts, allowing in-depth studies of the structure and dynamics of these cosmic phenomena and their role in the production of elements of the *r*-process. The huge FOV, rapid slewing, and adaptable exposure times are crucial to capturing the early stages of these events. Furthermore, real-time data transmission of ULTRSAT and the swift alert system will work in conjunction with ground-based telescopes and other space observatories, forming a worldwide network of rapid response astronomical resources. This cooperation will enhance the scientific outcomes from transient events, enabling multi-wavelength and multi-messenger studies that offer a comprehensive understanding of astrophysical phenomena.

Vera C. Rubin Observatory—The upcoming Rubin Observatory LSST [156] is designed for a comprehensive 10-year survey of the southern sky. The LSST, with its 8.36 m aperture Simonyi Survey Telescope and a unique 9.6 deg^2 field of view located in Chile, aims to significantly increase the volume and quality of imaging data over a 10-year period and is expected to be operational in August 2025. It will utilize multiple bands (*sdssu*, *ps1__g*, *ps1__r*, *ps1__i*, *ps1__z*, and *ps1__y*) to deliver subarcsecond image quality and provide nightly alerts of astrophysical events around the world in real-

time [66]. LSST exhibits distinct movement capabilities in its azimuth and elevation directions: In the azimuth direction, it moves at a rate of 7 deg.s^{-1} over a range of 360 deg, while in the elevation direction, it moves at 3.5 deg.s^{-1} over a range of 90 deg [207]. Given the disparity in the range of movements, a weighted average of 4:1 is used to calculate a typical slew rate (see Eq. 1.17). This weighting reflects the azimuth's greater significance because of its higher speed and wider range. The typical slew rate (TSR) is therefore calculated as follows:

$$\text{TSR} = \frac{(4 \times \text{Azimuth Rate}) + \text{Elevation Rate}}{5} \tag{1.15}$$

$$= \frac{(4 \times 7) + 3.5}{5} \tag{1.16}$$

$$= 6.3\,\text{deg.s}^{-1} \tag{1.17}$$

The LSST focuses on key scientific themes such as probing dark energy and dark matter, exploring transient optical phenomena, mapping the Milky Way, and cataloging solar system objects. Its features a flexible scheduling system to handle unexpected events and enhance scientific outcomes. The survey includes a primary wide-fast deep survey, fields equipped with a 3.2-gigapixel camera, advanced data processing, and specialized mini or microsurveys [156].

Zwicky Transient Facility—The ZTF [63, 142, 190, 108]) is a leading time-domain astronomy observatory that efficiently builds an all-sky library, designed with an emphasis on maximizing the speed of the volumetric survey. This innovative approach combines the significant elements of limiting magnitude, expansive field of view, efficient exposure, and reduced overhead into a single metric. This metric effectively captures the observatory's ability to quickly scan the cosmos for new astrophysical phenomena.

Central to ZTF's operational excellence is the "Archon" controller, a sophisticated system that ensures pixel-synchronous readout, an important component for maintaining the pristine quality of the captured images. Complementing this is a state-of-the-art biparting shutter, custom-developed to significantly minimize beam obscuration. This shutter operates with exceptional swiftness, significantly enhancing the observatory's cycle of observation and enabling it to keep pace with the transient sky. In its quest to map the transient and variable universe, ZTF demonstrates remarkable proficiency in processing both streaked Near-Earth objects and point-like moving objects. It employs dedicated pipelines designed for the meticulous task of identifying, linking tracklets and then fitting orbits, showcasing its advanced capabilities in tracking and studying the motion of celestial objects [63]. A distinctive feature of ZTF is its wide field of view multi-band optical imagery, which extends a vast 47 deg^2. This expansive reach is facilitated by the use of specialized bands, namely $ztfg$, $ztfr$, and $ztfi$. ZTF is a public-private project that routinely acquires 30 s images in the bands that cover the entire available northern night sky every two nights. Due to its cadence, ZTF has one of the most complete records of the contemporary dynamic sky. This capability enables the detection of transients in the early stages of their active phase [142, 190, 108,

109]. ZTF's systematic candidate filtering down potential candidates from thousands to a manageable few by checking brightness changes and historical data. Its comprehensive follow-up strategy employs an extensive network of telescopes and instruments, allowing in-depth photometric and spectroscopic studies [99]. These features enable ZTF to quickly identify and examine transients, positioning it as an essential observatory alongside with LSST and ULTRSAT. Figure 1.14 presents a comparison of the FOV of ZTF alongside LSST and other large-survey cameras.

From these observatories, initiatives such as Global Rapid Advanced Network Devoted to Multi-messenger Addicts (GRANDMA) and the Nuclear-physics and Multi-Messenger Astrophysics (NMMA) group monitor GWs along with their EM counterparts, with the goal of integrating this information. Their aims include understanding the *r*-process, determining the EOS for NSs, and estimating the expansion rate of the universe through the consolidation of these data.

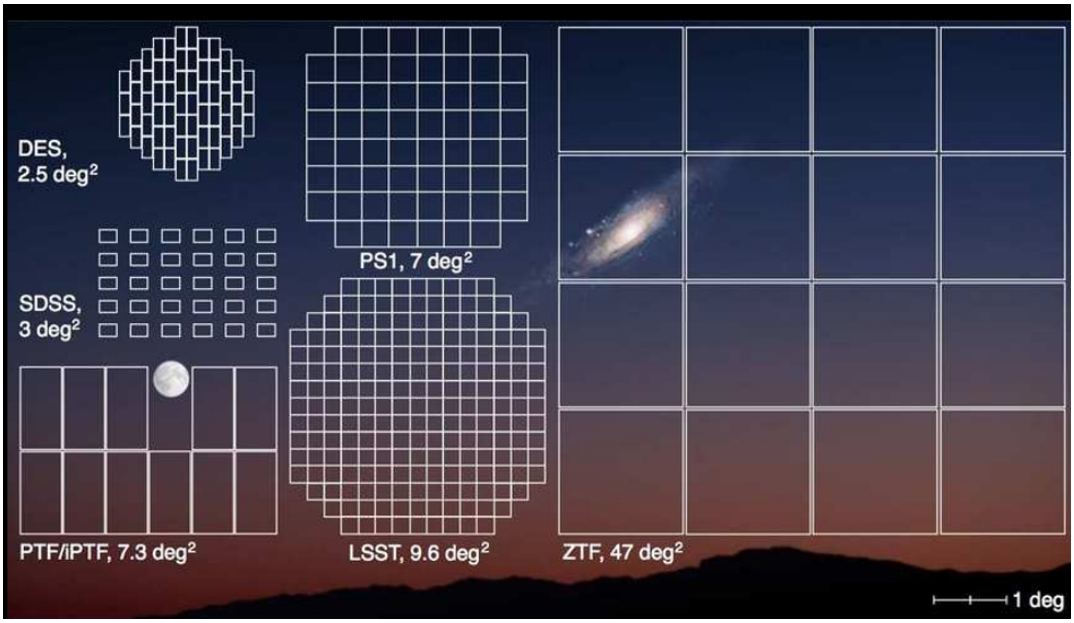

Figure 1.14: Comparative analysis of the FOV for the ZTF camera with other major survey cameras, such as LSST. Both the Moon and the Andromeda Galaxy (M31) are depicted to scale. Figure credit: ZTF, https://www.ztf.caltech.edu/ztf-camera.html.

1.7 GRANDMA consortium

The GRANDMA consortium is an international collaboration in the field of astrophysics. It comprises an extensive network of 30 telescopes located in 23 observatories, which involve 42 institutions from 18 different countries [50, 49]. This vast assembly is dedicated to the swift detection and analysis of optical phenomena. One of the key strengths lies in its wide geographical distribution, which facilitates continuous monitoring of the sky and enhances the potential for observing transient astronomical

events. GRANDMA has made significant contributions to observation campaigns such as O3a and O3b, showcasing the remarkable capabilities of global scientific collaboration in advancing our understanding of the universe. This inclusion extends the reach and impact of GRANDMA in multi-messenger astronomy, highlighting the importance of diverse global participation in scientific endeavors. Furthermore, GRANDMA's approach to participatory science allows amateur astronomers to make significant contributions to the field, specifically within the *Kilonova-Catcher* KNC[1] initiative [50]. During the recent "ReadyforO4" campaign [33] to follow up on transients revealed by ZTF, GRANDMA evaluated the potential of its team, which followed up eight transient events. Observations were conducted using multiple filters and telescopes, demonstrating the invaluable role of citizen science in cutting-edge astronomical research. Figure 1.15 shows the 77 telescopes that participate in the GRANDMA KNC citizen science program.

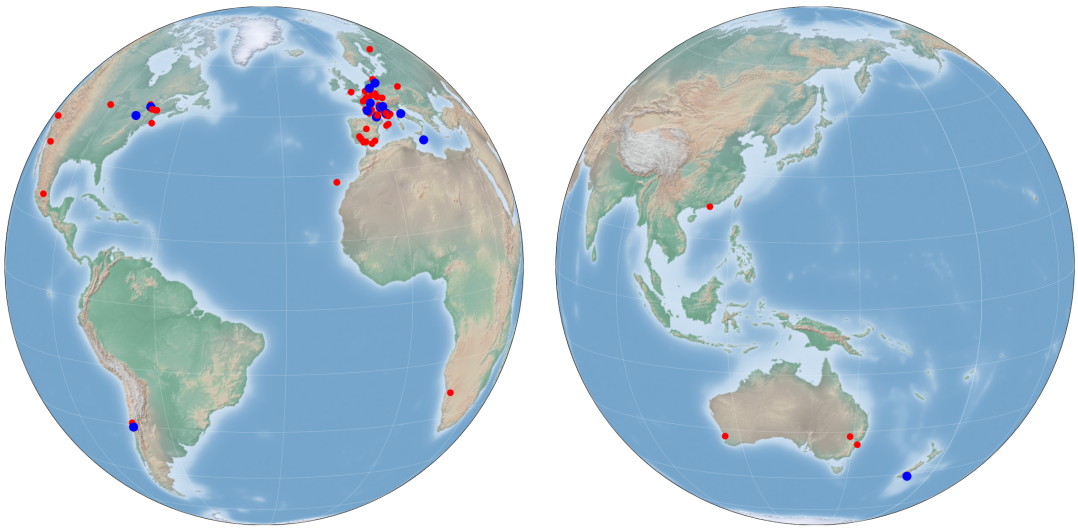

Figure 1.15: Global distribution of the 77 telescopes participating in the GRANDMA citizen science program KNC, the telescopes used for the "ReadyforO4" campaign are marked in blue, while the remaining telescopes in the network are indicated in red. This figure is reproduced from the GRANDMA colaboration publications [33].

1.8 Conclusion

In this chapter I have explored the implications of GR and its importance in multi-messenger astronomy. I highlight the physics of compact objects, such as BHs and NSs, and their mergers, which could lead to an transient known as KN. Advances in GWs astronomy from LIGO, Virgo, KAGRA, and future missions like LISA, will help probe the physics of compact objects. If mergers produce EM counterparts, they will constrain the nature of NS, allow independent measurement of the universe's expansion rate,

[1] http://kilonovacatcher.in2p3.fr

and study *r*-process nucleosynthesis. Coincident detection requires mastering statistics and detector capabilities. The next chapter examines current and upcoming observing campaigns.

Outline

***

Through Chapter 1, I have gradually introduced the necessary concepts and tools, starting from GR to multi-messenger astronomy. The search for EM counterparts of GWs, particularly KNe, is crucial to understanding the production of heavy elements and the evolution of cosmic chemical elements. Their combination with GWs provides an opportunity to independently constrain the properties of the binary system. However, this combination faces several significant challenges. One key issue is our limited understanding of KNe, the radioactive explosions that occur during the BNSs merger or NSBHs. The resolution of this issue involves improving alerts by reducing the detection areas provided by GWs to enable the detection of potential electromagnetic counterparts. The capability of UV, optical, and NIR telescopes, such as ULTRSAT for UV, and optical telescopes like ZTF and Rubin Observatory, to detect these phenomena is essential. Finally, these data help answer fundamental questions such as: What is the EOS of NS ? and What is the value of the universe's expansion rate? These are independent projects, but share a common goal, to which I have tried to provide answers during my doctoral thesis.

Chapter 2—The O3 of aLIGO/AdVirgo/KAGRA has significantly advanced GW astronomy with another BNS merger and the first NSBH merger detections. In this chapter, I explore CBCs simulations using the PDB/GWTC-3 distribution, guided by the latest projections from the IGWN. The simulations aim to provide a foundation for precise EM follow-up strategies, optimizing future scientific results. With enhanced detector capabilities, this research seeks to expand astrophysical knowledge and prepare for future multi-messenger observations.

Chapter 3—In multi-messenger astrophysics, combining GW, EMs signals and neutrino data independently constrains NS mergers and their extreme environments. These messengers provide complementary observations to probe different aspects and improve understanding of the system. Although still emerging, integrating GW and EMs observations uncovers fundamental Universe properties, from cosmic expansion to atomic matter formation. The observation of GW170817, a BNS merger detected in both GW and EMs spectra, has advanced nuclear physics by using the NMMA framework to explore dense matter and improve H_0 measurements. This framework, which merges theoretical models with diverse observational data, has significantly impacted astrophysics. Here, we introduce NMMA, measure universal expansion, constrain the EOS, and present the "ReadyforO4" campaign of the GRANDMA collaboration.

Chapter 4—Building upon advances in GW astronomy, this section delves into the refinement of EM counterpart detection strategies. Using accurate algorithms and comprehensive skymaps, the aim is to enhance the efficiency of telescopic observations. This work reviews the ULTRSAT mission, the Rubin Observatory and the ZTF,

focusing on their roles in detecting transient events. Introducing the Gravitational-wave Electromagnetic Optimization (gwemopt) scheduling tool, I discuss simulated EM detection rates throughout the ongoing and forthcoming observational periods and review the efficiencies of such detections. It underscores the importance of rapid classification of transient events and underscores the contributions of each observatory to multi-messenger astronomy, setting the stage for future investigations.

Chapter 5—Significant progress in GWs and EM research has led to the creation of platforms like *SkyPortal* for effective discovery, follow-up, and management of transient events. With the increasing number and sensitivity of telescopes such as ZTF and the forthcoming Rubin Observatory's LSST, a surge in transient alerts has occurred. Astronomers require efficient methods to pinpoint critical events. To this end, I developed an analysis service integrating *Fink broker*, *NMMA*, and *Skyportal* to study rapid transient light curves.

Chapter 6—Since the 2015 detection of GWs, the IGWN has enhanced detector sensitivity. However, complex *non-linear* noise from operational and environmental factors often masks GW signals, making them undetectable at standard thresholds. The `DeepClean` algorithm addresses this by isolating GW signals from both *stationary* and *non-stationary* noise, crucial for improving data analysis precision in astrophysics and GW astronomy. This tool enables robust detection and detailed study of GWs from cosmic events, enhancing our cosmic understanding. I present the initial application of `DeepClean` in the Virgo GW detector and summarize key findings in Conclusion.

Chapter 7—-This chapter summarizes the key findings of this PhD dissertation in the Conclusion.

Chapter 2

PDB/GWTC-3 Distribution in Ligo.Skymap

***

This work outlines my role in the development of the paper *Updated Observing Scenarios and multi-messenger Implications for the IGWN O4 and O5*, which was published in *The Astrophysical Journal*. The project was a collaborative effort with a team of 17 members, including interns, researchers, and PhD candidates, under my coordination [163]. In addition, a supplementary document that I have produced for the LIGO Scientific Collaboration (LSC) in order to update the S/N threshold, is also discussed. This supplement is documented as T2300385-v1[1] and published at the LIGO DCC (Document Control Center). My contributions included everything from incorporation of the PDB/GWTC-3 distribution to formulating the proposal of the ZTF, as well as managing the simulation campaign for "observing scenarios," making statistical predictions and analyzing the O4. The simulations produced for this purpose are currently available to the user community in the IGWN User Guide[2].

[1] https://dcc.ligo.org/LIGO-T2300385

[2] https://emfollow.docs.ligo.org/userguide/capabilities.html

2.1 S/N threshold warning

During the initial phase of the O4 observation campaign by LIGO/Virgo/KAGRA, only the LIGO detectors were fully operational. In Section 2.5.1, we identified a discrepancy between our predictions and the observational results from this phase, revealing the need to adjust the S/N threshold from 8 to 10 to better align with the actual data. This adjustment was confirmed through additional simulations I conducted using several signal detection pipelines from CBC, including GstLAL [192, 278, 123], MBTA (Multi-Band Template Analysis; [55]), PyCBC [81, 213], and SPIIR [149, 185]. Detailed methods are provided in Section 2.5.1.

Based on this study, I propose adopting an S/N cutoff threshold of 10 for future observing scenarios in the LIGO/Virgo/KAGRA collaboration. However, despite our recommendation for an S/N > 10, this threshold is not applied to the estimations for the upcoming O5 campaign. This decision is due to political and institutional factors. The Virgo and KAGRA detectors currently face challenges that make it unlikely they will reach the predicted sensitivities used in our simulations. The reliability of our results depends on the detectors achieving these sensitivities. While this is true for the LIGO detectors, whose predicted and measured sensitivities for O4a are nearly identical (as shown in Tables 2.5.1, which uses the predicted sensitivities, and 2.6, which uses the measured sensitivities), it is not the case for Virgo and KAGRA.

In conclusion, although it would be best to base the S/N threshold of 10 for O5 only on the LIGO detectors, this is not possible due to political reasons. Therefore, in this chapter, we use an S/N of 8 for the next O5 campaign in order to include all the network detectors, even though we recommend using 10.

2.2 Background

Accurate assessments of the sensitivity, detection probabilities, and localization accuracy of the global detector network are crucial for the astronomical community's strategic planning of observation campaigns and the design of future telescopes and missions. "Observing scenarios" simulate the detection and localization of GW events, providing realistic forecasts of the network's efficacy during the O4 and O5 [260, 26]. Recent scenarios [223] have been meticulously calibrated to public alerts from O3, enhancing localization precision by simulating the actual S/N threshold of GW and integrating single-detector searches [138, 212]. These studies explore compact objects, *r*-process nucleosynthesis, and cosmological expansion [209, 91, 223]. Observing run O4 was initiated with LHO and LLO in operation, achieving a BNS range of 140-165 Mpc. Following a commissioning break, Virgo joined in March 2024 with a BNS range of 55 Mpc, in conjunction with KAGRA in Spring 2024. This will elevate the network to its full four-detector capacity, augmenting the detection and localization capabilities for GW events. By simulating realistic *astrophysical* distributions of mass, spin, and sky locations for CBCs , I evaluated the detection probabilities across this network, estimat-

ing the distributions of sky-localization areas and distances for *detected* events, as well as the cumulative event detection rate.

2.3 Population models

This section introduces the PDB/GWTC-3 distribution, based on the PDB model in [122] and [25]. It covers NSs and BHs identified by the IGWN earch pipelines, classified into three subpopulations: BNS, NSBH, and BBH.

2.3.1 Incorporation of external distribution in Ligo.Skymap

In the context of IGWN, the LRR distribution [17] is essential, especially during the O3. As discussed in [17] and [223], it significantly enhances predictive capabilities. For the BNS subpopulation, a truncated Gaussian mass distribution is used centered on $1.33\,M_\odot$ with a range $[1,3]\,M_\odot$ and a standard deviation of $0.09\,M_\odot$, represented as $p(m) \sim \mathcal{N}(\mu, \sigma^2)$. Moreover, the spin magnitudes are uniformly distributed between $[0, 0.05]$. For BBHs, the mass sampling follows a truncated distribution of the power law $p(m) \propto m^a$ over the range $[3,50]\,M_\odot$, with $a = -2.3$, according to [250]. The mass pairing criterion is set as $m_2 \leq m_1$, with spins uniformly distributed below 0.99. In both cases, the spins are either only aligned or anti-aligned spins, i.e., the possibility of misaligned spin and precessing systems is neglected.

Subsequent analyzes conducted by the LIGO/Virgo/KAGRA collaboration during the O3 suggest the need for an adjustment in the mass distribution for NSs and low-mass BHs . This leads to the integration of the PDB/GWTC-3 model [122]. This adjustment, based on comprehensive GW detection analyzes, indicates a reinforced power law below $2.4\,M_\odot$ with a confidence interval of 99.3%. Notable observations include: i) the GW190814 event, which presented the heaviest NS to date at $2.59^{+0.08}_{-0.09}\,M_\odot$ [15]. ii) the GW190917_114630 event, indicating a component below $3\,M_\odot$, suggesting a potential reclassification from a BH to an NS. iii) Recent astrophysical observations, particularly GW170817, align the nonrotating NS mass limit with the Tolman-Oppenheimer-Volkoff (TOV) limit, estimated at $2.2 - 2.5\,M_\odot$ [177, 247, 257, 188]. iv) Analysis of the mass distribution of BH from binary X-ray systems suggests a minimum BH mass around $5\,M_\odot$ [216, 124]. v) The evident divergence from a singular power law in the mass distributions of BBH and BNS [129, 21] further supports the PDB/GWTC-3 model for a refined understanding of the mass transition between NS and BH .

The PDB/GWTC-3 distribution, is derived from the population model described in [122] and [25] which I used to support the latest "observing scenarios". This distribution is divided into three subpopulations: BNS, NSBH, and BBH, defined by the mass of the primary component m_1 and the secondary component m_2, where $m_2 \leq m_1$. The maximum mass for a nonrotating NS, according to the TOV limit, is approximately $2 - 2.5\,M_\odot$, but rotating NSs can exceed this limit [57, 270]. A population analysis of all CBCs detected by the IGWN finds a sharp feature in the mass distribution at

$2.4^{+0.5}_{-0.5}\,M_\odot$ (90% credible interval). This characteristic is interpreted as a delineation between NS and BH due to its proximity to the TOV limit [122, 25]. In Figure 2.2, this boundary between NS and BH is depicted using a colored band. To provide a conservative upper limit on the number of events containing NS for follow-up programs, I adopt the upper bound 95% on the location characteristic of [122], delineating between NS and BH in $3\,M_\odot$. Although this may lead to some low-mass BBHs being classified as BNS or NSBH, it is preferable to the risk of misclassifying a potentially bright EM counterpart event as a BBH. This boundary choice at $3\,M_\odot$ also maintains consistency with previous analyses [17]. I follow [122], who proposed a resolution to this NSBH discrepancy using all publicly available CBCs in the GWTC-2.1 catalog in a single population analysis, thus avoiding the need for a priori classifications and instead allowing the population to select distinct subpopulations of CBCs. In the following, I use a similar procedure. I presented all publicly available CBCs in the GWTC-3 with a false alarm rate (FAR) of 0.25 year^{-1} [25] in Figure 2.1.

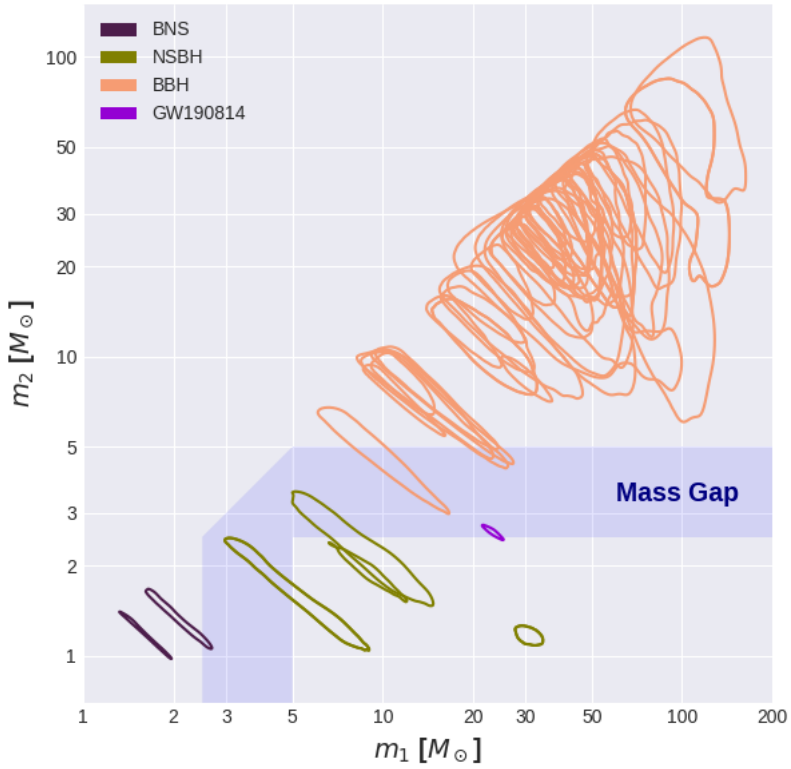

Figure 2.1: 90% posterior credible intervals for the component masses for all CBCs in the GWTC-3 catalog [25] study assuming uniform priors in detector frame masses and fixed FAR about 0.25 year^{-1} [25]. Events classified by the LIGO/Virgo/KAGRA collaboration as BNSs , NSBHs , and BBHs are shown in dark-violet, olive (green) and orange, respectively. The ambiguously classified event GW190814 is shown in dark purple. The gray band indicates the approximate location of the purported *lower-mass gap*. GW190814 is the only event within this region at more than 90% credibility. Used to support Kiendrebeogo et al. 2023 [163].

PDB/GWTC-3 represents a continuous function describing the full population,

eliminating the need to specify different models for each subpopulation [129]. The mass and spin distributions follow the PDB model from [122] and [25]. This model includes a broken power law with a notch filter $n(m|M_{\rm low}^{\rm gap}, M_{\rm high}^{\rm gap}, A)$ suppressing the merger rate between NSs and BHs by a factor of A. It also features a low-pass filter at the high-mass end of BHs, reflecting a potential tapering of the mass distribution. The component mass distribution is thus given by:

$$\begin{aligned} p(m|\lambda) \propto & n(m|M_{\rm low}^{\rm gap}, M_{\rm high}^{\rm gap}, \eta_{\rm low}, \eta_{\rm high}, A) \times h(m|M_{\rm min}, \eta_{\rm min}) \\ & \times l(m|M_{\rm max}, \eta_{\rm max}) \\ & \times \begin{cases} \left(m/M_{\rm high}^{\rm gap}\right)^{\alpha_1} & \text{if } m < M_{\rm high}^{\rm gap} \\ \\ \left(m/M_{\rm high}^{\rm gap}\right)^{\alpha_2} & \text{if } m \geq M_{\rm high}^{\rm gap} \end{cases} . \end{aligned} \tag{2.1}$$

with $1 \leq m/M_\odot \leq 100$;
here, $n(m|M_{\rm low}^{\rm gap}, M_{\rm high}^{\rm gap}, \eta_{\rm low}, \eta_{\rm high}, A) = \left(1 - A h(m|M_{\rm low}^{\rm gap}, \eta_{\rm low}) l(m|M_{\rm high}^{\rm gap}, \eta_{\rm high})\right)$;

$$\text{where, } \begin{cases} h(m|M_{\rm min}, \eta_{\rm min}) = 1 - l(m|M_{\rm min}, \eta_{\rm min}) \\ \\ l(m|M_{\rm max}, \eta_{\rm max}) = \left(1 + (m/M_{\rm max})^{\eta_{\rm max}}\right)^{-1} . \end{cases}$$

$h(m|m_{\rm min}, \eta_{\rm min})$ and $l(m|m_{\rm max}, \eta_{\rm max})$ are the low-mass and high-mass tapering functions, respectively. The 1D mass distribution, $p(m|\lambda)$, is shown in Figure 2.2 for a specific choice of λ (λ represents the 12 parameters of the model; see Table 2.1

The 2D mass distribution is constructed assuming that both the primary and secondary masses are drawn from $p(m|\lambda)$ and related via a "pairing function" [130, 115]. As defined in [130], the pairing assumed here is a power law in the mass ratio, $q \equiv m_1/m_2$. Explicitly,

$$p(m_1, m_2|\Lambda) \propto p(m = m_2|\lambda) p(m = m_1|\lambda) \left(\frac{m_2}{m_1}\right)^{\beta} . \tag{2.2}$$

The values of the hyperparameters $\Lambda = \{\lambda, \beta\}$ are listed in the Table 2.1 and were chosen by fitting this model to all CBCs in GWTC-3 and choosing the maximum a posteriori value for Λ. The effects of neglecting the hyperparameter uncertainty are estimated in Table 2.1.

The PDB model assumes a spin distribution with isotropically oriented component spins and uniform component spin magnitudes. The spin magnitude distribution for objects with masses less than ($m < 2.5\, M_\odot$) is defined in the range of $[0, 0.4]$, and that for objects with masses larger than $2.5\, M_\odot$ is defined in the range $[0, 1]$.

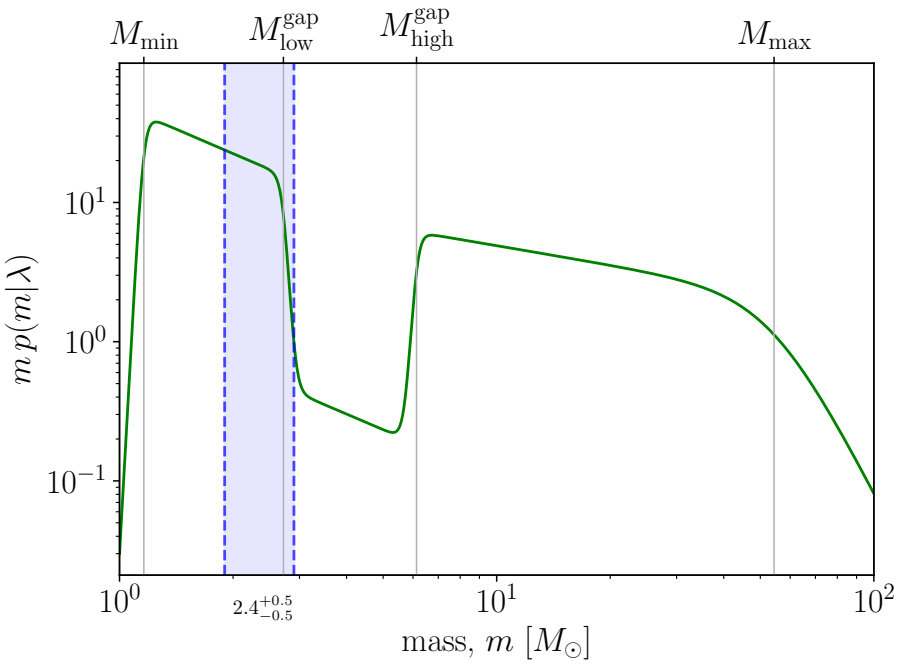

Figure 2.2: The 1D PDB mass distribution, $p(m|\lambda)$ on the interval $[1, 100]\,M_\odot$ for a specific choice of hyperparameters λ. See Table 2.1 in subsection 2.3.2, for the other parameters of the mass distribution. The color band show a delineation between NS and BH at 90% credible interval. Modified from Kiendrebeogo et al. 2023 [163].

2.3.2 Values of Hyperparameters

We fix the parameters in both of our assumed models for the astrophysical distribution of compact binary mergers. These population model parameters, termed "hyperparameters" in hierarchical Bayesian analysis, are listed in Table 2.1 for the PDB/GWTC-3 model. They were selected because they correspond to the maximum hyperposterior value obtained by fitting the PDB model to the GWTC-3 data [25]. Consequently, we do not consider the full posterior uncertainty in these hyperparameters. To estimate the effect of neglecting this uncertainty on the number of detected events in each subpopulation, I compare the predicted uncertainty of the astrophysical merger rate from the full PDB analysis [25] to those assumed in this work. The percentage of uncertainty ($\frac{90\%\text{CI}}{\text{mean}}$) in Table 2.2 for the PDB/GWTC-3 model is 171% for BNS, NSBH, and BBH each. In contrast, the percent error reported by [25] is 229%, 178%, and 68% for BNS, NSBH, and BBH events, respectively. Thus, I conclude that I underestimate the uncertainty in the merger rate for BNS and NSBH by factors of 1.34 and 1.04, respectively, and overestimate the error for the BBH merger rate by a factor of 2.5. This discrepancy likely arises because the BBH mass spectrum is better constrained compared to the NS containing events, resulting in relatively minor additional uncertainty introduced by fitting the hyperparameters. In contrast, for NSBH and BNS, only approximately four events are used to constrain the shape of the low-mass end of the distribution (see the Figure .2.1.

Naively translating the additional uncertainty in the astrophysical merger rate to an uncertainty in the annual number of detected events in run O4b yields an increase in the uncertainty of 12.2 events for BNS, an increase of 0.24 events for NSBH, and a decrease of 104 events for BBH, assuming symmetric errors. These adjustments are approximate and are intended to provide an estimate of the effect of neglecting the uncertainty in population hyperparameters under the PDB/GWTC-3 model. A similar estimate is not available for the LRR model, as I am unaware of any population fit performed using that framework in the GWTC-3 data. The distinction between the maximum a posteriori (MAP) underlying population and the entire hyperposterior underlying population is illustrated in Figure 5 of [122].

Table 2.1: Summary of Population Model parameters. The first several entries describe the rate and mass distribution parameters, and the last two entries describe the spin distribution parameters. Used to support Kiendrebeogo et al. 2023 [163].

Parameter	Description	Value
α_1	Spectral index for the power law of the mass distribution at low mass.	-2.16
α_2	Spectral index for the power law of the mass distribution at high mass.	-1.46
A	Lower-mass gap depth.	0.97
$M_{\rm low}^{\rm gap}$	Location of lower end of the mass gap.	$2.72 M_\odot$
$M_{\rm high}^{\rm gap}$	Location of upper end of the mass gap.	$6.13 M_\odot$
$\eta_{\rm low}$	Parameter controlling how the rate tapers at the low end of the mass gap.	50
$\eta_{\rm high}$	Parameter controlling how the rate tapers at the high end of the mass gap.	50
$\eta_{\rm min}$	Parameter controlling tapering of the power law at low mass.	50
$\eta_{\rm max}$	Parameter controlling tapering of the power law at high mass.	4.91
β	Spectral index for the power-law-in-mass ratio pairing function.	1.89
$M_{\rm min}$	Minimum mass of the mass distribution.	$1.16 M_\odot$
$M_{\rm max}$	Onset location of high-mass tapering.	$54.38 M_\odot$
$a_{\rm max,NS}$	Maximum allowed component spin for objects with mass $< 2.5 M_\odot$.	0.4
$a_{\rm max,BH}$	Maximum allowed component spin for objects with mass $\geq 2.5 M_\odot$.	1

2.3.3 PDB/GWTC-3 Masses and Spin Distribution

A dataset comprising 10^6 CBCs was generated from the PDB model, designated as the PDB/GWTC-3 distribution. These samples were then segregated into three distinct subpopulations based on their mass characteristics: NSs were identified as objects with masses below $3 M_\odot$, and BHs as objects with masses above this threshold. This segregation yielded 892,762 BNS systems, 35,962 NSBH systems, and 71,276 BBH systems. Figure 2.3 illustrates the Gaussian kernel density estimator (KDE) across the PDB/GWTC-3 dataset.

A significant difference between the LRR and PDB/GWTC-3 distributions lies in the mass range covered by each model. The LRR distribution is limited to objects

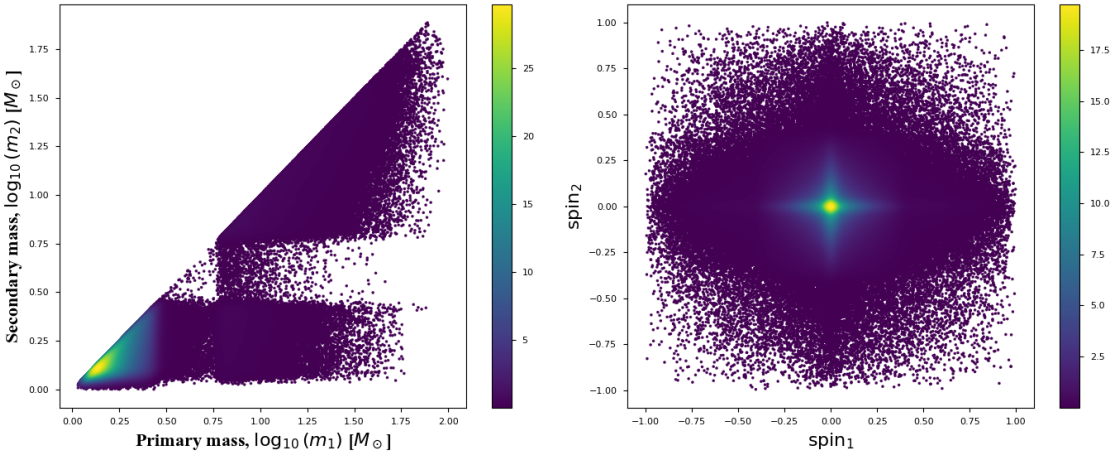

Figure 2.3: Gaussian KDE of the PDB/GWTC-3: The left panel displays the 2D mass distributions for the components of each CBCs category, with all axes on a logarithmic scale. The right panel shows the spin distributions for the same CBCs categories, providing insights into the spin characteristics of the population. The color density in both panels represents the number of CBCs events per pixel, illustrating the density and variation within the distributions. Used to support Kiendrebeogo et al. 2023 [163].

with masses not exceeding $50\,M_\odot$, in contrast to the PDB/GWTC-3 distribution, which accommodates objects up to $100\,M_\odot$, thus including higher-mass BHs. However, the tapering effect of the PDB mass distribution beyond $M_{\max} = 54.38\,M_\odot$ serves to moderate the occurrence of exceedingly high-mass BHs within the latter distribution.

As presented in [163], Figure 2.4 illustrates the structured pipeline used for “observing scenarios", comprehensively summarizing the methodology. The subsequent sections provide a detailed discussion on each phase of the process.

2.4 Prediction and scenarios

2.4.1 Simulation campaign

I used the public software suite `ligo.skymap`[3], which facilitates reading, writing, generation and visualization of GW sky maps from the IGWN. This integration with EM observations aims to deepen our understanding of the universe. Drawing intrinsic parameters, masses, and spins of CBCs from the PDB/GWTC-3 distribution, I distributed this sample uniformly in comoving volume and isotropically in both sky location and orbital orientation, adhering to the expectation that GW sources are not spatially clustered or preferentially oriented toward or away from Earth. To achieve this, I calculated the range R as the maximum sensitivity distance or the radius of an equivalent Euclidean

[3] https://git.ligo.org/leo-singer/ligo.skymap

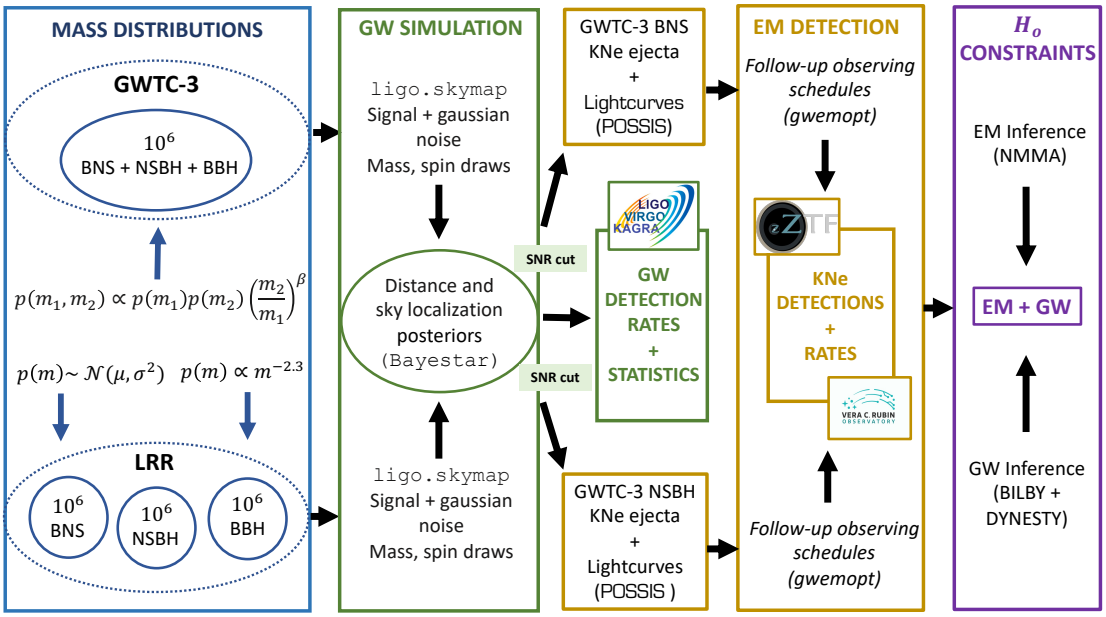

Figure 2.4: Flowchart of observing scenarios process. Here, $\mu = 1.33M_{\odot}$, and $\sigma = 0.09M_{\odot}$, then in LRR case, m represents the primary mass m_1 or secondary mass m_2 , since they are drawn in the same way with $m_2 \leq m_1$. Used to support Kiendrebeogo et al. 2023 [163].

sphere. This "soft" range enabled us to uniformly assign each sample within a sensitive spatiotemporal volume, $\frac{4}{3}\pi R^3 = V_z$, where V_z represents the comoving volume, adjusted by a factor of $(1+z)$ due to the expansion of the Universe. Within this volume, I uniformly and isotropically distributed a set of distances and sky locations for my CBCs samples, adopting the cosmological parameters as outlined in [30]. To simulate the GW signals from these CBCs, Gaussian noise was incorporated.

The source code for these simulations is publicly accessible, from the drawing of intrinsic parameters[4] to the statistical production of sky maps[5], including the filtering of CBCs events that exceed the S/N threshold[6], and their sky-localization[7] on GitHub[8] [261]. The network S/N threshold is determined by the square root of the sum of the squares of the individual detectors' S/N.

Following the methodology outlined in [223], I applied an S/N threshold of 8. This simulation yields estimates of the sky-localization areas of the GW for all subpopulations, the luminosity distance, and the comoving volume, providing a 90% credible prediction of the comoving region and the volume containing the total posterior probability. The localization of the sky area, according to [17] and [223], is facilitated by BAYESian TriAngulation and Rapid localization (BAYESTAR)[9], a rapid localization

[4] https://lscsoft.docs.ligo.org/ligo.skymap/tool/bayestar_inject.html
[5] https://lscsoft.docs.ligo.org/ligo.skymap/tool/ligo_skymap_stats.html
[6] https://lscsoft.docs.ligo.org/ligo.skymap/tool/bayestar_localize_coincs.html
[7] https://lscsoft.docs.ligo.org/ligo.skymap/tool/bayestar_localize_coincs.html
[8] https://github.com/lpsinger/observing-scenarios-simulations/tree/v2
[9] http://dcc.ligo.org/P1500071/public/html

algorithm used in IGWN alerts [263]. BAYESTAR computes the source location based on the output from the detection pipeline, producing sky-localizations with latencies of only a few seconds. In addition, it offers distance estimates as an integral part of the sky-localization. Specifically, for each line of sight, the posterior probability distribution of the distance is approximated as a Gaussian function multiplied by the square of the distance, providing three-dimensional (3D) sky maps that include position and distance information, as I show in Figure 2.5.

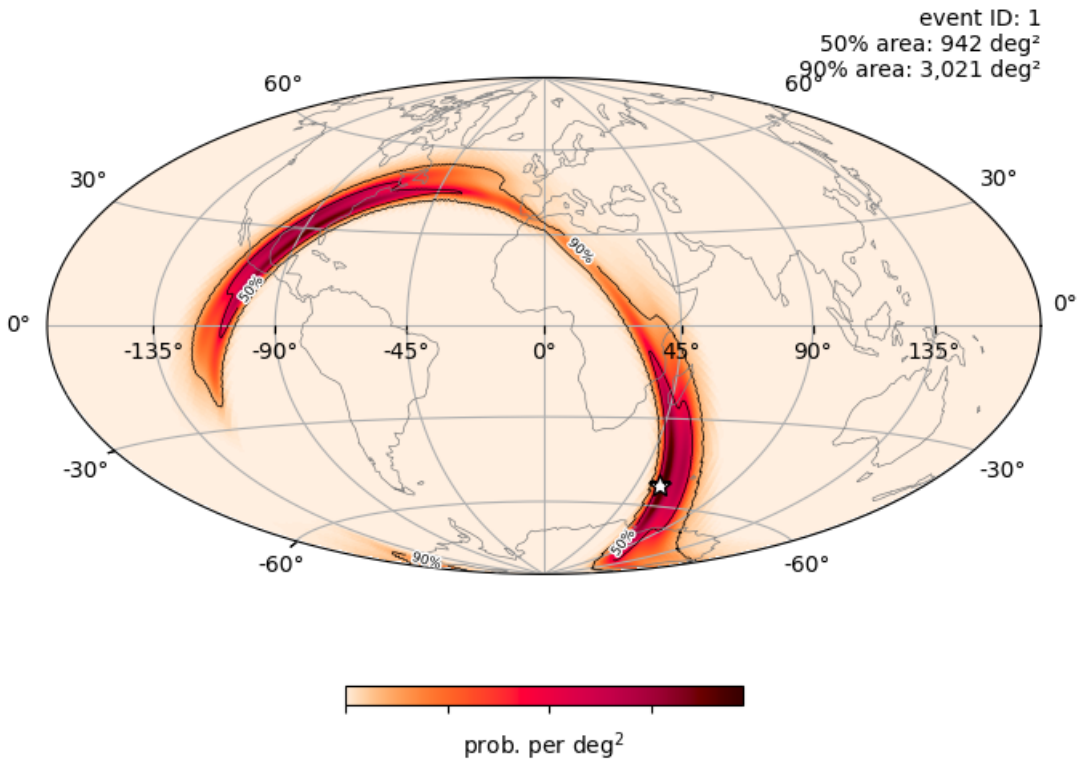

Figure 2.5: GW localization skymap for a BNS merger from my simulation, localization performed with BAYESTAR. The skymap illustrates the probability per square degree of the source location, with contour levels marking the credible regions 50% and 90%. The area 50% covers 942 square deg^2, while the area 90% encompasses 3,021 square deg^2, providing an estimated region for follow-up observations. The white star indicates the actual location of my BNS.

According to IGWN, four detectors, namely LHO, LLO, Virgo, and KAGRA [9], will operate during O4 and O5. In my simulations, I adopt this configuration, assuming that each detector operates with a 70% duty cycle independently. However, an update indicates that KAGRA and Virgo will begin the run with LHO and LHO later in O4 (e.g., O4b). The noise PSD, or sensitivity curves[10], are applied for each observing run and detector. The publicly available noise curves in LIGO-T2200043-v3[11] are used.

For O4, I utilized `aligo_O4high.txt`, `avirgo_O4high_NEW.txt`, and

[10] https://observing.docs.ligo.org/plan/index.html
[11] https://dcc.ligo.org/T2200043-v3/public

`kagra_10Mpc.txt` for LIGO (LHO, LHO), Virgo, and KAGRA, respectively, while for O5, `AplusDesign.txt`, `avirgo_O5low_NEW.txt`, and `kagra_128Mpc.txt` were used. The first phase of O4 (O4a) involved only LIGO's detectors. To measure the performance of the interferometers, I calculated the BNS inspiral range for a 1.4 $M_{\odot}$ binary system detected with S/N = 8, during the observation runs O4a, O4b and O5. The distances (in megaparsecs) from the BNS inspiral are detailed in Table 2.3.

The simulations assume an astrophysical merger rate within a frame comoving with the Hubble flow, averaged over a non-olving mass and spin distribution. Using the merger rate per unit comoving volume per unit proper time provided by the PDB (pair) model in the first row of Table II in [25], I standardized my merger rates to the closest match to the PDB/GWTC-3 distribution. The initial distribution was normalized with the total rate density of mergers, integrated across all masses and spins, fixed at $240^{+270}_{-140}\,\mathrm{Gpc}^{-3}\mathrm{yr}^{-1}$. These astrophysical density rates are reproduced in Table 2.2. During the O4a observing run, I took the opportunity to evaluate the real sensitivity of the LIGO detectors, **H1** and **L1**. This evaluation yielded the *Measured PSD* for each detector, which was used throughout the O4a to determine the real value of the BNS Inspiral range. For subsequent observing runs, O4b and O5, I refer to the *Ideal PSD* values mentioned above.

Table 2.2: The merger rate per unit comoving volume used for PDB/GWTC-3 (`GWTC-3`) distributions. Used to support Kiendrebeogo et al. 2023 [163].

Distribution	**BNS**	**NSBH**	**BBH**
Merger rate density (Gpc^{-3} yr^{-1})			
PDB/GWTC-3	210^{+240}_{-120}	$8.6^{+9.7}_{-5}$	$17.1^{+19.2}_{-10}$

Table 2.3: The cosmology-Corrected Inspiral Sensitive Distance (in Mpc) for Runs O4a and `O4b` from a GW Strain PSD : O4a using *Measured PSD* , O4b and O5, using *Ideal PSD*.

Run	**L1**	**H1**	**V1**	**K1**
BNS average range in Mpc				
O4a	165	145	off duty	off duty
O4b	224	224	95	37
O5	494	494	183	390

2.4.2 Statistical results of observing scenarios

The outcomes of my "observing scenarios," including sky-localization FITS files, are publicly accessible through the repository [164]. These simulations were instrumental in estimating the detection rates of the IGWN for the O4a, O4b, and O5 observing

runs. In Figure 2.6, I provide a comprehensive summary of the detection results derived from my set of simulations. In Table 2.5.1, I present the predicted annual detection rates for CBCs during O4a, O4b, and O5. The confidence interval combines both the *log-normal* distribution of the merger rate and uncertainties from the Poisson counting statistics. The low number of NSBH predicted by the PDB model is due to the existence of a nearly empty mass gap in that model, combined with a pairing function [130] that favors equal-mass binaries.

NSBHs must *straddle* the mass gap, with one component on each side. This leads to asymmetric mass ratios, which are in turn disfavored by the model fit, as most binaries in the population are consistent with being equal mass. A version of the PDB model with a partially filled mass gap would predict more NSBH events relative to the other types of CBCs. The notation `HL` refers to operational status where only LHO and LLO are active, applicable to the O4a observing run. Conversely, `HLVK` indicates a scenario where all four detectors, including Virgo (V) and KAGRA (K), are operational, representing an optimal configuration for detection capabilities.

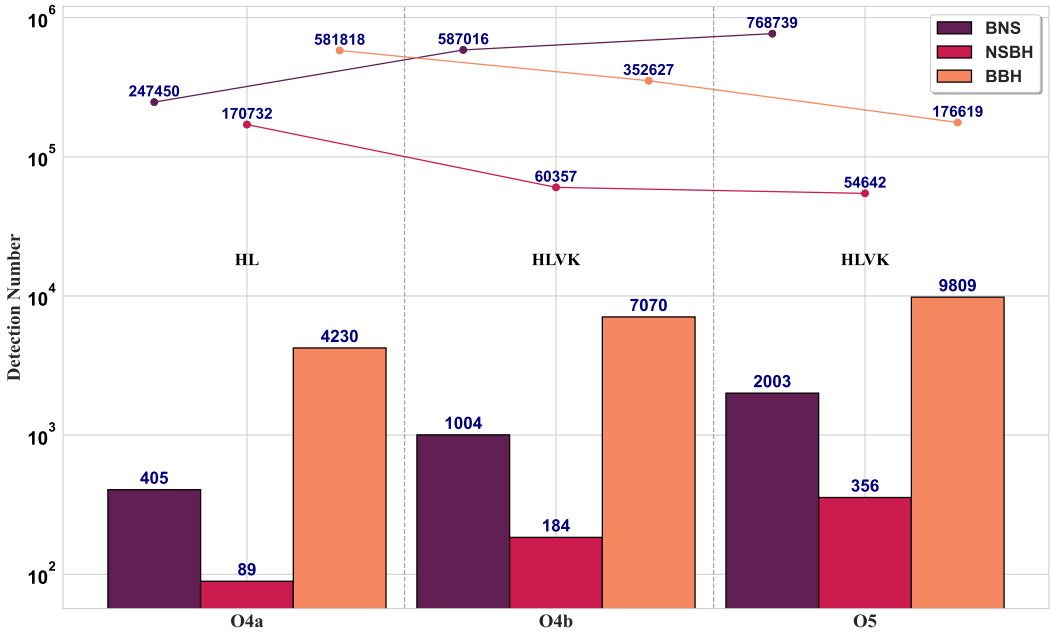

Figure 2.6: Evolution of simulated GW detection numbers across observation runs O4a, O4b, and O5. The bar chart delineates the detected events that exceed the S/N threshold for BNS, NSBH, and BBH populations. Colored dots represent the respective total number of simulated injections, indicating the underlying statistical sampling size. Lines connecting the dots illustrate the trend in the volume of simulations performed across different observation runs. These detections are key for inferring the astrophysical rates and understanding the population properties of CBCs. Adapted from Kiendrebeogo et al. 2023 [163].

In Table 2.5, I also provide statistics on the sky-localization area of the GW signal, the luminosity distance, and the moving volume. The sky-localization area (volume) is given as the 90% credible region, defined as the smallest area (volume) that

Table 2.4: Annual Detection Rates for CBCs that I expect for the Runs O4a, O4b and O5, using PDB/GWTC-3 distribution. These uncertainties do not incorporate the Monte Carlo method, but only combine both the *log-normal* distribution of the merger rate and the *Poisson counting statistics*. Adapted from Kiendrebeogo et al. 2023 [163] and User Guide[2].

RUN	Network	BNS	NSBH	BBH
		Annual Number of Detections		
O4a	HL	11^{+17}_{-8}	2^{+4}_{-2}	123^{+157}_{-71}
O4b	HLVK	36^{+49}_{-22}	6^{+11}_{-5}	260^{+330}_{-150}
O5	HLVK	180^{+220}_{-100}	31^{+42}_{-20}	870^{+1100}_{-480}

encompasses 90% of the total posterior probability. This corresponds to the area (volume) of the sky that must be covered to have a 90% chance of including the source. I have adopted the same statistical treatment process as the one used in [223]. The results of the simulation of the GWTC-3 distribution are also available in the IGWN Public Alerts User Guide[2].

There are notable differences that arise from the improved mass distributions measured in PDB/GWTC-3, derived from the maximum a posteriori fit to all compact binaries detected so far. This represents a significant departure from the normal and power law distributions for masses previously assumed by LRR. Coupled with the inclusion of single-detector triggers, these differences markedly diverge from previous reports. I focus exclusively on the ideal scenario where all four detectors are operational, specifically during the O4b and O5 runs. The PDB/GWTC-3 distribution accounts for an increase in the predicted number of detected events by approximately a factor of $(0.83\%/0.22\%) = 3.772$ for O4b and $(1.22\%/0.48\%) = 2.542$ for O5. When broken down by population type, the estimated annual detection rate is approximately 2 (BNS) and 5 (BBH) times higher for PDB/GWTC-3, but drops to ~ 0.6 for NSBH. The median luminosity distance predicted by PDB/GWTC-3 is about 1.14 (O4b) and 1.19 (O5) times greater for BNS, 1.36 (O4b) and 1.31 (O5) times for NSBH, and 2.44 (O4b) and 2.36 (O5) times for BBH events, respectively, compared to LRR. Similarly, the median sensitive volume increases by approximately 1.7 (O4b), 1.6 (O5) for BNS, 1.9 (O4b), 2.0 (O5) for NSBH, and 8.14 (O4b), 6.65 (O5) for BBH. For sky-localizations, the results are broadly consistent with previous findings. For instance, during O4b, PDB/GWTC-3 predicts an area approximately 11% smaller for the BNS subpopulation than that from LRR, while for BBH, PDB/GWTC-3 predicts an area approximately 52% larger. The full results of the LRR distribution can be found in [163].

In Figure 2.7, following [223] I illustrate the cumulative annual detection rate distribution as a function of the 90% credible area, 90% credible comoving volume, and luminosity distance anticipated for the actual and the upcoming observing runs. The shaded bands denote the 5%–95% variation attributable to uncertainties in the density of the astrophysical merger rate. To elucidate the pursuit of EM counterparts to GW events, I compared the observational capabilities of prominent optical telescopes such

Table 2.5: Summary Statistics for O4a, O4b and O5. These recorded values are given as 90% credible interval calculated with the 5% and 95% quantile. Those uncertainties have been described by Monte Carlo sampling. Used to support the IGWN User Guide [2].

Run	Network	BNS	NSBH	BBH
		Median 90% Credible Area (deg^2)		
O4a	HL	1870^{+150}_{-110}	2210^{+550}_{-350}	2561^{+70}_{-78}
O4b	HL	1860^{+250}_{-170}	2140^{+480}_{-530}	1428^{+60}_{-55}
O5	HLVK	2050^{+120}_{-120}	2000^{+350}_{-220}	1256^{+48}_{-53}
		Median 90% Credible Comoving Volume (10^6 Mpc^3)		
O4a	HL	$25.2^{+4.3}_{-5.6}$	116^{+27}_{-40}	3740^{+250}_{-220}
O4b	HLVK	$67.9^{+11.3}_{-9.9}$	232^{+101}_{-50}	3400^{+310}_{-240}
O5	HLVK	376^{+36}_{-40}	1350^{+290}_{-300}	8580^{+600}_{-550}
		Median Luminosity Distance (Mpc)		
O4a	HL	274^{+15}_{-11}	501^{+27}_{-46}	2067^{+62}_{-43}
O4b	HLVK	398^{+15}_{-14}	770^{+67}_{-70}	2685^{+53}_{-40}
O5	HLVK	738^{+30}_{-25}	1318^{+71}_{-100}	4607^{+77}_{-82}
		Sensitive Volume : Detection Rate/ Merger Rate: (Gpc^3)		
O4a	HL	$0.0553^{+0.0067}_{-0.0061}$	$0.305^{+0.081}_{-0.068}$	$7.22^{+0.26}_{-0.25}$
O4b	HLVK	$0.172^{+0.013}_{-0.012}$	$0.78^{+0.14}_{-0.13}$	$15.15^{+0.42}_{-0.41}$
O5	HLVK	$0.827^{+0.044}_{-0.042}$	$3.65^{+0.47}_{-0.43}$	$50.7^{+1.2}_{-1.2}$

as the ZTF [62], and the forthcoming Rubin Observatory's (LSST; [156]), alongside a near-ultraviolet telescope, ULTRSAT [259]. This comparison underscores their sky survey capabilities relative to the coverage provided by the GW detectors.

2.5 Analysis of the O4a run

The operational dynamics of GW detectors significantly influence the live time and detection capabilities. Given that each of the four detectors operates with an independent duty cycle 70%, I calculated a 5.67% probability that only one detector will be online at any given time, assuming $4 \times 70\% \times (30\%)^3$. For two detectors observing, as was the case during the O4a run, the probability increases to $2 \times 70\% \times (30\%) = 42\%$

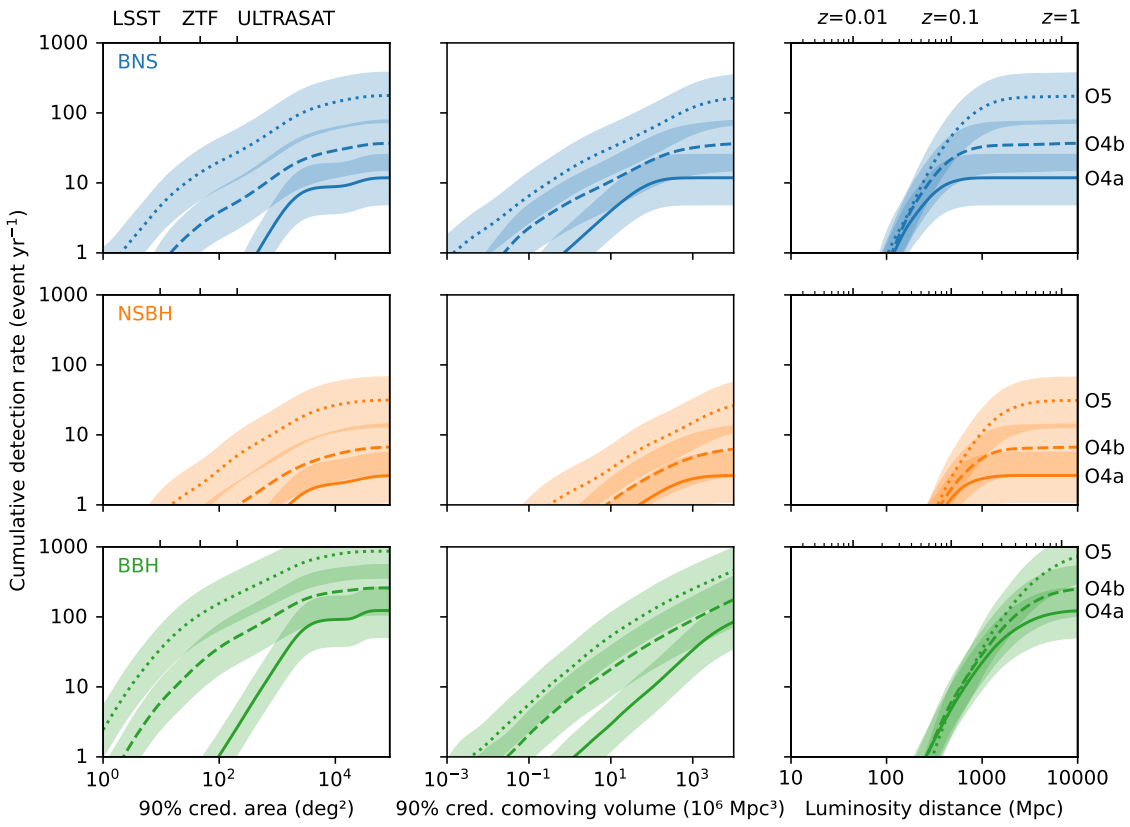

Figure 2.7: Cumulative histograms showing the 90% credible area, 90% credible comoving volume, and luminosity distance for detectable events during the O4a, O4b, and O5 observing runs. The analysis includes uncertainties in the estimated merger rate, Monte Carlo uncertainty due to the finite sample size of the simulation, and Poisson fluctuations in the detected number of sources per year. The rates are presented for three subpopulations: BNS (top row), NSBH (middle row), and BBH (bottom row). The shaded bands represent the inner 90% confidence interval, accounting for the uncertainties mentioned above. For comparison with telescope sky surveys, the FOVs for LSST, ZTF, and ULTRSAT are shown in the left panels. Adapted and used to support the User Guide[2].

of the time with only one detector online. The first half of the fourth observing run, O4a, spanned from May 24, 2023, to January 16, 2024, with only LIGO's detectors operational. The LHO (H1) and LHO (L1) were independently active 67.5% and 69% of the time, respectively, resulting in both detectors being active 53.4% of the time. There were periods 29.7% of the time when only a single detector was operational and 16.6% when neither detector was operational. These calculations, provided by GW Open Science Center[12] (GWOSC), indicate an average operational duty of 68.25% for each detector. In the O4a run, the actual probability that only one detector is on duty at any given time is derived from the operational dynamics of the detectors rather than the previously stated $2 \times 68.25\% \times (31.75\%) = 42.66\%$. This concurrence underscores my

[12] https://gwosc.org

estimation of the operational dynamics and the effectiveness of the detector network during the observing cycle. This outcome reflects our expectations about the operational status of 70%. During the O4a observational period, a total of 92 GW events were publicly announced, providing a rich dataset for analysis. This dataset included 1 potential BNS merger, 6 potential NSBH mergers, 81 likely BBH mergers, and 11 events confirmed to be terrestrial in origin. This diversity and volume of detections serve as a critical benchmark for evaluating the effectiveness of the detector network and the accuracy of our operational dynamics estimations.

2.5.1 Adjusting to S/N=10: Aligning predictions with O4a observations

The initial nine-month period of the O4a observing run yielded an invaluable dataset against which to benchmark our simulation predictions, originally computed over a period of one year. Upon analyzing this observational dataset, a tangible discrepancy emerges between our theoretical models, which posit an S/N threshold of 8, and the empirically gathered data. This deviation is particularly salient within the BNS and BBH subpopulations, which warrants a critical assessment of our detection threshold parameters. In particular, absent from this comparative study are the NSBH events, which the PDB/GWTC-3 model appears to disadvantage. This omission could be a contributing factor to the observed disparities. By recalibrating the S/N threshold to 10, coupled with the measured sensitivity curves (*measured PSD*) pertinent to the O4a run, I observe a realignment of the predicted and observed detection rates. Table 2.6 delineates these predictive discrepancies and their convergence after adjustment.

Table 2.6: Comparison of Predicted and Observed Detection Rates at Different S/N Thresholds During the O4a.

RUN	Detection Type	Time	S/N	BNS	NSBH	BBH
			Number of Detections			
O4a	Simulation	**1 year**	**8**	12^{+17}_{-9}	1^{+4}_{-2}	115^{+147}_{-67}
			10	5^{+10}_{-5}	0^{+0}_{-0}	60^{+78}_{-36}
	Observation	**9 months**	**N/A**	1 ?	6	81

The motivation to increase the S/N threshold to 10 is supported by the recent work of [86], which focuses on the performance of low-latency GW alert systems in anticipation of the O4. Detailed analysis of infrastructure and software improvements was conducted through Mock Data Challenge (MDC) simulations, encompassing 5×10^4 injections from February 16 to March 28, 2023. This analysis, which recovered 1489 BNS, 1105 NSBH, and 1920 BBH injections, offers insights into real-time search capabilities, event detection efficiency, and rapid estimation of binary system properties. Following this methodology, my analysis aimed to assess the detection capabilities of various GW detection pipelines, including GstLAL [192, 278, 123], MBTA (Multi-

Band Template Analysis; [55]), PyCBC [81, 213], and SPIIR [149, 185], which are GW search pipelines. The analysis compares the combined S/N with the FAR for each pipeline. Figures 2.8 and 2.9 support the rationale for adopting an S/N threshold of 10, illustrating a logarithmic density and a median FAR compared to the combined network S/N. The data reveal a concentration of events slightly below an S/N of 10, corresponding to a FAR of approximately 10^{-4}. This distribution suggests that an S/N of 10 is a more effective threshold for confirming CBCs events. Furthermore, a FAR threshold of 1/month associated with a significant public alert threshold before trial factors aligns with an S/N between 10 and 12, depending on the CBCs pipeline. These visual and statistical analyses advocate for the adoption of an S/N threshold of 10 for CBCs detection confirmation in future "observing runs," enhancing both the alignment of my simulations with observed data and the overall reliability of my predictive frameworks in GW astrophysics. GW detections are subject to stringent verification processes before being released as public alerts. The current criterion for such dissemination is related to the event's FAR. Specifically, an event is made publicly known if its FAR is less than or equal to 2 per day (see the user guide[13], [17]). This stringent standard ensures that only the most credible events are communicated to the public.

2.5.2 GW230529: A milestone in gravitational-wave astronomy

The fourth observing run (O4a) of the aLIGO and partner observatories documented a significant event, GW230529, only detected by the LIGO LLO on May 29, 2023. During this time, the LIGO LHO was offline and neither Virgo nor KAGRA participated in the O4a run [89]. This event featured the coalescence of a compact binary system with component masses estimated at $3.6^{+0.8}_{-1.2} M_\odot$ and $1.4^{+0.6}_{-0.2} M_\odot$, which falls within the mass gap of $2.5 - 5 M_\odot$ traditionally observed between NSs and BHs .

This detection has critical implications in GW astronomy, confirming the presence of compact objects within the mass gap, thus challenging established mass classifications for NSs and BHs . Previously, the boundary between NS and BH was considered at $2.5 M_\odot$ based on integrations of GWTC-2.1 data [122]. However, my observations and subsequent adjustments suggest raising this limit to $3 M_\odot$, in order to minimize misclassifications of low-mass BHs as NSs, crucial for accurate identification of events with potential EM counterparts. GW230529 with a mass of BH in the $2.5 - 4.5 M_\odot$ range significantly improves the capabilities of the PDB/GWTC-3 distribution models to resolve discrepancies in the classification of the mass of NS-BH . It demonstrates the existence of merger events in previously ambiguous mass ranges and supports the calibration of mass classification thresholds to more accurately reflect the astrophysical properties of compact objects [25, 122]. The implications of this discovery extend beyond the correction of mass spectrum classifications. They enhance our understanding of the compact object mass spectrum and pave new paths for multi-messenger astronomy, essential for our ongoing investigations into the EM counterparts of GW events. This event aligns with adjustments in the PDB/GWTC-3 model which incorporates a refined understanding of the mass transitions between NSs and BHs , critical for pre-

[13] https://emfollow.docs.ligo.org/userguide/analysis/index.html

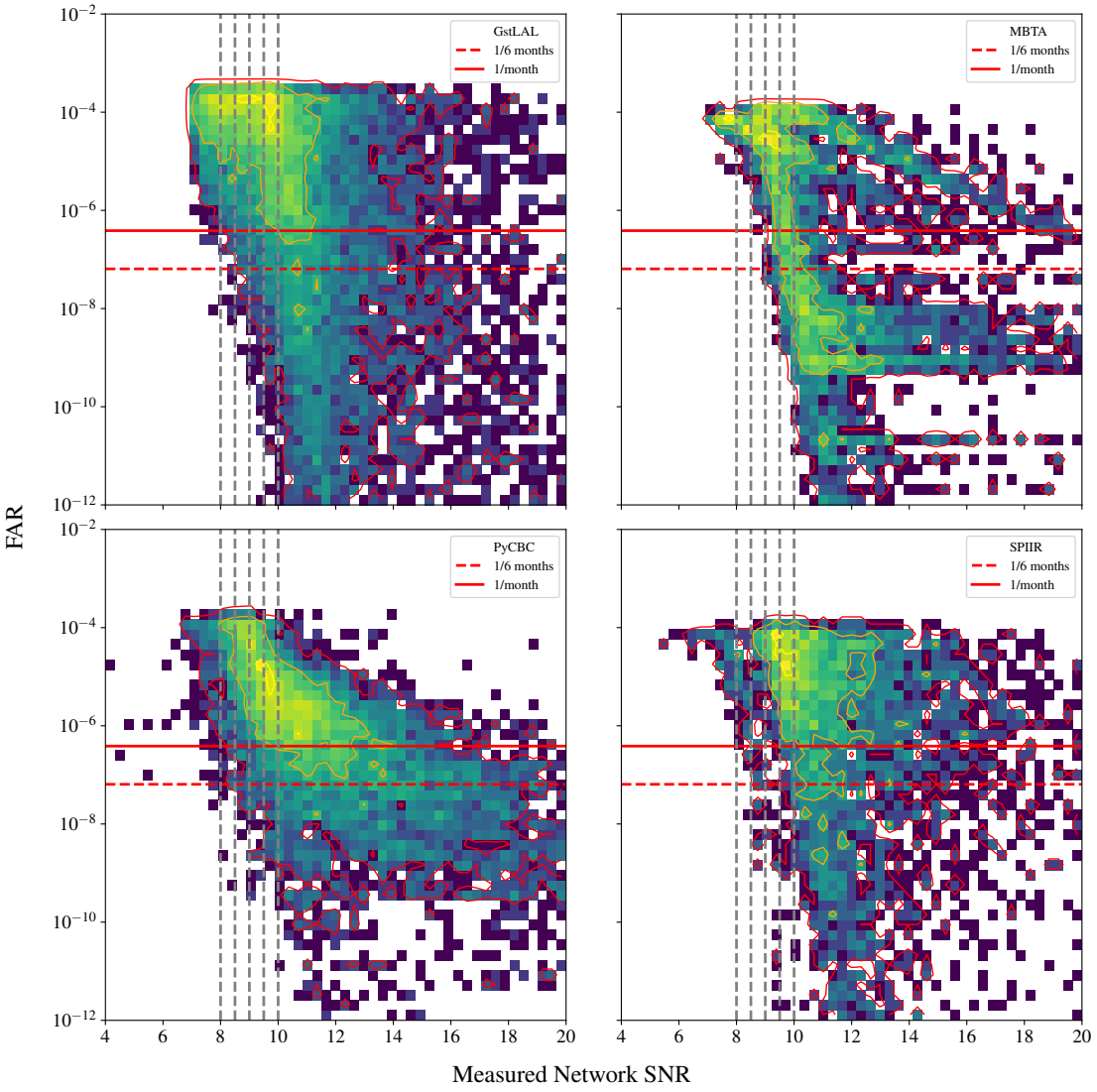

Figure 2.8: Log density plot of FAR compared to the measured network S/N individual CBCs pipelines during an MDC cycle. The vertical lines are at S/N of 8 to 10 by increments of 0.5. I see the highest density of events for an S/N just under 10, and a FAR close to 10^{-4}. Used to support the LIGO DCC, T2300385-v1[1].

dicting and analyzing future GW observations [129, 21].

2.5.3 ZTF proposal for GW follow-up and triggering criteria

This research forecasts the utility of GW detector data for astronomers, covering existing and anticipated data sets. Such forecasts are crucial for those analyzing GW data as well as for investigators seeking EM signatures of NS mergers, notably KN events [281, 161]. I present simulation outcomes to strategically align the ZTF with this scientific mission. Our analysis delineates both the methodology and the results of utilizing ZTF for the detection of EM counterparts, with a focus on KN light curves. This ap-

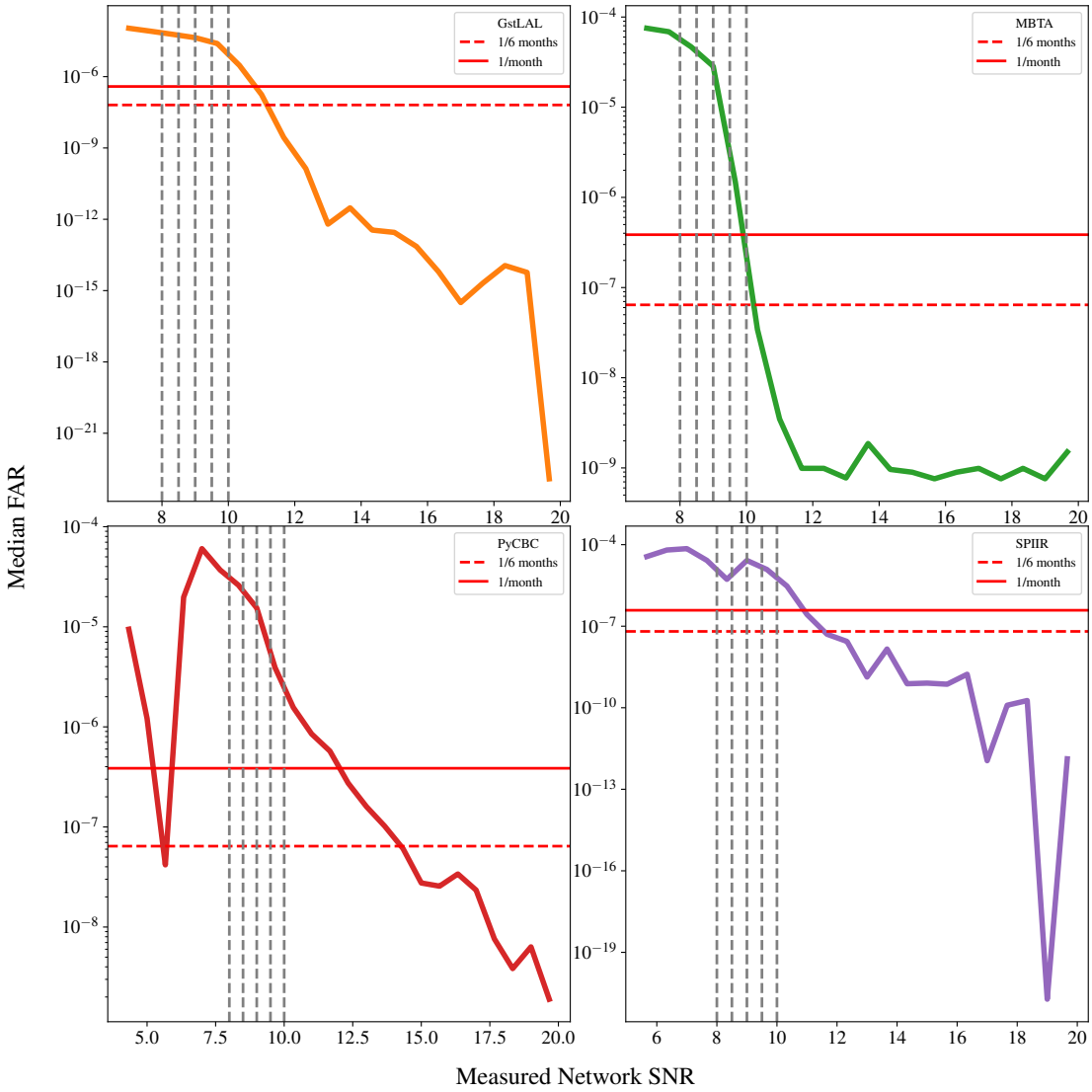

Figure 2.9: Comparison of the median FAR in a given S/N bin to the measured network S/N during an MDC cycle for individual CBCs pipelines. The vertical lines are at S/N of 8 to 10 by increments of 0.5. I find the measured network S/N to be approximately between 10-12, depending on the CBCs pipeline, for a FAR threshold of 1/month, which is the significant public alert threshold before trials factor. Used to support the LIGO DCC, T2300385-v1[1].

proach optimizes ZTF's contribution to the field, enhancing our understanding of the multi-messenger universe.

The release of low-latency GW event properties via the General Coordinates Network (GCN) notices offers critical information for deciding whether to allocate telescope time to a given GW event. Parameters such as the FAR, the probability of astrophysical origin (p-astro), the likelihood of the GW merger involving a NS (HasNS), the probability of a remnant post-merger (HasRemnant), and the Bayes factor for coherence across multiple detectors (log(BCI)) provide indirect indicators of an event's astrophys-

ical significance and potential for EM counterparts. Table 2.7 presents our proposed ZTF triggering criteria based on these low-latency metrics. An event that meets all "Go-deep" requirements justifies the initiation of target-of-opportunity (TOO) observations if the event's localization and distance fall within ZTF's operational capabilities. A "Go-wide" designation prompts adjusting public ZTF survey fields to cover the event localization within standard 30-second exposures. Events classified as "Deliberate" or "No Go" require human review to determine the appropriateness of the trigger. Given the reduction in the threshold for public alert release to two per day in O4a, establishing precise triggering criteria is essential for the judicious use of telescope resources.

In this proposal, I determine the anticipated annual number of triggers within 400 Mpc during the O4b and O5 observing runs, based on projections from Table 2.5.1 as shown in Figure 2.10. I got this by assuming an AT2017gfo like KN event [105, 266, 7] with $M_{\rm abs} \sim -16$ magnitude at peak brightness, and considering ZTF's limiting magnitude of $m_{\rm AB} \approx 22$ in 300-second exposures, I estimate ZTF's capability to detect KNe within this distance range. While NSBH mergers are expected to be rare within 400 Mpc, with 0–2 events anticipated during the O4b and O5 runs, my analysis projects an average of $< N >= 13$ ($< N >= 18$) BNS mergers within this distance during O4 (O5), offering significant opportunities for counterpoint searches.

Furthermore, we evaluated the distribution of GW events by sky area. Figure 2.11 presents the fraction of O4/O5 triggers with 90% confidence regions within the specified sky area thresholds. Assuming an average 8 hour night and ZTF's effective coverage of ~ 50 deg^2, employing a three-filter tiling strategy (i.e., $g-r-g$), we find that utilizing ZTF Partnership time alone (30% of the night) enables complete coverage of the localization for approximately 30% of GW alerts. Incorporating the private Caltech allocation (50% of the night) increases this coverage to nearly 40%, and taking advantage of the public survey time (100% of the night) allows complete localization coverage for 50% of events. These metrics, derived from our dataset, facilitate the estimation of necessary TOOs and time requests for successful GW follow-up campaigns with wide field telescopes, offering invaluable insights for developing Rubin Observatory's future triggering strategy.

2.5.4 Preparing GW parameters for EM counterpart studies

I have developed a script[14], designed to extract critical parameters such as masses, spins, distance, GPS time, and sky angular coordinates. These parameters are essential for predicting the potential emergence of UV, optical, and infrared signals during the coalescence of compact binary systems. This extracted information is then utilized by BILBY [53] for processing CBCs events, facilitating Bayesian estimation of light curve parameter estimation (PE) based on these intrinsic GW parameters.

[14] https://github.com/weizmannk/ObservingScenariosInsights/blob/main/src/Subpopulation_Splitter.py

Table 2.7: Triggering Based on GW Candidate Event Properties. Used to support kiendrebeogo et .al 2023[163].

Parameter	Go-deep	Go-wide	Deliberate	No Go
Strategy	300 s Push distance	30 s Push localization	Action Item: human interaction	
Frequency of triggers	1 per month 3 nights	2 per month 5 nights		
FAR min(FAR) - 'Best'	$<$ 1 per century Any pipeline	$<$ 1 per decade Any pipeline	1 per year - century	$>$ 1 per year All pipelines
max(p-astro)	> 0.9	> 0.9	0.1–0.9	< 0.1
HasNS	> 0.9	> 0.9	0.1–0.9	< 0.1
log(BCI)	> 4	> 4	-1 to 4	< -1
HasRemnant?	> 0	> 0	...	$= 0$
pBNS/pNSBH	> 0	> 0	...	$= 0$

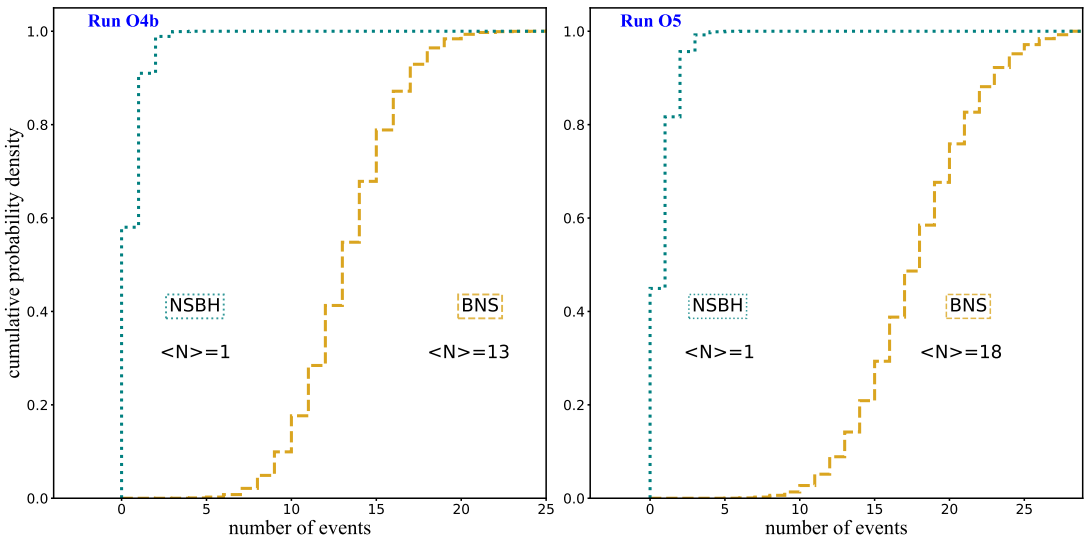

Figure 2.10: Cumulative histograms of 100,000 realizations of the number of BNS and NSBH mergers predicted to be detected during O4b and O5 within 400 Mpc based on the observing scenarios predictions in this chapter. The mean number of expected detections is quoted for each merger type. Used to support Kiendrebeogo et al. 2023 [163].

2.6 Conclusion

In this chapter, I have performed a detailed simulation study on CBCs using the PDB/GWTC-3 distribution, following the latest projections from the IGWN. The sim-

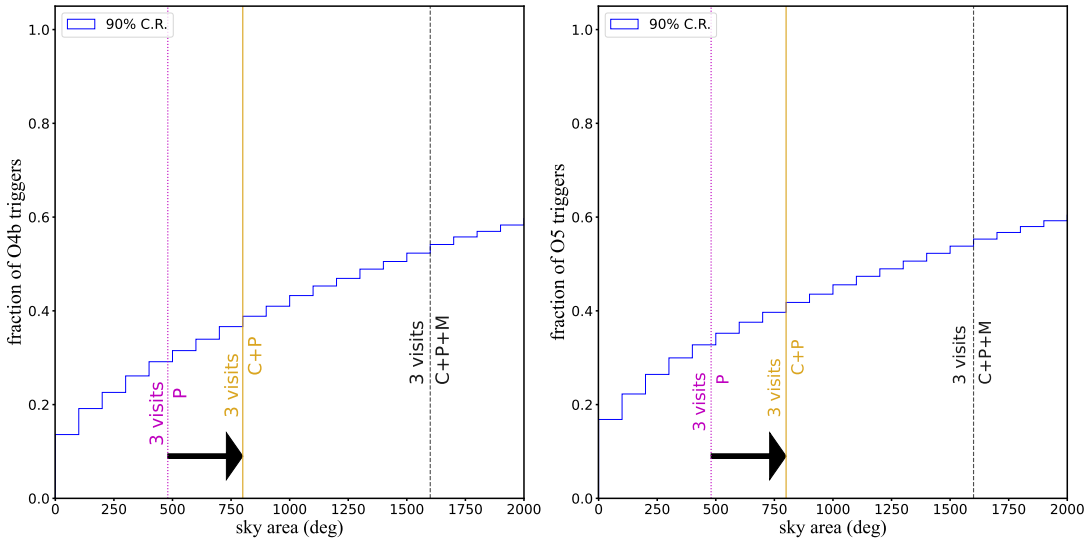

Figure 2.11: Cumulative histogram of simulated GW skymaps for O4b and O5 that satisfy our triggering criteria as a function of the 90% credible region. With both Caltech and Partnership time spanning ∼50% of the night (corresponding to a maximum area of 800 deg^2), we could fully probe the localization for nearly 40% of all events. Used to support Kiendrebeogo et al. 2023 [163].

ulations focused on improving EM follow-up strategies and improving scientific outcomes for future observations. The findings highlight the crucial role of GW observatories in advancing our understanding of the universe and potentially influencing the cosmological expansion rate. The results of my work are particularly valuable for those analyzing GW data and seeking EM counterparts to BNS mergers. This integration aims to decode the complexities of the universe, providing fresh perspectives on its expansion dynamics and significant events. Future chapters will discuss methods to identify and analyze GW counterparts to improve detection strategies and enrich our knowledge of cosmic evolution and structure.

Chapter 3

The Nuclear Multi-messenger Astronomy framework

***

In this chapter, I discuss my contributions to the NMMA framework, *An updated nuclear-physics and multi-messenger astrophysics framework for BNS mergers*, published in *Nature Communications* [217]. This also includes a summary of my contributions to light curve constraints from the GRANDMA "ReadyforO4" campaign [33] and my results on H_0, supporting Kiendrebeogo et al. 2023 [163].

3.1 NMMA and GRANDMA collaborations

NMMA team—The NMMA team consists of astrophysicists and code developers from various specialized fields with the aim of facilitating the combined analysis of GW and their EMs counterparts to deepen our understanding of the *r*-process, EOS of NS, and H_0. The primary goal is to enable the next simultaneous detection of GW , GRB , and KN. As a full member of the NMMA team, I contributed to developing this platform, including coding and deploying it on GitHub, making it public and accessible. My contributions within the NMMA team focus on scripts for adjusting light curves from KNe and SNe, directly linked to my doctoral project. These contributions simulate the estimation parameters of KNe based on data from “observing scenarios" discussed in Chapter 2, aiding in combining the posteriors from the two-messenger simulations. For HT Condor users, my scripts submit multiple jobs across the International GW Network clusters. I also provided a user installation tutorial for the *Unix* and *Mac OS* systems, later enhanced by other collaborators and including the *Windows* system. Although significant, these only represent part of the scientific potential of NMMA. Other collaborators have developed aspects I do not discuss here, but are available on GitHub[1]. NMMA is a dynamically evolving platform, continuously improving.

GRANDMA collaboration—GRANDMA is a collaboration of over a hundred scientists[2] from more than 18 countries, including Burkina Faso through my involvement. It is also supported by amateur astronomers in the citizen science program "*Kilonova-Catcher*". Within this collaboration, I served as a shifter, monitoring transients, analyzing data, and constraining the nature of light curves published in [33].

3.2 Background

The observation of GW170817 [104], resulting from a BNS merger on August 17, 2017, by the Advanced LIGO and Virgo interferometer network, marked a moment of great importance in astronomy. This event highlights the potential of multi-messenger observations, enabling the astrophysical community to explore the nature of NS, their internal composition, and their critical role in cosmic nucleosynthesis and various astrophysical phenomena. The EOS is essential for understanding atomic nuclei behavior under extreme pressures and temperatures, typical of events such as nuclear collisions and core collapse. The multi-messenger approach, especially via BNS mergers, offers insights into matter under these conditions, enhancing our grasp of the universe’s expansion, measured by the H_0. Our NMMA framework[217] is a fundamental tool for studying compact object mergers. Using Bayesian parameter inference, NMMA merges observational data from the EMs spectrum with astrophysical system properties, enriching nuclear physics and cosmology knowledge. As a Python library, NMMA connects EMs observations with the characteristics of the binary system, promoting advances in nuclear physics and cosmology. It enables detailed analyses of BNS mergers, elucidates

[1] https://github.com/nuclear-multi-messenger-astronomy/nmma/tree/main

[2] https://grandma.ijclab.in2p3.fr/who-we-are/team/

matter properties under extreme conditions, and refines our understanding of the expansion rate of the universe. The ability of NMMA to identify the potential nature of fast optical transients highlights its key role in addressing the challenges of time-domain astronomy. The NMMA framework has been crucial in NS merger studies, providing information on matter states under extreme conditions and clarifying the EOS at supranuclear densities. It has refined measurements of key cosmological constants, including the H_0, underscoring its importance in astrophysics. Recent advancements have enabled the integration of an extensive array of light curve models, which is essential for analyzing phenomena related to compact object mergers.

3.3 Inference of astrophysical light curves

In NMMA, light curve fitting is executed through two principal methodologies. The initial method entails constraining observational data acquired from telescopic observations, notably from the ZTF [62, 142, 190, 108], a time–domain optical survey with a very wide field of view (FOV) of 47 deg^2 mounted on the Samuel Oschin 48-inch (1.2 m) Telescope at the Palomar Mountain, the future Rubin Observatory's (LSST; [156]), a large (8.4 m), wide-field (9.6 deg^2 FOV) ground-based telescope designed to conduct deep 10 yr survey of the Southern sky, and additional telescopes equipped with NMMA compatible filters. The alternate method integrates GW parameters from events involving BNS and NSBH systems. These events and their GW parameters, including masses, luminosity distances, spins, and GPS time detections (which I have recently integrated to improve the accuracy of estimation), are elaborated on in Chapter 2 and the study by [163]. Such parameters, essential for analysis, are processed using `BILBY`, a Bayesian inference tool [53], with input data presented in "dat" or "json" formats. To facilitate parameter estimation within the NMMA, `BILBY` is harnessed to analyze the chosen light curve models. This process is supported by sophisticated samplers, including *Dynesty* [148] and *PyMultiNest* [126], which generate simulated observational data reflective of the input parameters. These instruments facilitate a comprehensive exploration of parameter spaces and engender posterior distributions, thus ensuring the fidelity of light curve simulations predicated on the observational or GW data input. Bayesian inference, crucial in the NMMA's analytical framework, is employed to apply rigorously selected models to meticulously prepared data, with the objective of identifying the set of parameters that most accurately represents the observed light curve. This foundational methodology enables the progressive refinement of hypothesis probabilities in light of emerging evidence, establishing itself as critical to the conduct of astrophysical light curve analyses. NMMA enhances light curve analysis by incorporating innovative techniques such as photometry enhancement and model interpolation, thereby increasing both the precision and the analytical depth. This progression expands NMMA's repertoire with an array of models for light curve simulation, ranging from the empirically derived *SVDLightCurveModel* to theoretical constructs like *SimpleKilonovaLightCurveModel*, *GRBLightCurveModel*, *KilonovaGRBLightCurveModel*, and *GenericCombineLightCurveModel*. Accurate specification of parameters is imperative for precise simulations, mirroring the diversity of astrophysical phenomena encoun-

tered. NMMA effectively simulates a wide range of events, offering a complete set of tools for multi-messenger astrophysics light curve analysis.

3.4 Light curve models

Accurate modeling of transient light curves is vital to interpret observational data. The NMMA framework provides tools and models for describing light emissions post-stellar events, essential for understanding EM signal evolution from BNS mergers. These models use **Bayesian inference** to analyze multi-messenger signals, incorporating all data on the EOS of a NS [114, 218, 274]. Our analysis employs Bayesian inference with models for signals from BNS, NSBH mergers, SNe, and GRBs. The framework effectively uses Bayes' theorem to compute posterior probability distributions $p(\vec{\theta}|x,\mathbf{M})$ for parameters $\vec{\theta}$, using mock data x and model $\mathbf{M}$.

$$p(\vec{\theta}|x,\mathbf{M}) = \frac{p(x|\vec{\theta},\mathbf{M})\ p(\vec{\theta}|\mathbf{M})}{p(x|\mathbf{M})}, \tag{3.1}$$

where $p(x|\vec{\theta},\mathbf{M})$, $p(\vec{\theta}|\mathbf{M})$, and $p(x|\mathbf{M})$ are the likelihood, prior, and evidence, respectively.

3.4.1 Kilonova models

In NMMA, these include the `Bu2019lm`, `Bu2019nsbh` from POSSIS, and `Ka2017` models.

POSSIS—The POSSIS-based grid of KN models [75, 114, 77] covers the parameter space for BNS (`Bu2019lm` model) and NSBH (`Bu2019nsbh` model) mergers. The POSSIS tool, a sophisticated Monte Carlo radiative transfer code, is enhanced for accurate modeling of KNe , emphasizing the significance of nuclear heating rates, thermalization efficiencies, and opacities in KN simulations. These models are characterized by key parameters like the dynamical ejecta mass ($M_{\rm ej}^{\rm dyn}$), disk wind ejecta mass ($M_{\rm ej}^{\rm wind}$), half opening angle (Φ), and observation angle ($\Theta_{\rm obs}$). The updated POSSIS code, as detailed in [77], demonstrates the nuanced impact of these parameters on KN light curves and spectra, offering a more comprehensive and accurate representation of these complex phenomena.

Ka2017—Presented in [160], the `Ka2017` model elucidates the EM emission from BNS. It highlights the critical influence of ejected mass ($M_{\rm ej}$), expansion velocity ($v_{\rm ej}$), and composition on the characteristics of KNe ($X_{\rm lan}$). The model is key for analyzing light curves and spectra, using a sophisticated Monte Carlo code for multidimensional analysis and resolving the radiation transport equation in expanding relativistic speeds.

We also incorporate other BNS KN models such as `Bu2022mv` [40], which is a derivative of the POSSIS framework, and `LANL2022` [287]. These models extend the parameter space beyond that of POSSIS by incorporating both disk wind ejecta velocity ($v_{\rm ej}^{\rm wind}$) and dynamical ejecta velocity ($v_{\rm ej}^{\rm dyn}$), allowing for a more nuanced exploration of the kinematic properties of KN ejecta.

Ejecta constraints—We begin by evaluating the upper limits 90% possible from the sample considered here (KNe for these objects), then constrain them for the parameters of the ejecta model $M_{\rm ej}^{\rm dyn}$ and $M_{\rm ej}^{\rm wind}$, as well as a systematic contribution to the dynamical ejecta α and the fraction of disk mass contributing ζ. This enables us to make an empirical constraint of the fraction of the disk contributing to KNe . We constrain $M_{\rm ej}^{\rm dyn}$ to 10–40% and $M_{\rm ej}^{\rm wind}$ to 10–30%. We also want to differentiate between prompt collapse and the formation of a hypermassive and/or supramassive NS.

3.4.2 Supernova models

In the NMMA framework, three models, `Piro2021`, `nugent-hyper`, and `salt3` analyze SNe. The `Piro2021` model focuses on shock cooling SNe , `nugent-hyper` on Type Ic/b SNe (SNe Ic/Ib) , and `salt3`, the spectral adaptive light curve template, on SNe Ia. The latter two use *sncosmo*[3]. These models interpret complex light curve patterns, enhancing our understanding of SN explosion mechanisms and progenitor systems.

Piro2021—The `Piro2021` model [226] is particularly adept at capturing the early-time light curves of SNe, which are crucial for understanding the physics of shock breakout and cooling. The model emphasizes key parameters: the mass of the extended material ($M_{\rm e}$), the radius of this material ($R_{\rm e}$), representing the size of the SN's outer layers, and the energy imparted during the shock ($E_{\rm e}$), which influences the intensity and duration of the cooling emission.

nugent-hyper—The `nugent-hyper` model [179], is designed for SNe Ic/Ib , calibrated to the peak intrinsic luminosity of SN 1998bw. The primary adjustable parameter in this model is the absolute magnitude. Within the context of *sncosmo*, we also provide a prior file called `sncosmo-generic.prior`, which includes parameters such as luminosity distance, timeshift, and `supernova_mag_boost`, the latter adjusting the absolute magnitude of the SN.

salt3—The `salt3` model [162] advances the spectral energy distribution (SED) modeling for SNe Ia for accurate cosmological distances. It builds on `salt2` [145, 144], G improving uncertainty estimates and color and stretch separation in light curves. Key parameters are: x_0, for flux normalization; x_1, for time-dependent light curve variations; and c, for color correction. With a larger dataset, `salt3` extends wavelength coverage to 2000–11000 Å, includes I and iz bands, and enhances cosmological analysis precision by reducing calibration errors and Hubble scatter.

[3] https://github.com/sncosmo/sncosmo

3.4.3 Gamma-ray burst

For GRBs , we use `afterglowpy`[4] [276] (named **TrPi2018** in the code), which provides a comprehensive framework for simulating synchrotron emission from relativistic blast waves in the GRB afterglows. This model is crucial for understanding the complex dynamics of GRB emissions, particularly in relation to jet structures and observer perspectives. The key parameters of the `TrPi2018` model include the isotropic kinetic energy ($E_{\mathrm{K,iso}}$), the angle of collimation of the jet (θ_c), the viewing angle (θ_v), the constant density of the circumburst (n), the spectral slope of the electron distribution (p), and the fractions of energy imparted to the electrons (ε_e) and the magnetic field (ε_B). These parameters allow for detailed exploration of the afterglow's characteristics, offering insights into the nature of GRB events and their observational signatures.

3.5 NMMA in GRANDMA "ReadyforO4" Campaign

The "ReadyforO4" observational campaign, conducted by the GRANDMA consortium from 1 April to 30 September 2021, represents an important achievement in multi-messenger astrophysics by revealing how fast we can react after a transient alert [33]. This campaign was designed to categorize astrophysical events detected from ZTF alerts into three distinct categories: moving objects, fast transients (such as KNe and GRB), and slow transients (such as SNe). Categorization was facilitated by Fink, a community broker adept at processing large volumes of time domain alert streams, including those from the ZTF survey [199] and the upcoming data processing for Rubin Observatory [156]. Of more than 35 million potential candidates, approximately one hundred passed our rigorous selection criteria. Of these, six were closely followed by the GRANDMA network, which incorporates both professional and amateur astronomers. My classification of rapid KNe was predicated on the optical source decay rate that exceeded 0.3 mag/day.

During this period, eight significant transients were identified, including ZTF21abfmbix, ZTF21absvlrr, ZTF21abultbr, ZTF21abfaohe, ZTF21abbzjeq, ZTF21acceboj, and ZTF21ablssud, with ZTF21abotose undergoing intensive observations. Using a dual phase classification approach within the NMMA pipeline, an initial **linear regression fitting** technique was applied to identify KN light curves, succeeded by fits using **NMMA light curve models** tailored for KNe , SNe, and GRBs , to determine their nature. The comprehensive methodology and collaborative effort underpinning the "ReadyforO4" campaign not only demonstrate the GRANDMA consortium's capabilities in multi-messenger astronomy, but also contribute to our understanding of the light curve nature classification.

[4] https://github.com/geoffryan/afterglowpy

3.5.1 Linear fitting regression

In the realm of astrophysical research, the method of ML estimator (MLE) plays an integral role in delineating the characteristics of rapidly changing astronomical events.MLE operates on the premise that one can optimally deduce the parameters θ of a statistical model, assuming a priori knowledge of the true distribution of these parameters. The methodology involves fitting a mathematical model to the data, where the derived estimates are those that most likely produce the observed set of values from a sequence of measurements of a random variable. This process employs the concept of sufficient statistics S_{tt}, S_y, which encapsulate all the necessary data-derived information to accurately estimate the parameters θ. My defined ML estimation function is expressed as follows:

$$L(\theta) = L(a,b) \tag{3.2}$$
$$= \log P(\mathrm{y}|a,b,H) \tag{3.3}$$
$$= -\frac{1}{2}\sum_i \log 2\pi\sigma_i^2 - \frac{1}{2}\sum_i \frac{(\mathrm{y}_i - a\mathrm{t}_i - b)^2}{\sigma_i^2} \tag{3.4}$$

Here, σ_i represents the measurement error of the magnitude y_i at time t_i.

The sufficient statistics, S_{tt} and S_y, are identified as the points where the first partial derivatives of the log ML $L(\theta)$ equal zero.

$$\frac{\partial \log L}{\partial \theta} = 0$$

This leads to the following equations:

$$\begin{cases} S_{tt} = a\sum_i \frac{\mathrm{t}_i^2}{\sigma_i^2} + b\sum_i \frac{\mathrm{t}_i}{\sigma_i^2} = \sum_i \frac{t_i y_i}{\sigma_i^2} \\ S_y = a\sum_i \frac{\mathrm{t}_i}{\sigma_i^2} + b\sum_i \frac{1}{\sigma_i^2} = \sum_i \frac{y_i}{\sigma_i^2} \end{cases}$$

The optimal estimators a, b are obtained by solving these linear equations. Thus, my linear regression model is defined as $\mathrm{Y}_i = a\mathrm{t}_i + b$. Here, the parameter a signifies the rate of linear light evolution. A slow transient is characterized as an event in which the decay rate is either negative (indicating increasing brightness) or less than 0.3 mag/day in a specific observational filter. My goal was to identify transients that undergo rapid decreases or increases in brightness. I applied a linear regression procedure using a maximum likelihood estimation approach to estimate the slopes between two distinct times (see Figure 3.1). The results of this work are recorded in Table 3.1, where I present the transient evolution rates of the first seven days since the first detection by ZTF, as well as their fade rate since the peak of maximum magnitude.

In this process I am looking for transients that fade quickly in optics with a fade rate exceeding 0.3 mag/day, characteristic of KN. The results of this work are recorded

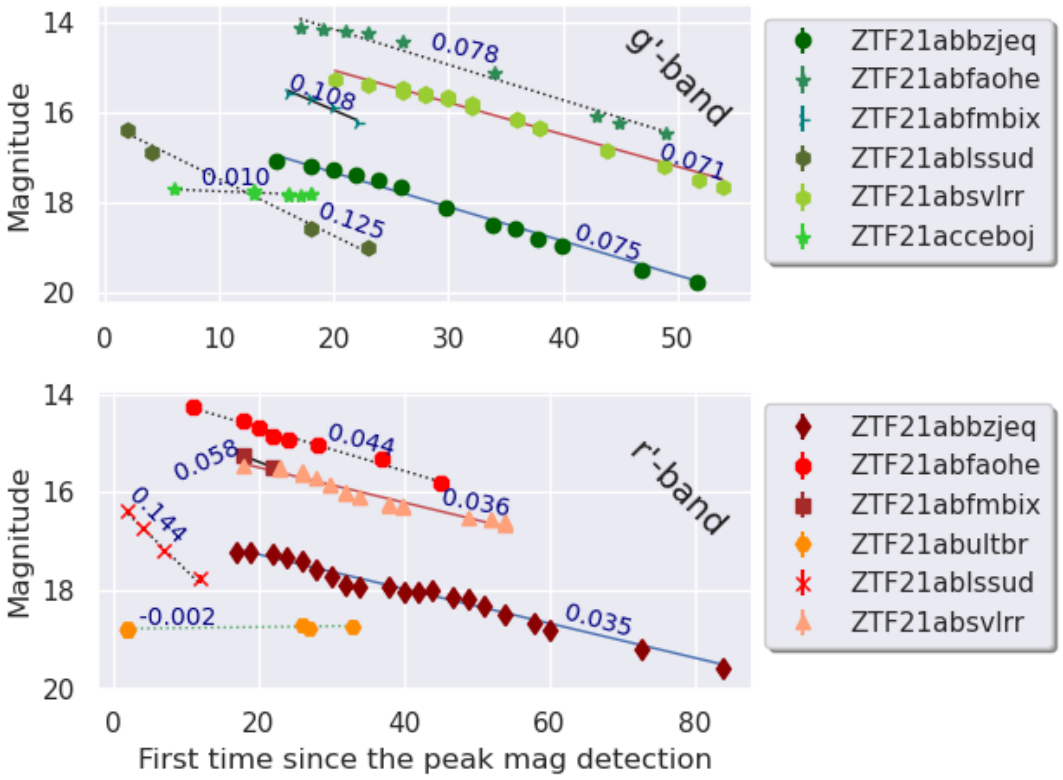

Figure 3.1: Linear fit of the transient light curves in the g'-band and r'-band, showing the evolution of the flux since the peak maximum magnitude for various transient events observed by ZTF. Each point represents the observed magnitude for a given transient on a particular day, with the numerical values indicating the rate of change in magnitude per day. This analysis enables the evaluation of the fading or brightening trends of these transients over time, providing insights into their underlying physical processes.

in Table 3.2, where the transient evolution rates of the first seven days since the first detection by ZTF as well as their fade rate since the peak of maximum magnitude are presented.

3.5.2 Constraining the nature of transients

The detection of AT2017gfo [280, 104, 208], which was preceded by the GW emission GW170817 [10] and the short GRB GRB170817A [139], marked the first observation of the join of a KN after a GW signal. KNe are rapid transient phenomena that emit across UV, optical, and infrared spectra. They are powered by the radioactive decay of heavy neutron-rich elements, which usually results from the coalescence and merger of the BNS and NSBH systems [195, 194, 181]. KNe are less luminous in the visible range and fade more rapidly [43] than SNe. The absolute peak magnitude of SNe ranges between $[-17, -19]$, while AT 2017gfo peaked at -16. SNe generally have a

Transients	*Filters*	*Mag Peak* (*mag*)	*7 first days* (*day*)	*evolve rate of 7 first days* (*mag.day*$^{-1}$)	*fade time since peak mag* (*day*)	*fade rate since peak mag* (*mag.day*$^{-1}$)
ZTF21abbzjeq	g'	17.07 ± 0.032	6.9	- 0.128	36.9	0.08
	r'	17.21 ± 0.039	7	- 0.28	66.9	0.035
ZTF21abfaohe	g'	14.12 ± 0.025	6	- 0.424	32	0.078
	r'	14.25 ± 0.042	3	- 0.09	34	0.044
ZTF21abfmbix	g'	15.6 ± 0.1	6	- 0.33	6	0.108
	r	15.3 ± 0.1	2	- 0.455	4	0.058
ZTF21ablssud	g'	16.38 ± 0.036	–	–	21	0.125
	r'	16.37 ± 0.055	–	–	10	0.144
ZTF21absvlrr	g'	15.28 ± 0.043	2	- 0.534	29	0.07
	r'	15.46 ± 0.033	5	- 0.402	31	0.043
ZTF21acceboj	g'	17.7 ± 0.077	3.9	- 0.03	12	0.01
	r'	17.4 ± 0.056	6.02	- 0.11	–	–
ZTF21abotose	g'	18.67 ± 0.16	4.02	0.28	14.01	0.06
	r'	18.56 ± 0.137	2	0.29	14 / 29	- 0.08 / 0.04
ZTF21abultbr	g'	–	–	–	–	–
	r'	18.69 ± 0.087	31	- 0.002	–	–

Table 3.1: Recording of daily magnitude scores of transient phenomena. These scores are, on the one hand, those of the first seven days following the ZTF first detection (column 5 of the table), and those since the peak of magnitude (last column of the table). For more details on the evolution of the ZTF21abotose which fades, rises, then fades again, see figure 3.1. Used to support [33]

decay rate below 0.3 mag/day, in contrast to the higher extinction rate of more than 0.5 mag/day observed for AT2017gfo. This section aims to evaluate the likelihood that the rapidly evolving optical transients are KNe , using observations from the ZTF in the g' and r' bands. My approach involves constraining the nature of these transients through four distinct light curve models, evaluated a posteriori for their correlation with the observational data. The models include: a KN model from [160] (`Ka2017`), a GRB afterglow model from [276] (`TrPi2018`), the SN light curves SN Ic/Ib model [179] (`nugent-Hyper`), and a shock cooling SN light curve model from [226] (`Piro2021`). The ideal model is one whose regression aligns closely with the observed light curve points, as determined by the Bayes factor of the model. A key criterion for model rejection is having at least one observational data point falling outside the estimation band of the model. The most suitable model ensures that its regression line effectively

Table 3.2: Simulation results for rapidly evolving transients using ZTF data, assessing their concordance with four distinct models: KN (Ka2017), SN (nugent-hyper), GRB afterglows (TrPi2018), and Shock Cooling (Piro2021). Bayes factors are presented in logarithmic form for comparative evaluation. Used to support [33].

Transients	Ka2017	TrPi2018	nugent-hyper	Piro2021	light curve
ZTF21abfmbix	−12.38	−15.95	−9.18	−10.1	Supernova Ia
ZTF21absvlrr	−9.78	−16.73	−9.91	−11.07	Supernova Ia
ZTF21abultbr	−2.73	−9.14	−5.24	−4.76	Supernova II
ZTF21ablssud	−6.32	−11.58	−9.83	−9.41	Cataclysmic Variable
ZTF21abfaohe	−12.3	−10.98	−7.47	−8.67	Supernova Ia
ZTF21abbzjeq	−8.22	−11.41	−7.49	−8.47	Supernova Ia
ZTF21acceboj	−16.52	−19.44	−14.52	−15.6	Supernova IIb
ZTF21abotose	−6.37	−10.62	−7.41	−7.49	Shock Cooling - Supernova IIp

encompasses the set of observed data points.

Results—In Table 3.2, I present my findings for each transient, definitively classified as non-moving objects through the analysis of their light curves using ZTF data. Utilizing the models previously described, I have identified the transients ZTF21abfmbix, ZTF21absvlrr, ZTF21abultbr, ZTF21abfaohe, ZTF21abbzjeq, and ZTF21acceboj as typical SN candidates. It is important to note that ZTF21abfmbix is listed twice, indicating its strong SN characteristics in our analysis. Furthermore, my results suggest that ZTF21abotose is consistent with both shock cooling and GRB afterglow models in its early stages. However, its brightness increase at later stages aligns more closely with the shock cooling scenario exclusively. Additionally, ZTF21ablssud is well modeled by a GRB framework. Yet, considering its galactic latitude $\ell = 5.7$ degrees and its resemblance to numerous known cataclysmic variables, we propose that it is more likely to be a cataclysmic variable. Figure 3.2 shows an application of NMMA fitting to the transient "ZTF21acceboj," that NMMA has classified as a SN IIb.

Classification of ZTF21abotose event—ZTF21abotose, also known as SN2021ugl, displayed initial characteristics of both KN and SN types. Early observations showed compatibility with shock cooling models. The event's increasing brightness over time supported these models, indicating that late-stage phenomena were primarily due to shock-heated material cooling, rather than GRB afterglow. Initially, ZTF observations suggested ZTF21abotose might be a KN event, but spectroscopic analysis later confirmed it as a SN IIb. This type is marked by early hydrogen lines that fade, indicating a core-collapse of a massive star with a significantly stripped hydrogen envelope. This finding confirms the event as a stellar explosion, not a merger-driven KN.

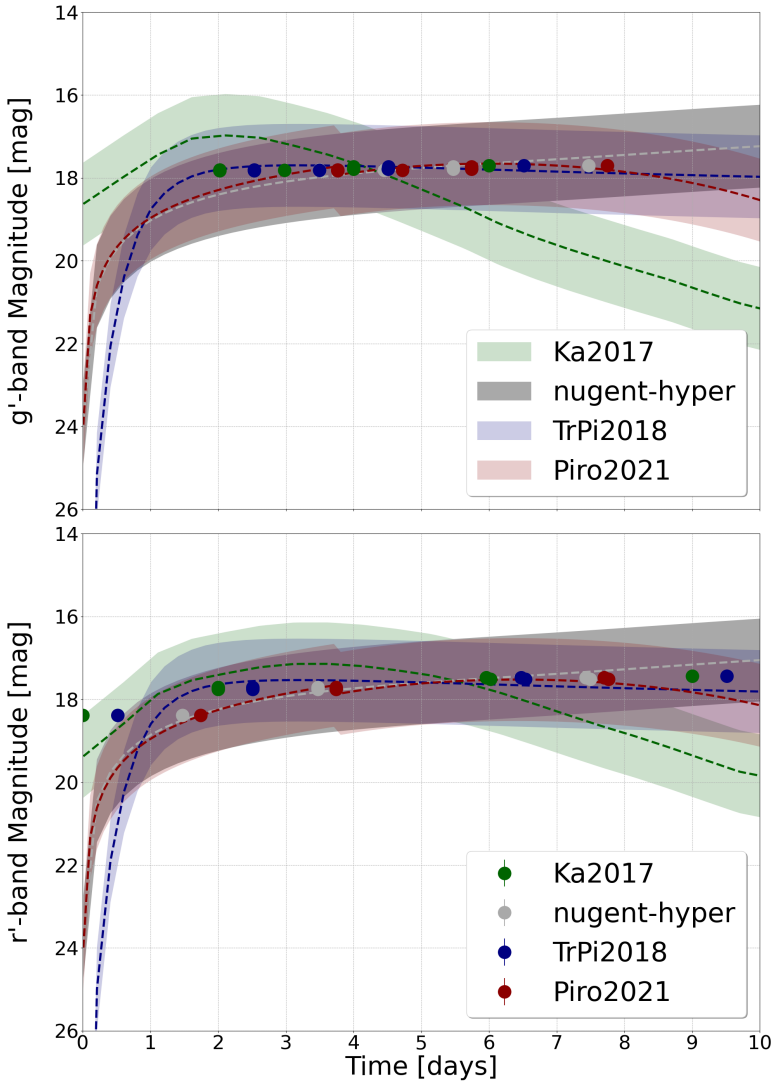

Figure 3.2: Comparative analysis of light curve models against the observed data for the transient event ZTF21acceboj, which has been classified as a SN IIb through NMMA fitting procedures. The figure displays the magnitudes of the g'-band and r'-band over a period of ten days. Model predictions from `Ka2017` (green), `nugent-hyper` (gray), `TrPi2018` (blue), and `Piro2021` (red) are overlaid with the observed photometric data points (colored dots). The shaded regions represent the confidence intervals for each model, illustrating the range of possible light curve behaviors based on the underlying physical parameters of each model. This graphical representation underscores the varying degrees of fit each model has to the observed data, highlighting the predictive power and limitations inherent in the current modeling approaches.

3.6 Equation of state and Hubble-Lemaître constant

Despite the advances with the independent measurement of the H_0 [5] and the constraints on the EOS of ultra-dense matter [11, 113], traditional analyzes have isolated

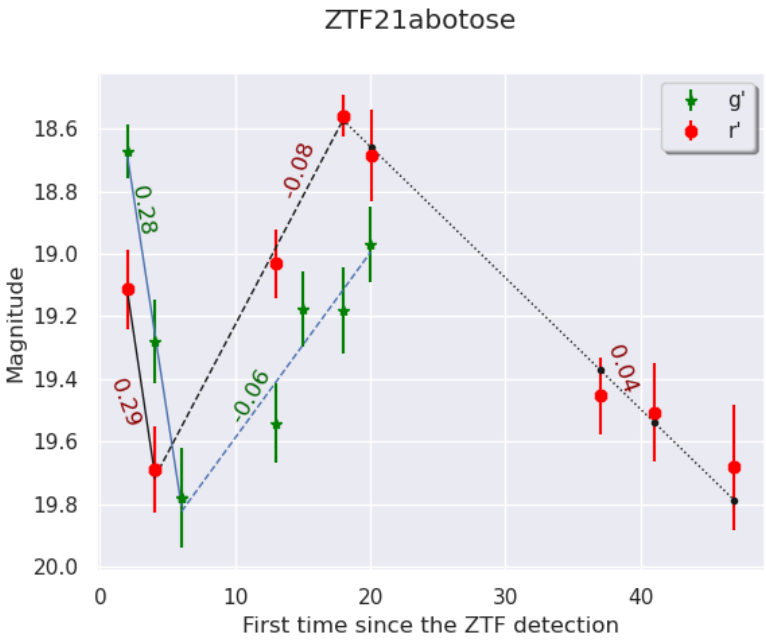

Figure 3.3: Here I plot the light curve fitting of ZTF21abotose using a linear regression model. The g'-band data (green) and r'-band data (red) are depicted with their respective observational error bars. Linear fits to the data are represented by the dashed lines, indicating the transient's fading pattern over the first 47 days since the ZTF detection. Numerical values adjacent to the data points denote the rate of change in magnitude, evidencing a more rapid decline in the g'-band compared to the r'-band. This behavior is characteristic of the cooling and expansion processes following the SN event.

the evaluation of different messengers. NMMA integrates analyses across GW , KN, and GRB signals, enhancing our understanding of NS properties and the universe's expansion rate. This approach provides a holistic view of the behavior of ultra-dense matter by leveraging the unique strengths of each messenger type. The GW data yield crucial information, including tidal deformability $\tilde{\Lambda} = \frac{16}{3}\frac{(m_1+12m_2)m_1^4\Lambda_1+(m_2+12m_1)m_2^4\Lambda_2}{(m_1+m_2)^5}$, chirp mass $\mathcal{M}_c = \frac{(m_1m_2)^{3/5}}{(m_1+m_2)^{1/5}}$, and mass ratio $q = m_2/m_1$, while EM counterparts offer insights into the dynamics of the remnant accretion disk ($M_{\rm ej}^{\rm dyn}$), which is the dynamical ejecta is the matter expelled at the moment of the merger from tidal stripping of the NSs and from the compact binary coalescences (CBCs) contact interface [245, 246] and wind ejecta ($M_{\rm ej}^{\rm wind}$), produced through remnant accretion disk winds, which can be driven by neutrino energy, magnetic fields, viscous evolution and/or nuclear recombination energy [193]. In our NMMA framework, we employ the `BILBY` [53] software package for GW posterior parameter estimation, integrating GW posterior distributions with potential EMs counterparts for a more accurate constraint of the EOS of NS and the H_0. We adopted the IMRPHENOMD_NRTIDALV2 waveform model for the GW posterior simulation[112], selecting the EOS parameters with the highest likelihood estimates for a comprehensive understanding of NSs and the expansion of the universe [155].

3.6.1 Equation of state

The collision of two NSs is among the most violent events in the universe and is associated with a variety of observables ranging from GW and possibly neutrino signatures to EMs signals covering the entire frequency band. These phenomena provide crucial insight into the extreme conditions found within NSs , where matter is compressed to densities that exceed those of an atomic nucleus. In the context of NS , EOS plays a crucial role in describing how matter responds to the relationship between densities (ρ), pressures (p) and temperatures (T). A significant aspect of this relationship is constrained by chiral effective field theory (chiral EFT, [120, 186]), which offers a sophisticated framework to investigate interactions within neutron matter. In particular, this approach is effective for densities ranging between 1 and 2 n_{sat} [273], where $n_{sat} = 0.16\ \mathrm{fm}^{-3}$ represents the density of nuclear saturation [147, 189]. The predictive power of chiral EFT interactions extends the understanding of nuclear forces from experimentally accessible scenarios to dense neutron-rich environments characteristic of NS cores. The degeneracy pressure, originating from the Pauli Exclusion Principle, is crucial for NS structural integrity. This quantum mechanical phenomenon prevents identical fermions from occupying the same quantum state, generating a repulsive pressure that counteracts gravitational collapse. Remarkably, NSs exhibit superfluidity at low temperatures ($T \approx 0$ K), offering a unique laboratory for studying ultradense matter and its properties. The degeneracy pressure, originating from the Pauli Exclusion Principle, is crucial for NS structural integrity.

A fundamental aspect of the EOS analysis involves the speed of the sound equation, $c_s = c\sqrt{\frac{\partial p}{\partial \rho}}$, where $0 \leq c_s \leq c$ and c is the speed of light. This equation provides limited insight into the complex nature of ultradense NS matter on its own. Thus, chiral EFT, constrained up to approximately $12 n_{\mathrm{sat}}$ by theoretical uncertainties and the speed of sound, is employed for a deeper understanding. By integrating EOS constraints from chiral EFT at low densities with high-density observations, and using the speed of sound as a facilitator, we solve the Tolman-Oppenheimer-Volkoff (TOV) equations. This methodology allows for the estimation of the NS radii and tidal deformabilities as mass functions, providing a comprehensive understanding of the NS properties. Following the methodology in our paper [217], we constrain NS EOS using analyses of KN AT2017gfo, GW170817, and GRB1708107. Using Gaussian process regression, constraints on KN and source properties are derived as associated with GW170817.

AT2017gfo: KN analysis—For the analysis of the KN AT2017gfo, we focused on the UV, optical, and infrared observations recorded between 0.5 to 10 days post-merger. Utilizing the comprehensive *grizyJHK* AB magnitude photometry data provided by [266], our analysis adheres to the methodologies outlined in [93]. To links physical system parameters to the emitted light curves, we employed `Bu2019lm` to be our KN model, built with POSSIS, a 3 dimensional Monte Carlo radiative transfer code (see the Sec. 3.4). This approach allowed us to systematically examine the light emission properties across different wavelengths, providing valuable insights into the ejecta's composition and the NS merger's environmental conditions. The method employed for light curve analysis involved sparse interpolation of the data onto a uniform

time grid, followed by a detailed singular value decomposition (SVD) to identify principal components that reflect the co-varying nature of the data. We leveraged Gaussian Process Regression (GPR; [234, 220]) to interpolate the principal components, allowing us to predict light curves and spectra for various parameter sets within the ejecta models $M_{\rm ej} = \alpha + M_{\rm ej}^{\rm dyn} + \zeta \times M_{\rm ej}^{\rm wind}$, where α accounts for an additional component of the ejecta mass not captured by other variables, providing flexibility in modeling complex ejecta dynamics, while ζ serves as a conversion factor, crucial for quantifying the portion of the disk mass ejected as wind, and uniformly sampled between 0 and 1. [93], perform a similar computation but on bolometric luminosities, light curves in standard filters, and spectra. This surrogate model approach provided a robust statistical framework to infer bolometric luminosities, temperatures, and radii, significantly contributing to our understanding of the KN's behavior and its underlying physics. This GPR approach not only improves prediction accuracy but also provides quantifiable uncertainty estimates, thereby offering insightful inferences into the dynamical properties of the KN event and contributing profoundly to our comprehension of its underlying physics.

GRB170817A: Gamma-ray Burst afterglow analysis—Short GRBs are predicted to originate from NS mergers, a connection that was confirmed by GW170817 and GRB170817A. For the study of the afterglow resulting from GRB170817A, we concentrated on the multi-wavelength observations spanning from radio to X-ray frequencies, documented from moments post the merger up to several weeks thereafter. Using the extensive data set collated by [277]. The synthetic light curve models, derived using `TrPi2018` model [248]. This enabled a thorough exploration of the afterglow's emission characteristics across the EMs spectrum, revealing crucial insights into the jet dynamics and the interstellar medium interaction. Our investigation deepens the understanding of the GRB's physical mechanisms, highlighting the significance of synergistic multi-messenger observations in astrophysical explorations. The analytical approach adopted for decomposing the light curve data involved a meticulous SVD to unearth the principal components that capture the essence of the data's variability. Central to our modeling effort was the quantification of the isotropic energy of the jet, $E_{\rm o}$, which is intricately modeled to account for various contributing ejecta components. The intricate dynamics between the jet and its surrounding environment were encapsulated in the following formulations: $E_0 = \varepsilon M_{\rm disk}(1-\zeta)$, where ε represents the efficiency of conversion from disk mass, $M_{\rm disk}$, to energy, and ζ accounts for the fraction of disk mass not contributing to the observed emission due to various loss mechanisms.

Result—To constrain the EOS, I demonstrate the ability to constrain the radius of a 1.4 $M_\odot$ NS , focusing on the median values within the 90% confidence interval (CI). By incorporating all available observational data, I combine information from GW170817 and AT2017gfo, further enhancing our analysis with data from GRB170817A. In Fig. 3.4, I employed equal tail of the "corner" plot [131] to quantify the overlap between the parameters and the credible interval rather than the highest density interval (HDI) (the one used in our NMMA paper [217]), using marginalized 1- and 2-dimensional posteriors over the remaining parameters. My analysis, integrating GW170817 and AT2017gfo data, refined the radius estimates for a 1.4 $M_\odot$ NS to $R_{1.4} = 11.86^{+0.45}_{-0.50}$ km and further to $R_{1.4} = 11.98^{+0.32}_{-0.44}$ km upon incorporating insights

from GRB170817A. These findings underscore the critical role of synergistic observations in the elucidation of the EOS of NSs .

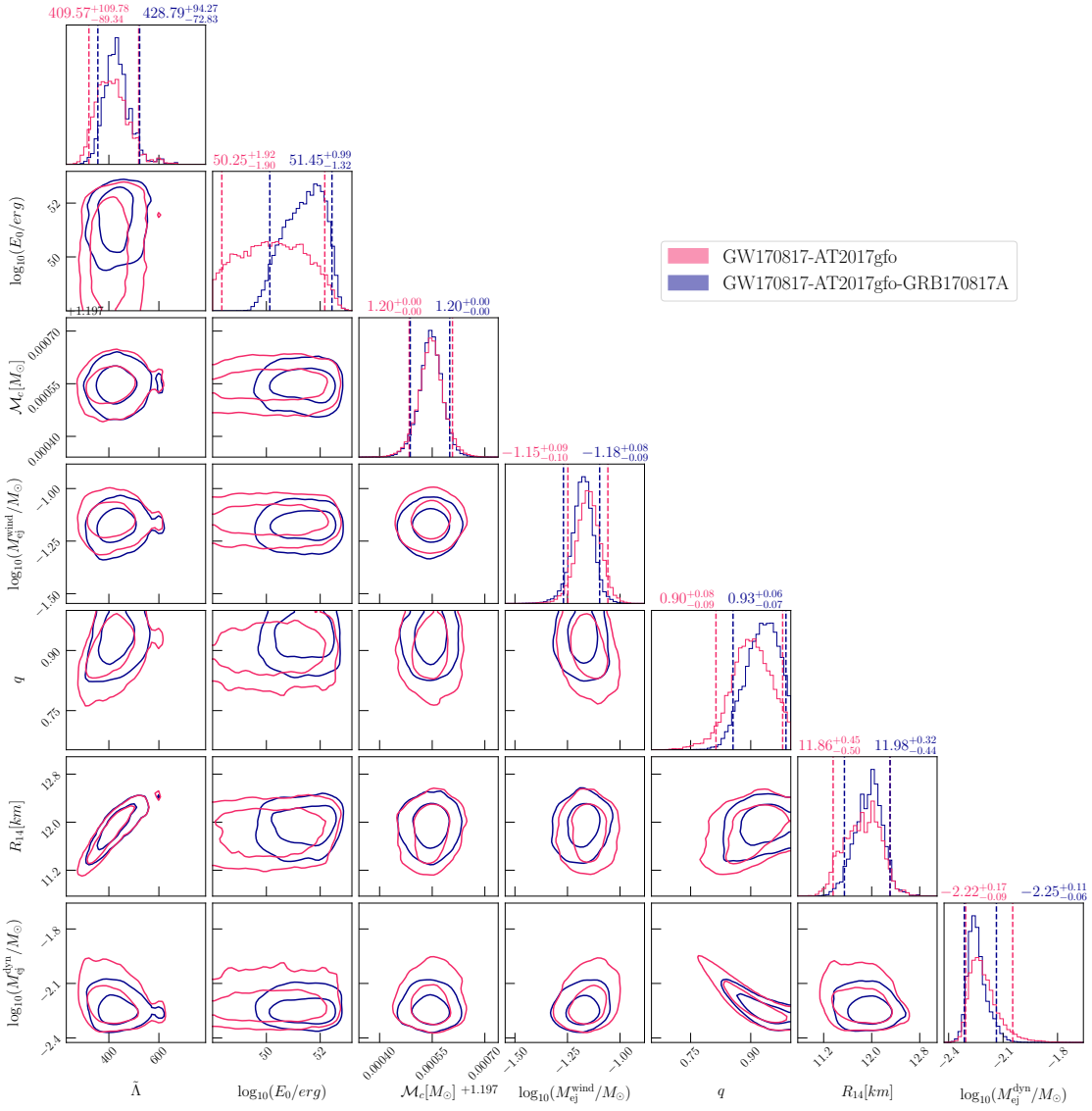

Figure 3.4: Corner plot analysis of GW170817, AT2017gfo, and GRB170817A data to infer key parameters of the NS merger. Confidence regions at 68%, and 95% levels for several parameters are depicted, including the mass of the dynamical ejecta ($M_{\rm ej}^{\rm dyn}$), the mass of the disk wind ejecta ($M_{\rm ej}^{\rm wind}$), the GRB jet's isotropic energy ($\log_{10} E_0$), the chirp mass ($\mathcal{M}_c$), the mass ratio (q), the tidal deformability ($\tilde{\Lambda}$), and the radius ($R_{1.4}$) of a 1.4 $M_\odot$ NS. The median values and 90% CI are indicated for the 1D distributions. Analyses based on GW170817 and AT2017gfo are presented in red, and the extended analysis including GRB170817A is shown in blue, facilitating direct comparison between these scenarios. Modified from our NMMA paper [217].

3.6.2 Hubble-Lemaître constant constraints

I simulate joint GW and EMs signal analyses as detailed in Chapter 2, focusing on PSD noise for the O4b and upcoming O5 runs. To improve efficiency, we employ the relative binning method for the 20 Hz GW analysis, using a uniform prior for the luminosity distance [157]. The study focuses on the 30 loudest sources by network S/N for O4 and O5, selected based on CBC distributions from PDB/GWTC-3 exceeding S/N=8. The IMRPHENOMD_NRTIDALV2 model and EOS parameters are used for GW simulations, with signals injected into Gaussian noise based on the O4 and O5 PSD predictions. GW parameter estimation uses the `BILBY` [53] library and the `DYNESTY` algorithm [242, 268]. I used the same priors apply to KN inferences, using the NMMA framework to estimate KN properties and the luminosity distance [76, 77]. Then the EMs parameters for the ZTF and Rubin Observatory are also estimated within NMMA simulation. Phenomenological relations [113] link binary and ejecta masses in 30 BNS systems, and I identify nine (seven) potential BH formations in O4 (O5) without ejecta. The process is summarized in the flow chart of Figure 4 in Chapter 2 to derive H_0." To estimate H_0, we analyze the posterior luminosity distance distributions from GW and EMs simulations, including the GW170817 and AT2017gfo results, using a consistent KN model. Using a standard cosmology, the linear Hubble relation for nearby events helps us to deduce H_0, with adjustments for luminosity-distance volumetric priors as described in [5].

For residual 21 (23) O4b (O5) BNS mergers with an EMs counterpart, the inferred luminosity distance are adapted from both GW and EMs simulations to determine the posterior distribution for H_0. This also includes the inferred luminosity distance posteriors of the GW signal GW170817 from [8, 6] and the KN signal AT2017gfo, yielding a total of 22 (24) O4 (O5) BNS coalescences. Given that all BNS systems are within a 300 Mpc range or a minimal redshift regime, the appropriate linear Hubble relation for nearby events is assumed as

$$cz \approx H_0 d_L, \tag{3.5}$$

where d_L and z are the luminosity distance and redshift, respectively c the speed of light, and H_0 the rate of the universe expansion. The analysis adjusts the luminosity distance prior by introducing a factor $1/H_0^4$, as in [5].

We calculate injected redshifts using distances and the H_0 from our O4 (O5) sample, defined by a Gaussian distribution with a standard deviation of 1%. Our approach, which does not consider the distance-inclination angle degeneracy, improves H_0 measurements by incorporating GW and KN data as per [113]. Although we focused on the 30 loudest GW signals linked to potential KN observations, we acknowledge the need for broader investigations to address selection biases from our sampling method and redshift estimations of host galaxies. The influence of BNS mass on H_0 is significant, as high-mass systems that rapidly become BHs are excluded from H_0 evaluations. Despite no evident biases in current results, the robustness of our methods suggests that future studies should refine bias corrections, particularly as we consider larger datasets and higher redshifts. Our emphasis on loud GW signals could introduce biases re-

lated to signal selection, host galaxy redshifts, and BNS masses, necessitating further methodological improvements.

Discussion—I calculate injected redshifts using the distances and the H_0 from our O4 (O5) sample, defined by a Gaussian distribution with a 1% standard deviation. This approach, which does not consider the distance-inclination angle degeneracy, improves the H_0 measurements by incorporating GW and KN data as in [113]. Although I focused on the 30 loudest GW signals linked to potential KN observations, we acknowledge the need for broader investigations to address selection biases from our sampling method and redshift estimations of host galaxies. The influence of BNS mass on H_0 is significant, as high-mass systems that rapidly become BHs are excluded from H_0 evaluations. Despite no evident biases in current results, the robustness of our methods suggests future studies should refine bias corrections, particularly as we consider larger datasets and higher redshifts. Our emphasis on loud GW signals could introduce biases related to signal selection, host galaxy redshifts, and BNS masses, necessitating further methodological improvements.

ZTF—In Figure 3.5, I show the H_0 results for the ZTF scenario from GW and EMs data, in addition, the results when combining GW+EM information and contrast these with state-of-the-art measurements. The uncertainties of our results are reported at 90% credible interval. The projected BNS detection rate is marked as a gray dashed line from Table 5 of kiendrebeogo et al. 2023[163]. The injection value of $H_0 = 67.74\ \mathrm{km\,s^{-1}Mpc^{-1}}$ from the Planck measurement of the Cosmic Microwave Background [30] have been used.

In ZTF-O4b (left panel), a single GW+EM observation yields $H_0 = 61.26^{+17.73}_{-18.97}\ \mathrm{km\,s^{-1}Mpc^{-1}}$, which does not provide a strong constraint on the H_0 due to considerable uncertainties. Combining the 22 BNS events of O4b, including GW170817 and AT2017gfo, the calculated value is $H_0 = 66.37^{+0.58}_{-0.95}\ \mathrm{km\,s^{-1}Mpc^{-1}}$. Despite the presence of systematic biases, these combined data hint at a possible resolution of the Hubble tension, highlighting the influence of additional GWs and associated KNe
.

In ZTF-O5 (right pane), a single GW+EM observation results in $H_0 = 61.26^{+17.73}_{-18.97}\ \mathrm{km\,s^{-1}Mpc^{-1}}$, which aligns with previous O4b findings. When 24 events in the O5 BNS are considered together, the estimate increases to $H_0 = 66.74^{+0.39}_{-0.33}\ \mathrm{km\,s^{-1}Mpc^{-1}}$.

Rubin—In Figure 3.6,the H_0 estimate for the Rubin Observatory scenarios of O4b and O5 are detailed using the same injection value of $H_0 = 67.74\ \mathrm{km\,s^{-1}Mpc^{-1}}$ than the ZTF case.

The left panel displays Rubin Observatory-O4b. The analysis reveals that approximately two combined GW+EM observations for O4b yield $H_0 = 62.56^{+5.27}_{-4.70}\ \mathrm{km\,s^{-1}Mpc^{-1}}$. Then a comprehensive data set of 22 events during O4b is available, and the calculated $H_0 = 67.01^{+0.43}_{-0.53}\ \mathrm{km\,s^{-1}Mpc^{-1}}$ approaches the expected value.

In the right panel I show the result of Rubin Observatory-O5. Approxi-

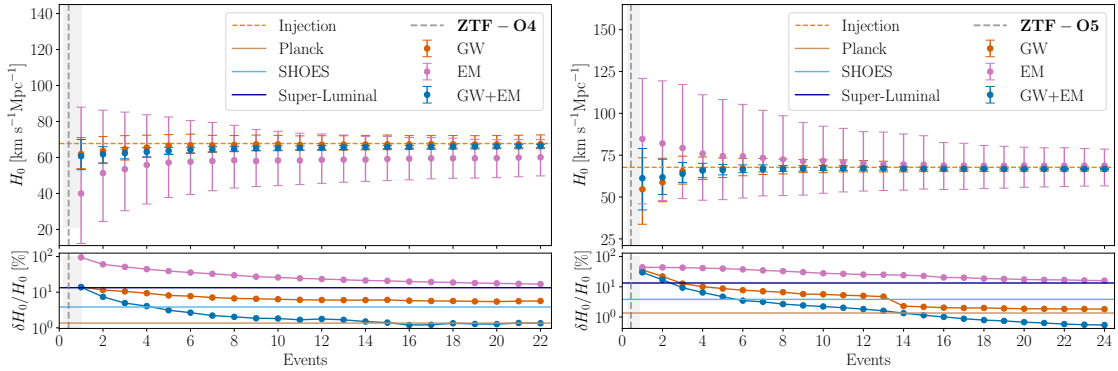

Figure 3.5: H_0-estimates for the ZTF observation scenarios for O4b (left panel) and O5 BNS samples (right panel). The H_0 estimates from our GW simulations are shown in orange, the EMs simulations are shown in violet, and the combined GW+EM results are shown in blue, while the relative errors are shown in the bottom panels. Indicate the expected detection rates for O4b and O5 in alignment with Table 5 of [163] as a gray dashed line and show the credible interval 90% as gray-shaded regions. In the bottom panel, I contrast our results with the Planck measurement of the cosmic microwave background ([30]; Planck, violet), to the Hubble measurement via SNe Ia ([238];SHOES, light blue), and to the H_0 measurement of superluminal motion of the jet in GW170817 ([152]; superluminal, gray). All uncertainties are reported at a credible interval 90%. Used to support kiendrebeogo et .al 2023[163]

mately five such observations in O5 provide $H_0 = 65.30^{+2.31}_{-2.99}$ km s^{-1}Mpc^{-1}, aligning closely with the predicted results. Similarly, for O5, the determination of $H_0 = 66.23^{+0.39}_{-0.33}$ km s^{-1}Mpc^{-1} corroborates the initial estimations.

My work indicates that measurements H_0 with subpercent accuracy can be achieved by integrating GW+EM data with an adequate count of KNe observations. Moreover, note that although the analysis currently considers only distance measurements from the KNe , additional data, such as the GRB afterglow, could potentially decrease uncertainties by resolving the ambiguities between distance and inclination.

3.7 Conclusion

This research demonstrates the scientific capabilities of the NMMA platform, which not only constrains light curves from transient objects, but also integrates GW and EMs data. This integration enables detailed analyses of BNS mergers and NSBH mergers, revealing properties of matter in extreme environments and enhancing our understanding of the expansion rate of the universe, reflected by the H_0 . The NMMA platform constrained the EOS for a 1.4 $M_\odot$ NS to $R_{1.4} = 11.98^{+0.32}_{-0.44}$ km using data from GWs, KNe , and GRB bursts from GW170817. It also refined the H_0 estimates using simulated light curve data with the ZTF and Rubin Observatory. Future enhancements to the NMMA framework are essential to increase precision, optimize follow-up observa-

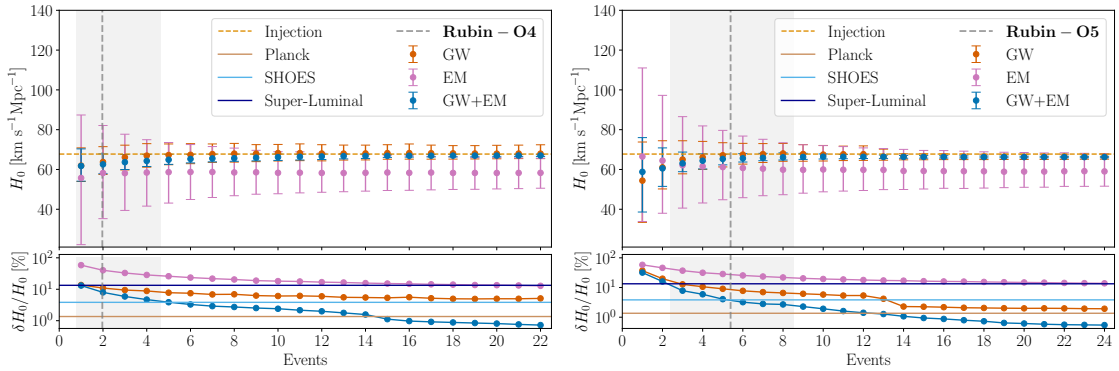

Figure 3.6: The H_0-estimates for Rubin Observatory observation scenarios for O4b (left panel) and O5 BNS samples (right panel). The H_0 estimates from our GW simulations are shown in orange, the EMs simulations are shown in violet, and the combined GW+EM results are shown in blue, while the relative errors are shown in the bottom panels. Indicate the expected detection rates for O4b and O5 in alignment with Table 5 of [163] as a gray dashed line and show the credible interval 90% as gray-shaded regions. In the bottom panel, I contrast our results with the Planck measurement of the cosmic microwave background ([30]; Planck, violet), to the H_0 measurement via SNe Ia [238];SHOES, light blue), and to the H_0 measurement of superluminal motion of the jet in GW170817 ([152]; superluminal, gray). All uncertainties are reported at a credible interval 90%. Used to support kiendrebeogo et .al 2023[163]

tions, and better utilize skymaps and telescope data. These improvements will expand our cosmic knowledge and refine techniques for studying transient events in the universe.

Chapter 4

Predictions for detection rates and science with gravitational-wave counterparts

***

In this chapter, I present the results of my contributions to improving, particularly the update of the algorithm to detect EM counterparts of GW, gwemopt. My work facilitated the integration and connection of gwemopt[1] with the NMMA[2] framework presented in Chapter 3. Various simulations were conducted to evaluate the impact of telescopes such as ZTF, the Rubin Observatory, and the forthcoming ULTRSAT during the observation campaigns O4a, O4b, and O5 of the IGWN GW. The results of the run O5 simulations were used to support the work of "ULTRSAT WG2 Work package", which has not yet been published at the time of writing this thesis.

[1] https://github.com/skyportal/gwemopt/tree/main
[2] https://github.com/nuclear-multi-messenger-astronomy/nmma/tree/main

4.1 Background

GW sky maps, while providing limited directional information, require detailed probability maps based on the direction and distance of the sky for effective detection of the GW counterpart [265, 64]. The broad sky coverage required for GW observations demands sophisticated algorithms for counterpart characterization. This study focuses on the release of probability skymaps by IGWN, underscoring the challenges in optimizing telescope efforts due to varying configurations and conditions, and highlighting the need for advanced techniques in follow-up observations. The key to this is the rapid classification of fast transients, particularly with decay rates exceeding 0.3 mag/day for KNe, essential for understanding variable and transient phenomena. We have increased our ability to study these events, necessitating innovative approaches such as the NMMA [3] framework [217], which employs Bayesian inference for multi-messenger signals with EOS of NS data [114, 218, 274], and gwemopt [95, 96], which optimizes follow-up observations using skymaps and telescope data.

4.2 Telescopes configuration in gwemopt

This section explores the various parameters and strategies gwemopt employ to tailor telescope settings for optimal detection and analysis of the EM counterparts. gwemopt tool is a highly specialized scheduler designed to optimize follow-up observations of GW events. Segmenting the observational process into stages such as tiling, time allocation, and planning significantly enhances the efficiency of these critical observations. It analyzes skymaps and telescope parameters to segment the process into stages: tiling, time allocation, and planning using potential EM counterpart light curve information. gwemopt's primary goal is to streamline the planning of TOO telescope observations by segmenting GW skymaps into manageable 'tiles' based on telescope FOV, allocating observation time efficiently, and considering essential factors like tile probability and observability to maximize coverage. The "iterative" and "overlapping" methods introduced by gwemopt are crucial to maximize coverage and minimize overlap in multi-telescope networks. It also proposes synchronized multi-telescope observations worldwide for comprehensive coverage across different bands and temporally separated visits to the same sky patch. This approach significantly improves the efficiency and probability of detecting and studying transient cosmic events [95, 219].

Within gwemopt, various astronomical observation systems, including ultraviolet and optical, are configured[4]. As part of my research, I have integrated scripts into the gwemopt framework that incorporate configurations for terrestrial telescopes such as ZTF and LSST, as well as the upcoming space telescope, ULTRSAT. Detailed in the subsections "Ground-Based Telescopes" and "Space Telescope", these configurations are adaptable to other telescopes, especially space telescopes, which face fewer constraints than ground-based ones. To facilitate the use of gwemopt with NMMA, I added

[3] https://github.com/nuclear-multimessenger-astronomy/nmma

[4] https://github.com/skyportal/gwemopt/tree/main/gwemopt/data/config

a script to NMMA to simulate light curve detection[5] that interfaces with gwemopt.

4.2.1 Ground-based telescopes

These include the Asteroid Terrestrial-impact Last Alert System (ATLAS; [275]) with a FOV of 29.2 deg^2 reaching a limit in the $i \sim 18.7$ mag band (5σ, 30s), BlackGEM [68] with a FOV of 8.12 deg^2 reaching a limit in the $g \sim 23$ mag band (5σ, 300s), the ZTF [63, 142, 190, 108], an optical study of the temporal domain with a very wide FOV of 47 deg^2 reaching a limit in the $ztfr \sim 20.4$ mag band (5σ, 30s), and the upcoming Rubin Observatory (LSST; [156]) with a large 9.6 deg^2 FOV designed to conduct a comprehensive 10-year survey of the southern sky, reaching a limit in the $ps1\_\_r \sim 24.4$ mag band (5σ, 30s), and many others.

4.2.2 Space telescopes

These include the Nancy Grace Roman Space Telescope (Roman; [44]), which is observable in the near-infrared with capabilities up to $F158 \approx 26$ mag (5σ, 30s), slated for 2027. Another significant mission, the UVEX [171], is scheduled for 2030. ULTRSAT [259], with a 204 deg^2 FOV, will detect objects up to magnitude 22.5 (5σ, 900s) and will operate in 2026.

Among all these astronomical platforms, I am particularly interested in the capabilities of detecting EM counterparts. ULTRSAT and UVEX will operate in the ultraviolet domain, and the Rubin Observatory and ZTF operate on the ground in the optical domain. For ZTF, I consider a base sensitivity in the $ztfg$, $ztfr$ and $ztfi$ bands with magnitudes $ztfg \sim 21.7$, $ztfr \sim 21.4$, and $ztfi \sim 20.9$ [38]. The Rubin Observatory covers $sdssu$, $ps1\_\_g$, $ps1\_\_r$, $ps1\_\_i$, $ps1\_\_z$, and $ps1\_\_y$ bands with magnitudes $sdssu = 23.9$, $ps1\_\_g = 25.0$, $ps1\_\_r = 24.7$, $ps1\_\_i = 24.0$, $ps1\_\_z = 23.3$, and $ps1\_\_y = 22.1$. For ULTRSAT , I consider the $ultrasat$ band with a magnitude of $ultrasat = 22.5$ and 300s of exposure time (instead of 900s). The EM light curves for ULTRSAT are generated using *sncosmo*[6], using the radial positioning of its bandpass ($ultrasat$) for detailed astronomical analysis, based on data from [259], which we have joined in *sncosmo* for this purpose. Table 4.1 presents the configuration parameters required for gwemopt to simulate and detect the EM counterpart, as used in my studies.

4.2.3 Sky grid generation

For the LSST, ZTF, and ULTRSAT missions, I used the Hierarchical Equal Area iso-Latitude Pixelization (HEALPix) method to create a sky grid, ensuring efficient and uniform coverage essential for tasks such as cosmic microwave background analysis and GW event localization [140]. HEALPix divides the celestial sphere into equal-area

[5] https://github.com/nuclear-multimessenger-astronomy/nmma/blob/main/nmma/em/detect_lightcurves.py
[6] https://github.com/sncosmo/sncosmo

Table 4.1: Configuration of telescopes

Parameter	**LSST**	**ZTF**	**ULTRASAT**
FOV [deg]	1.75	6.86	14.28
FOV Type	Circle	Square	Square
Filter	ps1__r	ztfr	ultrasat
Limiting Magnitude [mag]	24.4	20.4	22.5
Exposure Time [s]	30	30	300
Filter Change Time [s]	N/A	60	N/A
Slew Rate [deg/s]	6.3	2.7	0.5
Readout Time [s]	2	10	20
Minimum Altitude [deg]	30	30	0
Overhead per Exposure [s]	0	10.0	0
Maximum Exposure Time [s]	N/A	600	N/A
Latitude [deg]	-30.1716	33.3563	N/A
Longitude [deg]	-70.8009	-116.8648	N/A
Elevation [m]	2207.0	1742.0	35786000
Operational dates	2025	operational	2026

tiles, each uniquely indexed, supporting multi-resolution analysis and adaptive refinement. The adaptability of HEALPix is shown in the dynamic calculation of the NSIDE parameter, adjusted according to the FOV of different missions to enhance the resolution for smaller observational fields. The parameter NSIDE is essential for resolution, representing the divisions per base-resolution pixel side to attain higher resolution. The total pixel count on the sphere is $12 \times \text{NSIDE}^2$. Increasing NSIDE enhances the resolution by reducing pixel size, which is crucial for accurate astronomical and cosmological studies, especially in detailed sky mapping. I apply `dorado-scheduling`[7] intended for ultraviolet follow-up of GW events, further exemplifies the utility of HEALPix in creating an efficient grid structure. For example, the tessellation grid generated for the ULTRSAT mission (NSIDE = 8), with its uniform coverage, highlights HEALPix's ability to render spherical data on a two-dimensional map with equitable area distribution. This methodology resulted in a denser grid for missions with smaller FOVs, such as LSST (NSIDE = 32), illustrating the method's ability to provide detailed coverage where needed while maintaining computational efficiency. Similarly, for ZTF (NSIDE = 16), the calculated NSIDE ensures an optimal balance between resolution and computational demand.

My study underscores the indispensibility of HEALPix in modern astronomical surveys and multi-messenger astronomy, offering an unparalleled tool for spatial index-

[7] https://github.com/nasa/dorado-scheduling

ing and sky coverage. Furthermore, the module's functions facilitate the selection of points on the unit sphere with approximately uniform density per unit area, considering the average area per tile. Notably, in `dorado-scheduling`, methods like geodesic() and healpix() are restricted to certain tile numbers to ensure coverage, the number of tiles being the smallest possible number that is greater than or equal to $4\pi/\text{area}$ [264]. The following example demonstrates how to employ the `dorado-scheduling` tool to generate a tessellation grid for the ULTRSAT mission, showcasing one of the potential applications of this versatile tool. Although tailored for ULTRSAT with an area of 204 deg^2, the approach is adaptable to various missions. The command for generating the ULTRSAT tessellation grid is shown below:

```
dorado-scheduling skygrid --area "204 deg2" --output "ULTRASAT.tess" --method "healpix"
```

This example illustrates the process of creating a sky grid using HEALPix coordinates, serving as a template that can be adapted for various astronomical missions and research needs. In Figure 4.1, I show the sky grid coverage for the LSST, ZTF, and ULTRSAT telescopes. The *skygrid generation* [8] script in the GitHub repository "ObservingScenariosInsights" calculates the HEALPix NSIDE parameter for a given area generates the sky coordinates and records the tessellation format for gwemopt, allowing the figure reproduction[9].

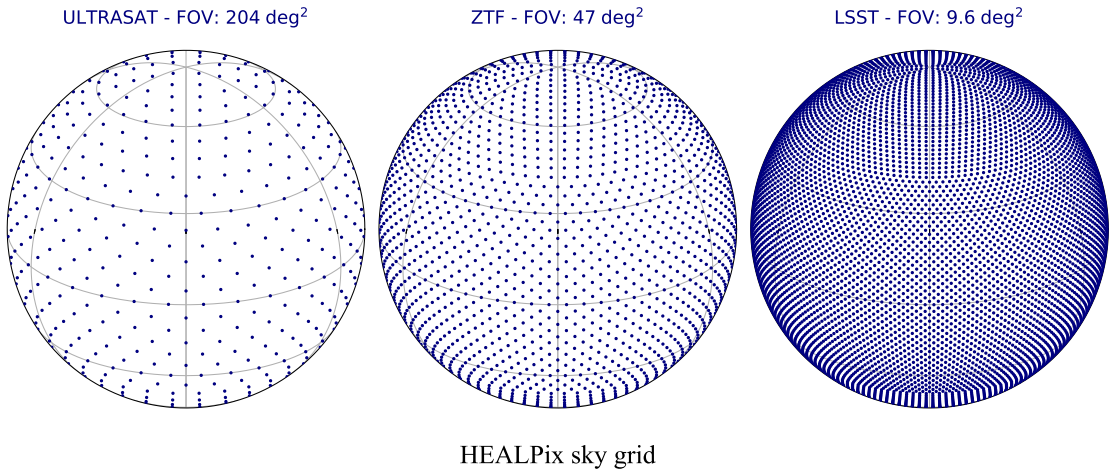

Figure 4.1: This figure shows the HEALPix sky grid coverage for each telescope, displayed on an 'astro globe'. Subplots indicate the FOV for ULTRSAT (204 deg^2), ZTF (47 deg^2), and LSST (9.6 deg^2). Tessellations partition the celestial sphere, aiding large-scale surveys. Generated with `dorado-scheduling`, the plots highlight varied sky coverages and support the " ULTRSAT WG2 Work package" paper.

[8] https://github.com/weizmannk/ObservingScenariosInsights/blob/main/ultrasat/skygrid_generation.py
[9] https://github.com/weizmannk/ObservingScenariosInsights/blob/main/ultrasat/skygrid_plot.py

4.3 Simulation follow-up

4.3.1 lightcurves

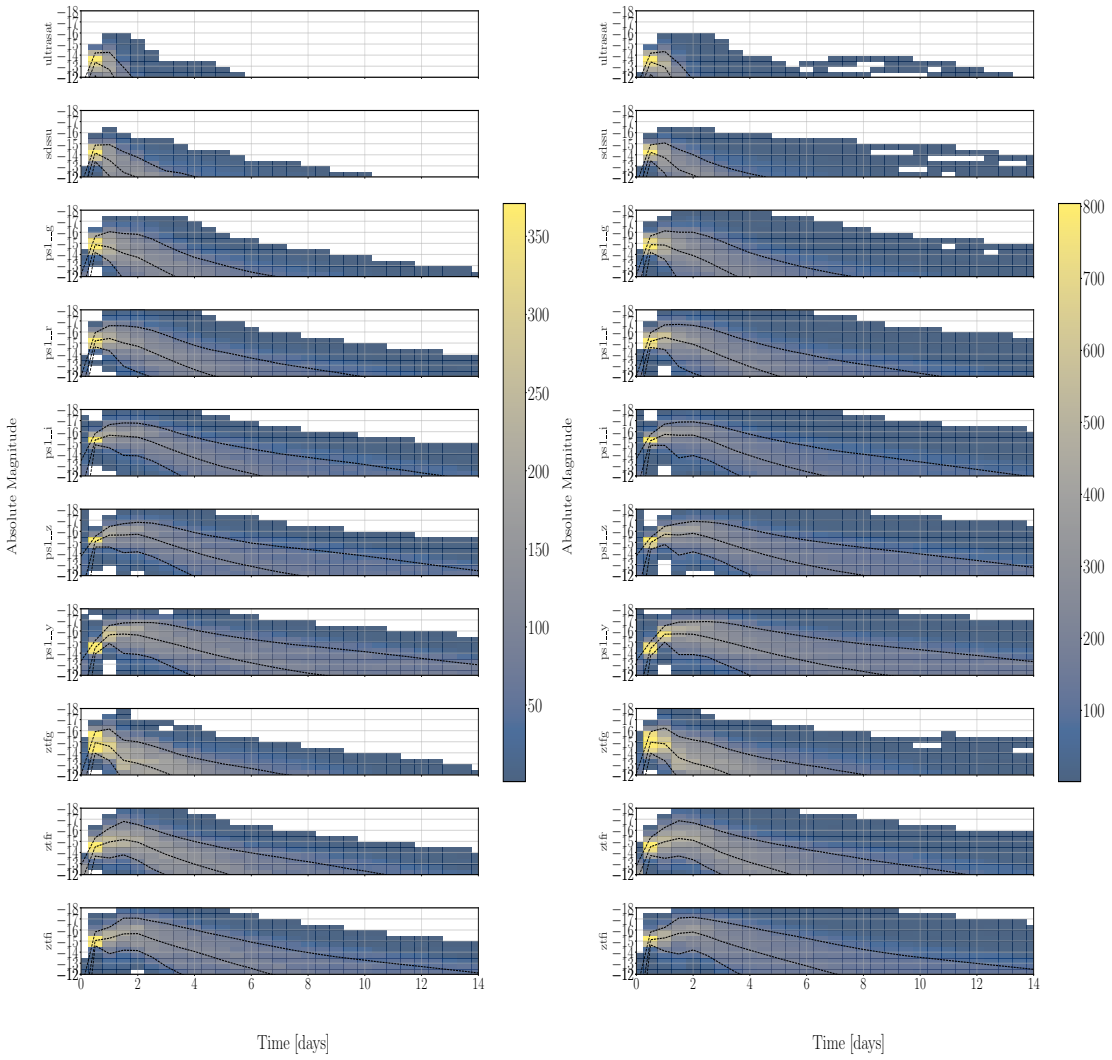

Figure 4.2: Two-dimensional histograms of simulated BNS light curves for observing runs O4b (left) and O5 (right), spanning ultraviolet to near-infrared bands (*ultrasat*, *sdssu*, *ps*1__*g*, *ps*1__*r*, *ps*1__*i*, *ps*1__*z*, *ps*1__*y*, *ztfg*, *ztfr*, and *ztfi*) to include all bands used by the ULTRSAT, ZTF, and LSST surveys considered in this work. Each panel contains three dashed lines representing the 10th, 50th, and 90th percentiles. The color bar indicates the number of detections across different bands.

In our efforts to detect KNe, I used the `Bulla2019lm` model, powered by the three-dimensional Monte Carlo radiative transfer code POSSIS [75, 77]. Unlike traditional approaches, POSSIS requires input opacities, which circumvents the direct solution of the radiative transfer equation. This methodology accelerates computational processes and simplifies parameter space exploration. Validation against the GW170817

observation enhances the model's reliability. The model incorporates key parameters such as the mass of dynamic ejecta $M_{\rm ej}^{\rm dyn}$, the mass of disk wind ejecta $M_{\rm ej}^{\rm wind}$, the half-opening angle Φ and the observation angle $\Theta_{\rm obs}$, with Φ sampled between 15° and 75°. To refine the precision of the model, I used Gaussian process regression for grid-based interpolation [93, 94], facilitating the generation of KN light curves corresponding to compact binary coalescence events anticipated during the O4a (initiated in May 2023) and subsequent periods kiendrebeogo et .al 2023 [163, 230].

Simulating light curves for BNS and NSBH scenarios, as outlined in Chapter 2, begins with predicting dynamical and disk wind ejecta masses. In the BNS cases, I adopt dynamical ejecta fits from [93] and disk wind ejecta fits from [114]. For NSBH mergers, dynamical ejecta predictions follow [133], with disk wind ejecta fits from [169]. Notably, NSBH configurations often preclude KNe events due to mass ratios conducive to the NS's direct plunge into the black hole. My simulation methodology, which focuses on BNS mergers within the `PBD/GWTC-3` distribution, emphasizes the prediction of ejecta masses, given the higher prevalence of BNS events over NSBH mergers, which are limited by the subset of NSBH injections that produce nonzero ejecta masses. Using the NMMA framework, we inferred posterior distributions of KNe properties and luminosity distances based on POSSIS-modeled KNe templates for BNS merger scenarios. In my methodology for simulating light curves, I draw upon the strategies established for ZTF, LSST, and ULTRSAT to ensure comprehensive coverage across different observational frameworks tailored to GW event follow-ups. For ZTF, we adhere to the Phase-II public cadence and the private *ztfi* band survey cadence, using KDE fits to inform our revisit cadences. Each visit involves a randomly assigned observing filter sequence, supplemented by 300-second TOO observations in the *ztfg* and *ztfr* bands during the initial one or two days post-trigger, contingent on GW localization areas being greater or lesser than 1000 deg^2. These procedures are in line with the practices of the ZTF collaboration during O3 [161], incorporating methods to simulate magnitude uncertainties through skew normal fits to forced photometry uncertainties and employing KDE fits to determine forced photometry upper limits for filtering out fainter measurements. The criterion for the acceptance of the light curve focuses on achieving a S/N greater than 3 [45]. Extending these principles to the LSST, my simulation framework is crafted following the strategy from [46], integrating 300-second TOO observations across all available LSST bands to facilitate prompt, wide-field documentation of KNe light curves, a critical component in the multi-messenger astronomy landscape. This approach ensures that I capture the early and evolving stages of KNe emissions, reflecting the operational capabilities expected of the Rubin Observatory. Additionally, for ULTRSAT, 900s TOO observations were incorporated, broadening our observational scope to encompass a wider array of transient astrophysical phenomena triggered by GW events.

Figures 4.2, 4.3, and 4.4 present histograms of simulated light curves and peak magnitudes across the ULTRSAT, ZTF, and LSST bands for O4b and O5 observation runs, highlighting the extensive predictive capabilities of the NMMA.

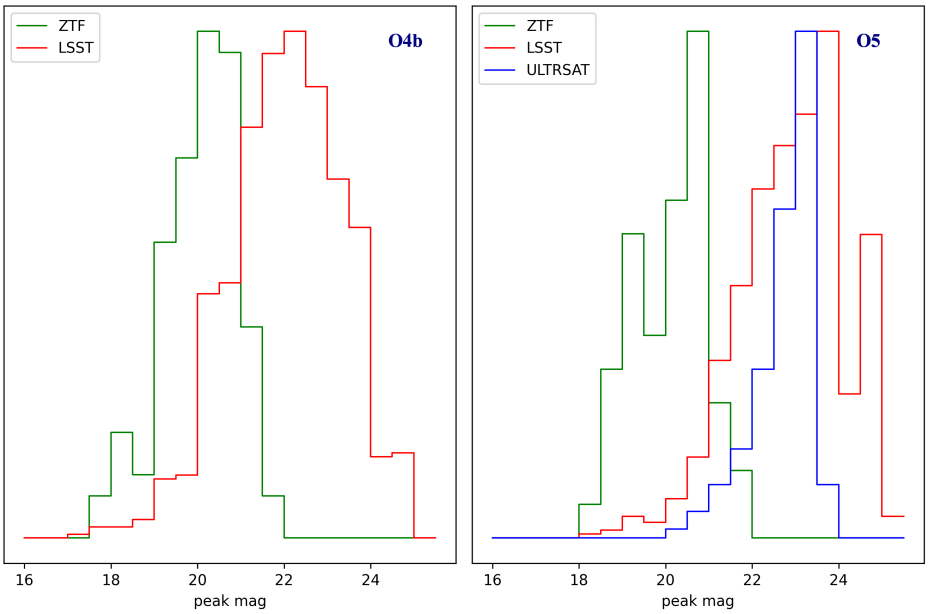

Figure 4.3: One-dimensional histograms of peak magnitudes across ULTRSAT (blue), ZTF (green), and LSST (red) bands for BNS events during the O4b and O5 observing runs. The left panel illustrates O4b, while the right panel focuses on O5.

4.3.2 Optimizing algorithm strategy with gwemopt

The gwemopt software optimizes the EM follow-up of GW events by efficiently tiling the sky, distributing observatory time, and managing observations in different telescope setups. This includes considerations for FOV, filters, exposure times, and limiting magnitudes. By introducing 'iterative' and 'overlapping' techniques, gwemopt advances existing scheduling models from individual telescopes to network-wide operations, increasing the chances of detecting transient events [95]. These methods adapt flexibly to various scheduling algorithms, bolstering the utility of the tool [42, 99, 97]. Developed in Python, gwemopt interfaces seamlessly with GraceDB and HEALPix formats to process GW skymaps. Orchestrates the tiling of the sky, time allocation, and sequencing of observations, taking into account the diurnal and observational constraints. Significantly, gwemopt elevates the efficiency of EM counterpart identification within multi-messenger astronomy by streamlining the entire process from sky tiling to observation scheduling [96]. Employing algorithms like the Greedy Algorithm, it ensures a judicious allocation of telescope time, prioritizing high-probability observation targets to optimize both immediate returns and overall strategic objectives. gwemopt also enables multi-night imaging plans, covering a variety of operational and observational conditions [96]. In Figure 4.5, I illustrate the workflow from GW alerts to telescope detection via the gwemopt pipeline, including steps such as:

- **GraceDB Integration:** Downloads GW skymaps and event data, including the time of the event and delay between detector signals and EM emissions.
- **Telescope Configuration:** Uses configuration files detailing telescope specifica-

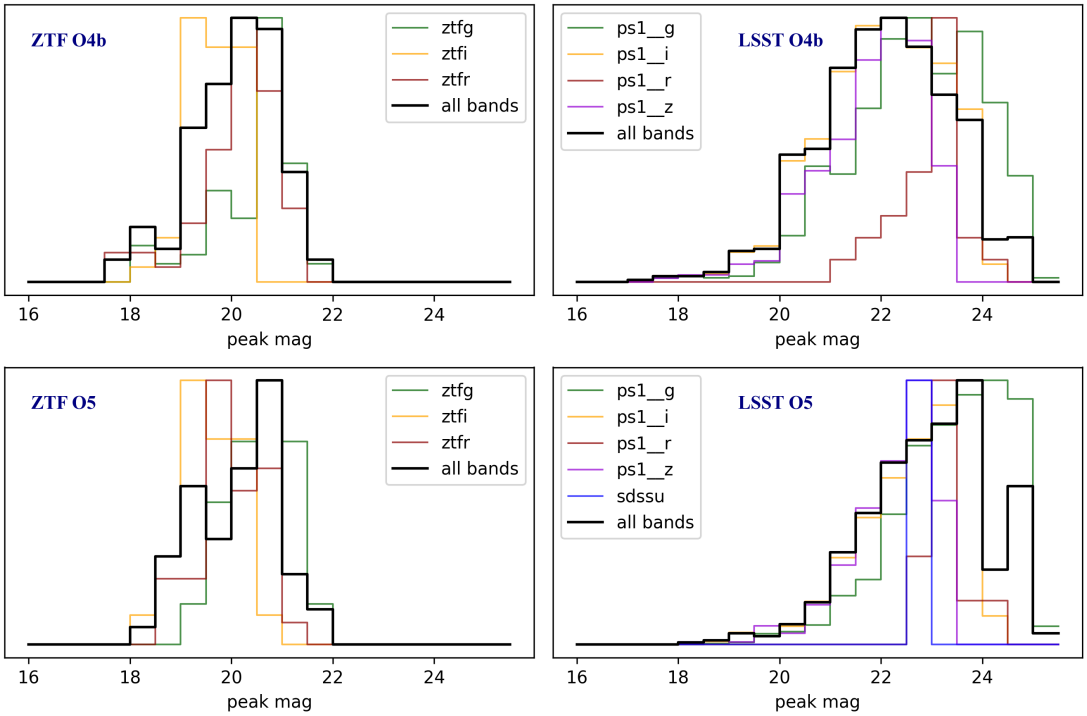

Figure 4.4: One-dimensional histograms of peak magnitudes in ZTF and LSST bands for BNS mergers. The left panels depict ZTF peak magnitudes for O4 (top) and O5 (bottom), with the right panels showcasing analogous data for the LSST. A black line across both panels indicates peak magnitudes detected in all telescope bands during the O4 and O5 simulation runs.

tions such as filter types, limiting magnitudes, exposure times, site locations, and FOV dimensions.

- **Skymap Tiling:** Implements algorithms to tile the sky with minimal overlap, optimizing the coverage of probability-rich areas.
- **Time Allocations:** Assigns observation times to tiles, employing metrics to maximize the likelihood of imaging a GW counterpart within given constraints.
- **Scheduling:** Schedules the observations, optimizing for factors such as airmass and lunar brightness to ensure the best possible observational conditions.

4.3.3 Kilonova detection dates

Using the “observing scenarios" of GW parameters from kiendrebeogo et .al 2023 [163] that have passed the S/N threshold of 8, I provide a projection of KN detections from GW event localizations, considering telescope sensitivities and FOVs. The data is recorded in zenodo [164]. I simulated distributions for BNS events across the O4a, O4b, and O5 observation runs, injecting 405, 1004, and 1990 events, respectively. All events were within a redshift of $z \leq 1.98$, making them suitable for NMMA analysis.

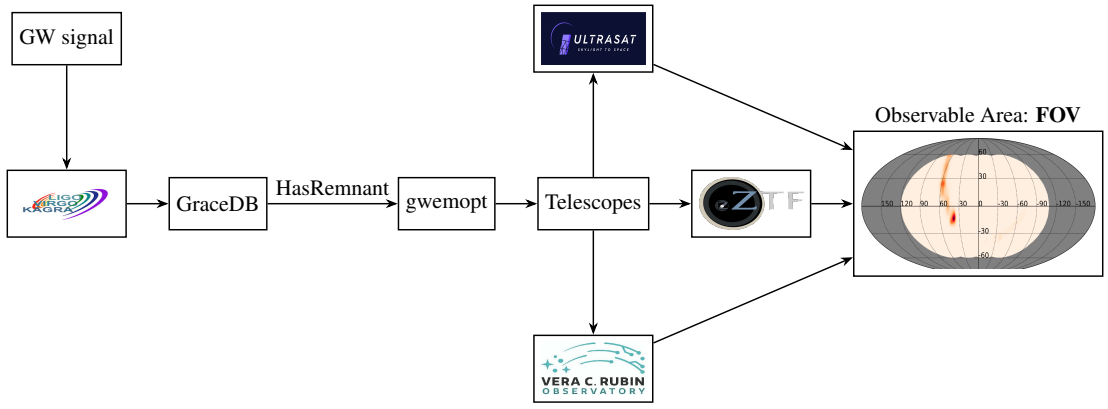

Figure 4.5: Flowchart illustrating the sequential process of detecting and following up on **GW !**events using tools such as GW detectors, GraceDB, gwemopt, and various telescopes.

My analysis considered the absolute peak magnitudes across various bands for ZTF, LSST, and ULTRSAT, and 2D probability coverage. ULTRSAT's forecasts apply only to O5, since it will launch in 2026 after O4a and O4b are concluded.

During O4a, O4b, and O5 runs, ZTF detects 41, 67, and 57 simulated KN events, respectively, while LSST identified 100, 224, and 346 KN events, demonstrating their strong detection capabilities for injected BNS KN events, as illustrated in Figure 4.6. However, ULTRSAT's detections during the O5 run were lower, with only 10 KN events, depicted in Figure 4.7.

By integrating the EM counterpart detection fractions with the annual detection rates of the CBCs presented in Chapter 2, Table 2.4, I provide predictions for the KN detection rates in the upcoming observational runs. These predictions are based on specific assumptions detailed previously, including the progressive improvement in detector sensitivities across the O4a, O4b, and O5 runs. Such enhancements are pivotal for extending the detectable range of CBCs, thus increasing the probability of identifying their EM counterparts. The analysis reveals a clear evolution in the detection capabilities of the telescopes in line with the sensitivity upgrades. Specifically, for the ZTF, I anticipate detection rates of 1^{+1}_{-1} , 2^{+3}_{-1} and 5^{+6}_{-3} for the O4a, O4b, and O5 runs, respectively. For LSST, the expected detection rates are 3^{+4}_{-2}, 8^{+11}_{-5}, and 31^{+38}_{-17} for the same runs. Meanwhile, ULTRSAT is projected to achieve a detection rate of 1^{+1}_{-1} during the O5 run. These results are highlighted in Figure 4.8, which illustrates the anticipated annual KN detection rates in different "observing scenarios". LSST excels at detecting KN events due to its enhanced sensitivity, wide spectrum coverage, advanced technology and strategic operations. This analysis highlights the importance of technological progress and strategic planning in astronomy.

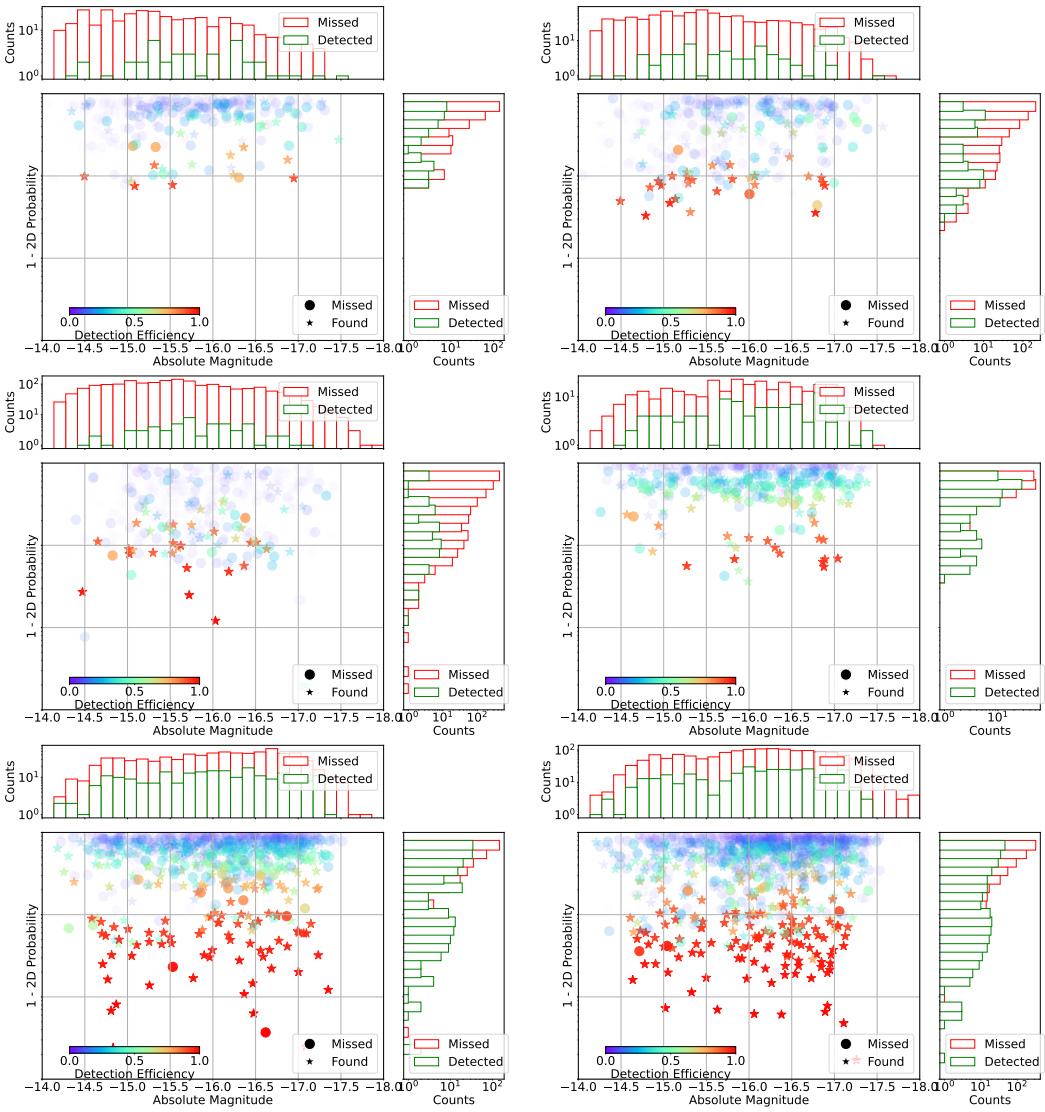

Figure 4.6: Comparative distributions of detected and missed BNS injections across observational runs by ZTF and LSST. The left panels present detections by ZTF for O4a (top), O4b (middle), and O5 (bottom) runs, while the right panels display corresponding detections by LSST. Each panel shows BNS light curves and their detection probabilities, with color bar and transparency levels representing the 3D probability of transient detection based on simulated injections. Marginalized 1D histograms above and to the right of each panel indicate the distributions of detected (in green) and missed (in red) BNS injections.

4.3.4 Analysis of EM detection efficiencies and consistency in the observational run O5

In my analysis of KNe detection efficiency, I focus on the O5 observational run, comparing it to O4a and O4b due to O5's higher KN detection rates. The study examines the non-linear relationship between observational coverage and detection probability

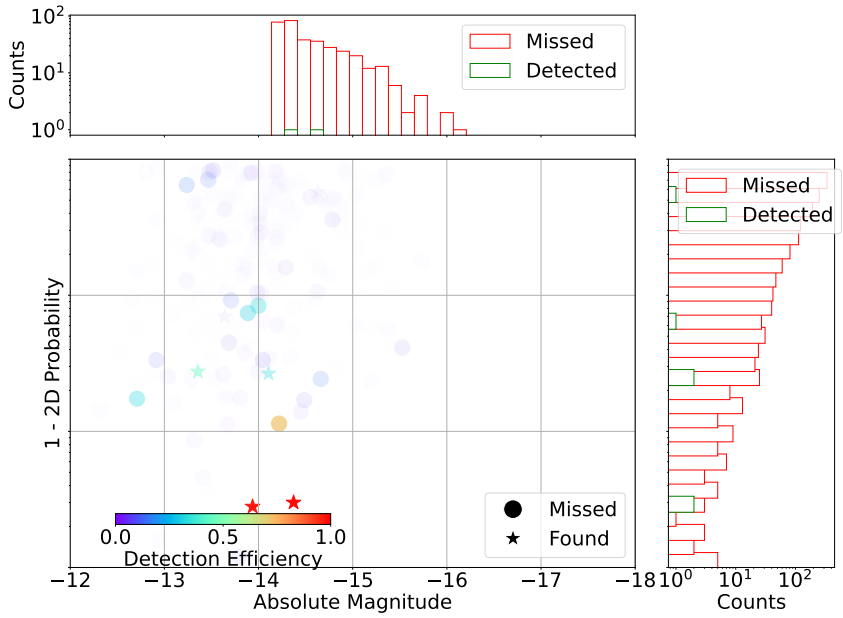

Figure 4.7: Detection performance of ULTRSAT for BNS injections during the O5 run. The plot illustrates BNS light curves alongside detection probabilities, with the color bar and transparency indicating the 3D probability of detecting transients from simulated injections. Marginalized 1D histograms above and to the right of the plot compare the distributions of detected (in green) versus missed (in red) BNS injections, highlighting ULTRSAT's observational impact.

for BNS by LSST, ZTF, and ULTRSAT. It highlights that while a strategy covering 25% of the localization area should theoretically produce detections 25% of the time, significant deviations occur, particularly when efficiencies are below 0.5. Events detected with efficiency below 0.5 are termed "inconsistencies", while those above 0.5 are "consistent". These discrepancies are marked for each observatory in the right panel of Figure 4.9, while the left panel categorizes the detections by status. This analysis emphasizes the importance of refined KN detection strategies to improve future reliability and effectiveness.

4.4 Conclusion

In this work, I focussed on optimizing EM counterpart detection for GW events, using advanced algorithms, detailed skymaps, and the capabilities of telescopes such as ULTRSAT , LSST, and ZTF. Using simulations and the gwemopt tool, I investigated EM detection rates and efficiencies (specifically KN), with LSST showing superior capabilities due to its sensitivity, spectrum coverage, and technological advancements. This analysis emphasizes the importance of strategic planning in enhancing astronomical observations and sets a foundation for future multi-messenger astronomy efforts. The findings will support the upcoming article " ULTRSAT WG2 Work Package", predicting ULTRSAT's ability to detect KN signatures during the O5 observation cam-

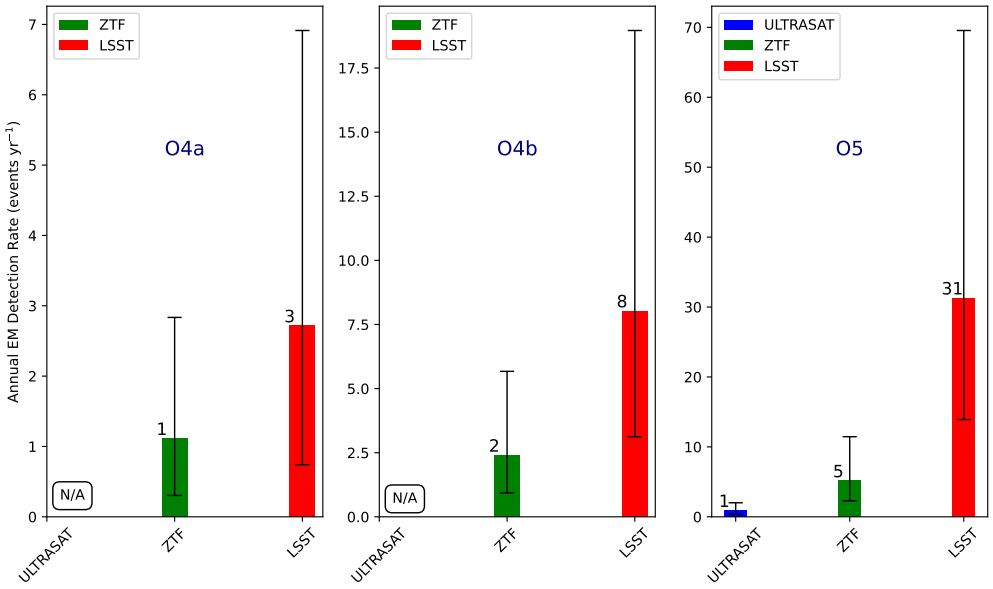

Figure 4.8: BNS Annual EM Detection Rates for LSST, ZTF, and ULTRSAT. This figure shows annual KN detection rates for BNS events by the LSST, ZTF, and ULTRSAT across observation runs O4a, O4b, and O5. The bars indicate the median EM detection rates from the GW data, and the error bars show the range of estimates. The red bars represent LSST, the green bars ZTF, and the blue bars ULTRSAT, each annotated with the median value to highlight expected annual BNS detections. The visualization illustrates the distinct detection capabilities of each observatory across different runs, reflecting the dynamic nature of BNS related transient EM event observations.

paign. The methodologies can be adapted to evaluate other telescope detection capabilities.

The ability to coordinate multiple telescopes improves precision and sky coverage, marking a significant advancement in gwemopt. With the upcoming operational status of GW detectors such as the Einstein Telescope, Cosmic Explorer and LISA, significant data management challenges will arise. Manual processing of potential EM counterparts will become impractical. Applications such as Skyportal are crucial for time-domain astronomy, facilitating the collection and analysis of telescope data alerts. Integrating multiple analysis platforms to receive and discriminate alerts about transients allows for efficient posting on Skyportal, saving astronomers time and focusing efforts on significant transients.

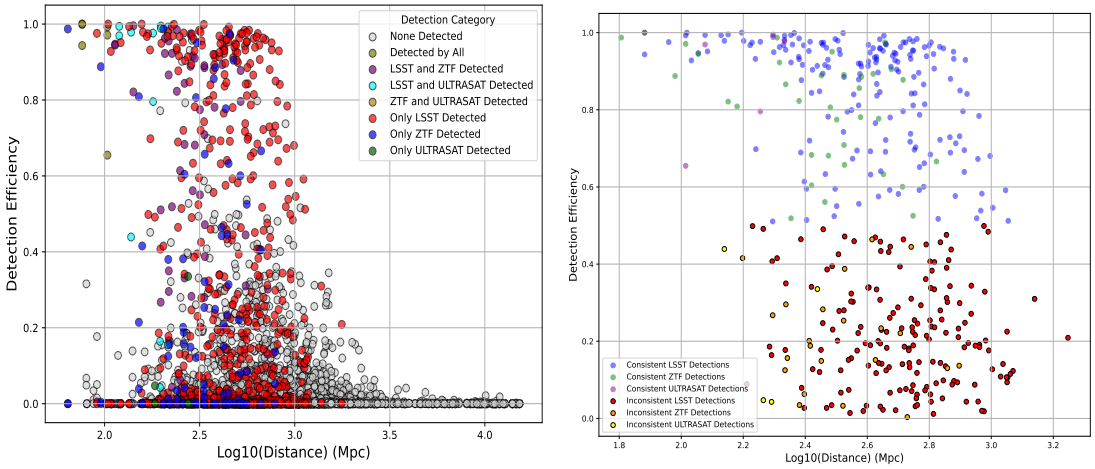

Figure 4.9: **Left:** Overview of BNS KN detection efficiencies by LSST, ZTF, and ULTRSAT during O5, colored by status. Scatter points show detection capabilities by distance, with transparency indicating the 3D detection probability from simulations. **Right:** Comparative analysis of reported and actual detection efficiencies for LSST, ZTF, and ULTRSAT. "Inconsistencies" (detection probability < 0.5), especially those with efficiencies below 0.5, are emphasized, illustrating the nonlinear relationship between coverage and detection probability, highlighting the complexity of KN detections.

Chapter 5

Real-time Analysis of the light curves of Fast-Evolving Transients

***

In this chapter, I introduce the **NMMA-SkyPortal**[1], an autonomous pipeline that combines the NMMA framework with *Fink broker* and *SkyPortal* to filter the ZTF transient alerts. Filtered alerts are displayed on *SkyPortal*, where their photometric data is analyzed using the NMMA framework. The process focuses on fitting the light curve with models for KNe, SNe Ia, SNe II,SNe Ic/Ib, and GRBs. This integration allows astronomers to efficiently prioritize the pertinent events for their studies, significantly saving time. In the context of these efforts, I have developed the *NMMA Analysis Service*, which has been integrated within *Skyportal*, to constrain and discriminate the nature of light curves. The pipeline is the first version of *NMMA Analysis Service*. My collaborators have incorporated a second version of this analysis service in *Fritz*[2]. *Fritz* serves as the scientific data platform for ZTF Phase II and ZTF-O4. The *NMMA Analysis Service* integrated into *Fritz* was used to support the scientific publication [98].

[1] https://github.com/weizmannk/nmma-skyportal
[2] https://github.com/fritz-marshal/fritz

5.1 Background

Multi-messenger astronomy, which encompasses the sophisticated detection and analysis of EM counterparts to GW events, is rapidly evolving. This field is instrumental in decoding the dynamics behind the most energetic phenomena in the universe. The ZTF [62, 142, 190, 108] plays a crucial role in this domain by conducting systematic searches for KN counterparts to BNS and NSBH merger candidates during the IGWN observing runs. It also searches for other transients, such as isolated KNe, SNe, and GRBs [139, 251, 22, 251], processing these through the *Fink Broker* [199]. This broker enhances alert capabilities by annotating them with additional data, including classifications from machine learning models. The upcoming GW observing runs, specifically O5 and LIGO/Virgo/KAGRA/LIGO-India's fifth observing run (O6), are critical to refine methods to track KNe transients, which are essential to understand *r*-process nucleosynthesis [195, 181, 84]. Given the rapid optical fading of KNe, predicted to exceed 0.3 mag/day [105], prompt and accurate identification is paramount. In this context, the next generation of telescopes, such as Rubin Observatory's LSST [156]) and ULTRSAT [259], will take on a decisive role.

SkyPortal serves as a key coordination and management tool in our GW searches. This Web application not only schedules telescopes and selects candidates for follow-up observations, but also facilitates the dissemination of results through a user-friendly interface. By integrating the **SkyPortal Fink Client**[3], we have developed the ability to ingest optical alerts from *Fink Broker* and filter them using *Fink filters*, a package designed to target specific alert types. The alerts are then added to my user group in *SkyPortal*, where each transient is assigned a unique identifier. This ensures that if the source already exists, only new photometric points are added to the existing dataset. As ZTF captures new measurements, these are uploaded to *SkyPortal* and locally downloaded for analysis by our NMMA [217] framework. This process involves fitting light curves with models of KNe, SNe, and GRBs integrated within NMMA. The results of these analyses are then reposted in *SkyPortal*, allowing group members to continually refine the nature of the light curves as new data become available. This enables users to continue or discontinue follow-up based on the event's scientific relevance to their interests.

5.2 SkyPortal

SkyPortal—SkyPortal serves as a key tool in time-domain astronomy, redefining collaborative engagement and the management of astronomical datasets (see Figure 5.1). This platform differs from traditional offline data examination methods by integrating analytical tools directly within the data management infrastructure. A notable feature of this integration is the interactive periodogram within the photometry panel, which enables detailed analysis of variable astronomical entities directly within the application

[3] https://github.com/skyportal-contrib/skyportal-fink-client

[98]. Moreover, *SkyPortal* improves access to essential photometry statistics through PhotStats, which provide summary statistics for filtering for transients. This access is supported by a comprehensive application programming interface (API), significantly improving the efficiency of data analysis. An API is a set of rules that allows different software applications to communicate, facilitating data exchange and interaction. *SkyPortal* acts as a comprehensive platform for managing and analyzing astronomical data, especially pertinent to transient phenomena and aims to be recognized as a "transient full-stack ecosystem," surpassing the traditional functionalities of a Target and Observation Manager (TOM, [283]). It integrates a wide range of features, such as telescope scheduling for observatories like ZTF and the upcoming LSST, optimizing observations, managing spatial catalogs, and performing advanced astronomical data analysis within a unified software environment. Its integration with alert brokers such as *Fink Broker* and ALerCE [132], which process and annotate optical survey alerts, ensures effective communication between alert issuers and the scientific community.

Additionally, platforms such as the Gamma-ray Coordinates Network (GCN) [262] and the Scalable Cyberinfrastructure for Multi-messenger Astrophysics (SCiMMA) [4] are integral in distributing alerts to the astronomical community. Their integration with *SkyPortal* enhances the ability of the platform to transmit important alert information quickly and efficiently, ensuring that astronomers are well prepared for timely follow-up and analysis of transient events.

Analysis platform—Recent expansions of *SkyPortal* include the integration of third-party analysis service, improving its analytical capabilities. This enhancement enables the implementation of machine learning models for transient classification and incorporates various Bayesian inference tools, such as NMMA [217], MOSFiT [143], and SNCosmo [56]. These tools are used for detailed light curve fitting and analysis, providing insights into the statistical likelihood of different models and characterizing transients. The results of these analyses are integrated into *SkyPortal* through webhooks, which improves the data set and allows detailed analysis in the application. A webhook is a user-defined HTTP callback that transmits real-time data to a specified URL when triggered by specific events. Once an analysis is completed, its results are automatically uploaded to *SkyPortal* via the webhook. I use a similar process to implement my *NMMA analysis service* within *SkyPortal*, which filters the alerts initially classified as KNe, SNe, and GRBs by *Fink Broker* to post in my *NMMA-SkyPortal* group. In the long term, this filtering will selectively focus on the potential KNe, which is of my primary interest. The photometric data from these transients are analyzed through the NMMA framework, which fits their light curves to different models and provides calculations on Bayesian factors. In the end, these results are reposted in the *NMMA-SkyPortal* group. This process of analyzing follow-up photometry will repeat as often as new data from the same object are captured.

[4] https://scimma.org

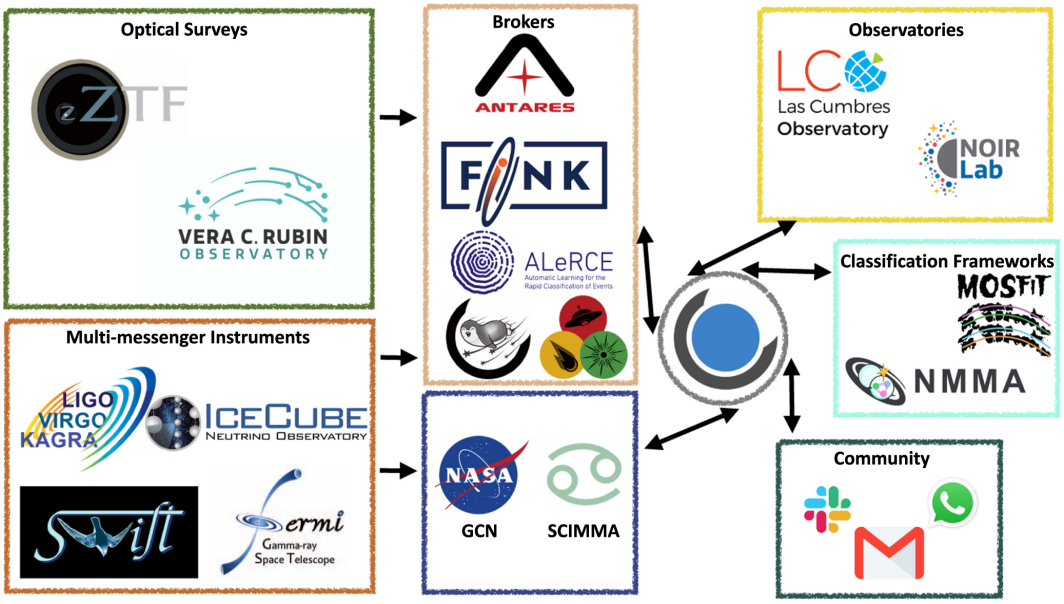

Figure 5.1: A schematic representation of the *SkyPortal* ecosystem from [98], showcasing its interconnectivity with various optical surveys, brokers, observatories, classification frameworks, multi-messenger instruments, and the broader astronomical community. This diagram exemplifies the integral function of *SkyPortal*as a nexus for managing and analysing data in the dynamic domain of time-domain astronomy.

5.3 Transient selection and analysis framework

The ability to efficiently filter and analyze alerts from large-scale optical surveys is crucial for time-domain astronomy. My approach uses the services of the *Fink Broker* to process the ZTF data. As an alert broker, Fink[5] serves as an intermediary between alert issuers and the scientific community, in this case, me, providing tools for efficient analysis of alert data from telescopes and surveys. The Fink filter[6] package , which is open-source, collects and stores alert data from large astronomical surveys, enhancing them with additional information from other catalogs, and applies machine learning techniques to classify events. This enriched data are then redistributed for further scientific analysis and potential follow-up observations. Fink is recognized among Rubin Observatory community brokers for its commitment to community-driven development, adherence to open source principles, and integration of the latest advances in big data and machine learning technologies. Using Fink's sophisticated infrastructure, I pinpoint promising candidates from the ZTF alert require further examination. These candidates are then processed through the **SkyPortal Fink Client**[3], which integrates my selection criteria for transients as detailed in Section 5.3.1. The API of *SkyPortal* interacts with Fink at five-second intervals, ensuring timely updates. Alerts fetched by the **SkyPortal Fink Client** include a unique object identifier, which facilitates the creation of new candidates or the updating of existing sources in the database [31]. If the

[5] https://skyportal-fink-client.readthedocs.io
[6] https://github.com/astrolabsoftware/fink-filters

source already exists, only the new photometric data are added. This smooth communication between the *Fink Broker* and my *SkyPortal* environment continues as long as the process is active, which is useful for updating previously recorded alerts and for real-time detection of new events. The selected alerts undergo detailed analysis within the NMMA framework [217]. This analysis yields outputs such as Bayes factors and corner plots estimating transient parameters that help discern the nature of light curves from implemented models, in my case, SNe, KNe, and GRBs. *SkyPortal*'s API reposts updates each time new simulations are performed, enabling interested astronomers to refine their decision making based on these results [283, 98].

Note: The integration of the *Fink broker* into our workflow is essential to filter the ZTF alerts to identify the most promising targets, thus optimizing telescope follow-up time and research examination.

5.3.1 Target identification and selection

My selection criteria are designed to capture a broad spectrum of transient phenomena within the observational capabilities of the ZTF, classifying them on the basis of unique characteristics and detection methodologies. I prioritize early SN Ia candidates (`early_sn_ia_candidates`), KN candidates identified through advanced machine learning techniques (`kn_candidates`), and those exhibiting rapid decay rates exceeding 0.3 mag/day (`rapid_decay_kn_candidates`). Moreover, I include orphan GRBs (`orphan_grbs`). Figure 5.2 shows my process to poll the Fink alert pool in *SkyPortal*. This focused approach significantly improves the efficiency and specificity of my transient selection process, which is crucial for isolating events suitable for a comprehensive NMMA framework. In *SkyPortal*, I have designated a group named *NMMA-SkyPortal* for collaborative follow-up and analysis. Members of this group aim to monitor and quickly access information on specific alerts filtered from the Fink broker to the `SkyPortal` platform as shown in Figure 5.3. They can then download the data and perform their own analyses. Upon receiving an alert that meets our filters, the transient is posted directly to *SkyPortal* in the *NMMA-SkyPortal* group section. Based on the relevance of the event, members of the group can share significant events of high relevance with other groups within *SkyPortal*. This sharing enables collaborative studies and improves data quality, enhancing our collective research capabilities.

In cases where an astronomer interested in using the NMMA framework to analyze a specific event is not a member of the *NMMA-SkyPortal* group or has needs not addressed by my analysis pipeline, an alternative implementation of *NMMA analysis service* is available within *Fritz*. This service operates on principles similar to mine, but has slightly different goals by enabling the analysis of light curves from optical telescopes within the *SkyPortal* ecosystem and includes SNCosmo [56] among other tools. Unlike the automated process within *NMMA-SkyPortal*, this service provides the advantage of a user interface, which allows those who may not be familiar with the methodologies of NMMA and SNcosmo to use these tools. They can refine their understanding of the light curve of a specific event and plan appropriate follow-up actions.

```
2024-04-12 08:40:55 fink: Fink Taxonomy posted with id 3
[08:40:55 fink] Fink Taxonomy posted with id 3
2024-04-12 08:40:58 fink: Received alert from topic fink_sn_candidates_ztf with classification SN candidate
[08:40:58 fink] Received alert from topic fink_sn_candidates_ztf with classification SN candidate
2024-04-12 08:41:00 fink: Candidate with source: ZTF24aaemydm, classified as a SN candidate added to SkyPortal
[08:41:00 fink] Candidate with source: ZTF24aaemydm, classified as a SN candidate added to SkyPortal
2024-04-12 08:41:00 fink: Received alert from topic fink_sn_candidates_ztf with classification SN candidate
[08:41:00 fink] Received alert from topic fink_sn_candidates_ztf with classification SN candidate
2024-04-12 08:41:01 fink: Candidate with source: ZTF24aahjkdw, classified as a SN candidate added to SkyPortal
[08:41:01 fink] Candidate with source: ZTF24aahjkdw, classified as a SN candidate added to SkyPortal
2024-04-12 08:41:01 fink: Received alert from topic fink_sn_candidates_ztf with classification SN candidate
[08:41:01 fink] Received alert from topic fink_sn_candidates_ztf with classification SN candidate
2024-04-12 08:41:02 fink: Candidate with source: ZTF24aailpdv, classified as a SN candidate added to SkyPortal
[08:41:02 fink] Candidate with source: ZTF24aailpdv, classified as a SN candidate added to SkyPortal
2024-04-12 08:41:02 fink: Received alert from topic fink_sn_candidates_ztf with classification SN candidate
[08:41:02 fink] Received alert from topic fink_sn_candidates_ztf with classification SN candidate
2024-04-12 08:41:03 fink: Candidate with source: ZTF24aahznqd, classified as a SN candidate added to SkyPortal
[08:41:03 fink] Candidate with source: ZTF24aahznqd, classified as a SN candidate added to SkyPortal
2024-04-12 08:41:03 fink: Received alert from topic fink_sn_candidates_ztf with classification SN candidate
[08:41:03 fink] Received alert from topic fink_sn_candidates_ztf with classification SN candidate
2024-04-12 08:41:05 fink: Candidate with source: ZTF24aaivfjo, classified as a SN candidate added to SkyPortal
[08:41:05 fink] Candidate with source: ZTF24aaivfjo, classified as a SN candidate added to SkyPortal
2024-04-12 08:41:05 fink: Received alert from topic fink_sn_candidates_ztf with classification SN candidate
[08:41:05 fink] Received alert from topic fink_sn_candidates_ztf with classification SN candidate
2024-04-12 08:41:07 fink: Candidate with source: ZTF24aajgmzr, classified as a SN candidate added to SkyPortal
[08:41:07 fink] Candidate with source: ZTF24aajgmzr, classified as a SN candidate added to SkyPortal
2024-04-12 08:41:07 fink: Received alert from topic fink_sn_candidates_ztf with classification SN candidate
[08:41:07 fink] Received alert from topic fink_sn_candidates_ztf with classification SN candidate
2024-04-12 08:41:09 fink: Candidate with source: ZTF24aaemydm, classified as a SN candidate added to SkyPortal
[08:41:09 fink] Candidate with source: ZTF24aaemydm, classified as a SN candidate added to SkyPortal
```

Figure 5.2: This screenshot illustrates the utilization of *Fink broker*'s API to filter and select potential KNe, SNe, and GRB afterglow candidates from the ZTF alerts. The process efficiently identifies and streams classified transient events into *SkyPortal*for monitoring and further investigation. In this excerpt, the system is specifically polling for SNe events, as indicated by the recorded classifications.

5.3.2 Navigating within Skyportal

The *Skyportal* platform uses numerous tools to facilitate navigation and provide rapid access to information on specific transients. This capability is essential for individuals planning observations or for collaborative groups, such as GRANDMA [51]. GRANDMA uses this platform to receive alerts from various collaborations, including IGWN, GCN [262], and instruments such as the ZTF, with the goal of following multi-messenger transients. Figure 5.4 displays the interface that provides detailed information about the transient **ZTF24aaemydm**, initially classified by *Fink Broker* as a potential candidate for SN. **ZTF24aaemydm** has Users can track this candidate to monitor its evolution through additional observations with other instruments or utilizing photometric or spectroscopic data from ZTF observations accessible via *Skyportal*, as depicted in Figure 5.5.

Subsequently, fitting these data with SN, GRB, or KN models can confirm the initial classification or lead to a reclassification based on new insights. This process of classification refinement is the primary focus of my work. In addition, *Skyportal* includes sections for user-generated summaries and comments on transient events. As data acquisition from telescopes and results compiled through the *NMMA analysis service* are updated in the group, members can comment and add relevant information, contribute insight to improve understanding of the evolving transients.

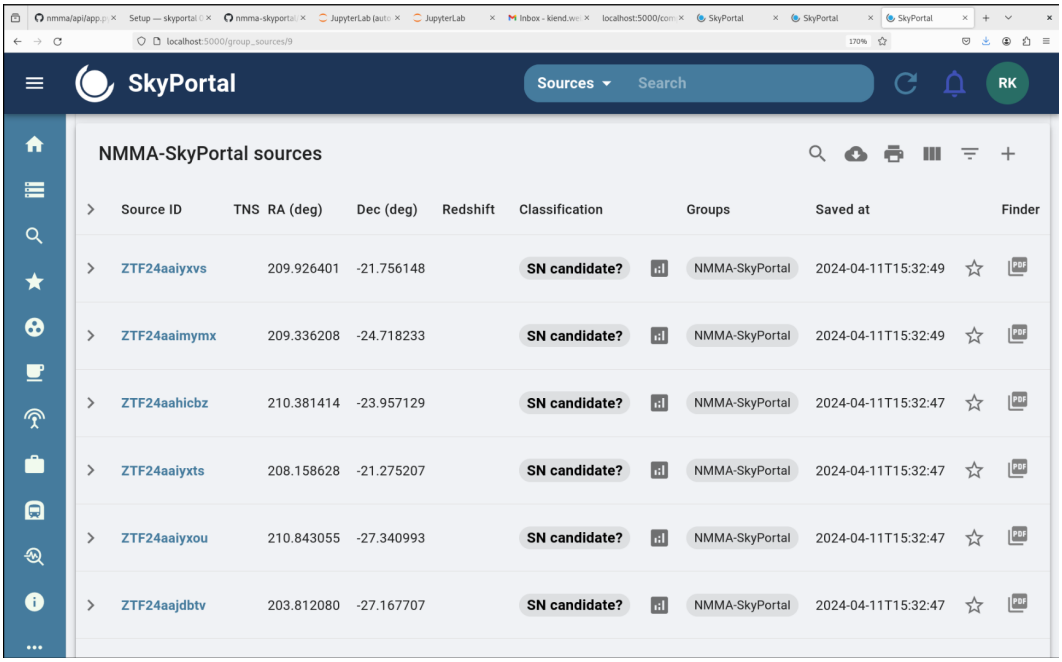

Figure 5.3: The *NMMA-SkyPortal* group's interface within *SkyPortal*, displaying ZTF alerts that have been filtered according to predefined criteria. The table lists SN candidates with essential details such as Source ID, RA, Dec, Redshift, and Classification. This interface underpins our strategy for the rapid identification and further investigation of transient phenomena, enabling members to efficiently download and analyse data.

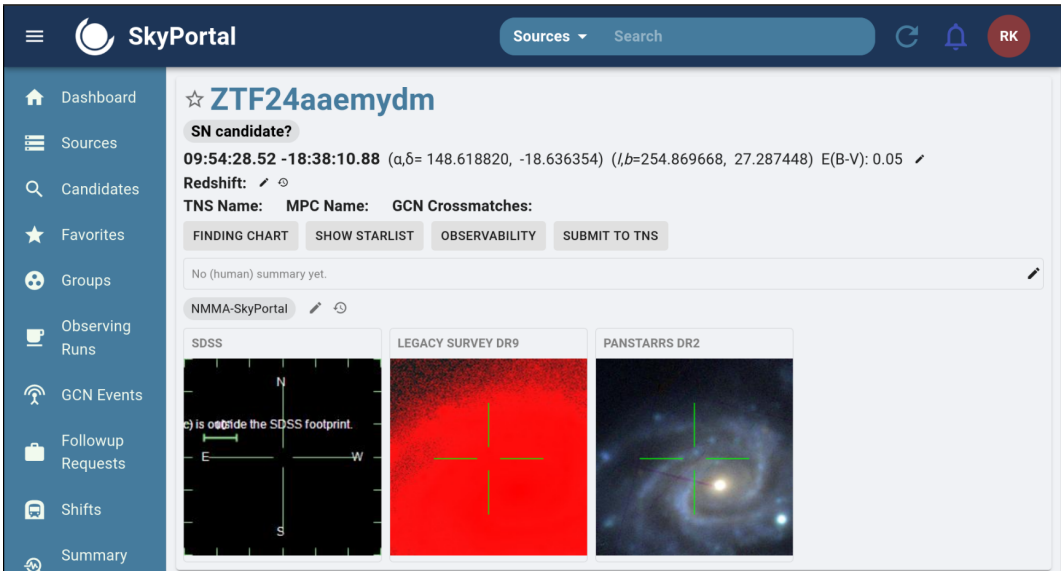

Figure 5.4: *Skyportal* interface showing detailed information on the transient **ZTF24aaemydm**, highlighting the tools available for follow-up observations and data analysis.

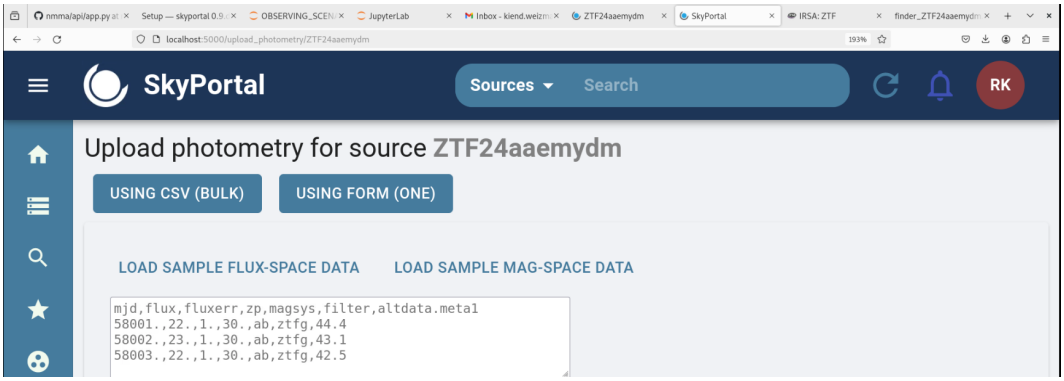

Figure 5.5: Interface of *Skyportal* for uploading photometry data, illustrating the method for tracking transient **ZTF24aaemydm** using observational data to confirm or reclassify its nature.

5.3.3 Model integration and simulation refinement

Within the NMMA framework, we integrate specific models for the interpretation of identified transient events, including KNe, SNe, and GRBs. For KN candidates, the `Bu2019lm` model from POSSIS [75, 114, 77] is utilized, which spans the parameter spaces for BNS mergers (`Bu2019lm` model) and NSBH mergers (`Bu2019nsbh` model). The afterglows of the GRB are modeled with the `TrPi2018` model, integrated into the `afterglowpy` toolkit[7] [276]. Additionally, we apply SN models such as `Piro2021` for Shock Cooling SNe [226] and `nugent-hyper` for SNe Ic/Ib [179], allowing for precise characterization of their evolving light curves. Each new observation from ZTF allows me to refine my analyses, thereby increasing the scientific utility of the data for the multi-messenger astronomy community and optimizing the allocation of resources for follow-up observations. The results of these model fits are promptly posted on *SkyPortal*, facilitated by the robust process supported by Tornado[8]. This system improves the real-time data processing capabilities of `SkyPortal`, efficiently managing persistent connections and enabling live updates essential for such a collaborative platform.

My primary objective within the *NMMA analysis service* pipeline is to inform the interested about the probable nature of a transient, rather than to definitively classify it. "Human" intervention is often essential, particularly when light curves suggest multiple phenomena. An example of such a case is the transient event ZTF21abotose, discussed in Chapter 2, which initially exhibited characteristics of both KNe and SNe. In NMMA analysis, the early light curve of ZTF21abotose matched the shock cooling model (`Piro2021`) and GRB afterglow model (`TrPi2018`). However, a subsequent detailed spectroscopic analysis later confirmed it as SN IIb. Although our predictions based on model selection are often accurate, a deeper examination of the data and additional considerations are necessary to fully ascertain the nature of a transient. The ability to discern the nature of numerous light curves based on our model selections remains one of the most effective ways to enable astronomers to save time by quickly

[7] https://github.com/geoffryan/afterglowpy
[8] https://github.com/tornadoweb/tornado

determining the relevance of a transient alerted by Fink according to their specific research interests.

5.3.4 Data analysis and framework integration

The methodology uses the *Fink broker* API to filter and retrieve ZTF alerts for targeted transients. Once new candidates are detected within our specified classifications are detected, they are promptly uploaded to `SkyPortal` via its API. Upon reaching *SkyPortal* with all the additional information, only the photometry table is downloaded in CSV format and adapted to the structure of the NMMA framework for analysis. My environment setup is in an "AST200029" allocation (PI Coughlin) of **Jetstream2** at Indiana University. This local support facilitates the analysis process with NMMA, particularly in the adjustment of the light curve. This process provides essential data on the transient detection times and characteristics. The results of these analyzes, such as Bayes factors and light curve adjustments, are shared via *SkyPortal*. This procedure is repeated as often as new data are collected on the same event and is applied to all models integrated into the NMMA framework.

As a test case, I present the fit of the transient **ZTF24aaemydm**, initially classified as a potential SN event, using four light curve models. This transient, revealed by Fink alerts, was detected on 2024-02-12 06:07:57.999 UTC, with a redshift of $z = 0.0126$ corresponding to a luminosity distance of 56.37 Mpc. The subsequent classification revealed it as a SN II event with a probability of 0.91. The models tested include KN model `Bu2022Ye`, displayed in Figure 5.6, SN Ic/Ib `nugent-hyper` shown in Figure 5.7, the `TrPi2018` (GRB) depicted in Figure 5.8, and `Piro2021` (Shock Cooling) shown in Figure 5.9.

Kilonova model—As illustrated in Figure 5.6, the fit of **ZTF24aaemydm** using the `Bu2022Ye` model diverges significantly from the photometric data in the early observations, excluding the possibility of this event being associated with a KN. Astronomers interested in such phenomena can ignore this event from further follow-up efforts after the initial detections.

Type Ic/b Supernova—When fitting the `nugent-hyper` model, although there is compatibility with the zfi-band, it does not align well with the other bands over time. By the second day, those searching for SN Ic/Ib events can redirect their focus to more promising targets, while maintaining a minimal watch on this one, as shown in Figure 5.7.

GRB afterglow—Using `TrPi2018` with **ZTF24aaemydm** shows good fits in the zfg and zfr-bands but slight divergence with the zfi-band. However a quick analysis shows an early rise in brightness followed by a slight plateau and then a gradual decrease as presented in Figure 5.8, which is not aligned with a typical afterglow behavior, where the fading is pronounced and follows a power law decay, so this is not a GRB.

Shock cooling—The `Piro2021` model provides an excellent fit across all three

ZTF filters, facilitating those interested in Shock Cooling event to focus their follow-up efforts and potentially organize their own observation campaigns from the first detection. Figure 5.9 confirms this alignment. Indeed, observing the rapid ascent of the light curve from 18.2 to a peak of 15.6 within just two days indicates the characteristics of a SN II, yet the subsequent swift decline without a prolonged plateau implies a transition to a SN IIb. In conclusion, **ZTF21aaemydm** is an example of Shock Cooling within a SN IIb supernova.

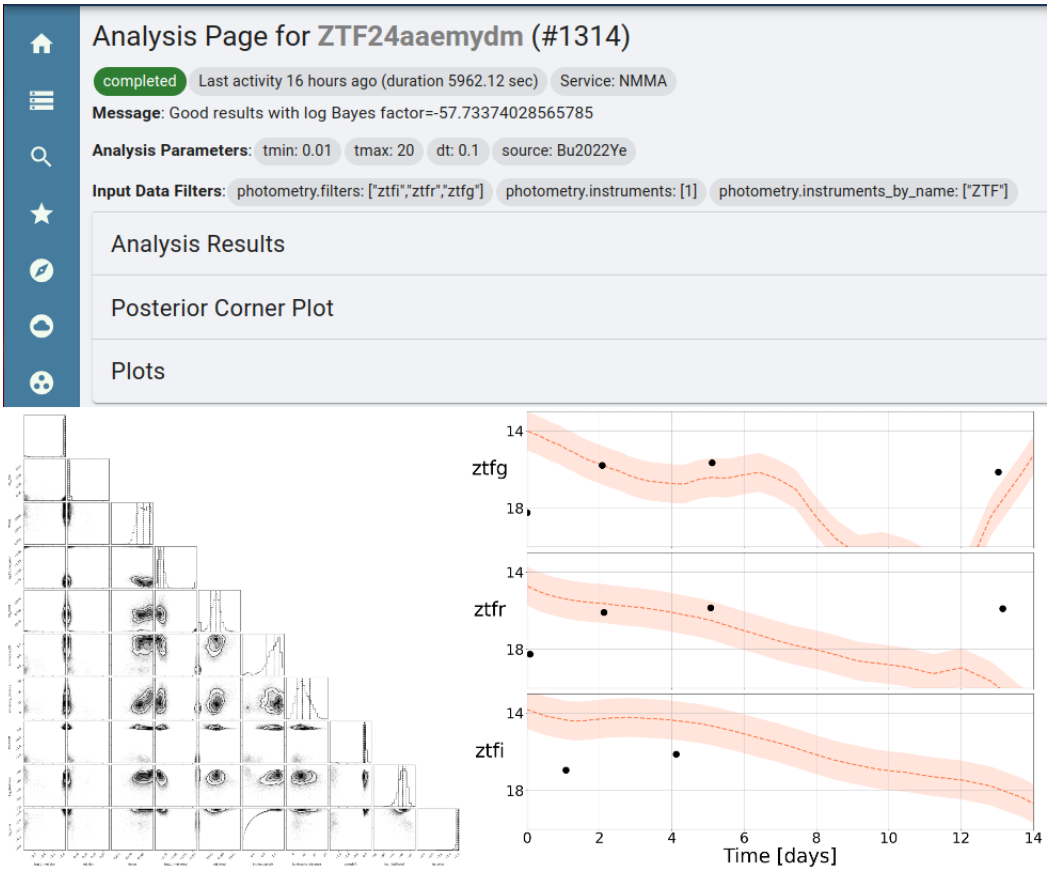

Figure 5.6: Plot of **ZTF24aaemydm** event using the `Bu2022Ye` model, with a Bayes factor log of -57.73, showing $ztfg$, $ztfr$ and $ztfi$-bands data. Displays observed magnitudes (black dots), theoretical model (dashed line), and confidence intervals (shaded orange).

5.3.5 ChatGPT integration in SkyPortal

SkyPortal allows users to add comments, enhancing the understanding of transients and their histories. A significant challenge for users, who deal with hundreds or thousands of active events, is keeping current with the knowledge and activities associated with each event. To address this, *SkyPortal* employs **ChatGPT** models to generate and display concise summaries at the source level [98], providing quick insights. It

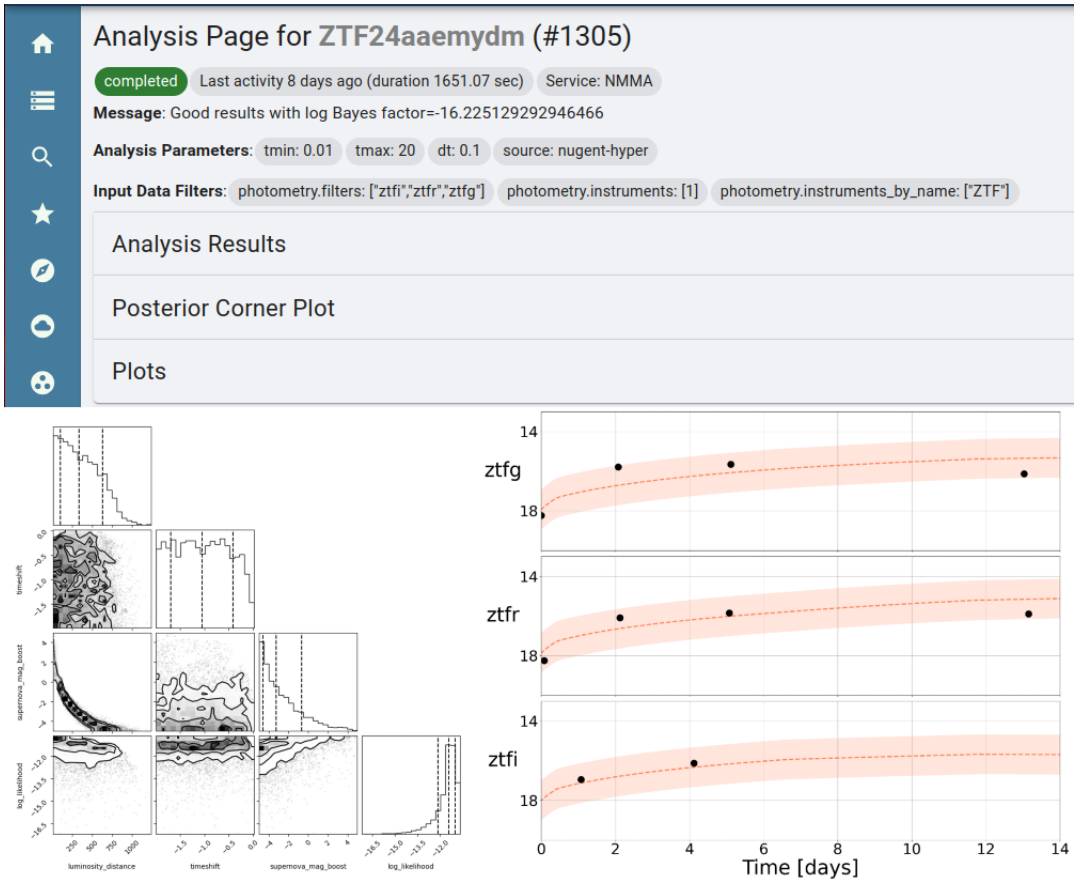

Figure 5.7: Plot of **ZTF24aaemydm** event using the `nugent-hyper` model, with a Bayes factor log of -16.22, showing $ztfg$, $ztfr$ and $ztfi$-bands data. Displays observed magnitudes (black dots), theoretical model (dashed line), and confidence intervals (shaded orange).

features a pre-configured service through the OpenAI API (`openai.ChatCompletion`) that provides summaries, including redshift and classifications. The default model is `gpt-3.5-turbo`, with an option to switch to the slower `gpt-4`. I applied this method to **ZTF24aaemydm**, as shown in Figure 5.10.

5.4 Conclusion

This study has facilitated the integration of significant astronomical analysis platforms, *Fink Broker* for transient filtering, *SkyPortal* for displaying these alerts, and NMMA for analysis services. The results, retrieved through the *SkyPortal* web page, enhance scientific processing by providing real-time updates on the evolution of a specific transient. This gives astronomers the flexibility to follow-up the event or to shift their focus to more promising targets. The pipeline is not intended to replace the foundational work of a researcher but rather to assist in planning his time and to allow real-time interaction with other colleagues through comments enabled within *SkyPortal*.

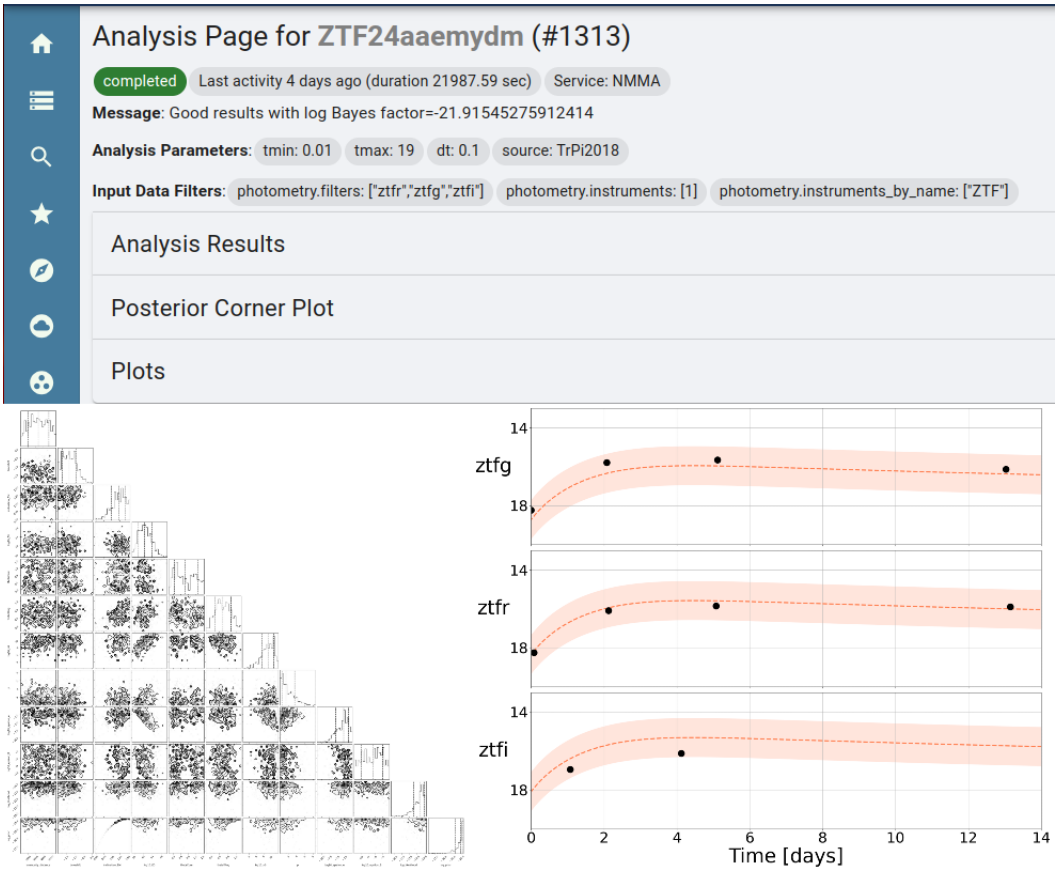

Figure 5.8: Plot of **ZTF24aaemydm** event using the `Trpi2018` model, with a Bayes factor log of -21.9, showing $ztfg$, $ztfr$ and $ztfi$-bands data. Displays observed magnitudes (black dots), theoretical model (dashed line), and confidence intervals (shaded orange).

In the short term, I want to optimize my analysis pipeline to cut computational costs. In the long term, we should consider preserving initial analyses to integrate these when new detections are made by the ZTF or future telescopes. The `TrPi2018` model, used for GRBs, requires up to seven hours per simulation, significantly delaying the results after each photometric update and hampered the real-time analysis. Enhancing this process will allow for the integration of the Rubin Observatory when it comes online alongside the ZTF, thus focusing exclusively on potential KN related alerts.

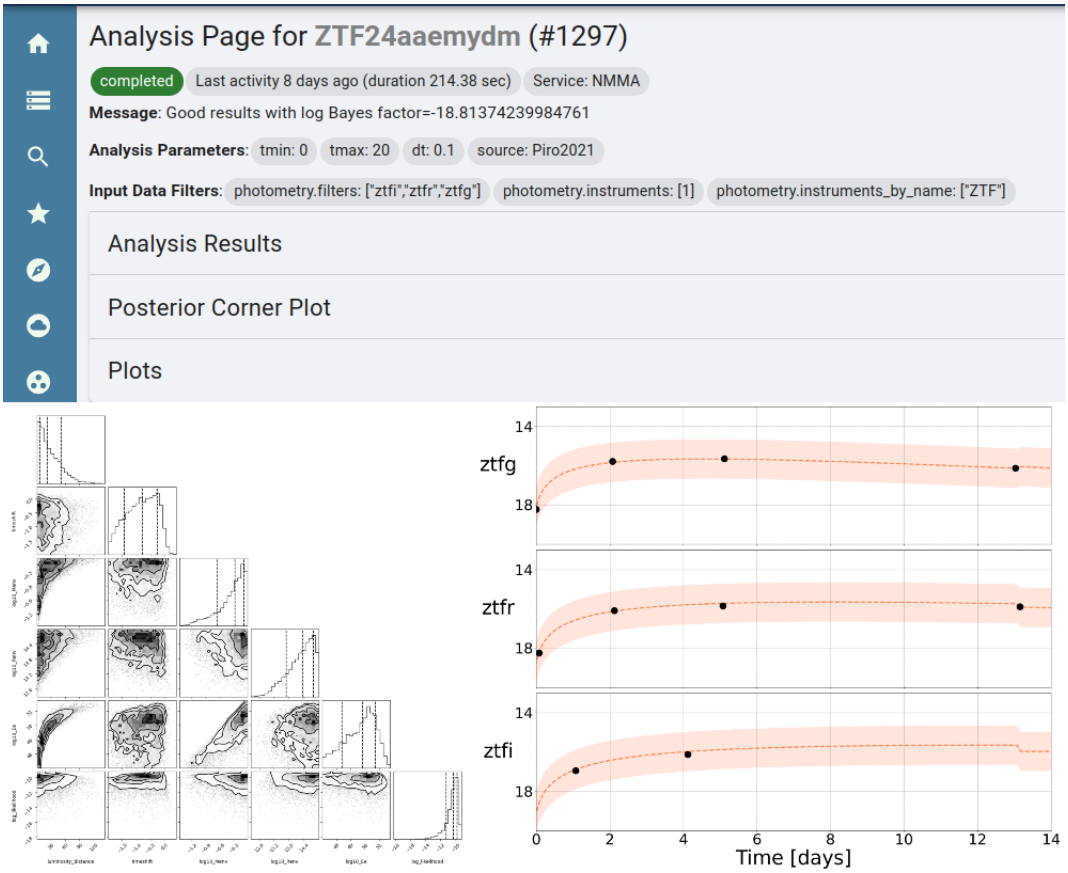

Figure 5.9: Plot of **ZTF24aaemydm** event using the `Piro2021` model, with a Bayes factor log of -18.81, showing $ztfg$, $ztfr$ and $ztfi$-bands data. Displays observed magnitudes (black dots), theoretical model (dashed line), and confidence intervals (shaded orange).

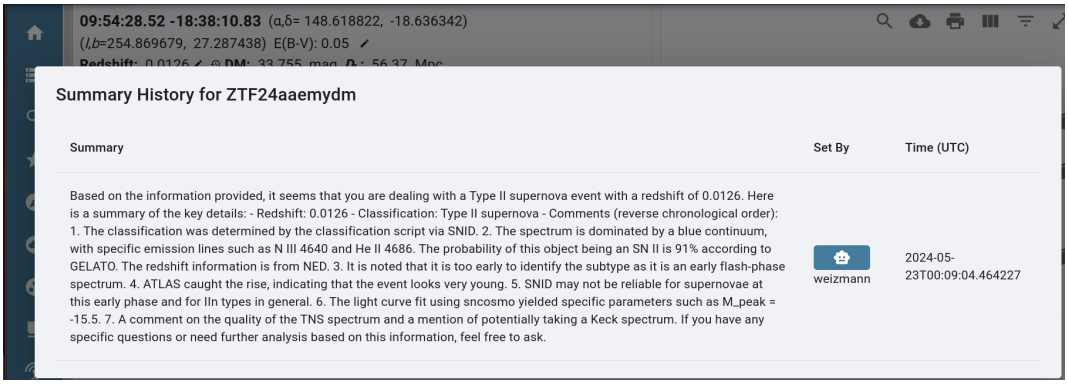

Figure 5.10: AI-generated summary of the event using the ChatGPT 3.5 completion service on **ZTF24aaemydm**, whithin *Skyportal*.

Chapter 6

DeepClean: *non-linear* Regression for Noise Reduction in the Virgo Detector

***

In this chapter, I detail my work on noise reduction in the Virgo detector, conducted as part of my PhD thesis, as a member of the Virgo collaboration, which comprises 129 institutions in 16 different countries, representing Burkina Faso, the first African country in the Virgo collaboration. This work involves the first and only analysis of the Virgo data using *DeepClean*. These efforts were made possible through the suggestions, recommendations and support of the Virgo DetChar and the LIGO DetChar groups. The results of this study will be published in a journal and are documented in Kiendrebeogo et al. 2024 (in preparation).

6.1 Background

GW events, such as GW150914 [23], GW170817 [24], and GW200105 [20], among others, have significantly improved our understanding of compact binary system mergers. However, many potential GW signals remain undetected, awaiting the successful mitigation of some noise sources. Several factors contribute to the noise, which is a combination of environmental noise, instrumental artifacts, quantum sensing noise, thermal fluctuations, and other unknown sources. The intricate interactions of these factors make it difficult to clearly discern GW signals [1]. Thus, identifying additional GW signals below the detection threshold is related to our ability to mitigate or subtract noise within the detectors, thus improving sensitivity. The Virgo detector, employing a Michelson-type interferometer with 3km long perpendicular arms (L = 3km), detects GW induced length changes. GWs cause space-time perturbations, altering length measurements and resulting in a GW strain of approximately $h \sim \frac{\Delta L}{L} = 10^{-21}$. Noise and sensitivity directly influence our ability to extract information from GW signals. As we progress in our noise reduction efforts in the detectors, we expect to uncover CBCs or other signals that would otherwise have remained hidden. The most recent update to the observation scenarios, as described in kiendrebeogo et al. 2023[163], reveals that approximately 0.83% of the CBC injected from the PDB/GWTC-3 distribution [25] have successfully met the detection threshold, set to S/N of 8. To improve S/N, both the LIGO [184] and Virgo [29] record several thousand of witness channels (probes and sensors). These witness channels independently measure noise from various sources. Some of them collect data to characterize environmental noise sources that couple with the GW readout channel and could subsequently be subtracted.

However, it is important to acknowledge that while noise subtraction methods, such as Wiener filtering, are widely used and perform perfectly, they face challenges in the presence of *non-stationary* noise. Furthermore, *non-linear* noise, arising from systems in which the output is not directly proportional to the input, creates complex and unpredictable noise patterns. This non-linearity can be due to a multitude of factors, including intricate physical processes within the detector or environmental influences [116]. On the other hand, *non-stationary* noise is characterized by its statistical properties that change over time, adding a layer of complexity to data analysis and signal processing. The dynamic variability of this noise type makes it particularly challenging to model and subtract from the data.

To meet this challenge, the *DeepClean* infrastructure has been developed to analyze the data generated by interferometers (IFO) when detecting GWs [215, 249]. *DeepClean* is designed as a 1D convolutional neural network (CNN) that uses witness sensors to estimate and subtract *non-linear* and *non-stationary noise* from GW data. This approach ensures that the astrophysical signal is preserved while improving the S/N, thus improving the reliability of GW signal detection.

Moreover, regarding the Virgo detector, it is worth noting that most electromagnetic noise comes from electrical sources, reaching their peak at the 50 Hz power line frequency. This electrical noise induces modulations in the main GW signal, leading to

the generation of symmetric sidebands around 50 Hz. During O3 observations, a feed-forward loop process was used to remove the Virgo mains and its associated sidebands, which affected the Virgo detector [37]. The importance of low frequency sensitivity in detectors is highlighted when it comes to the detection of high-mass binary mergers, as these systems typically undergo mergers at low frequency. Many GW signals may be hidden in noise, yet they become accessible for detection when noise is adequately minimized. As a result, the optimization of the scientific potential of IGWN detectors, especially in terms of enhancing pre-merger signal detectability, requires the effective implementation of noise reduction strategies.

6.2 Noise

6.2.1 Noise sources in GW readout signal

The GW readout is the process of detecting and interpreting changes in the output signal of the interferometer, measured primarily as differential arm length (DARM). This measurement of DARM represents the variations in the relative lengths of the instrument's arms caused by the presence of GW. However, in the absence of a GW, the output may show fluctuations due to various factors that contribute to the noise of the system, including fundamental, technical and environmental sources. These noise sources contribute with different and time-varying characteristics in amplitude and frequency. Noise components are crucial to understanding and improving the performance of the Virgo detector in identifying authentic GW signals [27, 74]. The **fundamental noise** includes inherent limitations of detector design materials and quantum mechanics. The thermal noise in the mirror coatings is a fundamental noise through the sensitivity in the 60-300 Hz. **Environmental noise** covers external influences like *seismic noise*, *atmospheric noise*, *external thermal fluctuations*, and *Newtonian noise*. **Technical noise** come from the design and operational aspects of the detector. Only non-fundamental noise can be subtracted. Thus, I prioritize mitigating measurable environmental and technical noise. Through the classification of noise into removable and non-removable categories, my objective is to enhance the sensitivity and accuracy of GW detectors, ensuring a clearer distinction between real GW signals and noise artifacts.

6.2.2 Noise reduction techniques

Noise reduction in GW detectors improves signal detectability and astrophysical analysis. Neural networks emerge as the leading approach due to their adaptability and robustness in managing complex data.

Wiener filtering—This is a fundamental filtering technique that is effective when the noise is *stationary*. It aims at minimizing the mean square error between estimated and true signals [286]. Its robustness is evident in GW event analysis by IGWN [2]. However, its performance declines with *non-stationary* and *non-linear* noise in

GW detectors, driven by complex environmental and instrumental fluctuations. This highlights the need for adaptive noise reduction strategies in GW astronomy.

NonSENS: Non-Stationary Estimation of Noise Subtraction—NonSENS offers an advanced method for identifying and removing *non-stationary* noise in GW detectors. It effectively handles noise from slow interferometer movements like angular fluctuations, which challenge traditional methods. Using witness signals to monitor noise changes, NonSENS achieves a stable, parametric noise subtraction, overcoming the complexities that impede standard noise reduction techniques, including those using deep neural networks (DNNs), which suffer from complex training and interpretability issues [279].

Adaptive Feed-Forward—The Feed-Forward technique in AdVirgo's. It applies directly to the primary detection channel (DARM), using a phase of the Uninterruptible Power Supply (UPS) as the witness channel. The technique measures the 50 Hz noise via the UPS, adjusts gain and phase to match DARM's noise, and uses a 50 Hz resonant filter to focus the correction on the target frequency. The adjusted signal is then used to counteract the 50 Hz noise in DARM. This method is adaptive and dynamically adjusts to noise variations for effective noise cancellation [37].

DeepClean approach–*DeepClean* uses CNNs to improve noise reduction in GW data analysis, processing strain readouts from GW interferometers, which include astrophysical signals and detector noise [215]. Its main objective is to reduce noise, enhancing the detectability of astrophysical signals at optimal S/N. *DeepClean* differentiates between witnessed and non-witnessed noise, utilizing witness sensors to monitor environmental and instrumental noise. The CNN models noise with trainable weights, capturing *non-linear* and *non-stationary* noise dynamics typical in GW interferometry. *DeepClean*'s architecture features a symmetric auto-encoder with multiple downsampling and upsampling layers, tailored to the sampling frequency and witness channel count. This configuration enables noise prediction across different data dimensions and uses batch normalization and tanh activation functions to boost generalization. The training minimizes a loss function based on the noise spectrum ratio of cleaned to original strain across all frequency bins. This approach allows *DeepClean* to effectively manage complex noise situations, significantly improving upon traditional methods like Wiener Filtering and Adaptive Feed-Forward, and complements machine learning algorithms like NonSENS [279].

As shown in Figure 6.1, architectures like *DeepClean* feature layers of nodes linked by weighted paths that process signal information [215]. Each node outputs a weighted sum of inputs, typically through an activation function. In the context of GW data analysis, such architectures are essential to distinguish noise from astrophysical signals in GW data analysis.

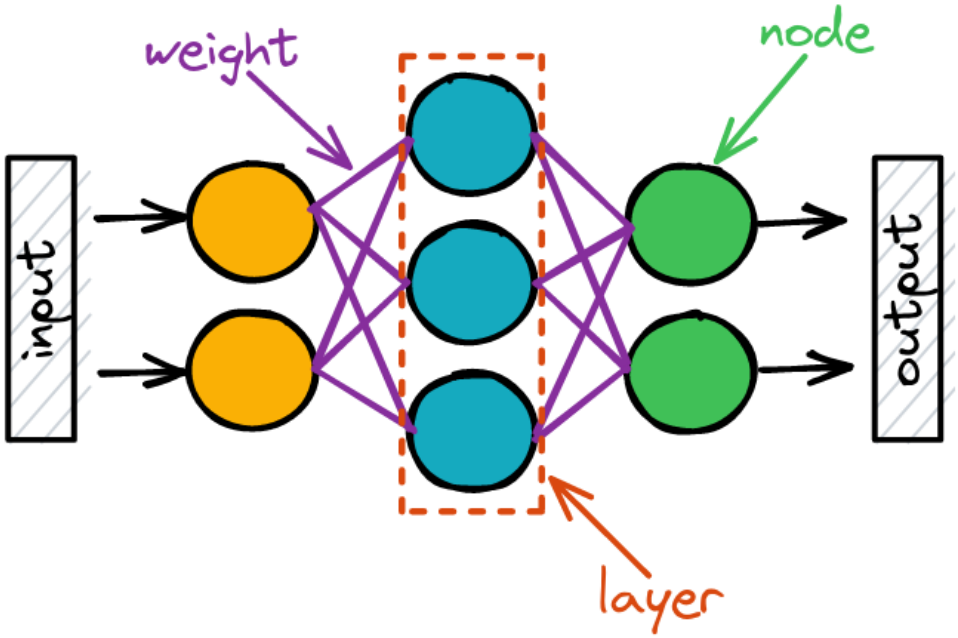

Figure 6.1: Schematic of a neural network that transmits information. The diagram illustrates the structural components that include the input nodes (gray), the hidden layers (blue), and the output nodes (green). The interconnections between nodes represent synaptic weights (purple), and the orange line marks the boundary of a single layer within the network. This simplified diagram illustrates the flow and processing of information through the network. Credit: Deep Learning Dictionary SYLLABUS.

6.3 Method

6.3.1 Mathematical formulation

In GW detection, the readout signal $h(t)$ is assumed to be:

$$h(t) = s(t) + n(t), \tag{6.1}$$

where $s(t)$ denotes potential astrophysical signals and $n(t)$ is the detector noise, including both intrinsic disruptions $n_{NR}(t)$, which are unalterable, and external noise $n_R(t)$, originating from environmental and technical factors:

$$n(t) = n_R(t) + n_{NR}(t). \tag{6.2}$$

To improve the sensitivity of GW detectors, LIGO and Virgo use thousands of autonomous auxiliary witness sensors to monitor removable noise components $n_R(t)$. These auxiliary sensors record independent instances of noise, enabling the classification of noise into two distinct groups: witnessed and non-witnessed noise. Witnessed noise, in particular, is the removable noise, while non-witnessed noise constitutes the

non-removable noise or noise not recorded by some witness auxiliary sensors. The *DeepClean* system, leveraging data from these witness sensors, forecasts and subtracts noise to enhance the analysis of astrophysical signals [215]. A neural network function $\mathcal{F}(w_k;\vec{\theta})$ processes the witness sensors $w_k(t)$ to estimate both *stationary* and *non-stationary* noise components $n_R(t)$, optimizing parameters $\vec{\theta}$ by minimizing a loss function J_{ASD}.

$$\begin{cases} n_R(t) = \mathcal{F}(w_k, \vec{\theta}), \\ \vec{\theta} = \text{argmin}_{\theta'} J_{ASD}\left[h(t), \mathcal{F}(w_i(t);\vec{\theta}')\right]. \end{cases} \tag{6.3}$$

Subtracting $n_R(t,\vec{\theta})$ from the GW readout $h(t)$ yields the residual signal $r(t,\vec{\theta})$, which contains astrophysical signals $s(t)$ and non-removable noise $n_{NR}(t)$ similar to Equation 6.4.

$$r(t,\vec{\theta}) = h(t) - n_R(t,\vec{\theta}) = s(t) + n_{NR}(t) \tag{6.4}$$

The loss function J_{ASD} is defined as:

$$J_{ASD} = \frac{1}{f_{\text{high}} - f_{\text{low}}} \int_{f_{\text{low}}}^{f_{\text{high}}} \sqrt{\frac{PSD_r(f)}{PSD_h(f)}}\, df, \tag{6.5}$$

where $PSD_h(f)$ represents the PSD derived from the GW readout signal as a function of frequency f, and $PSD_r(f)$ represents the PSD of the residual signal, $r(t)$, as a function of frequency f. In addition, in the analysis, the mean squared error (MSE) has been selected as the loss function.

With the MSE also used as a loss metric [215]:

$$\text{MSE} = \frac{1}{N} \sum_{k=1}^{N} \left(h(t) - \mathcal{F}(w_k(t);\vec{\theta})\right)^2. \tag{6.6}$$

In the process of weight optimization, *DeepClean* employs the ADAM optimizer to efficiently navigate the gradient space and minimize the loss function [165]. This optimization algorithm is particularly well suited to handle large data sets and complex network architectures characteristic of GW data analysis. Building on the foundation of robust weight optimization, enhancements to the *DeepClean* method have been realized through the integration of a CNN architecture. This is conceived as a fully convolutional auto-encoder, a sophisticated design choice that facilitates the network's ability to capture spatial hierarchies and abstract features within the data [215]. Validated with real LIGO data, the enhanced *DeepClean* network has shown its effectiveness in reducing noise influences without distorting the GW signals, which is a testament to the method's advanced noise filtering capabilities. The refined loss function encapsulates a dual component structure that marries the amplified amplitude spectral density (ASD)

with the MSE, offering a comprehensive measure of the network's performance. This combined loss function, expressed as

$$J = J_{ASD} + \text{MSE}, \tag{6.7}$$

enables a balanced optimization, ensuring that both the spectral characteristics and the time-domain fidelity of the signal are preserved during the noise reduction process. The incorporation of this composite loss function exemplifies the meticulous approach adopted in GW data analysis, striving to maintain the integrity of potential astrophysical signals.

6.3.2 Philosophy of the process

The *DeepClean* project employs a thorough methodology for data set preparation, training, and noise reduction, beginning with the acquisition and pre-processing of raw data from the Virgo detector. This includes both GW signals and auxiliary witness sensor data ($w_k(t)$, which are normalized and filtered to prepare for CNN analysis [249, 215]. The CNN architecture is designed to discern complex noise patterns within GW data, employing convolutional layers, activation functions, and pooling layers, with regularization techniques to prevent overfitting. The training process is fine-tuned through hyperparameters using in [249], ensuring the model efficiently learns the relationship between witness sensor data and noise components. The validation and testing phase is crucial to assess the model's ability to generalize to new data and confirm its efficacy with different GW signals. After training, the model applies its learned parameters for noise reduction, significantly improving signal clarity. This process is rigorously evaluated by comparisons of original and cleaned signals, with improvements in S/N and ASD serving as key metrics. The comprehensive methodology encapsulated by *DeepClean* is depicted in Figure 6.2. This figure illustrates the end-to-end process from initial data preparation to final noise reduction. This integrated approach highlights the systematic effort that has been made to accurately model and mitigate noise within GW detectors. Ultimately, this improves both the fidelity and reliability of the data analysis, leading to more confident detection and characterization of GW signals.

6.4 A Virgo O3b Mock Data Challenge

To assess the performance of *DeepClean*, I conducted a thorough analysis on the O3b data from the Virgo detector, recorded during the Virgo O3b Mock Data Challenge (MDC). The MDC was designed to test and improve low-latency analysis pipelines with real observational data from the O3b session. I examined a continuous stretch of data `Hrec_hoft_raw_20000Hz` and the useful witness channels, spanning two days, 18 hours and 15 minutes, from February 7, 2020, 16:19:27 UTC to February 10, 2020, 10:35:01 UTC. This period was selected for its extensive coverage and the significant coherence observed between strain and auxiliary channels in the Virgo O3b dataset essential for *DeepClean*'s effective deployment and evaluation of *DeepClean*. The models

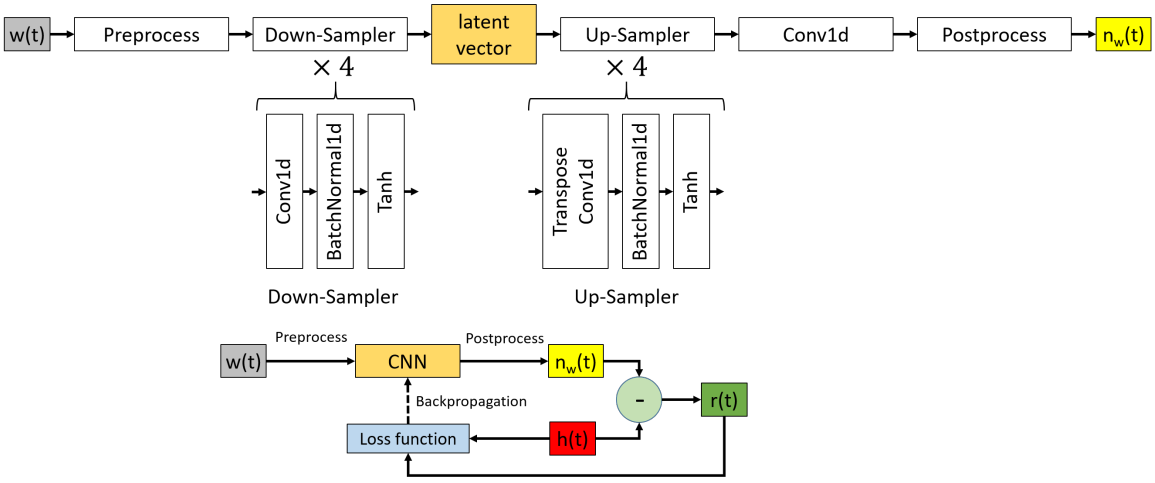

Figure 6.2: The figure presents the architecture of the *DeepClean* system and the associated data processing sequence. *DeepClean* processes input in the form of time series data acquired from an array of witness sensors. The data undergo a transformation through a convolutional autoencoder network, which consists of a series of four convolutional layers for the reduction of dimensionality, followed by an equal number of transpose-convolutional layers responsible for dimensionality expansion. Each convolutional operation is succeeded by batch normalization and hyperbolic tangent (tanh) activation. The final convolutional layer culminates in a one-dimensional representation aimed at predicting noise. The lower diagram delineates the training regime for *DeepClean*, using the ADAM optimization algorithm to iteratively converge on a minimum of the defined loss function through gradient descent. The figure is from [249].

were trained in 1024 s, 2048 s, and 4096 s segments with a training interval of 100,000 s, each cleaning its respective data segment. I first focus to reduce the noise in three frequency bands, including 98 to 110 Hz, 142 to 162 Hz, and 197 to 208 Hz, in order to mitigate the noise *non-stationary* and *non-linear* that could mask the GW signals.

As a reminder, at the beginning of this study, the target frequency was 50 Hz, with the sidebands around it. However, given that the feed-forward system addresses the main disturbances in Virgo, we have shifted our focus to other frequency ranges where we observe significant noise, aiming to further improve the overall noise reduction.

ASD Improvement—I quantified *DeepClean*'s efficacy by comparing the ASD of the post-process data (labeled V1:DC) against the ASD of the original dataset (labeled V1:ORG), where V1 denotes the Virgo detector. The original MDC dataset is indicated by "ORG," and the results after *DeepClean* processing are designated by "DC." Figures 6.3, 6.4, and 6.5 exhibit a considerable enhancement in signal quality within the respective targeted frequency ranges of 98-110 Hz, 142-162 Hz, and 197-208 Hz. These improvements substantiate the effectiveness of the *DeepClean* algorithm in advancing noise reduction in GW data analysis.

The efficacy of *DeepClean* varied significantly with the duration of the training segments. Although segments of 1024 s and 2048 s were used, the results were sub-

optimal compared to those obtained from the 4096 s segments. This discrepancy can be attributed to the addition of unintended artifacts during the noise removal process with shorter segments, likely a consequence of the inherent non-stationary data during O3b. The data set is characterized by periods in which the auxiliary sensors exhibit high coherence with the readout channel for durations as brief as 200 s, followed by incoherence intervals. Longer training segments, such as 4096 s, are advantageous, as they encompass a broader spectrum of these variable conditions, thereby improving the model's ability to accurately predict and mitigate noise. Consequently, training in 4096 s segments proved to be more effective, capturing a wider range of situational variations and leading to superior noise reduction results.

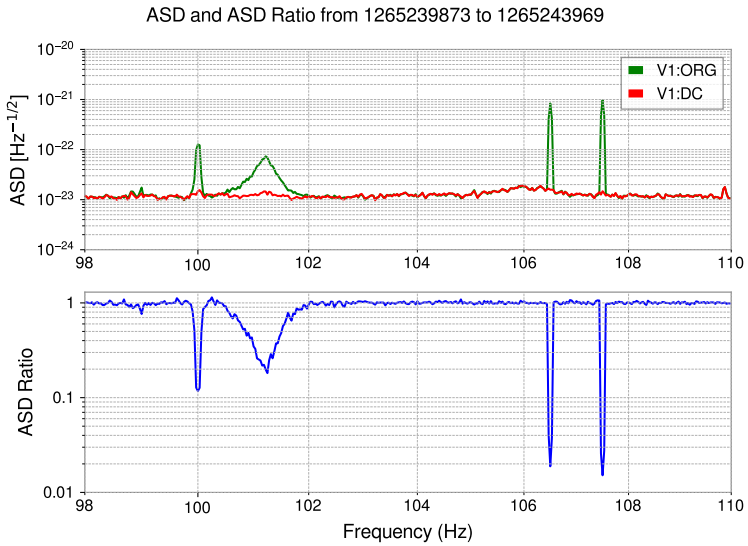

Figure 6.3: ASD and ASD ratio comparison for the Virgo detector data in the 98-110 Hz frequency band. The green trace represents the ASD of the original Mock Data Challenge (MDC) set from Virgo (V1:ORG), the red trace depicts the ASD after processing with the *DeepClean* algorithm (V1:DC), and the blue trace shows the ratio of the two ASDs. This panel demonstrates the noise reduction capabilities of *DeepClean* within this specific frequency range.

6.4.1 Witness sensors

In the pursuit of enhanced sensitivity for GW detection within the Virgo interferometer, a comprehensive analysis of witness channels was performed identify within specific frequency bands, namely 98–110 Hz, 142–162 Hz and 197–208 Hz. To guess among a thousand channels which ones are the most important, I consider the coherence better witness channels and the GW strain channel. I consider the output of the BruCo analysis [1], and select those that record a coherence rate greater than 0.5. This coherence must occur at least five times during February and March 2020. Each witness channel is

[1] https://vim.virgo-gw.eu/?config=1

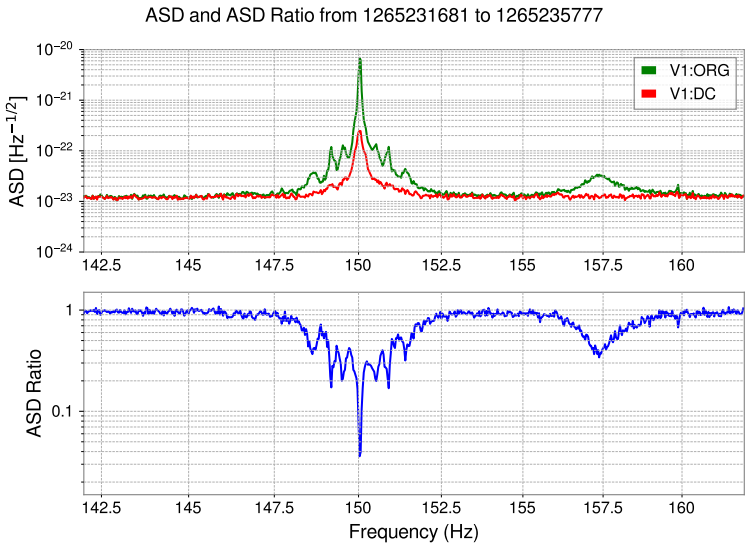

Figure 6.4: ASD and ASD ratio comparison for the Virgo detector data in the 142-162 Hz frequency band. The green trace is the ASD of the original data (V1:ORG), the red trace is after *DeepClean* processing (V1:DC), and the blue trace indicates the ASD ratio. The effectiveness of the *DeepClean* algorithm in reducing noise in this mid-frequency range is highlighted here.

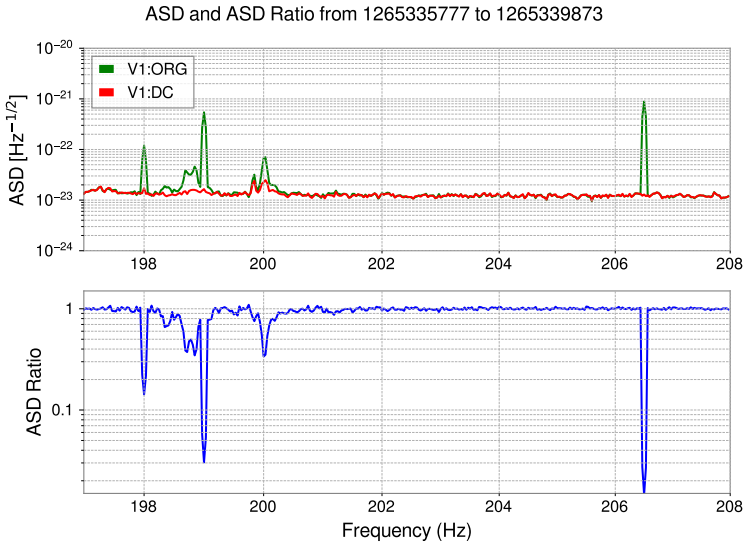

Figure 6.5: ASD and ASD ratio comparison for the Virgo detector data in the 197-208 Hz frequency band. The green, red, and blue traces represent the original ASD, the ASD post *DeepClean*, and their ratio, respectively. This figure underscores the reduction of noise achieved by *DeepClean* in the higher frequency domain.

tested for its noise removal effects. Many are excluded from the final list because they introduce additional noise despite reducing some or because they have no effect,thus

increasing the computational cost. For each frequency band I list the main witness channels (for more, cf. **Virgo Logbook**[2]) .

98 to 110 Hz:

- `V1:CAL_WE_MIR_Z_NOISE`: Injects and monitors longitudinal noise in the west end mirror for calibration and sensitivity.
- `V1:CAL_NE_MIR_Z_NOISE`: Injects and monitors longitudinal noise in the North End mirror for calibration and sensitivity.
- `V1:INJ_IMC_QD_FF_DC_V`: Measures the DC voltage of the Input Mode Cleaner.

197 to 208 Hz:

- `V1:CAL_WE_MIR_Z_NOISE`: Injects and monitors longitudinal noise in the west end mirror for calibration.
- `V1:INJ_Tpro_processed_packets`
- `V1:SDB_EDB_Tpro_processed_packets` and `V1:SDB2_Tpro_processed_packets`: Impacts data quality via suspension database processing.
- `V1:ENV_IB_CT_FINGER_ACC_Y`: Monitors environmental vibrations.
- `V1:ENV_CEB_MAG_W`: Monitors magnetic fields and detects magnetic noise.
- `V1:INJ_IMC_QD_FF_I_H` and `V1:INJ_IMC_REFL_I_POST`: Injection Mode Cleaner control signal from the in-phase demodulated quadrant photodiode.
- `V1:SQZ_CC_Tpro_processed_packets`: Squeezing control system packets.

142 to 162 Hz: Given the complex contributions of 167 witness channels in this frequency range to noise reduction, a full listing is omitted. Key acronyms like **ASC** (Alignment Sensing and Control), **INJ** (Injection), **ACT** (Actuation), and **ENV** (Environment) are emphasized to highlight the main systems that maintain the operating integrity of the interferometer [27].

6.4.2 Training and cleaning process

The *DeepClean* algorithm was rigorously trained on frequency bands 98–110 Hz, 142–162 Hz, and 197–208 Hz, known for significant *non-linear* and *non-stationary* noise, to enhance its ability to detect and reduce noise that could obscure GW signals. Following [249], I use the same hyperparameters. The pre-processed data is segmented into overlapping kernels (distinct from the convolution filter kernel in CNN architecture). These

[2] https://logbook.virgo-gw.eu/virgo/

kernels are organized into batches of fixed size (*batch_size*). For this analysis, 8s kernels with 7.75s overlap were used. Training data is fed to *DeepClean* in batches of 32 kernels. During training, *DeepClean* calculates the loss, backpropagates gradients, and updates weights using the ADAM optimizer[165].

6.4.3 Performance estimation

In the pursuit of evaluating the *DeepClean* algorithm's efficacy, particularly after the noise reduction process, I conduct statistical analysis, using CBC waveforms. This analysis aims to verify that denoising preserves the integrity of the original GW signals and to examine any improvements in the credible intervals of the estimated parameters due to noise subtraction.

Gravitational wave generation and event selection—In this research, I use the *Bilby* Bayesian inference library [53] to generate, BBH signals. I use a uniform distribution for component masses m_1 and m_2, ensuring the total mass M matches coalescence frequencies at the last stable orbit frequency $f_{\rm ISCO}$, i.e., BBH events with $f_{\rm ISCO}$ in these bands. The $f_{\rm ISCO}$ is given by,

$$f_{\rm ISCO} = \frac{c^3}{6^{1.5}\pi GM}, \tag{6.8}$$

where c is the speed of light, G the gravitational constant, and M the total mass of the binary system. This equation guides the selection of m_1 and m_2, specifically targeting those within the frequency bands of 98–115 Hz, 142–162 Hz, and 197–215 Hz. I target these frequency bands due to their excessive noise, ensuring the *DeepClean* algorithm's effectiveness in enhancing the detection and analysis of GW signals, particularly in the context of the pre-merger phase of CBC events. This approach not only optimized the selection of BBH systems, but also ensured that the analysis targeted GW signals predominant in the late inspiral phase. The uniform distribution of masses was pivotal for the focused application of the *DeepClean* algorithm, enhancing our capability to rigorously assess its noise reduction effectiveness in the critical pre-merger phase of CBC events.

Signal-to-noise ratio analysis—I inject a total of 6750 GW signals from BBH mergers into the MDC training set across three frequency bands: 98–110 Hz, 142–162 Hz, and 197–208 Hz. The S/N of each injected signal was evaluated using the match-filtering function in *PyCBC* [67]. I compare the maximal S/N values before and after applying the *DeepClean* process.

For the 98–110 Hz frequency band, my statistical analysis yielded a mean difference in S/N of $\mu \approx -0.02$ and a standard deviation of $\sigma \approx 0.2$, with 99.21% of the S/N differences within 5σ of the mean. Similarly, for the 197 to 208 Hz band, I observed a mean value of $\mu \approx -5 \times 10^{-4}$ and a standard deviation of $\sigma \approx 0.03$, with 99.96% of the differences within 5σ. The effectiveness of the *DeepClean* process across these bands demonstrates its ability to efficiently reduce noise without compromising the integrity

of the GW signals. In the 142–162 Hz frequency band, the analysis indicated a mean difference in S/N of $\mu \approx -0.04$ and a standard deviation of $\sigma \approx 0.24$. Here, 99.52% of the S/N differences fell within 5σ of the mean, showcasing a significant level of consistency in the performance of the *DeepClean* process. This consistency further underscores the *DeepClean*'s ability to enhance signal clarity across a broad range of frequencies.

Figures 6.6, 6.7, and 6.8 illustrate the distribution of S/N differences for the respective frequency bands, providing information on the distribution and effectiveness of the noise reduction technique applied. Half of the GW signals have an increase in S/N, while the remainder shows a decrease. Importantly, the *DeepClean* process did not degrade the GW signals.

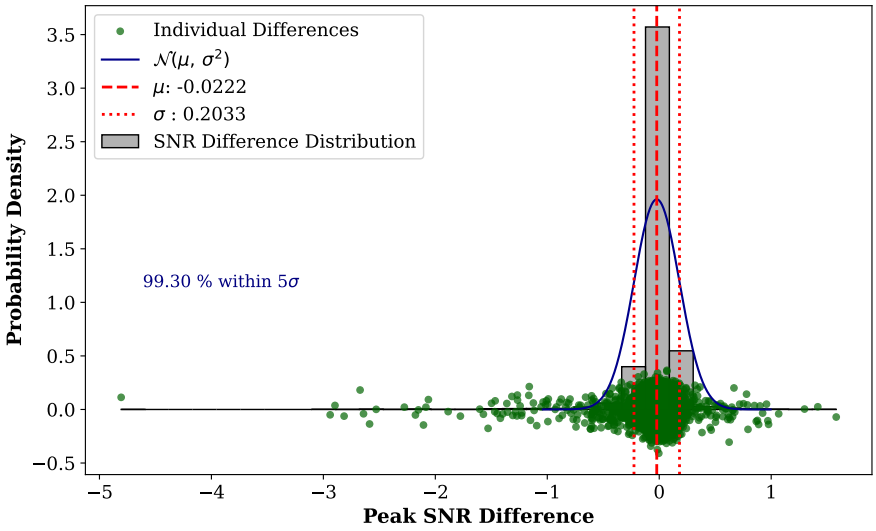

Figure 6.6: Distribution of S/N differences for BBH with f_{ISCO} between 98 and 110 Hz. Dark green dots show individual S/N differences, the blue line is the Gaussian fit, and the red dashed and dotted lines mark the mean (μ)) and standard deviation (σ). The gray bars show the histogram. Approximately 99. 3% of the differences lie within $\pm 5\sigma$ of the mean, confirming *DeepClean*'s effectiveness in preserving GW signal integrity.

6.4.4 Improvement of BNS inspiral range detection

The BNS inspiral range is a critical metric for GW detector sensitivity, indicating the maximum distance for detecting a BNS inspiral with an S/N of 8 [128, 87, 127]. I calculate the BNS inspiral range of O4a using measured PSD values from the LIGO detector. For O4b, we used the simulated PSD noise curves LIGO-T2200043-v3[3]. Table 6.1 shows the results.

The application of the *DeepClean* algorithm for noise suppression in GW detectors yields quantifiable improvements in the detection of the BNS inspiral range.

[3] https://dcc.ligo.org/T2200043-v3/public

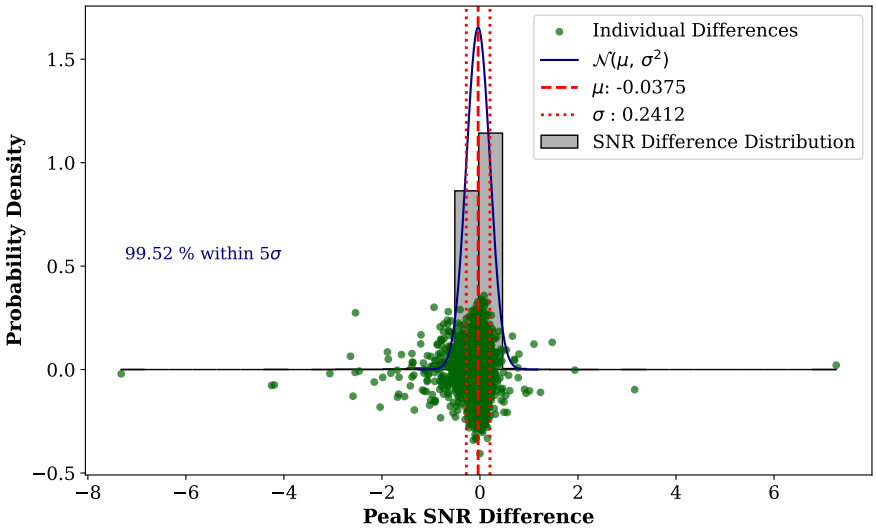

Figure 6.7: Distribution of S/N differences for BBH with f_{ISCO} between 142 and 162 Hz. The plot shows S/N differences as dark green dots and a Gaussian distribution as a blue line. The mean (μ) and the standard deviation (σ) are indicated by red dashed and dotted lines. The gray bars represent the histogram of S/N differences, with 99.52% within $\pm 5\sigma$ of the mean.

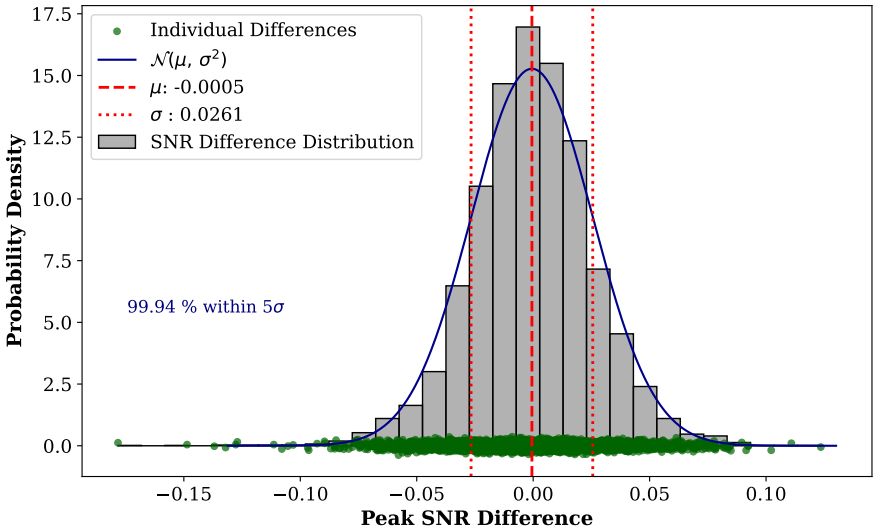

Figure 6.8: Histogram of S/N differences for BBH with f_{ISCO} falling within 197 and 208 Hz, shows by dark green dots. The Gaussian distribution is in blue, with mean (μ) and standard deviation (σ) in red dashed and dotted lines. Gray bars show 99.94% of values within $\pm 5\sigma$.

A comparative analysis conducted before and after the *DeepClean* implementation, reveal modest yet statistically significant enhancements. Specifically, within the noise-cleansed frequency band from 98–110 Hz, an average increase of approximately 0.2 Mpc was observed, corresponding to an improvement of 0.39%. In the 142–162 Hz band, the average gain was approximately 0.18 Mpc or 0.37%. Although cleaning

within the 197–208 Hz band results in a marginal increase of approximately 0.02 Mpc, translating to a 0.05% enhancement, it underscores the efficacy of the method. The Figure 6.9 evolution between each of the BNS inpiral values before and after cleaning.

These analyses are based on single-training sessions. Due to insufficient results, multi-training is crucial, allowing successive processing of multiple frequency bands.

Table 6.1: Cosmology-corrected inspiral range (Mpc) for O4a and O4b from GW strain.

Run	**L1**	**H1**	**V1**	**K1**
BNS inspiral range of the in Mpc				
O4a	165	145	*off duty*	*off duty*
O4b	224	224	95	37

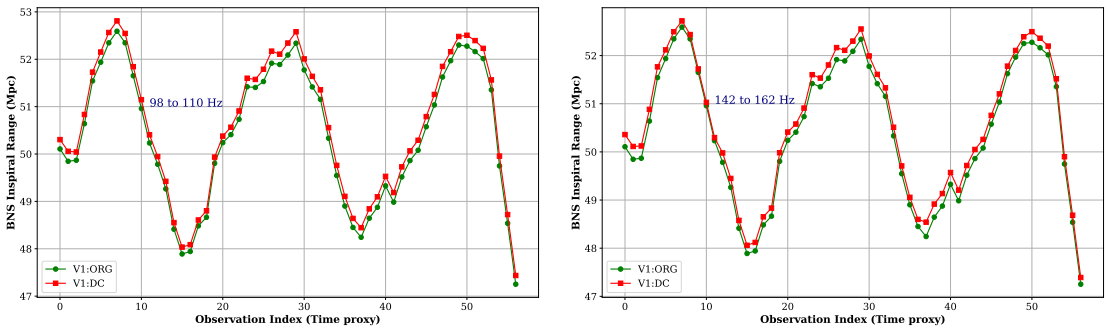

Figure 6.9: Sensitivity analysis of the BNS inspiral range for the 98-110 Hz (left) and 142-162 Hz (right) bands, using Virgo O3b MDC data from GPS 1265127585 to 1265352161. It demonstrates the *DeepClean* capabilities for BNS inspiral. The time index ("Time proxy") of each 4096s segment.

6.4.5 The multi-training process

Multi-training—Using a segmented multi-training approach that focuses on specific frequency bands from 15–20 Hz to 395–415 Hz throughout the entire operational range of 15 to 415 Hz has led to a notable enhancement of the BNS inspiral range by approximately 1.3 Mpc, or an increase of approximately 2.5%. This approach, by isolating and training in individual frequency bands, has yielded significant improvements in the sensitivity and operational range of the detector. Each band is treated as a distinct processing layer, with the 142–162 Hz band being the initial focus due to its use of 123 witness channels, which necessitates a substantial computational resource: at least 80 GB of RAM is required for processing 4096 seconds of Virgo O3b data. The output of this initial layer training provides the foundation for training of the subsequent layers in an iterative fashion. This process comprises 13 layers in total: 142–162 Hz,

15–20 Hz, 33–39 Hz, 55–65 Hz, 75–80 Hz, 98–110 Hz, 137–139 Hz, 197–208 Hz, 247–252 Hz, 295–305 Hz, 345–355 Hz, 355–367 Hz, culminating in the 395–415 Hz band. Each channel is associated with specific witness channels that demonstrate a certain level of coherence. The ASD for the original and cleaned data is presented in Figure 6.10. Furthermore, Figure 7.2 illustrates the inspiral range of the BNS before and after the data cleaning process. These figures underscore significant advances in the capabilities of the Virgo detector.

Future projections—The integration of Virgo into the O4b observation campaign, which began on April 10, 2024, and is projected to end in February 2025, provides an opportunity to enhance data monitoring and refine coherence optimization with witness channels. The average increase in the inspiral range for BNS during single-training is 0.13 Mpc. However, this increases to 1.3 Mpc with multi-training that combines 13 frequency bands between 15 and 415 Hz, representing a 10-fold improvement over single-training. Furthermore, I have identified at least 21 frequency bands with significant excess noise between 15 and 1360 Hz that are worth subtracting.

Given all of the above, I project that a comprehensive retraining across the frequency range from 15 to 2000 Hz could potentially increase the BNS inspiral range by approximately 10% to 20% during the O4b. We can select the most coherent MDC data for analysis, unlike the current study with only 40 days of saved data on the Virgo server in Cascina. This strategy involves adapting the real-time processing frameworks used in the LIGO detectors for the Virgo dataset, facilitating the transition to live and online data analysis. The adaptation will not only leverage the developments of the O4b campaign, but also prepare the operational framework necessary to implement advanced real-time noise regression techniques similar to those validated in LIGO [249].

6.4.6 Violin mode frequencies

In the analysis of GW detector data, particularly in the frequency range influenced by the violin modes, noise subtraction challenges arise. Violin modes refer to mechanical resonances in the suspension fibers of the test masses, which can significantly affect the detector's sensitivity. In my studies using BruCo[4], I observe that the coherence between the witness sensors and the main channel is limited to approximately 1000 Hz. In particular, within specific frequency bands dominated by the violin modes, no witness sensors exhibit sufficient coherence with the main channel to facilitate noise subtraction. As depicted in Figure 6.12, around the frequency band of 440–456 Hz, an absence of noise subtraction is evident.

This highlights the limitations of these methods based on the use of a witness channel to reduce noise. In the absence of coherent witness channels, these methods, including *DeepClean*, are completely ineffective.

[4] https://vim.virgo-gw.eu/?config=28

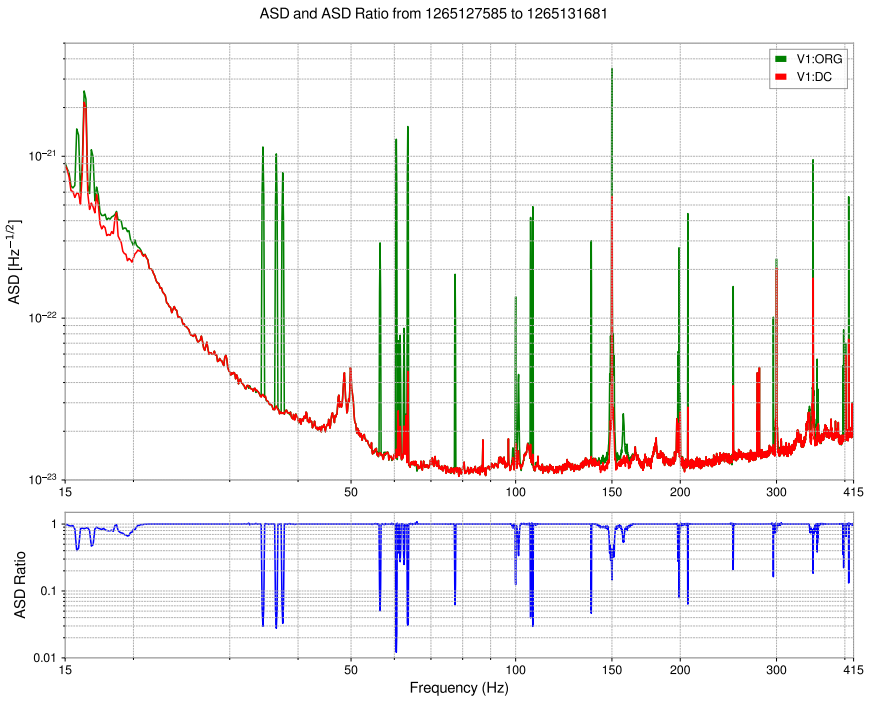

Figure 6.10: Comparison of ASD and ASD ratio across a 15 to 415 Hz frequency band. The original Mock Data Challenge (MDC) dataset from Virgo is represented by the green trace (V1:ORG), whereas the red trace (V1:DC) displays the ASD after processing with the *DeepClean* algorithm. The blue trace indicates the ratio of the two ASDs. These visualizations highlight the *DeepClean* algorithm's noise reduction efficacy across the specified frequency spectrum.

6.5 Challenges in Virgo detector data analysis

In this study of the *DeepClean* framework applied to the Virgo detector data, I initially aimed to use the O4a data set. Due to technical constraints, Virgo did not participate in the O4a with the LIGO detectors (L1, H1). Consequently, I shifted to the O3b data set from Cascina, Italy, hoping to refine my methodology for the upcoming O5.

The study faced several analytical challenges:

- **Substitution with O3b Data**: Due to the inaccessibility of O4a data, I had to use O3b data, affecting my ability to perform a comparative analysis with the LIGO detectors during the same run.
- **Dynamic auxiliary channels**: The names and existence of witness channels change over time, complicating the use of Virgo data.
- **High computational demands**: Analyzing Virgo data to capture the 150 Hz peak and its sidebands via ASC witness sensors required significant computational resources, often compromising between data depth and computing power.

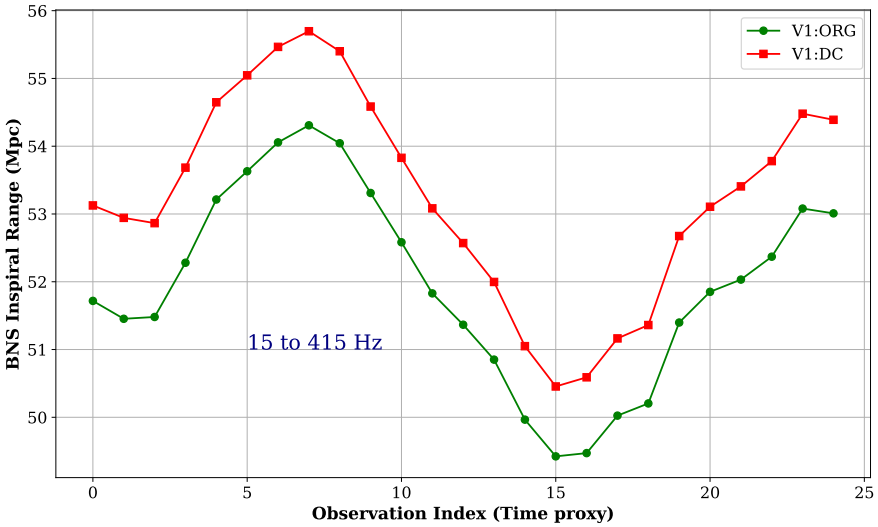

Figure 6.11: The BNS inspiral range for the original Virgo dataset (V1:ORG, green trace) and after cleaning with the *DeepClean* algorithm (V1:DC, red trace), over the frequency band of 15 to 415 Hz. The graph demonstrates the improvement in the detection range post-cleaning. The "Time proxy" indicates the time fraction for each post- and pre-cleaning phase.

- **Data access**: To address these high computational demands, the VirgoTool Python package was identified as a potential solution for reducing data reading times. However, integration challenges within my cluster's environment limited its utility. I propose enhancing the gwpy library with VirgoTool's data handling capabilities to improve computational efficiency in future studies.
- **Non-stationary** —The Virgo O3b dataset is non-stationary; a witness channel may be coherent for 200 seconds and then become incoherent, hindering noise reduction.

6.6 Conclusion

This work highlights the possibility of reducing some noise contamination of the Virgo data, which contributes to the detection of more astrophysical signals. The integration of the *DeepClean* framework represents a transformative approach to the treatment of complex noise, *non-linear* and *non-stationary* in the analysis of GW data. Using CNNs, the *DeepClean* algorithm substantially enhances the accuracy and sensitivity of the Virgo detector, important for the analysis of GW signals. The results are promising and the method can be used in the ongoing O4b campaign to assess the progress of noise reduction. This research successfully navigated computational and methodological challenges, including data substitution due to unforeseen constraints and the dynamics of auxiliary channels. Despite these obstacles, the commitment to improving the analytical precision remained strong. The effectiveness of *DeepClean*, confirmed

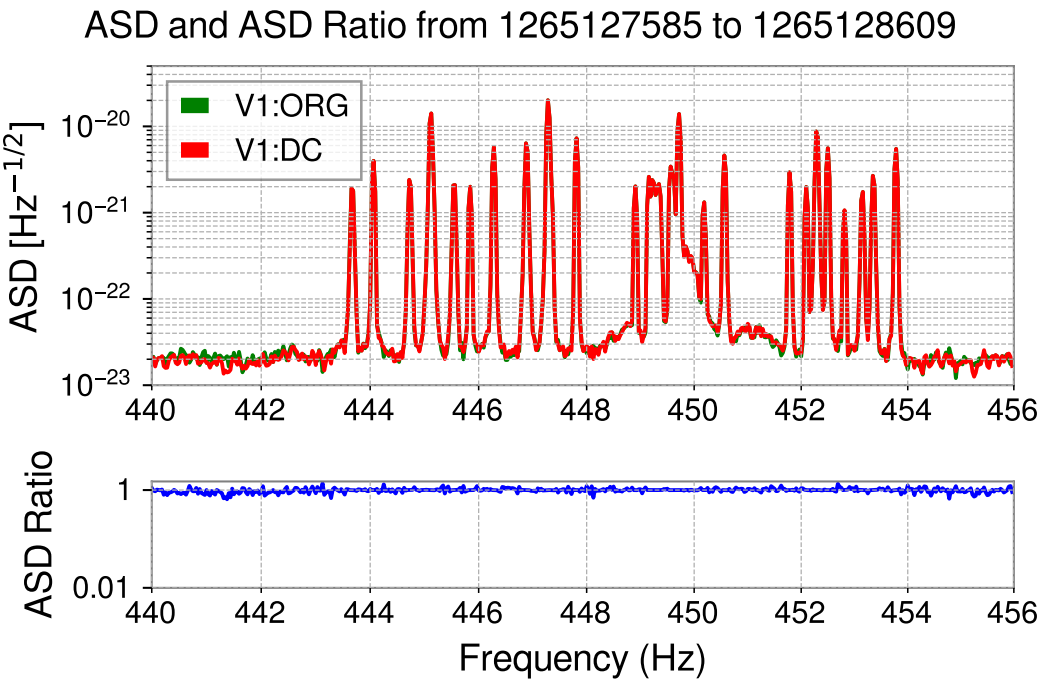

Figure 6.12: ASD and ASD ratio analysis in the 440-456 Hz band, highlighting violin mode resonances. The green trace (V1:ORG) shows the original ASD, the red trace (V1:DC) shows the ASD after *DeepClean* processing, and the blue trace shows their ratio. This plot indicates *DeepClean*'s limited noise reduction around violin modes, suggesting a lack of coherent witness sensors for noise subtraction in this band.

through extensive training and testing over specific frequency ranges, demonstrates its ability to effectively reduce noise while preserving the integrity of the GW signals. These efforts in offline data are crucial for setting up online processing for the upcoming O5 , enhancing real-time noise reduction in the Virgo detector and improving pre-merger GW signal detection.

A possible test is using *Bilby* to evaluate parameter estimation (PE) and assess the impact of noise reduction on masses m_1 and m_2. We must address the challenges before the O5 run. Enabling VirgoTool installation in personal environments or integrating it into *gwpy* would make Virgo data as accessible as LIGO data. A new CPU-based version of *DeepClean* considered by LIGO DetChar group could resolve the cost issue.

Chapter 7

Conclusion and Perspectives

***

During my PhD, I worked on projects developing cosmic probing tools and contributed to collaborations like NMMA, GRANDMA, Virgo, and LSC. In this chapter, I will revisit some of the results presented in previous chapters. I will discuss their significance and their impact on our understanding of compact binary mergers. This will provide an opportunity to highlight the challenges and difficulties encountered in achieving these results. Finally, I will outline my short-term perspectives, which primarily focus on the study of the interaction between dark matter and white dwarfs (WD), leading to low-luminosity SN Ia.

7.1 Conclusion

Chapter 2—I integrated the PDB/GWTC-3 distribution into LIGO.Skymap, enabling the simulation and localization of CBC events. This distribution, used for "observing scenarios," describes populations of BNSs, NSBHs, and BBHs [122, 25]. I presented the latest simulations covering both the current and the future observing run of the IGWN. It provides projections for astronomers interested in the data products by GW detectors, as well as EM counterparts to BNS mergers (Kiendrebeogo et al. 2023[163]). I simulated O6 predictions for researchers evaluating future telescope missions like UVEX and ULTRSAT.

The simulated data updated the IGWN User Guide[1] and were used for proposals for the ZTF [163], Nancy Grace Roman Space Telescope (Roman) [44], UVEX, and Rubin Observatory telescopes. Then I suggested raising the detection threshold from 8 to 10 to better reflect our predictions at observation time (Table 7.1). The detection of GW230529 [89], an NSBH with BH mass between 2.5-4.5 $M_\odot$, previously in the "Mass Gap" (2.5-5 $M_\odot$), highlights the importance of the PDB/GWTC-3 distribution, proposing limits at 2.5 $M_\odot$ between NS and BH. We set this limit at 3 $M_\odot$, risking NSs falling into the BH category, maximizing our EM counterpart estimation.

Table 7.1: Comparison of Predicted and Observed Detection Rates at Different S/N thresholds During O4a.

RUN	Detection Type	Time	SNR	BNS	NSBH	BBH
			Number of Detections			
O4a	Simulation	**1 year**	**8**	12^{+17}_{-9}	1^{+4}_{-2}	115^{+147}_{-67}
			10	5^{+10}_{-5}	0^{+0}_{-0}	60^{+78}_{-36}
	Observation	**9 months**	**N/A**	1 ?	6	81

Chapter 3—I presented my contributions to the NMMA and GRANDMA collaborations. We have developed the NMMA framework [217], which constrains rapidly evolving transients by integrating GW data with EM observations. This aids in constraining the EOS of NS and estimating H_0 based on KN observations by telescopes like ZTF and Rubin Observatory during the O4a and O5 runs. I also used the NMMA tool to constrain light curves during the "ReadyforO4" observation campaign with the *Kilonova-Catcher* (KNC)[2] initiative [50] of the GRANDMA collaboration. I processed data for eight transients using MLE to determine if they were KNe, followed by NMMA analysis [33].

Chapter 4—As part of doctoral research, I also evaluated the impact of ZTF and upcoming telescopes such as Rubin Observatory's LSST and ULTRSAT in detecting KN during IGWN campaigns. The results, shown in Figure 7.1, supported the

[1] https://emfollow.docs.ligo.org/userguide/capabilities.html
[2] http://kilonovacatcher.in2p3.fr/

preparation of the "ULTRASAT WG2 - Work package". These efforts anticipate telescope cadences, compiled through simulations using NMMA and gwemopt, providing sky maps for event locations.

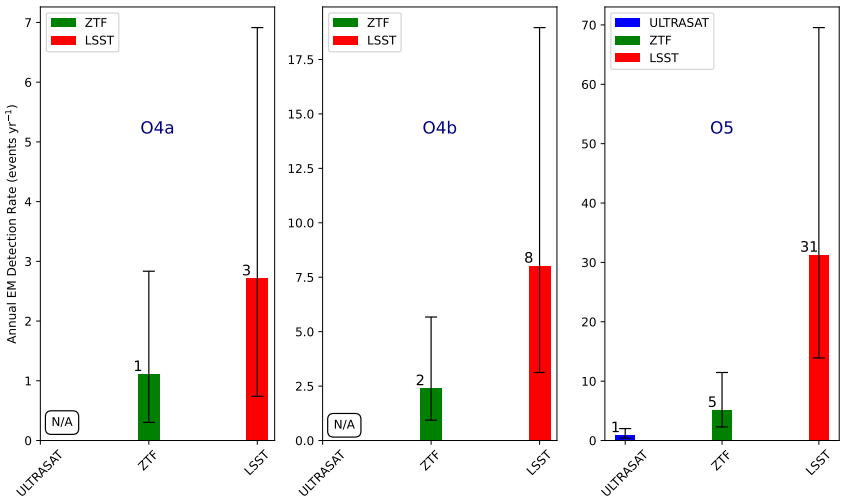

Figure 7.1: BNS Annual EM Detection Rates for LSST, ZTF, and ULTRSAT. This figure shows annual KN detection rates for BNS events by LSST, ZTF, and ULTRSAT during runs O4a, O4b, and O5. Bars indicate median EM detection rates from GW data, with error bars showing estimate ranges. Red bars represent LSST, green bars ZTF, and blue bars ULTRSAT, annotated with median values for expected annual BNS detections. The visualization highlights the distinct detection capabilities of each observatory across different runs, reflecting the dynamic nature of BNS related transient EM event observations.

Chapter 5—Given the proliferation of astronomical data and telescopes, I proposed a pipeline that discriminates the nature of light curves from transients revealed by ZTF. This integrates an NMMA analysis service with the time domain astronomy platform *SkyPortal* [98], providing real-time analysis to help astronomers anticipate the transient nature and save time. This pipeline can be adapted for other telescopes like LSST.

Chapter 6—In this chapter, I significantly reduced the noise in the Virgo detector, enabling the detection of potential GW signals otherwise masked by *non-stationary* noise. I configured the *DeepClean* algorithm for Virgo's data processing, integrating the readout channel and the auxiliary channels that measure independent environmental noise. This setup allows *DeepClean*, a CNN, to recognize and subtract noise from *non-stationary* and *stationary* during cleaning, improving Virgo's BNS inspiral range by approximately 1.35 Mpc from ≈55 Mpc in O3b, as shown in Figure 7.2. This study is a first for the Virgo detector, which prepares it for real-time data processing in the upcoming O5 campaign alongside LIGO.

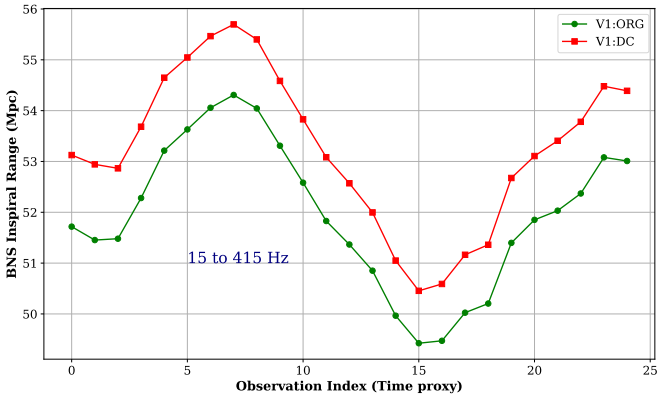

Figure 7.2: The BNS inspiral range for the original Virgo dataset (V1:ORG, green) and after *DeepClean* (V1:DC, red) over 15-415 Hz. The graph shows the detection range improvement post-cleaning. The "Time proxy" indicates the time fraction for each phase.

7.2 Challenge

Observing scenarios—We face numerous challenges in predicting the detection rates of GWs from our simulations. First, this is due to the limited size of the available sample, especially for BNSs, which are crucial for estimating the impact of EM counterparts . In addition, there is often a discrepancy between the ideal PSD from simulations and those measured by detectors during observations. This leads to predictions that do not accurately reflect reality, as evidenced by observations during O4a. The small sample size results in a limited understanding of the overall behavior of CBCs, contributing to wide error bars. These issues can improve as we detect more GW signals, which enhance the quantity and quality of data available for study. For the O4 campaign, we initially planned to observe with four detectors, but the sensitivities of the Virgo and KAGRA detectors were overestimated. Throughout the first phase (O4a), only the LIGO detectors were operational. This prevented an adequate comparative calculation between our predictions and the actual detections.

Furthermore, the PDB/GWTC-3 distribution used for our “observing scenarios" has an estimated lower and upper mass limit for NSs and BHs at 2.4 $M_{\odot}$, as per the Rate and Population (R&P) group. However, considering numerous scientific studies, observations, and our objectives to assess the impact of optical telescopes in EM detections, we have extended this limit to 3 $M_{\odot}$. This extension results in NSs with spins typically seen in BHs, often greater than 0.4. While this does not pose potential problems in our EM simulations, as NS spins are ignored, it may cause confusion for uninformed readers.

NMMA-Skyportal pipeline—The next generation of telescopes, such as the LSST at the Rubin Observatory and ULTRSAT, will observe a vast number of transient phenomena. With this proliferation of photometric data, it will be impossible for humans alone to classify all these events. *Skyportal* is a solution for real-time data pro-

cessing and visualization, serving as an interface between astronomical observatories and the astronomers. Beyond these capabilities, *NMMA-Skyportal* pipeline addresses the issue of observation time management by discriminating the nature of light curves. This allows astronomers to decide whether to continue or stop monitoring a specific event based on the evolution of the light curves in the first few days following detection. However, this pipeline is very costly and requires significant resource allocation.

The second version, though equally expensive, is associated with *Fritz*. It enables astronomers to conduct their own analyses by selecting parameters to fit light curve models and draw their own conclusions. Combining the advantages of these two versions would be beneficial in developing a third version. This version will allow users to identify a transient event and select light curve models based on the approach of the second version. It will iterate within the *NMMA analysis service* and post the appropriate result, continuing the analysis as soon as new photometric data for the same event is available, in line with the essence of the initial version

7.3 Perspectives

This doctoral thesis has highlighted several promising directions for future research, with a particular focus on advancing computational codes essential for data processing in multi-messenger astronomy. Each new detection of a multi-messenger counterpart enhances our understanding of complex astrophysical phenomena, such as the EOS for NSs, the H_0 constant, and the nucleosynthesis process known as the *r*-process. One fascinating area for future investigation is the potential interaction between dark matter and white dwarfs. Stellar evolution theory indicates that a runaway nuclear fusion reaction may occur in dense stellar objects such as white dwarfs and NSs. This reaction is triggered when the inward gravitational force at the star's core surpasses the outward thermal pressure from nuclear reactions, a condition common in objects containing degenerate matter. A particular area of interest is the *Ca-rich gap* transient, a subclass of faint luminosity SNe characterized by significant calcium ejection [72, 191]. Recent theories suggest that these SNe, which exhibit brightness levels between those of novae and more typical SNe, might be triggered by thermonuclear reactions induced by dark matter interactions within low-mass white dwarfs [267]. The unique observational characteristics of *Ca-rich gap* transients, including their spectral type and unusual locations relative to the centers of their host galaxies, challenge current models of stellar and binary evolution [107]. Investigating the role of dark matter, particularly primordial BHs, could provide critical insights into the mechanisms underlying *Ca-rich gap* transients and broaden our understanding of cosmological phenomena. This research could determine whether interactions with dark matter influence the dynamics of stellar explosions, such as SN Ia, which serve as crucial cosmic distance markers. If a significant portion of dark matter consists of primordial BHs, it might explain the observed frequency of *Ca-rich gap* transients.

The ongoing development of multi-messenger astronomy, through improved detection capabilities and refined data processing methodologies, remains essential. Each

new discovery not only enhances our astrophysical theories but also enriches our understanding of the cosmos. The integration of GW data with EM observations, especially in initiatives like NMMA, is important for expanding our understanding of the universe.

List of Figures

***

List of Tables

***

Bibliography

***

[1] J Aasi et al. “Advanced LIGO”. In: *Classical and Quantum Gravity* 32.7 (Mar. 2015), p. 074001. DOI: 10.1088/0264-9381/32/7/074001. URL: https://dx.doi.org/10.1088/0264-9381/32/7/074001.

[2] B P Abbott et al. “A guide to LIGO–Virgo detector noise and extraction of transient gravitational-wave signals”. In: *Classical and Quantum Gravity* 37.5 (Feb. 2020), p. 055002. DOI: 10.1088/1361-6382/ab685e. URL: https://dx.doi.org/10.1088/1361-6382/ab685e.

[3] B. Abbott et al. “GW170817: Observation of Gravitational Waves from a Binary Neutron Star Inspiral”. In: *Phys. Rev. Lett.* 119 (16 Oct. 2017), p. 161101. DOI: 10.1103/PhysRevLett.119.161101. URL: https://link.aps.org/doi/10.1103/PhysRevLett.119.161101.

[4] B. P. Abbott et al. “A Gravitational-wave Measurement of the Hubble Constant Following the Second Observing Run of Advanced LIGO and Virgo”. In: *Astrophys. J.* 909.2 (2021), p. 218. DOI: 10.3847/1538-4357/abdcb7. arXiv: 1908.06060 [astro-ph.CO].

[5] B. P. Abbott et al. “A gravitational-wave standard siren measurement of the Hubble constant”. In: *Nature* 551.7678 (2017), pp. 85–88. DOI: 10.1038/nature24471. arXiv: 1710.05835 [astro-ph.CO].

[6] B. P. Abbott et al. “GWTC-1: A Gravitational-Wave Transient Catalog of Compact Binary Mergers Observed by LIGO and Virgo during the First and Second Observing Runs”. In: *Phys. Rev. X* 9.3 (2019), p. 031040. DOI: 10.1103/PhysRevX.9.031040. arXiv: 1811.12907 [astro-ph.HE].

[7] B. P. Abbott et al. “Multi-messenger Observations of a Binary Neutron Star Merger”. In: *The Astrophysical Journal Letters* 848.2 (Oct. 2017), p. L12. ISSN: 2041-8213. DOI: 10.3847/2041-8213/aa91c9. URL: http://dx.doi.org/10.3847/2041-8213/aa91c9.

[8] B. P. Abbott et al. “Properties of the binary neutron star merger GW170817”. In: *Phys. Rev. X* 9.1 (2019), p. 011001. DOI: 10.1103/PhysRevX.9.011001. arXiv: 1805.11579 [gr-qc].

[9] B. P. Abbott et al. “Prospects for observing and localizing gravitational-wave transients with Advanced LIGO, Advanced Virgo and KAGRA”. In: *Living Rev. Rel.* 21.1 (2018), p. 3. DOI: 10.1007/s41114-020-00026-9. arXiv: 1304.0670 [gr-qc].

[10] B. P. Abbott et al. “Gravitational Waves and Gamma-Rays from a Binary Neutron Star Merger: GW170817 and GRB 170817A”. In: *The Astrophysical Journal Letters* 848.2 (Oct. 2017), p. L13. DOI: 10.3847/2041-8213/aa920c. URL: https://dx.doi.org/10.3847/2041-8213/aa920c.

[11] B. P. Abbott et al. “GW170817: Measurements of Neutron Star Radii and Equation of State”. In: *Phys. Rev. Lett.* 121 (16 Oct. 2018), p. 161101. DOI: 10.1103/PhysRevLett.121.161101. URL: https://link.aps.org/doi/10.1103/PhysRevLett.121.161101.

[12] B. P. Abbott et al. “GWTC-1: A Gravitational-Wave Transient Catalog of Compact Binary Mergers Observed by LIGO and Virgo during the First and Second Observing Runs”. In: *Physical Review X* 9.3 (Sept. 2019). DOI: 10.1103/physrevx.9.031040. URL: https://doi.org/10.1103%2Fphysrevx.9.031040.

[13] B.P Abbott et al. “Observation of Gravitational Waves from a Binary Black Hole Merger”. In: *Physical Review Letters* 116 (Feb. 2016). DOI: 10.1103/PhysRevLett.116.061102.

[14] BP Abbott and Soma Mukherjee. “Tests of general relativity with the binary black hole signals from the LIGO-Virgo catalog GWTC-1”. In: *PHYSICAL REVIEW D Phys Rev D* 100 (2019), p. 104036. URL: http://arxiv.org/abs/1903.04467.

[15] R. Abbott et al. “GW190814: Gravitational Waves from the Coalescence of a 23 Solar Mass Black Hole with a 2.6 Solar Mass Compact Object”. In: *The Astrophysical Journal Letters* 896.2 (June 2020), p. L44. DOI: 10.3847/2041-8213/ab960f. URL: https://doi.org/10.3847%2F2041-8213%2Fab960f.

[16] R. Abbott et al. “GWTC-2: Compact Binary Coalescences Observed by LIGO and Virgo during the First Half of the Third Observing Run”. In: *Phys. Rev. X* 11 (2 June 2021), p. 021053. DOI: 10.1103/PhysRevX.11.021053. URL: https://link.aps.org/doi/10.1103/PhysRevX.11.021053.

[17] R. Abbott et al. “Prospects for observing and localizing gravitational-wave transients with Advanced LIGO, Advanced Virgo and KAGRA”. In: *Living Reviews in Relativity* 23.1 (Sept. 2020). DOI: 10.1007/s41114-020-00026-9. URL: https://doi.org/10.1007%2Fs41114-020-00026-9.

[18] Abbott et .al. “Gravitational Waves and Gamma-Rays from a Binary Neutron Star Merger: GW170817 and GRB 170817A”. In: *Astrophys. J. Lett.* 848.2 (2017), p. L13. DOI: 10.3847/2041-8213/aa920c. arXiv: 1710.05834 [astro-ph.HE].

[19] Abbott et .al. “GW170104: Observation of a 50-Solar-Mass Binary Black Hole Coalescence at Redshift 0.2”. In: *Phys. Rev. Lett.* 118 (22 2017), p. 221101. DOI: 10.1103/PhysRevLett.118.221101. arXiv: 1706.01812 [gr-qc].

[20] Abbott et .al. "GW190425: Observation of a Compact Binary Coalescence with Total Mass $\sim 3.4 M_{\odot}$". In: *The Astrophysical Journal* 892.1 (Mar. 2020), p. L3. ISSN: 2041-8213. DOI: 10.3847/2041-8213/ab75f5. URL: http://dx.doi.org/10.3847/2041-8213/ab75f5.

[21] Abbott et .al. "Population Properties of Compact Objects from the Second LIGO-Virgo Gravitational-Wave Transient Catalog". In: *The Astrophysical Journal Letters* 913.1, L7 (May 2021), p. L7. DOI: 10.3847/2041-8213/abe949. arXiv: 2010.14533 [astro-ph.HE].

[22] Abbott et al. "Gravitational Waves and Gamma-Rays from a Binary Neutron Star Merger: GW170817 and GRB 170817A". In: *The Astrophysical Journal Letters* 848.2 (2017), p. L13. URL: http://stacks.iop.org/2041-8205/848/i=2/a=L13.

[23] Abbott et al. "GW151226: Observation of Gravitational Waves from a 22-Solar-Mass Binary Black Hole Coalescence". In: *Phys. Rev. Lett.* 116.24 (2016), p. 241103. DOI: 10.1103/PhysRevLett.116.241103. arXiv: 1606.04855 [gr-qc].

[24] Abbott et al. "GW170817: Observation of Gravitational Waves from a Binary Neutron Star Inspiral". In: *Phys. Rev. Lett.* 119 (16 Oct. 2017), p. 161101. DOI: 10.1103/PhysRevLett.119.161101. URL: https://link.aps.org/doi/10.1103/PhysRevLett.119.161101.

[25] Abbott et al. "Population of Merging Compact Binaries Inferred Using Gravitational Waves through GWTC-3". In: *Phys. Rev. X* 13 (1 Mar. 2023), p. 011048. DOI: 10.1103/PhysRevX.13.011048. URL: https://link.aps.org/doi/10.1103/PhysRevX.13.011048.

[26] Abbott et al. "Prospects for Observing and Localizing Gravitational-Wave Transients with Advanced LIGO and Advanced Virgo". In: *Living Reviews in Relativity* 19, 1 (Feb. 2016), p. 1. DOI: 10.1007/lrr-2016-1. arXiv: 1304.0670 [gr-qc].

[27] F Acernese et al. "Virgo detector characterization and data quality: results from the O3 run". In: *Classical and Quantum Gravity* 40.18 (Aug. 2023), p. 185006. DOI: 10.1088/1361-6382/acd92d. URL: https://dx.doi.org/10.1088/1361-6382/acd92d.

[28] F. Acernese et al. "Increasing the Astrophysical Reach of the Advanced Virgo Detector via the Application of Squeezed Vacuum States of Light". In: *Phys. Rev. Lett.* 123 (23 Dec. 2019), p. 231108. DOI: 10.1103/PhysRevLett.123.231108. URL: https://link.aps.org/doi/10.1103/PhysRevLett.123.231108.

[29] Acernese et al. In: 32.2 (Dec. 2014), p. 024001. DOI: 10.1088/0264-9381/32/2/024001. URL: https://dx.doi.org/10.1088/0264-9381/32/2/024001.

[30] P. A. R. Ade et al. “Planck 2015 results. XIII. Cosmological parameters”. In: *Astron. Astrophys.* 594 (2016), A13. DOI: 10.1051/0004-6361/201525830. arXiv: 1502.01589 [astro-ph.CO].

[31] S. Agayeva et al. *The GRANDMA network in preparation for the fourth gravitational-wave observing run*. 2022. arXiv: 2207.10178 [astro-ph.IM].

[32] Tomas Ahumada et al. *Discovery and confirmation of the shortest gamma ray burst from a collapsar*. 2021. arXiv: 2105.05067 [astro-ph.HE].

[33] V Aivazyan et al. “GRANDMA observations of ZTF/Fink transients during summer 2021”. In: *Monthly Notices of the Royal Astronomical Society* 515.4 (July 2022), pp. 6007–6022. ISSN: 0035-8711. DOI: 10.1093/mnras/stac2054. eprint: https://academic.oup.com/mnras/article-pdf/515/4/6007/45504788/stac2054.pdf. URL: https://doi.org/10.1093/mnras/stac2054.

[34] C. Akerlof et al. “Observation of contemporaneous optical radiation from a gamma-ray burst”. In: *Nature* 398.6726 (Apr. 1999), pp. 400–402. DOI: 10.1038/18837. arXiv: astro-ph/9903271 [astro-ph].

[35] T Akutsu et al. “Overview of KAGRA: Calibration, detector characterization, physical environmental monitors, and the geophysics interferometer”. In: *Progress of Theoretical and Experimental Physics* 2021.5 (Feb. 2021). 05A102. ISSN: 2050-3911. DOI: 10.1093/ptep/ptab018. eprint: https://academic.oup.com/ptep/article-pdf/2021/5/05A102/38109702/ptab018.pdf. URL: https://doi.org/10.1093/ptep/ptab018.

[36] K. D. Alexander et al. “The Electromagnetic Counterpart of the Binary Neutron Star Merger LIGO/Virgo GW170817. VI. Radio Constraints on a Relativistic Jet and Predictions for Late-time Emission from the Kilonova Ejecta”. In: *The Astrophysical Journal Letters* 848, L21 (Oct. 2017), p. L21. DOI: 10.3847/2041-8213/aa905d. arXiv: 1710.05457 [astro-ph.HE].

[37] Annalisa Allocca et al. “Interferometer Sensing and Control for the Advanced Virgo Experiment in the O3 Scientific Run”. In: *Galaxies* 8.4 (2020). ISSN: 2075-4434. DOI: 10.3390/galaxies8040085. URL: https://www.mdpi.com/2075-4434/8/4/85.

[38] Mouza Almualla et al. “Optimizing serendipitous detections of kilonovae: cadence and filter selection”. In: *Monthly Notices of the Royal Astronomical Society* 504.2 (Apr. 2021), pp. 2822–2831. ISSN: 1365-2966. DOI: 10.1093/mnras/stab1090. URL: http://dx.doi.org/10.1093/mnras/stab1090.

[39] Pau Amaro-Seoane et al. *Laser Interferometer Space Antenna*. 2017. arXiv: 1702.00786 [astro-ph.IM].

[40] Shreya Anand et al. *Chemical Distribution of the Dynamical Ejecta in the Neutron Star Merger GW170817*. 2023. arXiv: 2307.11080 [astro-ph.HE].

[41] I. Andreoni et al. “Follow Up of GW170817 and Its Electromagnetic Counterpart by Australian-Led Observing Programmes”. In: *Publications of the Astronomical Society of Australia* 34 (2017). DOI: 10.1017/pasa.2017.65. URL: https://doi.org/10.1017%2Fpasa.2017.65.

[42] Igor Andreoni et al. “A Strategy for LSST to Unveil a Population of Kilonovae without Gravitational-wave Triggers”. In: *Publications of the Astronomical Society of the Pacific* 131.1000 (May 2019), p. 068004. DOI: 10.1088/1538-3873/ab1531. URL: https://dx.doi.org/10.1088/1538-3873/ab1531.

[43] Igor Andreoni et al. “Constraining the Kilonova Rate with Zwicky Transient Facility Searches Independent of Gravitational Wave and Short Gamma-Ray Burst Triggers”. In: *The Astrophysical Journal* 904.2 (Nov. 2020), p. 155. ISSN: 1538-4357. DOI: 10.3847/1538-4357/abbf4c. URL: http://dx.doi.org/10.3847/1538-4357/abbf4c.

[44] Igor Andreoni et al. “Enabling kilonova science with Nancy Grace Roman Space Telescope”. In: *Astroparticle Physics* 155 (2024), p. 102904. ISSN: 0927-6505. DOI: https://doi.org/10.1016/j.astropartphys.2023.102904. URL: https://www.sciencedirect.com/science/article/pii/S0927650523000907.

[45] Igor Andreoni et al. “Fast-transient Searches in Real Time with ZTFReST: Identification of Three Optically Discovered Gamma-Ray Burst Afterglows and New Constraints on the Kilonova Rate”. In: *Astrophysical Journal* 918.2, 63 (Sept. 2021), p. 63. DOI: 10.3847/1538-4357/ac0bc7. arXiv: 2104.06352 [astro-ph.HE].

[46] Igor Andreoni et al. “Target-of-opportunity Observations of Gravitational-wave Events with Vera C. Rubin Observatory”. In: *The Astrophysical Journal Supplement Series* 260.1 (May 2022), p. 18. DOI: 10.3847/1538-4365/ac617c. URL: https://dx.doi.org/10.3847/1538-4365/ac617c.

[47] Eemeli Annala et al. “Gravitational-Wave Constraints on the Neutron-Star-Matter Equation of State”. In: *Phys. Rev. Lett.* 120 (17 Apr. 2018), p. 172703. DOI: 10.1103/PhysRevLett.120.172703. URL: https://link.aps.org/doi/10.1103/PhysRevLett.120.172703.

[48] Javier M. Antelis and Claudia Moreno. “Obtaining gravitational waves from inspiral binary systems using LIGO data”. In: *The European Physical Journal Plus* 132.1 (Jan. 2017). ISSN: 2190-5444. DOI: 10.1140/epjp/i2017-11283-5. URL: http://dx.doi.org/10.1140/epjp/i2017-11283-5.

[49] S Antier et al. “GRANDMA observations of advanced LIGO’s and advanced Virgo’s third observational campaign”. In: *Monthly Notices of the Royal Astronomical Society* 497.4 (June 2020), pp. 5518–5539. ISSN: 0035-8711. DOI: 10.1093/mnras/staa1846. eprint: https://academic.oup.com/mnras/article-pdf/497/4/5518/33706664/staa1846.pdf. URL: https://doi.org/10.1093/mnras/staa1846.

[50] S Antier et al. “The first six months of the Advanced LIGO’s and Advanced Virgo’s third observing run with GRANDMA”. In: *Monthly Notices of the Royal Astronomical Society* 492.3 (Nov. 2019), pp. 3904–3927. ISSN: 0035-8711. DOI: 10.1093/mnras/stz3142. eprint: https://academic.oup.com/mnras/article-pdf/492/3/3904/32788222/stz3142.pdf. URL: https://doi.org/10.1093/mnras/stz3142.

[51] S Antier et al. “The first six months of the Advanced LIGO’s and Advanced Virgo’s third observing run with GRANDMA”. In: *Monthly Notices of the Royal Astronomical Society* 492.3 (Nov. 2019), pp. 3904–3927. ISSN: 1365-2966. DOI: 10.1093/mnras/stz3142. URL: http://dx.doi.org/10.1093/mnras/stz3142.

[52] Stefano Ascenzi et al. “A luminosity distribution for kilonovae based on short gamma-ray burst afterglows”. In: *Monthly Notices of the Royal Astronomical Society* 486.1 (Mar. 2019), pp. 672–690. ISSN: 0035-8711. DOI: 10.1093/mnras/stz891. eprint: http://oup.prod.sis.lan/mnras/article-pdf/486/1/672/28320190/stz891.pdf. URL: https://doi.org/10.1093/mnras/stz891.

[53] Gregory Ashton et al. “BILBY: A user-friendly Bayesian inference library for gravitational-wave astronomy”. In: *Astrophys. J. Suppl.* 241.2 (2019), p. 27. DOI: 10.3847/1538-4365/ab06fc. arXiv: 1811.02042 [astro-ph.IM].

[54] J.-L. Atteia et al. “The Maximum Isotropic Energy of Gamma-Ray Bursts”. In: *Astrophys. J.* 837.2, 119 (2017), p. 119. DOI: 10.3847/1538-4357/aa5ffa. arXiv: 1702.02961 [astro-ph.HE].

[55] F Aubin et al. “The MBTA pipeline for detecting compact binary coalescences in the third LIGO–Virgo observing run”. In: *Classical and Quantum Gravity* 38.9 (Apr. 2021), p. 095004. DOI: 10.1088/1361-6382/abe913. URL: https://dx.doi.org/10.1088/1361-6382/abe913.

[56] Kyle Barbary et al. “SNCosmo: Python library for supernova cosmology”. In: *Astrophysics Source Code Library* (2016).

[57] Thomas W. Baumgarte, Stuart L. Shapiro, and Masaru Shibata. “On the maximum mass of differentially rotating neutron stars”. In: *Astrophys. J. Lett.* 528 (2000), p. L29. DOI: 10.1086/312425. arXiv: astro-ph/9910565.

[58] A. Bauswein, T. W. Baumgarte, and H.-T. Janka. “Prompt Merger Collapse and the Maximum Mass of Neutron Stars”. In: *Phys. Rev. Lett.* 111 (13 Sept. 2013), p. 131101. DOI: 10.1103/PhysRevLett.111.131101. URL: https://link.aps.org/doi/10.1103/PhysRevLett.111.131101.

[59] A. Bauswein, S. Goriely, and H.-T. Janka. “Systematics of Dynamical Mass Ejection, Nucleosynthesis, and Radioactively Powered Electromagnetic Signals from Neutron-star Mergers”. In: *The Astrophysical Journal* 773.1 (2013), p. 78. URL: http://stacks.iop.org/0004-637X/773/i=1/a=78.

[60] Andreas Bauswein et al. “Neutron-star Radius Constraints from GW170817 and Future Detections”. In: *The Astrophysical Journal Letters* 850.2, L34 (Dec. 2017), p. L34. DOI: 10.3847/2041-8213/aa9994. arXiv: 1710.06843 [astro-ph.HE].

[61] Andreas Bauswein et al. “Neutron-star Radius Constraints from GW170817 and Future Detections”. In: *The Astrophysical Journal Letters* 850.2 (Nov. 2017), p. L34. DOI: 10.3847/2041-8213/aa9994. URL: https://dx.doi.org/10.3847/2041-8213/aa9994.

[62] E. C. Bellm et al. “The Zwicky Transient Facility: Surveys and Scheduler”. In: *The Astronomical Society of the Pacific* 131.6 (June 2019), p. 068003.

[63] Eric C. Bellm et al. “The Zwicky Transient Facility: Surveys and Scheduler”. In: *Publications of the Astronomical Society of the Pacific* 131.1000 (Apr. 2019), p. 068003. DOI: 10.1088/1538-3873/ab0c2a. URL: https://dx.doi.org/10.1088/1538-3873/ab0c2a.

[64] Christopher P. L. Berry et al. “PARAMETER ESTIMATION FOR BINARY NEUTRON-STAR COALESCENCES WITH REALISTIC NOISE DURING THE ADVANCED LIGO ERA”. In: *The Astrophysical Journal* 804.2 (May 2015), p. 114. DOI: 10.1088/0004-637X/804/2/114. URL: https://dx.doi.org/10.1088/0004-637X/804/2/114.

[65] Swetha Bhagwat et al. “On choosing the start time of binary black hole ringdowns”. In: *Phys. Rev. D* 97 (10 May 2018), p. 104065. DOI: 10.1103/PhysRevD.97.104065. URL: https://link.aps.org/doi/10.1103/PhysRevD.97.104065.

[66] Federica B. Bianco et al. “Optimization of the Observing Cadence for the Rubin Observatory Legacy Survey of Space and Time: A Pioneering Process of Community-focused Experimental Design”. In: *The Astrophysical Journal Supplement Series* 258.1 (Dec. 2021), p. 1. DOI: 10.3847/1538-4365/ac3e72. URL: https://dx.doi.org/10.3847/1538-4365/ac3e72.

[67] C. M. Biwer et al. “PyCBC Inference: A Python-based parameter estimation toolkit for compact binary coalescence signals”. In: *Publ. Astron. Soc. Pac.* 131.996 (2019), p. 024503. DOI: 10.1088/1538-3873/aaef0b. arXiv: 1807.10312 [astro-ph.IM].

[68] S. Bloemen et al. “The BlackGEM Array: Searching for Gravitational Wave Source Counterparts to Study Ultra-Compact Binaries”. In: *Living Together: Planets, Host Stars and Binaries*. Ed. by S. M. Rucinski, G. Torres, and M. Zejda. Vol. 496. Astronomical Society of the Pacific Conference Series. July 2015, p. 254.

[69] Steven Bloemen. *High-Precision Studies of Compact Variable Stars*. Springer, 2014.

[70] Joshua S. Bloom et al. *Astro2010 Decadal Survey Whitepaper: Coordinated Science in the Gravitational and Electromagnetic Skies*. Version arXiv:0902.1527. Provided by the SAO/NASA Astrophysics Data System. Feb. 2009. DOI: 10.48550/arXiv.0902.1527. arXiv: 0902.1527 [astro-ph.CO]. URL: https://ui.adsabs.harvard.edu/abs/2009arXiv0902.1527B.

[71] Luca Boccioli and Lorenzo Roberti. "The Physics of Core-Collapse Supernovae: Explosion Mechanism and Explosive Nucleosynthesis". In: *Universe* 10.3 (2024). ISSN: 2218-1997. DOI: 10.3390/universe10030148. URL: https://www.mdpi.com/2218-1997/10/3/148.

[72] David Branch, E. Baron, and David J. Jeffery. *Optical Spectra of Supernovae*. 2001. arXiv: astro-ph/0111573 [astro-ph].

[73] Bernd Brügmann et al. "Numerical Simulations of Compact Binary Systems". In: *High Performance Computing in Science and Engineering, Garching/Munich 2007: Transactions of the Third Joint HLRB and KONWIHR Status and Result Workshop, Dec. 3–4, 2007, Leibniz Supercomputing Centre, Garching/-Munich, Germany*. Springer. 2009, pp. 3–18.

[74] A. Buikema et al. "Sensitivity and performance of the Advanced LIGO detectors in the third observing run". In: *Phys. Rev. D* 102 (6 Sept. 2020), p. 062003. DOI: 10.1103/PhysRevD.102.062003. URL: https://link.aps.org/doi/10.1103/PhysRevD.102.062003.

[75] M Bulla. "possis: predicting spectra, light curves, and polarization for multi-dimensional models of supernovae and kilonovae". In: *Monthly Notices of the Royal Astronomical Society* 489.4 (Sept. 2019), pp. 5037–5045. DOI: 10.1093/mnras/stz2495. URL: https://doi.org/10.1093%2Fmnras%2Fstz2495.

[76] M Bulla. "possis: predicting spectra, light curves, and polarization for multi-dimensional models of supernovae and kilonovae". In: *Monthly Notices of the Royal Astronomical Society* 489.4 (Sept. 2019), pp. 5037–5045. ISSN: 0035-8711. DOI: 10.1093/mnras/stz2495. eprint: https://academic.oup.com/mnras/article-pdf/489/4/5037/30739278/stz2495.pdf. URL: https://doi.org/10.1093/mnras/stz2495.

[77] M Bulla. "The critical role of nuclear heating rates, thermalization efficiencies, and opacities for kilonova modelling and parameter inference". In: *Mon. Not. Roy. Astron. Soc.* 520.2 (2023), pp. 2558–2570. DOI: 10.1093/mnras/stad232. arXiv: 2211.14348 [astro-ph.HE].

[78] A. Buonanno and T. Damour. "Effective one-body approach to general relativistic two-body dynamics". In: *Phys. Rev. D* 59 (8 Mar. 1999), p. 084006. DOI: 10.1103/PhysRevD.59.084006. URL: https://link.aps.org/doi/10.1103/PhysRevD.59.084006.

[79] M. Campanelli et al. “Accurate Evolutions of Orbiting Black-Hole Binaries without Excision”. In: *Phys. Rev. Lett.* 96 (11 Mar. 2006), p. 111101. DOI: 10.1103/PhysRevLett.96.111101. URL: https://link.aps.org/doi/10.1103/PhysRevLett.96.111101.

[80] Michele Cantiello et al. “A Precise Distance to the Host Galaxy of the Binary Neutron Star Merger GW170817 Using Surface Brightness Fluctuations”. In: *The Astrophysical Journal* 854.2 (Feb. 2018), p. L31. DOI: 10.3847/2041-8213/aaad64. URL: https://doi.org/10.3847%2F2041-8213%2Faaad64.

[81] Tito Dal Canton et al. “Real-time Search for Compact Binary Mergers in Advanced LIGO and Virgo’s Third Observing Run Using PyCBC Live”. In: *The Astrophysical Journal* 923.2 (Dec. 2021), p. 254. DOI: 10.3847/1538-4357/ac2f9a. URL: https://dx.doi.org/10.3847/1538-4357/ac2f9a.

[82] Brandon Carter. “Global structure of the Kerr family of gravitational fields”. In: *Physical Review* 174.5 (1968), p. 1559.

[83] S. Chandrasekhar. “The Maximum Mass of Ideal White Dwarfs”. In: *Astrophysical Journal* 74 (July 1931), p. 81. DOI: 10.1086/143324.

[84] Eve A. Chase et al. *Kilonova Detectability with Wide-Field Instruments*. 2021. arXiv: 2105.12268 [astro-ph.HE].

[85] Sylvain Chaty. *Accreting Binaries*. 2514-3433. IOP Publishing, 2022. ISBN: 978-0-7503-3887-5. DOI: 10.1088/2514-3433/ac595f. URL: https://dx.doi.org/10.1088/2514-3433/ac595f.

[86] Sushant Sharma Chaudhary et al. *Low-latency gravitational wave alert products and their performance in anticipation of the fourth LIGO-Virgo-KAGRA observing run*. 2023. arXiv: 2308.04545 [astro-ph.HE].

[87] Hsin-Yu Chen et al. “Distance measures in gravitational-wave astrophysics and cosmology”. In: *Classical and Quantum Gravity* 38.5 (Jan. 2021), p. 055010. DOI: 10.1088/1361-6382/abd594. URL: https://dx.doi.org/10.1088/1361-6382/abd594.

[88] R. Chornock et al. “The Electromagnetic Counterpart of the Binary Neutron Star Merger LIGO/Virgo GW170817. IV. Detection of Near-infrared Signatures of r-process Nucleosynthesis with Gemini-South”. In: *The Astrophysical Journal Letters* 848.2 (2017), p. L19. URL: http://stacks.iop.org/2041-8205/848/i=2/a=L19.

[89] The LIGO Scientific Collaboration, the Virgo Collaboration, and the KAGRA Collaboration. *Observation of Gravitational Waves from the Coalescence of a* $2.5-4.5\ M_{\odot}$ *Compact Object and a Neutron Star*. 2024. arXiv: 2404.04248 [astro-ph.HE].

[90] The LIGO Scientific Collaboration et al. *Sensitivity to Gravitational Waves from Compact Binary Coalescences Achieved during LIGO's Fifth and Virgo's First Science Run*. 2010. arXiv: 1003.2481 [gr-qc].

[91] Alberto Colombo et al. "Multi-messenger Observations of Binary Neutron Star Mergers in the O4 Run". In: *Astrophys. J.* 937.2 (2022), p. 79. DOI: 10.3847/1538-4357/ac8d00. arXiv: 2204.07592 [astro-ph.HE].

[92] Neil Cornish and Travis Robson. "Galactic binary science with the new LISA design". In: *Journal of Physics: Conference Series* 840 (May 2017), p. 012024. DOI: 10.1088/1742-6596/840/1/012024. URL: https://doi.org/10.1088%2F1742-6596%2F840%2F1%2F012024.

[93] Michael W Coughlin et al. "Constraints on the neutron star equation of state from AT2017gfo using radiative transfer simulations". In: *Monthly Notices of the Royal Astronomical Society* 480.3 (2018), pp. 3871–3878. DOI: 10.1093/mnras/sty2174. eprint: /oup/backfile/content_public/journal/mnras/480/3/10.1093_mnras_sty2174/1/sty2174.pdf. URL: http://dx.doi.org/10.1093/mnras/sty2174.

[94] Michael W Coughlin et al. "Multimessenger Bayesian parameter inference of a binary neutron star merger". In: *Monthly Notices of the Royal Astronomical Society: Letters* 489.1 (Aug. 2019), pp. L91–L96. ISSN: 1745-3925. DOI: 10.1093/mnrasl/slz133. eprint: http://oup.prod.sis.lan/mnrasl/article-pdf/489/1/L91/30032497/slz133.pdf. URL: https://doi.org/10.1093/mnrasl/slz133.

[95] Michael W Coughlin et al. "Optimizing Multi-Telescope Observations of Gravitational-Wave Counterparts". In: *Monthly Notices of the Royal Astronomical Society* (Sept. 2019). stz2485. ISSN: 0035-8711. DOI: 10.1093/mnras/stz2485. eprint: http://oup.prod.sis.lan/mnras/advance-article-pdf/doi/10.1093/mnras/stz2485/29808472/stz2485.pdf. URL: https://doi.org/10.1093/mnras/stz2485.

[96] Michael W Coughlin et al. "Optimizing searches for electromagnetic counterparts of gravitational wave triggers". In: *Monthly Notices of the Royal Astronomical Society* 478.1 (Apr. 2018), pp. 692–702. ISSN: 0035-8711. DOI: 10.1093/mnras/sty1066. eprint: https://academic.oup.com/mnras/article-pdf/478/1/692/25004514/sty1066.pdf. URL: https://doi.org/10.1093/mnras/sty1066.

[97] Michael W. Coughlin et al. "2900 Square Degree Search for the Optical Counterpart of Short Gamma-Ray Burst GRB 180523B with the Zwicky Transient Facility". In: *Publications of the Astronomical Society of the Pacific* 131.998 (Feb. 2019), p. 048001. DOI: 10.1088/1538-3873/aaff99. URL: https://dx.doi.org/10.1088/1538-3873/aaff99.

[98] Michael W. Coughlin et al. "A Data Science Platform to Enable Time-domain Astronomy". In: *The Astrophysical Journal Supplement Series* 267.2 (July 2023), p. 31. DOI: 10.3847/1538-4365/acdee1. URL: https://dx.doi.org/10.3847/1538-4365/acdee1.

[99] Michael W. Coughlin et al. “GROWTH on S190425z: Searching Thousands of Square Degrees to Identify an Optical or Infrared Counterpart to a Binary Neutron Star Merger with the Zwicky Transient Facility and Palomar Gattini-IR”. In: *The Astrophysical Journal Letters* 885.1 (Oct. 2019), p. L19. DOI: 10.3847/2041-8213/ab4ad8. URL: https://dx.doi.org/10.3847/2041-8213/ab4ad8.

[100] Michael W. Coughlin et al. “Measuring the Hubble constant with a sample of kilonovae”. In: *Nature Communications* 11.1 (2020), p. 4129. DOI: 10.1038/s41467-020-17998-5. URL: https://doi.org/10.1038/s41467-020-17998-5.

[101] Michael W. Coughlin et al. “Standardizing kilonovae and their use as standard candles to measure the Hubble constant”. In: *Phys. Rev. Research* 2 (2 Apr. 2020), p. 022006. DOI: 10.1103/PhysRevResearch.2.022006. URL: https://link.aps.org/doi/10.1103/PhysRevResearch.2.022006.

[102] Michael W. Coughlin et al. “Standardizing kilonovae and their use as standard candles to measure the Hubble constant”. In: *Phys. Rev. Research* 2 (2 Apr. 2020), p. 022006. DOI: 10.1103/PhysRevResearch.2.022006. URL: https://link.aps.org/doi/10.1103/PhysRevResearch.2.022006.

[103] D. A. Coulter et al. “Swope Supernova Survey 2017a (SSS17a), the optical counterpart to a gravitational wave source”. In: *Science* 358 (Dec. 2017), pp. 1556–1558. DOI: 10.1126/science.aap9811. arXiv: 1710.05452 [astro-ph.HE].

[104] D. A. Coulter et al. “Swope Supernova Survey 2017a (SSS17a), the optical counterpart to a gravitational wave source”. In: *Science* 358.6370 (Dec. 2017), pp. 1556–1558. ISSN: 1095-9203. DOI: 10.1126/science.aap9811. URL: http://dx.doi.org/10.1126/science.aap9811.

[105] Coulter et al. “Swope Supernova Survey 2017a (SSS17a), the optical counterpart to a gravitational wave source”. In: *Science* 358.6370 (2017), pp. 1556–1558. DOI: 10.1126/science.aap9811.

[106] P. S. Cowperthwaite, E. Berger, V. A. Villar, et al. “The Electromagnetic Counterpart of the Binary Neutron Star Merger LIGO/Virgo GW170817. II. UV, Optical, and Near-infrared Light Curves and Comparison to Kilonova Models”. In: *The Astrophysical Journal Letters* 848, L17 (Oct. 2017), p. L17. DOI: 10.3847/2041-8213/aa8fc7. arXiv: 1710.05840 [astro-ph.HE].

[107] Kishalay De et al. “The Zwicky Transient Facility Census of the Local Universe. I. Systematic Search for Calcium-rich Gap Transients Reveals Three Related Spectroscopic Subclasses”. In: *The Astrophysical Journal* 905.1 (Dec. 2020), p. 58. DOI: 10.3847/1538-4357/abb45c. URL: https://doi.org/10.3847%2F1538-4357%2Fabb45c.

[108] Richard Dekany et al. “The Zwicky Transient Facility: Observing System”. In: *Publications of the Astronomical Society of the Pacific* 132.1009 (Jan. 2020), p. 038001. DOI: 10.1088/1538-3873/ab4ca2. URL: https://doi.org/10.1088%2F1538-3873%2Fab4ca2.

[109] Richard Dekany et al. “The Zwicky Transient Facility: Observing System”. In: *Publications of the Astronomical Society of the Pacific* 132.1009 (Jan. 2020), p. 038001. DOI: 10.1088/1538-3873/ab4ca2. URL: https://doi.org/10.1088%2F1538-3873%2Fab4ca2.

[110] James B. Dent et al. “Gravitational waves from a black hole orbiting in a wormhole geometry”. In: *Phys. Rev. D* 104 (4 Aug. 2021), p. 044030. DOI: 10.1103/PhysRevD.104.044030. URL: https://link.aps.org/doi/10.1103/PhysRevD.104.044030.

[111] S. Dhawan et al. “Constraining the Observer Angle of the Kilonova AT2017gfo Associated with GW170817: Implications for the Hubble Constant”. In: *Astrophysical Journal* 888.2, 67 (Jan. 2020), p. 67. DOI: 10.3847/1538-4357/ab5799. arXiv: 1909.13810 [astro-ph.HE].

[112] Tim Dietrich et al. “Improving the NRTidal model for binary neutron star systems”. In: *Phys. Rev. D* 100.4 (2019), p. 044003. DOI: 10.1103/PhysRevD.100.044003. arXiv: 1905.06011 [gr-qc].

[113] Tim Dietrich et al. “Multimessenger constraints on the neutron-star equation of state and the Hubble constant”. In: *Science* 370.6523 (Dec. 2020), pp. 1450–1453. DOI: 10.1126/science.abb4317. arXiv: 2002.11355 [astro-ph.HE].

[114] Tim Dietrich et al. “New Constraints on the Supranuclear Equation of State and the Hubble Constant from Nuclear Physics – Multi-Messenger Astronomy”. In: *Science* 370 (2020), pp. 1450–1453. DOI: 10.1126/science.abb4317. arXiv: 2002.11355 [astro-ph.HE].

[115] Z. Doctor et al. “Black Hole Coagulation: Modeling Hierarchical Mergers in Black Hole Populations”. In: *Astrophysical Journal* 893.1, 35 (Apr. 2020), p. 35. DOI: 10.3847/1538-4357/ab7fac. arXiv: 1911.04424 [astro-ph.HE].

[116] J. C. Driggers et al. “Improving astrophysical parameter estimation via offline noise subtraction for Advanced LIGO”. In: *Phys. Rev. D* 99 (4 Feb. 2019), p. 042001. DOI: 10.1103/PhysRevD.99.042001. URL: https://link.aps.org/doi/10.1103/PhysRevD.99.042001.

[117] Peter P Eggleton. “Approximations to the radii of Roche lobes”. In: *Astrophysical Journal, Part 1 (ISSN 0004-637X), vol. 268, May 1, 1983, p. 368, 369.* 268 (1983), p. 368.

[118] Albert Einstein. *Näherungsweise Integration der Feldgleichungen der Gravitation*. Sitzungsberichte der Königlich Preußischen Akademie der Wissenschaften (Berlin). Jan. 1916.

[119] Albert Einstein. *Über Gravitationswellen*. Sitzungsberichte der Königlich Preußischen Akademie der Wissenschaften (Berlin). Jan. 1918.

[120] E. Epelbaum, H.-W. Hammer, and Ulf-G. Meißner. "Modern theory of nuclear forces". In: *Rev. Mod. Phys.* 81 (4 Dec. 2009), pp. 1773–1825. DOI: 10.1103/RevModPhys.81.1773. URL: https://link.aps.org/doi/10.1103/RevModPhys.81.1773.

[121] P. A. Evans et al. "Swift and NuSTAR observations of GW170817: Detection of a blue kilonova". In: *Science* 358.6370 (Dec. 2017), pp. 1565–1570. DOI: 10.1126/science.aap9580. arXiv: 1710.05437 [astro-ph.HE].

[122] Amanda Farah et al. "Bridging the Gap: Categorizing Gravitational-wave Events at the Transition between Neutron Stars and Black Holes". In: *The Astrophysical Journal* 931.2 (May 2022), p. 108. DOI: 10.3847/1538-4357/ac5f03. URL: https://doi.org/10.3847/1538-4357/ac5f03.

[123] Will M. Farr et al. "Counting and confusion: Bayesian rate estimation with multiple populations". In: *Phys. Rev. D* 91 (2 Jan. 2015), p. 023005. DOI: 10.1103/PhysRevD.91.023005. URL: https://link.aps.org/doi/10.1103/PhysRevD.91.023005.

[124] Will M. Farr et al. "The Mass Distribution of Stellar-mass Black Holes". In: *Astrophysical Journal* 741.2, 103 (Nov. 2011), p. 103. DOI: 10.1088/0004-637X/741/2/103. arXiv: 1011.1459 [astro-ph.GA].

[125] Stephen M. Feeney et al. "Prospects for Resolving the Hubble Constant Tension with Standard Sirens". In: *Phys. Rev. Lett.* 122 (6 Feb. 2019), p. 061105. DOI: 10.1103/PhysRevLett.122.061105. URL: https://link.aps.org/doi/10.1103/PhysRevLett.122.061105.

[126] F. Feroz, M. P. Hobson, and M. Bridges. "MultiNest: an efficient and robust Bayesian inference tool for cosmology and particle physics". In: *Monthly Notices of the Royal Astronomical Society* 398.4 (Sept. 2009), pp. 1601–1614. ISSN: 0035-8711. DOI: 10.1111/j.1365-2966.2009.14548.x. eprint: https://academic.oup.com/mnras/article-pdf/398/4/1601/3039078/mnras0398-1601.pdf. URL: https://doi.org/10.1111/j.1365-2966.2009.14548.x.

[127] Lee Samuel Finn. "Binary inspiral, gravitational radiation, and cosmology". In: *Phys. Rev. D* 53 (6 Mar. 1996), pp. 2878–2894. DOI: 10.1103/PhysRevD.53.2878. URL: https://link.aps.org/doi/10.1103/PhysRevD.53.2878.

[128] Lee Samuel Finn and David F. Chernoff. "Observing binary inspiral in gravitational radiation: One interferometer". In: *Phys. Rev. D* 47 (6 Mar. 1993), pp. 2198–2219. DOI: 10.1103/PhysRevD.47.2198. URL: https://link.aps.org/doi/10.1103/PhysRevD.47.2198.

[129] Maya Fishbach, Reed Essick, and Daniel E. Holz. "Does Matter Matter? Using the Mass Distribution to Distinguish Neutron Stars and Black Holes". In: *The Astrophysical Journal Letters* 899.1, L8 (Aug. 2020), p. L8. DOI: 10.3847/2041-8213/aba7b6. arXiv: 2006.13178 [astro-ph.HE].

[130] Maya Fishbach and Daniel E. Holz. "Picky Partners: The Pairing of Component Masses in Binary Black Hole Mergers". In: *The Astrophysical Journal Letters* 891.1, L27 (Mar. 2020), p. L27. DOI: 10.3847/2041-8213/ab7247. arXiv: 1905.12669 [astro-ph.HE].

[131] Daniel Foreman-Mackey. "corner.py: Scatterplot matrices in Python". In: *Journal of Open Source Software* 1.2 (2016), p. 24. DOI: 10.21105/joss.00024. URL: https://doi.org/10.21105/joss.00024.

[132] F. Förster et al. "The Automatic Learning for the Rapid Classification of Events (ALeRCE) Alert Broker". In: *The Astronomical Journal* 161.5 (Apr. 2021), p. 242. DOI: 10.3847/1538-3881/abe9bc. URL: https://dx.doi.org/10.3847/1538-3881/abe9bc.

[133] Francois Foucart, Tanja Hinderer, and Samaya Nissanke. "Remnant baryon mass in neutron star-black hole mergers: Predictions for binary neutron star mimickers and rapidly spinning black holes". In: *Phys. Rev. D* 98.8 (2018), p. 081501. DOI: 10.1103/PhysRevD.98.081501. arXiv: 1807.00011 [astro-ph.HE].

[134] R. H. Fowler. "On Dense Matter". In: *Monthly Notices of the Royal Astronomical Society* 87.2 (Dec. 1926), pp. 114–122. ISSN: 0035-8711. DOI: 10.1093/mnras/87.2.114. eprint: https://academic.oup.com/mnras/article-pdf/87/2/114/3623303/mnras87-0114.pdf. URL: https://doi.org/10.1093/mnras/87.2.114.

[135] A. S. Fruchter et al. "Long γ-ray bursts and core-collapse supernovae have different environments". In: *Nature* 441.7092 (May 2006), pp. 463–468. ISSN: 1476-4687. DOI: 10.1038/nature04787. URL: https://doi.org/10.1038/nature04787.

[136] Jonathan P. Gardner et al. "The James Webb Space Telescope". In: *Space Science Reviews* 123.4 (Apr. 2006), pp. 485–606. ISSN: 1572-9672. DOI: 10.1007/s11214-006-8315-7. URL: http://dx.doi.org/10.1007/s11214-006-8315-7.

[137] Neil Gehrels et al. "The Swift gamma-ray burst mission". In: *The Astrophysical Journal* 611.2 (2004), p. 1005.

[138] Patrick Godwin et al. "Incorporation of Statistical Data Quality Information into the GstLAL Search Analysis". In: *arXiv e-prints*, arXiv:2010.15282 (Oct. 2020), arXiv:2010.15282. arXiv: 2010.15282 [gr-qc].

[139] A. Goldstein et al. “An Ordinary Short Gamma-Ray Burst with Extraordinary Implications: Fermi-GBM Detection of GRB 170817A”. In: *The Astrophysical Journal* 848.2 (Oct. 2017), p. L14. DOI: 10.3847/2041-8213/aa8f41. URL: https://doi.org/10.3847/2041-8213/aa8f41.

[140] K. M. Górski et al. “HEALPix: A Framework for High-Resolution Discretization and Fast Analysis of Data Distributed on the Sphere”. In: *The Astrophysical Journal* 622.2 (Apr. 2005), p. 759. DOI: 10.1086/427976. URL: https://dx.doi.org/10.1086/427976.

[141] Eric Gourgoulhon. “Relativité générale”. Master. Lecture. Année universitaire 2013-2014
Observatoire de Paris, Mar. 2014. URL: https://cel.hal.science/cel-00366315.

[142] Matthew J. Graham et al. “The Zwicky Transient Facility: Science Objectives”. In: *Publications of the Astronomical Society of the Pacific* 131.1001 (May 2019), p. 078001. DOI: 10.1088/1538-3873/ab006c.

[143] James Guillochon et al. “MOSFiT: Modular Open Source Fitter for Transients”. In: *The Astrophysical Journal Supplement Series* 236.1 (May 2018), p. 6. DOI: 10.3847/1538-4365/aab761. URL: https://dx.doi.org/10.3847/1538-4365/aab761.

[144] J. Guy et al. “The Supernova Legacy Survey 3-year sample: Type Ia supernovae photometric distances and cosmological constraints”. In: *Astronomy & Astrophysics* 523, A7 (Nov. 2010), A7. DOI: 10.1051/0004-6361/201014468. arXiv: 1010.4743 [astro-ph.CO].

[145] Julien Guy et al. “SALT2: Using distant supernovae to improve the use of Type Ia supernovae as distance indicators”. In: *Astron. Astrophys.* 466 (2007), pp. 11–21. DOI: 10.1051/0004-6361:20066930. arXiv: astro-ph/0701828 [ASTRO-PH].

[146] R. Hainich et al. “The Metallicity Dependence of WR Winds”. In: 329 (Nov. 2017). Provided by the SAO/NASA Astrophysics Data System. DOI: 10.1017/S1743921317003623. URL: https://ui.adsabs.harvard.edu/abs/2017IAUS..329.....E.

[147] K. Hebeler et al. “Equation of State and Neutron Star Properties Constrained by Nuclear Physics and Observation”. In: *The Astrophysical Journal* 773.1 (July 2013), p. 11. DOI: 10.1088/0004-637X/773/1/11. URL: https://dx.doi.org/10.1088/0004-637X/773/1/11.

[148] Edward Higson et al. “Dynamic nested sampling: an improved algorithm for parameter estimation and evidence calculation”. In: *Statistics and Computing* 29.5 (Sept. 2019), pp. 891–913. DOI: 10.1007/s11222-018-9844-0. arXiv: 1704.03459 [stat.CO].

[149] Shaun Hooper et al. “Summed parallel infinite impulse response filters for low-latency detection of chirping gravitational waves”. In: *Phys. Rev. D* 86 (2 July 2012), p. 024012. DOI: 10.1103/PhysRevD.86.024012. URL: https://link.aps.org/doi/10.1103/PhysRevD.86.024012.

[150] K. Hotokezaka et al. “A Hubble constant measurement from superluminal motion of the jet in GW170817”. In: *Nature Astronomy* 3 (July 2019), pp. 940–944. DOI: 10.1038/s41550-019-0820-1. arXiv: 1806.10596 [astro-ph.CO].

[151] Kenta Hotokezaka et al. “A Hubble constant measurement from superluminal motion of the jet in GW170817”. In: *Nature Astron.* (2019). DOI: 10.1038/s41550-019-0820-1. arXiv: 1806.10596 [astro-ph.CO].

[152] Kenta Hotokezaka et al. “A Hubble constant measurement from superluminal motion of the jet in GW170817”. In: *Nature Astron.* 3.10 (2019), pp. 940–944. DOI: 10.1038/s41550-019-0820-1. arXiv: 1806.10596 [astro-ph.CO].

[153] Edwin Hubble. “A relation between distance and radial velocity among extra-galactic nebulae”. In: *Proceedings of the National Academy of Sciences* 15.3 (1929), pp. 168–173. DOI: 10.1073/pnas.15.3.168. eprint: https://www.pnas.org/doi/pdf/10.1073/pnas.15.3.168. URL: https://www.pnas.org/doi/abs/10.1073/pnas.15.3.168.

[154] Jarrod R. Hurley, Christopher A. Tout, and Onno R. Pols. “Evolution of binary stars and the effect of tides on binary populations”. In: *Monthly Notices of the Royal Astronomical Society* 329.4 (Feb. 2002), pp. 897–928. ISSN: 0035-8711. DOI: 10.1046/j.1365-8711.2002.05038.x. eprint: https://academic.oup.com/mnras/article-pdf/329/4/897/18418535/329-4-897.pdf. URL: https://doi.org/10.1046/j.1365-8711.2002.05038.x.

[155] S. Huth et al. “Constraining Neutron-Star Matter with Microscopic and Macroscopic Collisions”. In: *Nature* 606 (2022), pp. 276–280. DOI: 10.1038/s41586-022-04750-w. arXiv: 2107.06229 [nucl-th].

[156] Željko Ivezić et al. “LSST: From Science Drivers to Reference Design and Anticipated Data Products”. In: *Astrophysical Journal* 873.2, 111 (Mar. 2019), p. 111. DOI: 10.3847/1538-4357/ab042c. arXiv: 0805.2366 [astro-ph].

[157] Justin Janquart. *RelativeBilbying: a package for relative binning with bilby*. https://github.com/lemnis12/relativebilbying. 2022.

[158] Zhi-Ping Jin et al. “The Detection of an Extraordinarily-Luminous High-Redshift Optical/Ultraviolet Flare by Swift/UVOT”. In: *arXiv e-prints* (2023). arXiv: 2301.02407 [astro-ph.HE].

[159] O. Just et al. “Comprehensive nucleosynthesis analysis for ejecta of compact binary mergers”. In: *Monthly Notices of the Royal Astronomical Society* 448.1 (2015), pp. 541–567. DOI: 10.1093/mnras/stv009.

[160] Daniel Kasen et al. “Origin of the heavy elements in binary neutron-star mergers from a gravitational-wave event”. In: *Nature* 551.7678 (Oct. 2017), pp. 80–84. ISSN: 1476-4687. DOI: 10.1038/nature24453. URL: http://dx.doi.org/10.1038/nature24453.

[161] Mansi M. Kasliwal et al. “Kilonova Luminosity Function Constraints Based on Zwicky Transient Facility Searches for 13 Neutron Star Merger Triggers during O3”. In: *Astrophysical Journal* 905.2, 145 (Dec. 2020), p. 145. DOI: 10.3847/1538-4357/abc335. arXiv: 2006.11306 [astro-ph.HE].

[162] W. D. Kenworthy et al. “SALT3: An Improved Type Ia Supernova Model for Measuring Cosmic Distances”. In: *The Astrophysical Journal* 923.2 (Dec. 2021), p. 265. DOI: 10.3847/1538-4357/ac30d8. URL: https://dx.doi.org/10.3847/1538-4357/ac30d8.

[163] R. Weizmann Kiendrebeogo et al. “Updated Observing Scenarios and Multi-messenger Implications for the International Gravitational-wave Networks O4 and O5”. In: *The Astrophysical Journal* 958.2 (Nov. 2023), p. 158. ISSN: 1538-4357. DOI: 10.3847/1538-4357/acfcb1. URL: http://dx.doi.org/10.3847/1538-4357/acfcb1.

[164] R. Weizmann Kiendrebeogo et al. *Updated simulation of the next O4 and O5 observation and detection scenarios of the LIGO- Virgo-KAGRA collaboration using the LRR distribution described in Petrov et al.2022 (September 2022 edition).* Version 1. Feb. 2023. DOI: 10.5281/zenodo.7623166. URL: https://doi.org/10.5281/zenodo.7623166.

[165] Diederik P. Kingma and Jimmy Ba. “Adam: A Method for Stochastic Optimization”. In: *arXiv e-prints*, arXiv:1412.6980 (Dec. 2014), arXiv:1412.6980. DOI: 10.48550/arXiv.1412.6980. arXiv: 1412.6980 [cs.LG].

[166] S. Klimenko et al. “Method for detection and reconstruction of gravitational wave transients with networks of advanced detectors”. In: *Phys. Rev. D* 93 (4 Feb. 2016), p. 042004. DOI: 10.1103/PhysRevD.93.042004. URL: https://link.aps.org/doi/10.1103/PhysRevD.93.042004.

[167] Oleg Korobkin et al. “Axisymmetric Radiative Transfer Models of Kilonovae”. In: *The Astrophysical Journal* 910.2 (Apr. 2021), p. 116. DOI: 10.3847/1538-4357/abe1b5. URL: https://dx.doi.org/10.3847/1538-4357/abe1b5.

[168] Kenneth S. Krane. *Introductory Nuclear Physics*. 1987.

[169] Christian Jürgen Krüger and Francois Foucart. “Estimates for Disk and Ejecta Masses Produced in Compact Binary Mergers”. In: *Phys. Rev. D* 101.10 (2020), p. 103002. DOI: 10.1103/PhysRevD.101.103002. arXiv: 2002.07728 [astro-ph.HE].

[170] V. G. Kryvdyk. “Gravitational Collapse of Stars and the Methods of its Observations”. In: *Odessa Astronomical Publications* 28 (Jan. 2015), p. 21.

[171] S. R. Kulkarni et al. *Science with the Ultraviolet Explorer (UVEX)*. 2023. arXiv: 2111.15608 [astro-ph.GA].

[172] S. R. Kulkarni et al. "The Afterglow, Redshift and Extreme Energetics of the Gamma-Ray Burst of 23 January 1999". In: *Nature* 398.6726 (1999), pp. 389–394. DOI: 10.1038/18821. arXiv: astro-ph/9902272 [astro-ph].

[173] Xiaoyu Lai, Enping Zhou, and Renxin Xu. "Strangeons constitute bulk strong matter: Test using GW 170817". In: *The European Physical Journal A* 55.4 (Apr. 2019), p. 60. ISSN: 1434-601X. DOI: 10.1140/epja/i2019-12720-8. URL: https://doi.org/10.1140/epja/i2019-12720-8.

[174] F Lamy et al. "Imaging a non-singular rotating black hole at the center of the Galaxy". In: *Classical and Quantum Gravity* 35.11 (May 2018), p. 115009. DOI: 10.1088/1361-6382/aabd97. URL: https://doi.org/10.1088%2F1361-6382%2Faabd97.

[175] J. M. Lattimer and D. N. Schramm. "Black-hole-neutron-star collisions". In: *The Astrophysical Journal Letters* 192 (Sept. 1974), pp. L145–L147. DOI: 10.1086/181612.

[176] Jessica Lawrence et al. "A stochastic search for intermittent gravitational-wave backgrounds". In: *Phys. Rev. D* 107 (10 May 2023), p. 103026. DOI: 10.1103/PhysRevD.107.103026. URL: https://link.aps.org/doi/10.1103/PhysRevD.107.103026.

[177] Isaac Legred et al. "Impact of the PSR J0740 + 6620 radius constraint on the properties of high-density matter". In: *Phys. Rev. D* 104 (6 Sept. 2021), p. 063003. DOI: 10.1103/PhysRevD.104.063003. URL: https://link.aps.org/doi/10.1103/PhysRevD.104.063003.

[178] G. Lemaître. "Un Univers homogène de masse constante et de rayon croissant rendant compte de la vitesse radiale des nébuleuses extra-galactiques". In: *Annales de la Société Scientifique de Bruxelles* 47 (Jan. 1927), pp. 49–59.

[179] Andrew Levan et al. "GRB 020410: A Gamma-Ray Burst Afterglow Discovered by Its Supernova Light". In: *Astrophysical Journal* 624.2 (May 2005), pp. 880–888. DOI: 10.1086/428657. arXiv: astro-ph/0403450 [astro-ph].

[180] Li-Xin Li and Bohdan Paczynski. "Transient Events from Neutron Star Mergers". In: *The Astrophysical Journal Letters* 507.1 (1998), p. L59. URL: http://stacks.iop.org/1538-4357/507/i=1/a=L59.

[181] Li-Xin Li and Bohdan Paczyński. "Transient Events from Neutron Star Mergers". In: *The Astrophysical Journal* 507.1 (Nov. 1998), pp. L59–L62. DOI: 10.1086/311680. URL: https://doi.org/10.1086/311680.

[182] Jonas Lippuner et al. “Signatures of hypermassive neutron star lifetimes on r-process nucleosynthesis in the disc ejecta from neutron star mergers”. In: *Monthly Notices of the Royal Astronomical Society* 472.1 (Aug. 2017), pp. 904–918. ISSN: 0035-8711. DOI: 10.1093/mnras/stx1987. eprint: https://academic.oup.com/mnras/article-pdf/472/1/904/19717364/stx1987.pdf. URL: https://doi.org/10.1093/mnras/stx1987.

[183] Geoffrey Lovelace et al. “Nearly extremal apparent horizons in simulations of merging black holes”. In: *Classical and Quantum Gravity* 32.6 (Feb. 2015), p. 065007. DOI: 10.1088/0264-9381/32/6/065007. URL: https://dx.doi.org/10.1088/0264-9381/32/6/065007.

[184] LSC et al. “Advanced LIGO”. In: *Classical and Quantum Gravity* 32.7 (Mar. 2015), p. 074001. DOI: 10.1088/0264-9381/32/7/074001. URL: https://dx.doi.org/10.1088/0264-9381/32/7/074001.

[185] Jing Luan et al. “Towards low-latency real-time detection of gravitational waves from compact binary coalescences in the era of advanced detectors”. In: *Phys. Rev. D* 85 (10 May 2012), p. 102002. DOI: 10.1103/PhysRevD.85.102002. URL: https://link.aps.org/doi/10.1103/PhysRevD.85.102002.

[186] R. Machleidt and D.R. Entem. “Chiral effective field theory and nuclear forces”. In: *Physics Reports* 503.1 (2011), pp. 1–75. ISSN: 0370-1573. DOI: https://doi.org/10.1016/j.physrep.2011.02.001. URL: https://www.sciencedirect.com/science/article/pii/S0370157311000457.

[187] B. Margalit and B. Metzger. “Constraining the Maximum Mass of Neutron Stars from Multi-messenger Observations of GW170817”. In: *The Astrophysical Journal Letters* 850.2 (2017). DOI: 10.3847/2041-8213/aa991c.

[188] Ben Margalit and Brian D. Metzger. “Constraining the Maximum Mass of Neutron Stars from Multi-messenger Observations of GW170817”. In: *The Astrophysical Journal Letters* 850.2, L19 (Dec. 2017), p. L19. DOI: 10.3847/2041-8213/aa991c. arXiv: 1710.05938 [astro-ph.HE].

[189] Jérôme Margueron, Rudiney Hoffmann Casali, and Francesca Gulminelli. “Equation of State for Dense Nucleonic Matter from Metamodeling. I. Foundational Aspects”. In: *Phys. Rev. C* 97 (2 Feb. 2018), p. 025805. DOI: 10.1103/PhysRevC.97.025805. URL: https://link.aps.org/doi/10.1103/PhysRevC.97.025805.

[190] Frank J. Masci et al. “The Zwicky Transient Facility: Data Processing, Products, and Archive”. In: *The Astronomical Society of the Pacific* 131.995 (Jan. 2019), p. 018003. DOI: 10.1088/1538-3873/aae8ac. arXiv: 1902.01872 [astro-ph.IM].

[191] Paolo A. Mazzali et al. “A Common Explosion Mechanism for Type Ia Supernovae”. In: *Science* 315.5813 (2007), pp. 825–828. DOI: 10.1126/science.1136259. eprint: https://www.science.org/doi/pdf/10.1126/science.1136259. URL: https://www.science.org/doi/abs/10.1126/science.1136259.

[192] Cody Messick et al. “Analysis framework for the prompt discovery of compact binary mergers in gravitational-wave data”. In: *Phys. Rev. D* 95 (4 Feb. 2017), p. 042001. DOI: 10.1103/PhysRevD.95.042001. URL: https://link.aps.org/doi/10.1103/PhysRevD.95.042001.

[193] B. D. Metzger, E. Quataert, and T. A. Thompson. “Short-duration gamma-ray bursts with extended emission from protomagnetar spin-down”. In: *Monthly Notices of the Royal Astronomical Society* 385.3 (Apr. 2008), pp. 1455–1460. DOI: 10.1111/j.1365-2966.2008.12923.x. arXiv: 0712.1233 [astro-ph].

[194] B. D. Metzger et al. “Electromagnetic counterparts of compact object mergers powered by the radioactive decay of r-process nuclei”. In: *Monthly Notices of the Royal Astronomical Society* 406.4 (June 2010), pp. 2650–2662. ISSN: 0035-8711. DOI: 10.1111/j.1365-2966.2010.16864.x. URL: http://dx.doi.org/10.1111/j.1365-2966.2010.16864.x.

[195] Brian D. Metzger. “Kilonovae”. In: *Living Reviews in Relativity* 23.1 (Dec. 2019). ISSN: 1433-8351. DOI: 10.1007/s41114-019-0024-0. URL: http://dx.doi.org/10.1007/s41114-019-0024-0.

[196] Arthur I. Miller. “A Study of Henri Poincaré’s "Sur la Dynamique de l’Électron"”. In: *Archive for History of Exact Sciences* 10.3/4/5 (1973), pp. 207–328. ISSN: 00039519, 14320657. URL: http://www.jstor.org/stable/41133366 (visited on 04/03/2024).

[197] M Coleman Miller. “Implications of the Gravitational Wave Event GW150914”. In: *arXiv preprint arXiv:1606.06526* (2016). URL: https://doi.org/10.1007/s10714-016-2088-4.

[198] P Yu Minaev and AS Pozanenko. “The E p, i–E iso correlation: type I gamma-ray bursts and the new classification method”. In: *Monthly Notices of the Royal Astronomical Society* 492.2 (2020), pp. 1919–1936.

[199] Anais Möller et al. “fink, a new generation of broker for the LSST community”. In: *Monthly Notices of the Royal Astronomical Society* 501.3 (Nov. 2020), pp. 3272–3288. ISSN: 0035-8711. DOI: 10.1093/mnras/staa3602. eprint: https://academic.oup.com/mnras/article-pdf/501/3/3272/35655965/staa3602.pdf. URL: https://doi.org/10.1093/mnras/staa3602.

[200] A. M. Moore and M. M. Kasliwal. “Unveiling the dynamic infrared sky”. In: *Nature Astronomy* 3 (Jan. 2019), pp. 109–109. DOI: 10.1038/s41550-018-0675-x.

[201] Thomas A. Mooree. *A General Relativity Workbook*. University Science Books, 2013. ISBN: 978-1-891389-82-5.

[202] Elias R. Most et al. "New Constraints on Radii and Tidal Deformabilities of Neutron Stars from GW170817". In: *Phys. Rev. Lett.* 120 (26 June 2018), p. 261103. DOI: 10.1103/PhysRevLett.120.261103. URL: https://link.aps.org/doi/10.1103/PhysRevLett.120.261103.

[203] Norman Murray. "Star formation efficiencies and lifetimes of giant molecular clouds in the Milky Way". In: *The Astrophysical Journal* 729.2 (2011), p. 133.

[204] D. K. Nadyozhin. *Physics of Supernovae: theory, observations, unresolved problems*. 2008. arXiv: 0804.4350 [astro-ph].

[205] Ehud Nakar. "Short-hard gamma-ray bursts". In: *Physics Reports* 442.1-6 (2007), pp. 166–236.

[206] Ramesh Narayan, Shoji Kato, and Fumio Honma. "Global Structure and Dynamics of Advection-dominated Accretion Flows around Black Holes". In: *The Astrophysical Journal* 476.1 (Feb. 1997), p. 49. DOI: 10.1086/303591. URL: https://doi.org/10.1086/303591.

[207] Douglas R. Neill et al. "Baseline design of the LSST telescope mount assembly". In: *Ground-based and Airborne Telescopes V*. Ed. by Larry M. Stepp, Roberto Gilmozzi, and Helen J. Hall. Vol. 9145. International Society for Optics and Photonics. SPIE, 2014, p. 914518. DOI: 10.1117/12.2056432. URL: https://doi.org/10.1117/12.2056432.

[208] M. Nicholl et al. "The Electromagnetic Counterpart of the Binary Neutron Star Merger LIGO/Virgo GW170817. III. Optical and UV Spectra of a Blue Kilonova from Fast Polar Ejecta". In: *The Astrophysical Journal Letters* 848.2 (Oct. 2017), p. L18. DOI: 10.3847/2041-8213/aa9029. URL: https://dx.doi.org/10.3847/2041-8213/aa9029.

[209] Samaya Nissanke, Mansi Kasliwal, and Alexandra Georgieva. "IDENTIFYING ELUSIVE ELECTROMAGNETIC COUNTERPARTS TO GRAVITATIONAL WAVE MERGERS: AN END-TO-END SIMULATION". In: *The Astrophysical Journal* 767.2 (Apr. 2013), p. 124. DOI: 10.1088/0004-637X/767/2/124. URL: https://dx.doi.org/10.1088/0004-637X/767/2/124.

[210] Samaya Nissanke et al. *Determining the Hubble constant from gravitational wave observations of merging compact binaries*. 2013. arXiv: 1307.2638 [astro-ph.CO].

[211] Samaya Nissanke et al. "EXPLORING SHORT GAMMA-RAY BURSTS AS GRAVITATIONAL-WAVE STANDARD SIRENS". In: *The Astrophysical Journal* 725.1 (Nov. 2010), p. 496. DOI: 10.1088/0004-637X/725/1/496. URL: https://dx.doi.org/10.1088/0004-637X/725/1/496.

[212] Alexander H. Nitz et al. “A Search for Gravitational Waves from Binary Mergers with a Single Observatory”. In: *Astrophysical Journal* 897.2, 169 (July 2020), p. 169. DOI: 10.3847/1538-4357/ab96c7. arXiv: 2004.10015 [astro-ph.HE].

[213] Alexander H. Nitz et al. “Rapid detection of gravitational waves from compact binary mergers with PyCBC Live”. In: *Phys. Rev. D* 98 (2 July 2018), p. 024050. DOI: 10.1103/PhysRevD.98.024050. URL: https://link.aps.org/doi/10.1103/PhysRevD.98.024050.

[214] Ken’ichi Nomoto. “The fate of accreting white dwarfs: Type I supernovae vs. collapse”. In: *Progress in Particle and Nuclear Physics* 17 (1986), pp. 249–266. ISSN: 0146-6410. DOI: https://doi.org/10.1016/0146-6410(86)90020-7. URL: https://www.sciencedirect.com/science/article/pii/0146641086900207.

[215] Rich Ormiston et al. “Noise reduction in gravitational-wave data via deep learning”. In: *Phys. Rev. Res.* 2 (3 July 2020), p. 033066. DOI: 10.1103/PhysRevResearch.2.033066. URL: https://link.aps.org/doi/10.1103/PhysRevResearch.2.033066.

[216] Feryal Özel and Paulo Freire. “Masses, Radii, and the Equation of State of Neutron Stars”. In: *Annual Review of Astronomy and Astrophysics* 54.1 (Sept. 2016), pp. 401–440. DOI: 10.1146/annurev-astro-081915-023322. URL: https://doi.org/10.1146%2Fannurev-astro-081915-023322.

[217] Peter T. H. Pang et al. “An updated nuclear-physics and multi-messenger astrophysics framework for binary neutron star mergers”. In: *Nature Communications* 14.1 (Dec. 2023). ISSN: 2041-1723. DOI: 10.1038/s41467-023-43932-6. URL: http://dx.doi.org/10.1038/s41467-023-43932-6.

[218] Peter T. H. Pang et al. *Nuclear-Physics Multi-Messenger Astrophysics Constraints on the Neutron-Star Equation of State: Adding NICER’s PSR J0740+6620 Measurement*. 2021. arXiv: 2105.08688 [astro-ph.HE].

[219] B. Parazin et al. “Foraging with MUSHROOMS: A Mixed-integer Linear Programming Scheduler for Multimessenger Target of Opportunity Searches with the Zwicky Transient Facility”. In: *The Astrophysical Journal* 935.2 (Aug. 2022), p. 87. DOI: 10.3847/1538-4357/ac7fa2. URL: https://dx.doi.org/10.3847/1538-4357/ac7fa2.

[220] F. Pedregosa et al. “Scikit-learn: Machine Learning in Python”. In: *Journal of Machine Learning Research* 12 (2011), pp. 2825–2830.

[221] S. Perlmutter et al. “Measurements of Ω and Λ from 42 High-Redshift Supernovae”. In: *Astrophys. J.* 517 (1999), pp. 565–586. DOI: 10.1086/307221. arXiv: astro-ph/9812133 [astro-ph].

[222] P. C. Peters. “Gravitational Radiation and the Motion of Two Point Masses”. In: *Physical Review* 136.4B (Nov. 1964), pp. 1224–1232. DOI: 10.1103/PhysRev.136.B1224.

[223] Polina Petrov et al. *Data-driven Expectations for Electromagnetic Counterpart Searches Based on LIGO/Virgo Public Alerts*. Jan. 2022. DOI: 10.3847/1538-4357/ac366d. URL: http://dx.doi.org/10.3847/1538-4357/ac366d.

[224] E. Pian et al. “Spectroscopic identification of r-process nucleosynthesis in a double neutron-star merger”. In: *Nature* 551.7678 (Oct. 2017), pp. 67–70. ISSN: 1476-4687. DOI: 10.1038/nature24298. URL: http://dx.doi.org/10.1038/nature24298.

[225] Mikhail Piotrovich et al. “Possible Wormhole Candidates in Active Galactic Nuclei”. In: *Universe* 6.8 (2020), p. 120.

[226] Anthony L. Piro, Annastasia Haynie, and Yuhan Yao. “Shock Cooling Emission from Extended Material Revisited”. In: *The Astrophysical Journal* 909.2 (Mar. 2021), p. 209. ISSN: 1538-4357. DOI: 10.3847/1538-4357/abe2b1. URL: http://dx.doi.org/10.3847/1538-4357/abe2b1.

[227] Planck Collaboration et al. “Planck 2015 results. XIII. Cosmological parameters”. In: *Astronomy & Astrophysics* 594, A13 (Sept. 2016), A13. DOI: 10.1051/0004-6361/201525830. arXiv: 1502.01589 [astro-ph.CO].

[228] Thomas A. Prince et al. “LISA Optimal Sensitivity”. In: *Phys. Rev. D* 66 (12 Dec. 2002), p. 122002. DOI: 10.1103/PhysRevD.66.122002. URL: https://link.aps.org/doi/10.1103/PhysRevD.66.122002.

[229] M Punturo et al. “The Einstein Telescope: a third-generation gravitational wave observatory”. In: *Classical and Quantum Gravity* 27.19 (Sept. 2010), p. 194002. DOI: 10.1088/0264-9381/27/19/194002. URL: https://dx.doi.org/10.1088/0264-9381/27/19/194002.

[230] Kiendrebogogo R. Weizmann et al. *Simulated Detection and Localization in LIGO’s HL- Configuration for O4a Run, and LIGO/Virgo/KAGRA’s HLVK-Configuration for O4b and O5 Runs (November 2023 edition)*. Zenodo, Nov. 2023. DOI: 10.5281/zenodo.10078926. URL: https://doi.org/10.5281/zenodo.10078926.

[231] David Radice et al. “GW170817: Joint Constraint on the Neutron Star Equation of State from Multimessenger Observations”. In: *The Astrophysical Journal Letters* 852.2 (2018), p. L29. URL: http://stacks.iop.org/2041-8205/852/i=2/a=L29.

[232] David Radice et al. “GW170817: Joint Constraint on the Neutron Star Equation of State from Multimessenger Observations”. In: *The Astrophysical Journal Letters* 852.2 (Jan. 2018), p. L29. DOI: 10.3847/2041-8213/aaa402. URL: https://dx.doi.org/10.3847/2041-8213/aaa402.

[233] C L Ransome et al. “A systematic reclassification of Type IIn supernovae”. In: *Monthly Notices of the Royal Astronomical Society* 506.4 (July 2021), pp. 4715–4734. ISSN: 0035-8711. DOI: 10.1093/mnras/stab1938. eprint: https://academic.oup.com/mnras/article-pdf/506/4/4715/39592521/stab1938.pdf. URL: https://doi.org/10.1093/mnras/stab1938.

[234] C. E. Rasmussen and C. K. I. Williams. *Gaussian Processes for Machine Learning*. MIT Press, 2006. ISBN: 978-0-262-18253-9.

[235] J. C. Rastinejad et al. “A Systematic Exploration of Kilonova Candidates from Neutron Star Mergers during the Third Gravitational-wave Observing Run”. In: *Astrophysical Journal* 927.1, 50 (Mar. 2022), p. 50. DOI: 10.3847/1538-4357/ac4d34. arXiv: 2112.09701 [astro-ph.HE].

[236] J. C. Rastinejad et al. “Probing Kilonova Ejecta Properties Using a Catalog of Short Gamma-Ray Burst Observations”. In: *Astrophysical Journal* 916.2, 89 (Aug. 2021), p. 89. DOI: 10.3847/1538-4357/ac04b4. arXiv: 2101.03175 [astro-ph.HE].

[237] David Reitze et al. *Cosmic Explorer: The U.S. Contribution to Gravitational-Wave Astronomy beyond LIGO*. 2019. arXiv: 1907.04833 [astro-ph.IM].

[238] Adam G. Riess et al. “A 2.4% Determination of the Local Value of the Hubble Constant”. In: *Astrophys. J.* 826.1 (2016), p. 56. DOI: 10.3847/0004-637X/826/1/56. arXiv: 1604.01424 [astro-ph.CO].

[239] Adam G. Riess et al. “Observational evidence from supernovae for an accelerating universe and a cosmological constant”. In: *Astron. J.* 116 (1998), pp. 1009–1038. DOI: 10.1086/300499. arXiv: astro-ph/9805201 [astro-ph].

[240] Adam G. Riess et al. “Large Magellanic Cloud Cepheid Standards Provide a 1% Foundation for the Determination of the Hubble Constant and Stronger Evidence for Physics beyond ΛCDM”. In: *Astrophys. J.* 876.1 (2019), p. 85. DOI: 10.3847/1538-4357/ab1422. arXiv: 1903.07603 [astro-ph.CO].

[241] Luke F. Roberts et al. “The influence of neutrinos on r-process nucleosynthesis in the ejecta of black hole–neutron star mergers”. In: *Monthly Notices of the Royal Astronomical Society* 464.4 (2017), pp. 3907–3919. DOI: 10.1093/mnras/stw2622.

[242] I. M. Romero-Shaw et al. “Bayesian inference for compact binary coalescences with bilby: validation and application to the first LIGO–Virgo gravitational-wave transient catalogue”. In: *Mon. Not. Roy. Astron. Soc.* 499.3 (2020), pp. 3295–3319. DOI: 10.1093/mnras/staa2850. arXiv: 2006.00714 [astro-ph.IM].

[243] S. Rosswog, U. Feindt, O. Korobkin, et al. “Detectability of compact binary merger macronovae”. In: *Class. Quant. Grav.* 34.10 (2017), p. 104001. DOI: 10.1088/1361-6382/aa68a9. arXiv: 1611.09822 [astro-ph.HE].

[244] S. Rosswog et al. “Mass ejection in neutron star mergers”. In: *Astronomy & Astrophysics* 341 (Jan. 1999), pp. 499–526. eprint: astro-ph/9811367.

[245] S. Rosswog et al. “Mass ejection in neutron star mergers”. In: *Astronomy & Astrophysics* 341 (Jan. 1999), pp. 499–526. DOI: 10.48550/arXiv.astro-ph/9811367. arXiv: astro-ph/9811367 [astro-ph].

[246] S. Rosswog et al. “The first direct double neutron star merger detection: Implications for cosmic nucleosynthesis”. In: *Astronomy & Astrophysics* 615, A132 (July 2018), A132. DOI: 10.1051/0004-6361/201732117. arXiv: 1710.05445 [astro-ph.HE].

[247] Milton Ruiz, Stuart L. Shapiro, and Antonios Tsokaros. “GW170817, general relativistic magnetohydrodynamic simulations, and the neutron star maximum mass”. In: *Phys. Rev. D* 97 (2 Jan. 2018), p. 021501. DOI: 10.1103/PhysRevD.97.021501. URL: https://link.aps.org/doi/10.1103/PhysRevD.97.021501.

[248] Geoffrey Ryan et al. “Gamma-Ray Burst Afterglows in the Multimessenger Era: Numerical Models and Closure Relations”. In: *The Astrophysical Journal* 896.2 (June 2020), p. 166. ISSN: 1538-4357. DOI: 10.3847/1538-4357/ab93cf. URL: http://dx.doi.org/10.3847/1538-4357/ab93cf.

[249] Muhammed Saleem et al. *Demonstration of Machine Learning-assisted real-time noise regression in gravitational wave detectors*. 2023. arXiv: 2306.11366 [gr-qc].

[250] Edwin E Salpeter. “The luminosity function and stellar evolution.” In: *The Astrophysical Journal* 121 (1955), p. 161.

[251] V. Savchenko et al. “INTEGRAL Detection of the First Prompt Gamma-Ray Signal Coincident with the Gravitational-wave Event GW170817”. In: *The Astrophysical Journal Letters* 848.2 (Oct. 2017), p. L15. ISSN: 2041-8213. DOI: 10.3847/2041-8213/aa8f94. URL: http://dx.doi.org/10.3847/2041-8213/aa8f94.

[252] Gerhard Schäfer and Piotr Jaranowski. “Hamiltonian formulation of general relativity and post-Newtonian dynamics of compact binaries”. In: *Living Reviews in Relativity* 21.1 (Aug. 2018). ISSN: 1433-8351. DOI: 10.1007/s41114-018-0016-5. URL: http://dx.doi.org/10.1007/s41114-018-0016-5.

[253] B. F. Schutz. “Determining the Hubble constant from gravitational wave observations”. In: *Nature* 323 (Sept. 1986), p. 310. DOI: 10.1038/323310a0.

[254] Yuichiro Sekiguchi et al. “Dynamical mass ejection from binary neutron star mergers: Radiation-hydrodynamics study in general relativity”. In: *Phys. Rev. D* 91 (6 Mar. 2015), p. 064059. DOI: 10.1103/PhysRevD.91.064059. URL: https://link.aps.org/doi/10.1103/PhysRevD.91.064059.

[255] Stuart L. Shapiro and Saul A. Teukolsky. *Black holes, white dwarfs and neutron stars. The physics of compact objects*. 1983. DOI: 10.1002/9783527617661.

[256] Masaru Shibata and Kenta Hotokezaka. "Merger and Mass Ejection of Neutron Star Binaries". In: *Annual Review of Nuclear and Particle Science* 69.1 (Oct. 2019), pp. 41–64. ISSN: 1545-4134. DOI: 10.1146/annurev-nucl-101918-023625. URL: http://dx.doi.org/10.1146/annurev-nucl-101918-023625.

[257] Masaru Shibata et al. "Constraint on the maximum mass of neutron stars using GW170817 event". In: *Phys. Rev. D* 100 (2 July 2019), p. 023015. DOI: 10.1103/PhysRevD.100.023015. URL: https://link.aps.org/doi/10.1103/PhysRevD.100.023015.

[258] YU Shun-jing et al. "SVOM: a Joint Gamma-ray Burst Detection Mission". In: *Chinese Astronomy and Astrophysics* 44.2 (2020), pp. 269–282. ISSN: 0275-1062. DOI: https://doi.org/10.1016/j.chinastron.2020.05.009. URL: https://www.sciencedirect.com/science/article/pii/S0275106220300370.

[259] Y. Shvartzvald et al. *ULTRASAT: A wide-field time-domain UV space telescope*. 2023. arXiv: 2304.14482 [astro-ph.IM].

[260] L. P. Singer, L. R. Price, B. Farr, et al. "The First Two Years of Electromagnetic Follow-Up with Advanced LIGO and Virgo". In: *Astrophys. J.* 795.2 (2014), p. 105. DOI: 10.1088/0004-637X/795/2/105. arXiv: 1404.5623 [astro-ph.HE].

[261] Leo Singer, Weizmann Kiendrébéogo, and tnarikawa. *lpsinger/observing-scenarios-simulations: Version 2*. Version v2. Nov. 2022. DOI: 10.5281/zenodo.7305534. URL: https://doi.org/10.5281/zenodo.7305534.

[262] Leo Singer and Judith Racusin. "General Coordinates Network (GCN): NASA's Next Generation Time-Domain and Multimessenger Astronomy Alert System". In: *American Astronomical Society Meeting Abstracts*. Vol. 55. American Astronomical Society Meeting Abstracts. Jan. 2023, 108.02, p. 108.02.

[263] Leo P. Singer and Larry R. Price. "Rapid Bayesian position reconstruction for gravitational-wave transients". In: *Phys. Rev. D* 93 (2 Jan. 2016), p. 024013. DOI: 10.1103/PhysRevD.93.024013. URL: https://link.aps.org/doi/10.1103/PhysRevD.93.024013.

[264] Leo P. Singer et al. "HEALPix Alchemy: Fast All-Sky Geometry and Image Arithmetic in a Relational Database for Multimessenger Astronomy Brokers". In: *The Astronomical Journal* 163.5 (Apr. 2022), p. 209. DOI: 10.3847/1538-3881/ac5ab8. URL: https://dx.doi.org/10.3847/1538-3881/ac5ab8.

[265] Leo P. Singer et al. "THE FIRST TWO YEARS OF ELECTROMAGNETIC FOLLOW-UP WITH ADVANCED LIGO AND VIRGO". In: *The Astrophysical Journal* 795.2 (Oct. 2014), p. 105. DOI: 10.1088/0004-637x/795/2/105. URL: https://doi.org/10.1088%2F0004-637x%2F795%2F2%2F105.

[266] S. J. Smartt et al. “A kilonova as the electromagnetic counterpart to a gravitational-wave source”. In: *Nature* 551.7678 (Oct. 2017), pp. 75–79. ISSN: 1476-4687. DOI: 10.1038/nature24303. URL: http://dx.doi.org/10.1038/nature24303.

[267] Juri Smirnov et al. *White Dwarfs in Dwarf Spheroidal Galaxies: A New Class of Compact-Dark-Matter Detectors*. 2022. arXiv: 2211.00013 [astro-ph.CO].

[268] Joshua S. Speagle. “dynesty: a dynamic nested sampling package for estimating Bayesian posteriors and evidences”. In: *Mon. Not. Roy. Astron. Soc.* 493.3 (2020), pp. 3132–3158. DOI: 10.1093/mnras/staa278. arXiv: 1904.02180 [astro-ph.IM].

[269] Cosmin Stachie. “Compact binary merger searches in the era of multimessenger high energy astrophysics”. Theses. Université Côte d’Azur, Aug. 2021. URL: https://theses.hal.science/tel-03406790.

[270] Nikolaos Stergioulas. “Rotating Stars in Relativity”. In: *Living Rev. Rel.* 6 (2003), p. 3. DOI: 10.12942/lrr-2003-3. arXiv: gr-qc/0302034.

[271] E. Symbalisty and D. N. Schramm. “Neutron Star Collisions and the r-Process”. In: *Astrophysical Letters* 22 (Jan. 1982). Provided by the SAO/NASA Astrophysics Data System, p. 143. URL: https://ui.adsabs.harvard.edu/abs/1982ApL....22..143S.

[272] T. M. Tauris et al. “Formation of Double Neutron Star Systems”. In: *The Astrophysical Journal* 846.2 (Sept. 2017), p. 170. DOI: 10.3847/1538-4357/aa7e89. URL: https://dx.doi.org/10.3847/1538-4357/aa7e89.

[273] I. Tews et al. “Constraining the Speed of Sound inside Neutron Stars with Chiral Effective Field Theory Interactions and Observations”. In: *The Astrophysical Journal* 860.2 (June 2018), p. 149. ISSN: 1538-4357. DOI: 10.3847/1538-4357/aac267. URL: http://dx.doi.org/10.3847/1538-4357/aac267.

[274] Ingo Tews et al. “On the Nature of GW190814 and Its Impact on the Understanding of Supranuclear Matter”. In: *The Astrophysical Journal* 908.1 (Feb. 2021), p. L1. ISSN: 2041-8213. DOI: 10.3847/2041-8213/abdaae. URL: http://dx.doi.org/10.3847/2041-8213/abdaae.

[275] John L. Tonry. “An Early Warning System for Asteroid Impact”. In: *Publications of the Astronomical Society of the Pacific* 123.899 (Dec. 2010), p. 58. DOI: 10.1086/657997. URL: https://dx.doi.org/10.1086/657997.

[276] E. Troja et al. “The outflow structure of GW170817 from late time broadband observations”. In: *Monthly Notices of the Royal Astronomical Society* (Apr. 2018). DOI: 10.1093/mnrasl/sly061. arXiv: 1801.06516 [astro-ph.HE].

[277] E. Troja et al. “The X-ray counterpart to the gravitational-wave event GW170817”. In: *Nature* 551 (Oct. 2017), p. 71. DOI: 10.1038/nature24290. URL: https://doi.org/10.1038/nature24290.

[278] Leo Tsukada et al. “Improved ranking statistics of the GstLAL inspiral search for compact binary coalescences”. In: *Phys. Rev. D* 108 (4 Aug. 2023), p. 043004. DOI: 10.1103/PhysRevD.108.043004. URL: https://link.aps.org/doi/10.1103/PhysRevD.108.043004.

[279] G. Vajente et al. “Machine-learning nonstationary noise out of gravitational-wave detectors”. In: *Phys. Rev. D* 101 (4 Feb. 2020), p. 042003. DOI: 10.1103/PhysRevD.101.042003. URL: https://link.aps.org/doi/10.1103/PhysRevD.101.042003.

[280] V. A. Villar et al. “The Combined Ultraviolet, Optical, and Near-infrared Light Curves of the Kilonova Associated with the Binary Neutron Star Merger GW170817: Unified Data Set, Analytic Models, and Physical Implications”. In: *The Astrophysical Journal Letters* 851.1 (Dec. 2017), p. L21. DOI: 10.3847/2041-8213/aa9c84. URL: https://dx.doi.org/10.3847/2041-8213/aa9c84.

[281] Coughlin Michael W et al. “Implications of the search for optical counterparts during the first six months of the Advanced LIGO’s and Advanced Virgo’s third observing run: possible limits on the ejecta mass and binary properties”. In: *Monthly Notices of the Royal Astronomical Society* 492.1 (Dec. 2019), pp. 863–876. ISSN: 0035-8711. DOI: 10.1093/mnras/stz3457. eprint: https://academic.oup.com/mnras/article-pdf/492/1/863/31760484/stz3457.pdf. URL: https://doi.org/10.1093/mnras/stz3457.

[282] Stéfan J. van der Walt, Arien Crellin-Quick, and Joshua S. Bloom. “SkyPortal: An Astronomical Data Platform”. In: *Journal of Open Source Software* 4.37 (May 2019). DOI: 10.21105/joss.01247. URL: http://joss.theoj.org/papers/10.21105/joss.01247.

[283] Stéfan J. van der Walt, Arien Crellin-Quick, and Joshua S. Bloom. “SkyPortal: An Astronomical Data Platform”. In: *Journal of Open Source Software* 4.37 (May 2019). DOI: 10.21105/joss.01247. URL: http://joss.theoj.org/papers/10.21105/joss.01247.

[284] Shinya Wanajo et al. “Production of All the r-process Nuclides in the Dynamical Ejecta of Neutron Star Mergers”. In: *The Astrophysical Journal Letters* 789.2 (2014), p. L39. URL: http://stacks.iop.org/2041-8205/789/i=2/a=L39.

[285] J. M. Weisberg and Y. Huang. “RELATIVISTIC MEASUREMENTS FROM TIMING THE BINARY PULSAR PSR B1913+16”. In: *The Astrophysical Journal* 829.1 (Sept. 2016), p. 55. DOI: 10.3847/0004-637X/829/1/55. URL: https://dx.doi.org/10.3847/0004-637X/829/1/55.

[286] Norbert Wiener. “Extrapolation, Interpolation, and Smoothing of Stationary Time Series, with Engineering Applications”. In: 1949. URL: https://api.semanticscholar.org/CorpusID:125829144.

[287] R. T. Wollaeger et al. “A Broad Grid of 2D Kilonova Emission Models”. In: *The Astrophysical Journal* 918.1 (Aug. 2021), p. 10. DOI: 10.3847/1538-4357/ac0d03. URL: https://doi.org/10.3847/1538-4357/ac0d03.

[288] Stan E Woosley. “Gamma-ray bursts from stellar mass accretion disks around black holes”. In: *Astrophysical Journal, Part 1 (ISSN 0004-637X), vol. 405, no. 1, p. 273-277.* 405 (1993), pp. 273–277.

[289] Meng-Ru Wu et al. “Production of the entire range of r-process nuclides by black hole accretion disc outflows from neutron star mergers”. In: *Monthly Notices of the Royal Astronomical Society* 463.3 (2016), pp. 2323–2334. DOI: 10.1093/mnras/stw2156. URL: +%20http://dx.doi.org/10.1093/mnras/stw2156.

[290] Zhihan Yuan. “A critical review on Hubble tension”. In: (2021).